R CORONAE BOREALIS STARS: CHARACTERISTICS OF THEIR DECLINE PHASE

by

Ljiljana Skuljan

A THESIS

SUBMITTED IN PARTIAL FULFILMENT

OF THE REQUIREMENTS FOR THE DEGREE OF

DOCTOR OF PHILOSOPHY IN ASTRONOMY

IN THE UNIVERSITY OF CANTERBURY

University of Canterbury

2001

Abstract

R Coronae Borealis (RCB) stars belong to a rare class of variable stars characterized by sudden and unpredictable declines, which are believed to be caused by dust cloud obscuration. In spite of the fact that these stars are so rare (only about 40 are known in our Galaxy), there are many reasons for investigating them. The unusual variability and peculiar chemical composition make them unique among all known types of variable stars. Their evolution and the nature of their unpredictable minima are still not entirely understood. Very few observations of RCB stars during the decline phase exist. Only three RCB stars (R CrB, RY Sgr and V854 Cen) have been studied in detail and only a few declines have been completely covered by observations.

This thesis investigates the spectroscopic and photometric characteristics of RCB variables during their decline phases. A programme of photometric and spectroscopic observations of nine RCB and three HdC stars has been undertaken at Mt John University Observatory (MJUO) over a period of two and a half years. The programme includes some typical examples of RCB stars ($T_{\mathrm{eff}} \sim 7000$ K), as well as some cool ones ($T_{\mathrm{eff}} \sim 5000$ K). One of the most unusual of all RCB stars, V854 Cen, is also included.

The photometric observations, as part of the long-term monitoring of RCB stars at MJUO, have provided the *UBVRI* photometry and have served as a decline indicator. Complex colour changes during the declines were monitored and compared with the spectroscopy. The photometry during the recovery phases of the nine RCB stars in the last 12 years was used for studying the extinction properties of the gas obscuring the photosphere. An analysis of 26 different declines shows that the material causing the declines has extinction properties similar to those of the interstellar medium.

The medium and high-resolution spectroscopy has been obtained for six declines of different programme stars using the 1-m telescope at MJUO. Although the duration and depth of the declines are very different, they all show similar photometric and spectroscopic characteristics. The results have been compared with other observations and used to examine a simple line-region model ($\mathrm{E_1/E_2/BL}$), which attempts to describe the evolution and origin of emission lines during a decline. In general, the evolution of various emission lines observed in this work is consistent with their classification into these three groups. However, some characteristics of the emission lines indicate a different origin from that suggested by the model.

A very rich emission line spectrum was monitored during the 1998 decline of V854 Cen, while only the most prominent lines were observed in the other stars. Short-lived high-excitation lines from the initial decline phase, such as CI and OI, were classified as E_1. They show a characteristic, shock-induced red shift indicating the photospheric origin. Lines classified as E_2 are mainly from the low-excitation ions and neutral atoms. All lines from this group appear at the very beginning of the decline and are visible through to the late recovery phase, slightly blue-shifted relative to the stellar velocity. The lines of the low-excitation ions exhibit a complex structure with a strong central and two weaker components, one on each side. Their absolute flux evolution has been compared with the changes in the stellar continuum flux. The behaviour of these lines indicates that they are not affected by the dust cloud in the same way as the photospheric continuum. Assuming that the dust cloud is formed at about $2\,R_*$ and taking into account the acceleration obtained from the analysis of the high-velocity NaI D absorption lines, the position of the E_2 line emitting region was estimated to be about $3\,R_* - 5\,R_*$.

The third group (BL) consists of broad emission lines, which are a typical feature of all observed declines. The most prominent broad lines present in all RCB stars belong to the NaI D doublet. The observations demonstrate that these lines are the strongest in V854 Cen, due to the significant amount of material produced by its frequent declines. In contrast to the E_2 lines, whose fluxes have been found to decrease during the decline, the absolute flux of the broad lines stays constant throughout the whole decline phase. This is consistent with the idea that the broad emission is a permanent feature, whose visibility depends only on the photospheric brightness.

Various NaI D components (sharp and broad emission and high-velocity absorption) have been analysed in a number of RCB declines and presented in this thesis. The high-velocity blue-shifted NaI D absorption demonstrates similar velocities (between -230 km s^{-1} and -400 km s^{-1}), structure and behaviour in the different declines. The observations from the 1998 decline of V854 Cen clearly show that the high-velocity absorption lines can also appear during the initial decline phase. This suggests that they can be associated with the clouds formed in some previous declines, as well as with the current one. The spectroscopic observations of the 1998 decline of V854 Cen obtained in this thesis represent the first almost complete coverage of a decline of this star.

Contents

Chapter 1

Introduction

1.1   R Coronae Borealis stars as a class of variable stars

R Coronae Borealis (RCB) stars belong to a rare class of variable stars exhibiting quite unique variability. Their spectacular light fadings occur at irregular intervals, when the star declines rapidly by up to six magnitudes in a few weeks (see Figure 1.2). The recovery to normal light is significantly slower and may take months, or even years. The characteristic light curve of RCB stars distinguishes these objects from other classes of variable stars. The evolutionary status of RCB stars still remains unsolved. Only a small number of these stars have been observed: about 40 in our Galaxy (Milone 1990) and 13 in the LMC (Clayton et al. 2000, Alcock et al. 2001). This indicates either that they represent a rare and peculiar phase of evolution, or a common, but rapidly evolving stage. Both the unique nature of their variability and their unsolved evolutionary status make the RCB stars extremely interesting objects for study.

The prototype of the class was discovered about two hundred years ago, when Edward Pigott noticed a sudden fading of a star in the Northern Crown (Corona Borealis) by about five magnitudes (Pigott 1797). The star was later named R CrB and it is still the brightest RCB star known. At the beginning of the 20th century the first emission line spectrum from the decline phase was observed by Joy & Humason (1923). The first generally accepted model of RCB declines was suggested by Loreta (1934) and later by O'Keefe (1939). The model provided a basis for the explanation of RCB declines. The shape of the light curve and the evolution of the decline spectra were explained by the formation of a *carbon dust cloud* obscuring the star.

Over the last three decades numerous observations covering the decline phases of various RCB stars have been collected, providing an opportunity for a more detailed study. Since the RCB declines are unpredictable and the stars become relatively faint (down to 16^{m} in some cases), it is difficult to cover the whole decline phase, especially spectroscopically. Only a few declines of the brightest RCB stars have been monitored completely: the 1967 decline

of RY Sgr (Alexander et al. 1972), the 1988 decline of R CrB (Cottrell et al. 1990) and
the 1995/96 decline of R CrB (Rao et al. 1999). In addition, some sporadic observations
are available for a number of declines of R CrB, RY Sgr and V854 Cen. Extensive UV
spectroscopic coverage is also available for the 1982/83 and 1990/91 declines of RY Sgr
(Clayton et al. 1992a) and the 1991-94 declines of V854 Cen (Lawson et al. 1999). However,
the observational data so far have been insufficient for a satisfactory explanation of the
most important characteristics of RCB declines, including the processes triggering the light
fading, as well as the origin of the emission line spectra. Additional long-term, extensive
and simultaneous spectroscopic and photometric coverage of the decline phases of different
RCB stars, together with a more detailed model are required (Cottrell 1996) for a better
understanding of these unusual variable stars.

A majority of the RCB stars spectroscopically look like F–G supergiants, but with rel-
atively strong carbon lines and either weak or absent hydrogen lines (Clayton 1996). From
a sample of 18 RCB stars, Lambert & Rao (1994) found that 14 of them have a similar
chemical composition. Typically, hydrogen is under-abundant by a factor of 10^5, while car-
bon is over-abundant by a factor of 10 compared to normal stars. Nitrogen and sodium are
also over-abundant (Lambert & Rao 1994). Four stars were found to have rather unusual
composition (hydrogen-rich and iron-poor).

Most of the Galactic RCB stars have an effective temperature of about 7000 K (Lambert
& Rao 1994). However, a few stars show extreme values, from about 4000 K for S Aps and
WX CrA up to about 20000 K for the warm B-type stars (DY Cen and V348 Sgr). The
absolute brightness, M_V, in the range -4^m to -5^m ($L_* \approx 10^4 L_\odot$) was determined from a few
RCB stars in the LMC (Feast 1979), using their apparent magnitudes and the distance to the
LMC. A low mass of RCB stars (with a typical value of $0.8 - 0.9\ M_\odot$) was determined from
the evolutionary and pulsation studies (Weiss 1987). With a radius of about $50 - 100\ R_\odot$
and a surface gravity of $\log g \sim 0.5$, the RCB stars can be classified as supergiants.

The distribution of the RCB stars in our Galaxy (towards the galactic centre), and their
radial velocities, show that the majority of these stars belong to an older galactic population.
The parallaxes and proper motions (with high uncertainties) are known only for the brightest
RCB stars, as obtained by Hipparcos (Trimble & Kundu 1997, Cottrell & Lawson 1998).

In addition to the basic characteristics of the RCB stars described above, a number of
photometric and spectroscopic studies have revealed some new details characterizing both
the maximum light and the decline behaviour:

- All RCB stars show a variability at light maximum, with typical periods between 40
  and 100 days and with amplitudes between $0^m\!.1$ and $0^m\!.5$. It is believed that these
  variations are due to stellar pulsations, as confirmed from the observations of a few
  RCB stars (Clayton 1996, Lawson et al. 1992). Two RCB stars, RY Sgr and V854
  Cen, have well-determined regular pulsations of 38 and 43 days, respectively (Lawson

et al. 1990). On the other hand, the declines occur at irregular intervals. However, it seems that in the case of these two stars the time of the decline onset is correlated with the pulsation phase.

- A study of the radial-velocity variations (typically between ± 5 km s^{-1} and ± 10 km s^{-1}, but as high as ± 20 km s^{-1} in RY Sgr) shows a correlation with the magnitude variations (Lawson et al. 1990). The line splitting, interpreted as an indicator of a shock-wave propagating through the atmosphere, has been detected only in RY Sgr, which shows the highest radial-velocity variations (Lawson et al. 1991). The splitting was also found to be correlated with the pulsation period of the star (Cottrell & Lambert 1982, Lawson et al. 1991). A correlation between the equivalent widths of the absorption lines of the C_2 Swan and CN bands and the pulsation phase has been detected in R CrB (Clayton et al. 1995).

- The infrared photometry of RCB stars shows a clear IR excess due to circumstellar dust. The IR flux exhibits regular variations reflecting the photospheric pulsations. Neither these variations nor the total flux level change when a decline starts (Feast 1979). In addition, large long-term variations of the IR flux have been detected in RCB stars (Glass 1978). The temperature of the dust surrounding an RCB star, obtained from the IR photometry, is in the range 600 K to 900 K (Kilkenny & Whittet 1984). The dust extends to a distance of $10R_*$ to $90R_*$ (Walker 1985). It is still not clear whether the RCB stars undergo a continuous mass loss in addition to the one producing the obscuring dust cloud. The estimated mean rate of the mass loss ($d\mathfrak{M}/dt$) during a decline is in the range 3×10^{-8} to 1×10^{-6} $\mathfrak{M}_\odot$ per year (Fadeyev 1988).

1.2 Evolutionary models of RCB stars

The extreme hydrogen deficiency and a relatively high abundance of numerous heavy elements in RCB stars suggest that these stars are passing through a late evolutionary stage. In an H-R diagram the stars are located off the tip of the asymptotic giant branch (AGB), as seen in Figure 1.1.

The evolutionary origin of RCB stars is still not well understood. One cannot explain these stars as objects passing through the stage immediately following the AGB phase, considering the short time scale for reaching the planetary nebula (Asplund 1997). It turns out to be very difficult to achieve the required chemical composition (i.e. hydrogen-deficiency) through the mass loss characterizing this stage of the evolution. Two alternative evolutionary models of RCB stars have been considered in the last two decades: **F**inal helium-shell **F**lash (FF) and **D**ouble **D**egenerate (DD) models. In both cases, RCB stars are considered to be new-born supergiants, that have already started their final evolution towards the white
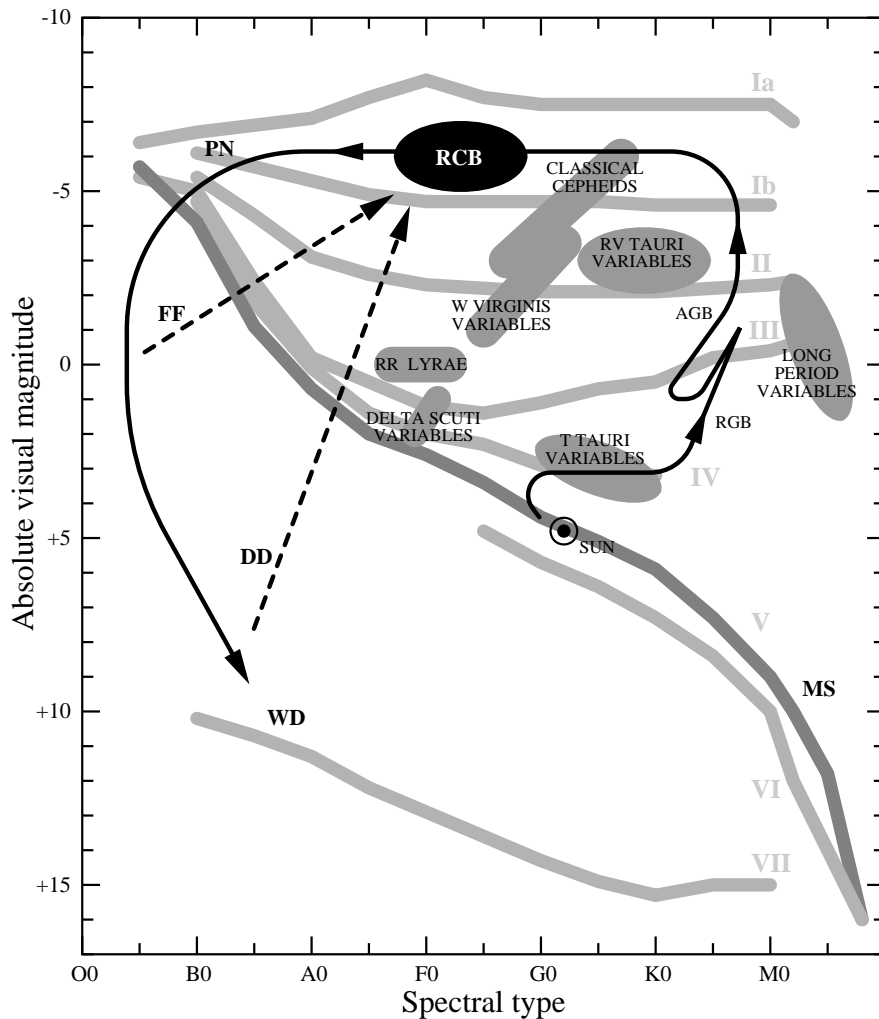
Figure 1.1: *Evolutionary models of RCB stars (adapted from Asplund 1997). From the main sequence (MS), a low-mass star evolves up along the red-giant branch (RGB). Then the star passes through the He-core flash before reaching the horizontal branch and the asymptotic giant branch (AGB). After this the star will rapidly evolve through a planetary-nebula stage (PN) before cooling down towards a white dwarf (WD). The RCB stars, however, have been suggested not to come directly from the AGB stage, but to be giants that were born-again through a final He-shell flash in a post-AGB star (FF model) or through a merging of two white dwarfs (DD model).*

dwarf stage (Figure 1.1). The FF model suggests that an RCB star originates from a white dwarf experiencing a final helium-shell flash (Renzini 1990). On the other hand, the DD model is based on a merging process of a close binary system of He and CO white dwarfs. The result is a single star with a helium-burning shell in the centre of a hydrogen-deficient envelope (Webbink 1984).

Neither of the two models mentioned above provides a satisfactory agreement with observations. The FF model predicts too short a lifetime for an RCB star (only about 100

years), while in the case of the DD model, the estimated number of CO-He white dwarf binary systems is too small to produce a sufficient number of RCB stars. Also, neither of the models can explain the peculiar composition of some RCB stars (Clayton 1996). In the case of the FF model, one should expect that the star is still surrounded by a planetary nebula. Indeed, this was observed in R CrB and UW Cen (Pollacco et al. 1991), but for most of the RCB stars the nebula has not been detected. It is also believed that the recently discovered Sakurai's object could be a new-born RCB star that has recently experienced the final He-shell flash (Asplund et al. 1997). The object is still surrounded by the nebula and has a chemical composition similar to RCB stars. The discovery of Sakurai's object provides strong support for the FF model, in which case some other processes have to be responsible for the peculiar abundance of the minority of RCB stars.

The RCB stars are also closely related to the other two groups of hydrogen-deficient stars: hydrogen-deficient carbon stars (HdC) and extreme helium stars (EHe). The chemical composition is similar, but the latter two groups do not exhibit a decline behaviour and do not show any IR excess (Clayton 1996). In addition, some of the EHe stars are spectroscopic binaries, which is not the case in RCB and HdC stars. There is also a belief that the HdC stars might be progenitors of the RCB stars, while the EHe stars are their descendents (Warner 1967, Jeffery 1996 and Asplund 1997).

1.3 Declines of RCB stars

The RCB stars are distinguished from other hydrogen-deficient carbon stars by their spectacular decline events, occurring at irregular intervals (Figure 1.2). During these phases the star exhibits many complex photometric and spectroscopic changes. Extensive and detailed studies of these changes from a number of different declines reveal important information on the nature of the declines and the origin of these unusual stars. Solving the problem of the origin of the RCB stars would also contribute to a better understanding of the final stages of stellar evolution. In addition, these stars are good laboratories for studying the complex processes of dust formation.

The RCB stars spend most of their lives at light maximum. A typical interval between two consecutive declines is roughly a few years. However, the frequency of the declines is different from one star to another. The star can remain at maximum light for several years before the next fading occurs, but sometimes a new fading can also start immediately, or even while the star is returning to its normal brightness. For example, XX Cam has had only one recorded (and brief) decline in the last hundred years, while V854 Cen has a decline almost every year, straight after recovering from the previous one (Clayton 1996). A typical RCB decline consists of a steep and short initial phase (typically a few weeks long) and a significantly slower recovery stage, that can take months, or even years. However the light
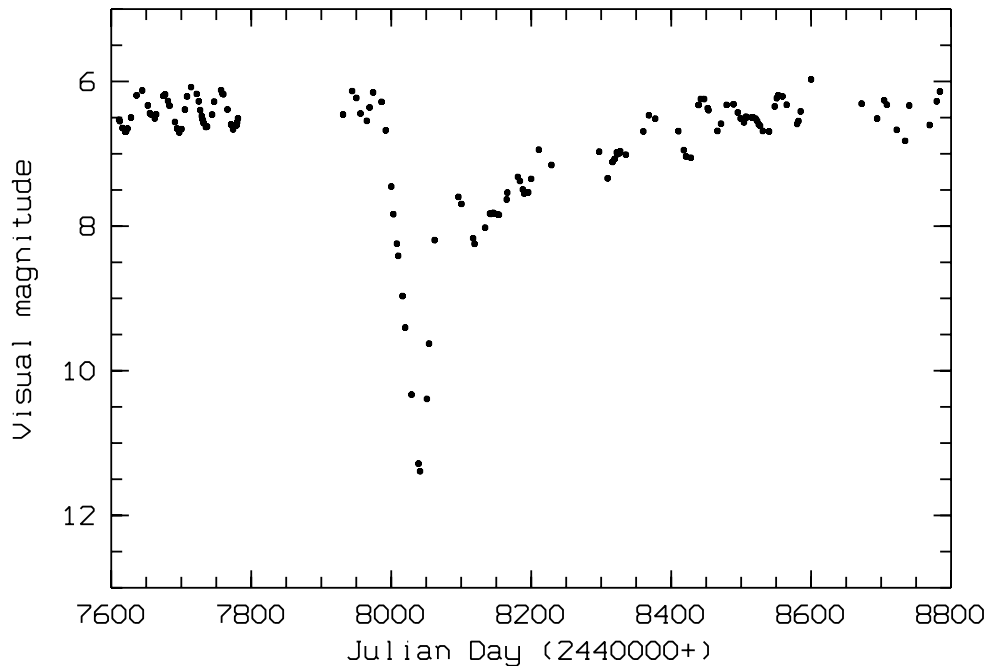
Figure 1.2: *A typical light curve of an RCB star (RY Sgr).*

curves show significant differences in their depth, duration and shape from one decline to another and from one star to another. Very often a decline exhibits a complex structure, with a number of subsequent fadings and partial recoveries. Also, the star can spend an extended period of time at minimum, or it can start recovering straight away.

In spite of the fact that RCB stars exhibit some differences in their temperatures and chemical compositions, they all show similar light curves. This indicates that a common physical mechanism seems to be responsible for all declines. As already mentioned above, the most generally accepted explanation of the RCB declines was proposed by Loreta (1934) and O'Keefe (1939). The characteristic variability of the RCB stars is explained by this model as an occultation event. A dust cloud is occasionally formed somewhere around the star and accelerated due to radiation pressure. When the cloud forms along the line of sight it will obscure the star and a decline will start. This scenario can explain the existence of light curves having different shapes, depths and durations. Each successive drop in brightness within a decline can be explained by a new dust cloud forming.

Many observational facts and theoretical calculations support the dust cloud hypothesis. An empirical model, developed by Pugach (1984) shows that the light curve and colour variations can be explained simply by the expansion of the dust cloud of a constant mass at a fixed location in front of the star. In this case, a decline is explained as a result of geometrical characteristics of a cloud moving away from the star. The dust cloud hypothesis is also supported by the infrared photometry. No photometric changes have been observed in the IR region during the decline, indicating that only a small amount of dust is produced

in any one decline and the dust does not form as a complete shell around the star (Clayton 1996). However, since all RCB stars show a significant IR excess, this suggests that there is a large amount of dust produced around the star through a number of dust formations occurring off the line of sight. For example, one of the RCB stars, Y Muscae, has not gone into a decline recently (Clayton 1996), but nevertheless the star has a significant IR excess indicating a dust shell similar to other 'active' RCB stars.

The photometric observations during a decline show that the fadings are always characterized by complex colour variations. During the initial phase the $B - V$ and $U - B$ colours can appear either bluer ('blue-type' decline, Cottrell et al. 1990), or redder ('red-type' decline) than at maximum light. As the star gets brighter (during the recovery phase) a strong reddening is observed, until the star returns to its normal brightness and colour. This reddening also indicates the obscuration of the photosphere by some kind of dust surrounding the star. The blueing in the early decline phase has been explained by the appearance of an additional light source, mainly in the form of line emission in the range 3900 Å to 5700 Å (Clayton et al. 1992b, Asplund 1995). In general, the colour variations depend on the actual amount of the photosphere and emission regions that are obscured by the dust.

Decline spectra

Probably the most interesting feature of an RCB decline is a rich emission-line spectrum that differs significantly from the normal absorption-line maximum light spectrum. When the dust cloud obscures the photosphere, the emission from the chromosphere and other surrounding regions becomes visible. This provides an opportunity (not found in other stars) to study various faint emission line regions surrounding the star.

The first extensive spectroscopic study of a decline was made by Alexander et al. (1972) of the 1967 decline of RY Sgr. Apart from this example, only a few detailed studies of other declines have been published (Cottrell et al. 1990, Rao et al. 1999). A number of other works offer only a partial decline coverage of the three brightest RCB stars: R CrB, RY Sgr and V854 Cen (in the visual region: Spite & Spite 1979, Lambert et al. 1990b, Rao & Lambert 1993, Vanture & Wallerstein 1995, Asplund 1995, Lawson 1992 and Rao & Lambert 2000; in the UV region: Clayton et al. 1992a and Lawson et al. 1999).

As the total intensity of the photospheric spectrum decreases, a rich emission line spectrum appears. Some of these lines are visible only during the initial decline phase, while the others stay in emission throughout the whole decline. The broad emission lines (such as CaII H&K and NaI D) are dominant especially during the late recovery phase. In addition to these emission components, a high-velocity NaI D absorption can be observed. As the star recovers, the photospheric absorption spectrum reappears and dominates the stellar light. Some spectroscopic changes prior to the decline onset were reported by Rao et al. (1999), as a distortion in the absorption profiles of the high-excitation lines, followed by the emission.

A typical decline spectrum of an RCB star consists of several different groups of spectral lines. The first classification of lines was made by Alexander et al. (1972), based on the line evolution throughout the decline. Three distinct groups of lines, named as E_1, E_2 and BL^1, were suggested by this model. However, in order to account for some new observational results, Rao et al. (1999) introduced a somewhat different classification of spectral lines: sharp emission lines, broad emission lines, onset related lines and shell absorption. This classification is more appropriate for the entire set of lines appearing during the decline. In addition, from a long series of the UV decline spectra of V854 Cen, obtained between 1991 and 1994, Lawson et al. (1999) reported a large variability in the line behaviour between declines, that is inconsistent with the simple $E_1/E_2/BL$ classification. For example, the Mg UV lines, expected to behave like BL lines in the visual region, were found to exhibit rapid variations similar to the E_1 and E_2 lines. Moreover, the typical time-scale for the emission line decay was found to vary from one decline to another. As suggested by Lawson et al. (1999), this can be explained by the initial size, extent and evolution of the obscuring dust cloud, as well as by the direction of motion of the cloud with respect to the line of sight.

E_1 lines. The largest group of spectral lines appearing during an RCB decline includes sharp emission lines of neutral and singly-ionized metals (such as MgI, SiI, CaI, FeI, ScII, TiII, BaII, YII, LaII and FeII). Some of these lines are short-lived (10–30 days) and are classified as E_1, according to Alexander et al. (1972). They have been observed with a blue shift of about 10 $km\,s^{-1}$ relative to the photospheric velocity (Clayton 1996). Their origin has been associated with the region closest to the star ('E_1 region'), that becomes obscured first during the decline (Alexander et al. 1972). On the other hand, Rao et al. (1999) found evidence for a connection between the E_1 group and the decline onset. The same authors extended the list to include the higher-excitation lines (with lower excitation potential, $\chi_L \geq 6$ eV) of CI, OI, SiII, CaI and KI. Rao et al. (1999) also noted that this spectrum is quite similar to the spectrum near maximum light, only with the lines in emission instead of absorption.

E_2 lines. The E_2 group consists of low-excitation emission lines of ScII, TiII, YII, BaII and FeII (Alexander et al. 1972). The lines are present throughout the whole decline phase. They typically fade in 50 to 150 days (Clayton 1996). The lines have been observed blue-shifted by about 10 $km\,s^{-1}$ relative to the stellar velocity (Clayton 1996) similar to the E_1 group. Rao et al. (1999) classified these lines during the 1995/96 decline of R CrB as low-excitation sharp emission lines. During this decline the low-excitation lines were seen composed of three components (with two side components slightly broader than the central one). The lines were not found to be affected by the decline in any way except in the total flux later during the decline. Their velocity, profile and degree of excitation and ionization stayed unchanged from the decline onset to the recovery phase. In addition, a line doubling

---

[1]Emission 1, Emission 2 and Broad Line groups.

in the cores of the ScII 4246 Å and NaI D lines was reported by Payne-Gaposchkin (1963) and confirmed by Lambert et al. (1990b) and Rao et al. (1999). This is interpreted as emission that stays visible during the light maximum, disturbing the absorption profiles. All of these observational facts support the idea that the E_2 lines are permanent features, visible mainly during the decline, when the photospheric continuum is significantly fainter. The observed decrease in the flux later during the decline can be explained by the obscuration of the line emitting region by the dust cloud. Some E_2 spectral lines can also be blended with the E_1 lines, especially singly-ionized metals: FeII, BaII, YII (Rao et al. 1999). This makes their behaviour more complex and difficult to study.

BL lines. Broad emission lines (BL) were first detected by Herbig (1949) during the 1948/49 decline of R CrB. They have also been observed during some other RCB declines (R CrB: Cottrell et al. 1990, Rao et al. 1999; V854 Cen: Whitney et al. 1992, Lawson 1992, Clayton et al. 1993b, Rao & Lambert 1993; RY Sgr: Asplund 1995; S Aps: Goswami et al. 1997, Skuljan & Cottrell 1999; MV Sgr: Pandey et al. 1996). The BL spectrum includes various lines, dominated by the low excitation lines of CaII H&K and NaI D (Clayton 1996). In addition, the lines of the CaII IR and MgI triplets, KI resonant lines, H_α, as well as the high-excitation lines of HeI, have been detected with broad components (Cottrell et al. 1990, Goswami et al. 1997, Rao et al. 1999). During the deep 1992 decline of V854 Cen (Rao & Lambert 1993) the forbidden lines of [OI], [SII] and [NII] were also identified with broad components. The list has been extended in the UV region with the lines of [CII], [CIII], MgII 2800 Å, MgI 2852 Å and CI (Lawson et al. 1999). The broad lines have a FWHM of about 200 km s^{-1}. They remain unpolarized during the decline, according to an observation of V854 Cen (Whitney et al. 1992), while the continuum is significantly polarized (up to 14% during the decline, compared to 0.1% at light maximum). The unpolarized emission lines suggest that the emission region is well separated from the dust cloud and not affected by the dust formation.

Shell absorption. The shell absorption components have been observed as parts of the NaI D and CaII H&K profiles mainly during the recovery phase (Vanture & Wallerstein 1995, Clayton et al. 1993b, Rao & Lambert 1993, Cottrell et al. 1990, Skuljan & Cottrell 1999). The lines have been identified at radial velocities of about -200 km s^{-1}. During the 1988 decline of R CrB (Cottrell et al. 1990) the shell absorption was observed during the initial decline phase as well. The components are supposed to originate from the gas dragged along with the dust cloud responsible for the decline (Clayton 1996).

Photospheric absorption. The photospheric absorption lines seem to stay unchanged during the early decline phase. However, a weakening of the absorption lines was noticed by Herbig (1949) during the deep minimum. At this stage the stellar surface is completely obscured by the dust cloud and the observed continuum is mainly composed of the photons scattered by the surrounding gas. The weakening of the photospheric absorption lines

was explained by a superimposed continuous and/or line emission (Payne-Gaposchkin 1963, Clayton 1996, Rao et al. 1999).

Models of RCB stars

A complete and satisfactory model of RCB stars that would be able to explain all observational facts has not yet been developed. The decline characteristics that have to be considered include the appearance and evolution of the emission line spectra during the decline, a possible correlation between the stellar pulsation and the beginning of the decline, as well as the characteristics of the high-velocity absorption (i.e. matching the time-scales of the dust cloud acceleration and dissipation with the duration of the decline).

The first model (Loreta 1934, O'Keefe 1939), based on the obscuration of the stellar photosphere by the dust cloud, is supported by the shape of the light curve and the evolution of the emission line spectra. However, the question of where and how the dust cloud forms and accelerates still remains unsolved. In general, two different approaches have been considered: a dust cloud forming far from the star, at about $20R_*$ (Loreta 1934, Fadeyev 1988), or close to the star, at about about $2R_*$ (Payne-Gaposchkin 1963).

The dust causing the decline has been proposed to be made of *amorphous* carbon (Hecht et al. 1984), which needs a temperature of about 1500 K to condense. Fadeyev (1988) first applied the classical nucleation theory to the RCB dust condensation, assuming homogeneous nucleation of carbon dust in a thermodynamic equilibrium. According to this calculation, the condensation of the dust at this temperature is possible only outside of about $20R_*$. The cloud then moves away and can obscure the photosphere and parts of the emitting regions. The main problem with this model is explaining the observed correlation between the stellar pulsation cycle and the decline onset found in two RCB stars, RY Sgr and V854 Cen. This is difficult to achieve assuming the dust cloud forming at $20\ R_*$. Also, this model cannot explain relatively short recovery times in some declines and the appearance of the high-velocity absorption. On the other hand, all these features can easily be explained by the $2R_*$ model (Clayton 1996), but it is difficult to get such a low condensation temperature close to the star. Recent work by Woitke et al. (1996) suggests that the temperature of the cloud can drop below 2000 K close to the star if non-LTE is considered, for example in the case of a shock wave propagating through the outer atmosphere. In such a model carbon monoxide (CO) plays an important role, since it radiates energy very efficiently. The CO bands have been detected in some RCB stars (Lambert 1986, Clayton et al. 1999b). Most recent studies (Rao et al. 1999, Rao & Lambert 2000) also provide some facts in favour of the dust formation closer to the star. In the first work, changes in the photospheric absorption spectra were observed prior to the decline, indicating that the triggering mechanism might be connected to the shock wave propagating through the atmosphere. In the second work, the molecular absorption lines of the C_2 Phillips system were identified in the spectra of

V854 Cen during the deep 1998 decline. The existence of this system suggests a relatively cold gas, below the condensation temperature for carbon.

In addition to the first RCB model described above, some alternative models have also been considered. One of them is based on a bipolar nebula with a high-velocity bipolar wind and a dusty equatorial torus with a radius of about $50R_*$ (Rao & Lambert 1993, Clayton et al. 1997). The thick torus of dust can obscure the photosphere and cause a decline, while the chromosphere is only partially covered. In such a case, the sharp emission lines originate from the unobscured regions of the stellar chromosphere, while the broad lines are attributed to the bipolar flow.

Another model, suggested by Humphreys & Ney (1974), includes a cool secondary star with an optically thick dust envelope that causes the decline. Such binary models have difficulties in explaining the asymmetry of the light curve and the irregularity of the declines. In addition, no observational evidence for a binary system in RCB stars have been reported so far. A similar binary system, with a compact white dwarf as a companion, was suggested for R CrB by Rao et al. (1999). The gas can flow from the main star through the accretion disk towards the white dwarf. This model provides a natural explanation for the source of excitation of the broad emission lines (including HeI). In this scenario the broad lines originate from the accretion disk. The line broadening is due to the motion of the gas in the disk close to the white dwarf. The optically thick broad lines (such as HeI) are emitted by the inner regions of the disk, while the lower-excitation lines (such as the NaI D and the forbidden lines) originate from the cooler outer regions. The shift of broad emission lines relative to the stellar radial velocity (found in some RCB stars) can be interpreted as the orbital motion of the broad line emitting region. If the RCB stars can be explained as binary systems, this would also support the DD evolutionary model described above. However, no proof has been found for the radial velocity variations of the star and/or the broad line emitting region.

Emission line regions

The idea of a dust cloud causing an RCB decline is also supported by the evolution and general behaviour of the spectral lines appearing during the decline. The sequential order in which the spectral lines decay, starting with the high-excitation sharp lines early in the decline, and followed by the low-excitation sharp and broad lines, as the decline progresses, is in agreement with the dust cloud model (Payne-Gaposchkin 1963). Alexander et al. (1972) noted that the fading of the emission lines during the decline phase makes sense if the star is surrounded by three distinct emission regions responsible for the E_1, E_2 and BL emission. Since the E_1 spectral lines decay first during the decline, the region responsible for this emission must have the smallest radius ($1.5R_* - 2R_*$). Then the E_2 and BL regions have to be at somewhat larger distances of about $10R_*$ (Clayton 1996). All these regions become
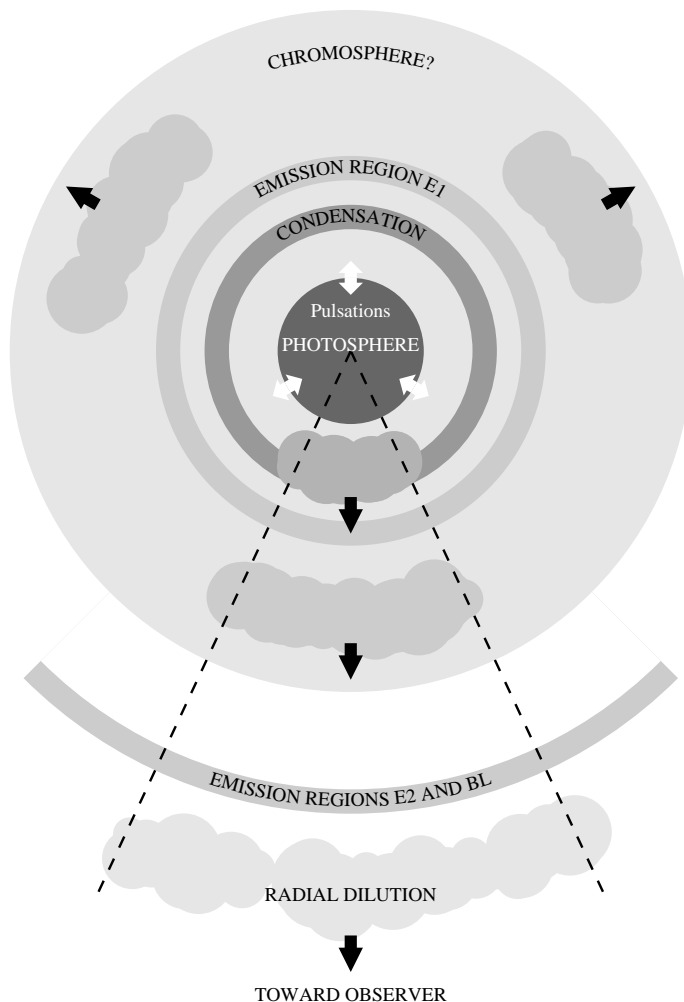
Figure 1.3: *A simplified view of various emitting regions surrounding an RCB star (adapted from Woitke 1997). The E_1 region, being the closest to the star, is obscured first by the dust cloud. This is then followed by the obscuration of the E_2 and BL regions found at somewhat larger distances.*

gradually obscured by the dust during the decline. This is presented in Figure 1.3. The E_2 and BL regions are placed at the same distance from the star, in accordance with the time scale of their decay. However they are always considered separately because of the large difference in their line widths.

The behaviour of spectral lines and their parameters throughout the decline phase can be used to derive the physical conditions in the emitting regions. Depending on the emission lines used, the physical conditions are found to correspond either to the stellar chromosphere (Payne-Gaposchkin 1963) or to the surrounding nebula (Rao & Lambert 1993, Asplund 1995). Observations in the UV region (Clayton et al. 1992a) indicate a temperature similar to the photospheric one, of about 5000 K for the regions responsible for the E_1 and E_2 lines. A range of temperatures and electron densities derived from the sharp and forbidden lines

$(2 \times 10^5 \leq n_e \leq 9 \times 10^7$ cm^{-3} and $5000 \leq T_{\text{exc}} \leq 7300$ K) was obtained by Pandey et al. (1996). On the other hand, the presence of the HeI lines, and also the CII and [CIII] lines in the UV region (Clayton 1996) indicates that a region with a higher temperature must exist. Surenndiranath et al. (1986) derived a temperature of ~ 20000 K and $n_e \sim 10^{11} - 10^{12}$ cm^{-3} from the HeI emission lines, assuming that electron collisions are the dominant excitation source in the gas. These conditions give a flux ratio of the HeI spectral lines very close to the observed one (Rao et al. 1999). The parameters obtained for the other broad lines are $n_e \sim 10^9$ cm^{-3} and $T_{\text{exc}} \sim 1 - 2 \times 10^4$ K (Asplund 1995, Lambert et al. 1990b). On the other hand a very low electron density, of only $n_e \sim 50$ cm^{-3}, for the region producing the forbidden lines in the 1992 decline of V854 Cen was found by Rao & Lambert (1993).

1.4   The aim of this thesis

This thesis is a result of a research project undertaken at the University of Canterbury and Mt John University Observatory in order to study the decline characteristics of a number of R Coronae Borealis stars. Since a relatively small number of observations of these stars has been published, more observational data, especially those covering the whole decline phase of different RCB stars, are needed for a better understanding of the nature of RCB declines. A world wide campaign (Cottrell 1996) was suggested in order to provide photometric, spectroscopic and polarimetric coverage of a number of RCB declines.

The programme list was composed of nine southern RCB stars and three HdC stars (see Table 1.1). Simultaneous photometric and spectroscopic observations have been carried out, so that various aspects of RCB declines could be examined. Regular photometric observations are part of the long-term monitoring of these stars at MJUO. They provide *UBVRI* photometry and also serve as an indicator of a decline. Intensive spectroscopic observations have been made using either the medium-resolution (MRS) or the échelle spectrograph during the decline phases of the programme stars and, less intensively, at light maximum. Only two stars from the list (RY Sgr and V854 Cen) are bright enough to be observed using the échelle spectrograph both at light maximum and throughout the decline phase (down to $\sim 10^{\text{m}}$). A summary of the declines covered during the observational programme of this thesis is given in Table 1.1.

The main scientific goals of the thesis are:

- to follow the evolution and to measure the basic parameters of the spectral lines throughout a number of decline phases of different RCB stars. This allows a comparison of the decline characteristics between different declines of one star and/or between different stars. Such an analysis contributes to a determination of the origin of various emission lines and also allow a test of the plausibility of the $E_1/E_2/BL$ model.

Table 1.1: *The list of RCB and HdC stars observed for this thesis. V – visual maximum magnitude (Lawson et al. 1990), ΔV – depth of the decline, Δt_{d} – duration of the initial decline phase, Δt_{r} – duration of the recovery phase.*

| Star | V | $B-V$ | Observations | Observed declines | | | |
				Decline	ΔV	Δt_{d} (days)	Δt_{r} (days)
V854 Cen	7.10	0.50	96 Apr – 98 Oct	98 Feb – 98 Aug	$\sim 6^{\mathrm{m}}$	~ 100	~ 60
S Aps	9.72	1.21	96 Apr – 98 May	96 Apr – 97 Sep	$\sim 6^{\mathrm{m}}$	~ 40	~ 300
RZ Nor	10.42	1.06	96 Apr – 98 Sep	97 Feb – 97 Jun	$\sim 2^{\mathrm{m}}$	~ 60	~ 60
UW Cen*	9.11	0.67	96 Apr – 98 May	95 Nov – ?	$\sim 7^{\mathrm{m}}$	–	–
V CrA*	9.95	0.72	96 Apr – 98 Oct	94 Feb – 98 Oct	$\sim 6^{\mathrm{m}}$	–	–
RS Tel	9.94	0.82	96 Apr – 98 Oct	97 Jun – 97 Nov	$\sim 1^{\mathrm{m}}$	~ 60	~ 90
RY Sgr	6.40	0.62	96 Apr – 98 Oct				
RT Nor	10.14	1.06	96 Apr – 98 Jun				
U Aqr	11.19	0.95	96 Apr – 98 Oct				
HD 148839	8.35	0.89	96 Apr – 98 May				
HD 137613	7.48	1.18	96 Apr – 98 May				
HD 182040	6.99	1.03	96 Apr – 98 Sep				

* Declines were complex, with a number of fadings and partial recoveries.

- to examine the behaviour of the blue-shifted high-velocity NaI D spectral lines, which are important for determining the time scale of the dust cloud dissipation and, therefore, the positions of the emission regions.

A possible investigation of the decline triggering mechanism has also been considered, having in mind numerous spectra collected at light maximum of various RCB stars. However, this was difficult to achieve due to the unpredictable declines and the fact that only the two brightest programme stars (RY Sgr and V854 Cen) were observable with the high-resolution spectrograph. The great majority of the observations were made using the medium-resolution spectrograph, with not enough resolving power to examine the possible subtle changes in the line profiles as the star approaches a decline.

The observational results of this thesis are presented in Chapters 2, 3 and 4. A detailed description of the photometric and spectroscopic observations, the reduction procedure and various techniques developed for the analysis of the spectral lines are given in Chapter 2. The 1998 decline of V854 Cen is presented in Chapter 3, while the declines of some other programme stars are given in Chapter 4.

A detailed discussion of the spectroscopic results obtained from the six RCB stars observed in this thesis, including the comparisons with existing observations and theoretical models, are given in Chapter 5.

Finally, some extinction properties of the material causing the decline are discussed in Chapter 6 using the photometry of all the programme stars.

Chapter 2

Observations and data reduction

2.1   Observing programme

The observing programme for this thesis includes photometry and spectroscopy of nine R Coronae Borealis and three hydrogen-deficient carbon stars, as already mentioned in Chapter 1. All observations have been obtained at Mt John University Observatory (MJUO), Lake Tekapo, New Zealand, except three spectra of V854 Cen kindly provided by D. L. Lambert (University of Texas at Austin). During the two and a half years of observations, from 1996 April until 1998 October, six declines of various RCB stars were observed. Four of them were complete (i.e. the spectra were obtained throughout the decline), while the other two were only partially covered (see Table 1.1, Chapter 1). The other programme stars were also regularly monitored, both photometrically and spectroscopically. The majority of observations were obtained using the medium-resolution spectrograph (MRS) attached to the 1-m telescope. The high-resolution (échelle) spectrograph was used occasionally, when the stars were brighter than $\sim 10^{\mathrm{m}}$ either during the decline phase or in light maximum.

In this chapter, the instrumentation used for obtaining the light curves and spectra of programme stars will be described. A detailed description of the medium-resolution spectrograph is given in Section 2.3. The spectroscopic reduction procedure, based on the MIDAS software package, will also be explained (Section 2.4). This procedure has been developed for the analysis of both the medium-resolution and high-resolution spectra. In addition, various techniques used for analysing the profiles of spectral lines observed during the RCB declines will also be described (Section 2.5). These include methods for fitting the line profiles, flux calibration of spectra and procedures for obtaining the line parameters, such as the equivalent width, radial velocity and absolute flux.

2.2   Photometric observations

Regular *UBVRI* photometric observations of RCB stars from the observing programme have been undertaken as part of the long-term monitoring of these stars at MJUO (Lawson et al. 1990). The observations have been carried out by either A. C. Gilmore or P. M. Kilmartin. The stars have been observed at maximum light, as well as during the declines. The photometry was mainly used as an indicator of a decline event, so that more intensive spectroscopic observations could be started. Complex colour changes during the declines were also monitored and compared with the spectroscopy. In addition, the photometry during the recovery phases of nine RCB stars was used for analysing the extinction properties of the gas obscuring the stars during the declines (see Chapter 6). For this purpose the photometry in the last 12 years (from 1986 April till 1998 December) was used.

The photometric observations have been obtained at MJUO on either the Boller and Chivens (B&C) or the Optical Craftsmen (O&C) telescope (both with a diameter of 0.6 m). The telescopes have been equipped with the automated single channel photometer based on either an EMI 9558B or 9202B photomultiplier tube. The filters used for the photometric observations are similar to those described by Bessell (1979).

The observations have been obtained differentially with respect to nearby comparison stars. Immediately before and after any observation of a variable star, the light from the sky, as well as from the comparison and check stars, is also collected. The differential magnitudes of variable stars, and those of nearby check stars, were then transformed to the standard system.

The reduction of the differential magnitudes to the standard system were done at MJUO using software written by A.C. Gilmore. At the beginning of the photometry reduction, the sky counts are interpolated and subtracted from all stars. The comparison star's counts and air mass are interpolated for the time of observation of the variable star. Then the differential V magnitude and colours ($B - V$, $U - B$, $V - R$ and $V - I$) of the variable star are calculated from the interpolated comparison star values. After this the differential magnitude of the variable star is transformed to the standard system using the photometric constants and the difference in air mass. The differential magnitudes and colours can then be added to the comparison star V magnitude and colours to give the corresponding standard values for the variable star. In addition, the heliocentric Julian Date (HJD) is calculated for the mid-time of the V integrations. The check star is reduced in exactly the same way as the variable star, so that it is an indicator of the accuracy of the differential photometry.

The mean V magnitude and colours for each star are normally obtained by averaging over several (about 3–6) successive measurements. When the star is brighter than $V \approx 11^{\mathrm{m}}$, a typical precision in V is about $0^{\mathrm{m}}\!.02$, while it is slightly worse for the colours ($0^{\mathrm{m}}\!.03$ for $B - V$, $V - R$ and $V - I$, and $0^{\mathrm{m}}\!.04$ for $U - B$). During a decline, when the star is getting significantly fainter, a typical uncertainty in V is less than about $0^{\mathrm{m}}\!.03$, while it can be as

high as $0\overset{m}{.}04$ for $B - V$, $V - R$ and $V - I$, and $0\overset{m}{.}05$ for $U - B$.

2.3   Spectroscopic observations

The MJUO observing equipment for this project was based on the 1-m cassegrain reflector and either the medium-resolution (MRS) or high-resolution (échelle) spectrograph. The spectrographs were mounted directly on the telescope, using the focal ratio of f/13.5. A description of the optical system of the MJUO 1-m telescope can be found in Nankivell et al. (1986).

2.3.1   High-resolution spectrograph

The high-resolution spectrograph used at MJUO is based on an échelle grating having 79 grooves per millimetre with the nominal value of the blaze angle of $\theta_B = \arctan(2) = 63.5°$.[1] An additional diffraction grating (150 groves per millimetre, blazed at 7000 Å in the first order) is used to separate the échelle orders. A thorium-argon lamp is used for wavelength calibration. For more details on the échelle spectrograph see Hearnshaw (1977). In 1997 April a focal reducer was installed in the spectrograph so that more diffraction orders are recorded on the CCD chip (Tobin et al. 1998).

The échelle spectrograph was used in combination with one of the two CCD detectors available at MJUO. The Thomson TH7882 CDA chip, incorporated in the Photometrics PM3000 CCD system, was used from 1996 April until 1997 July. The chip has 576×384 square pixels, each pixel having a side of 23 μm. For a more detailed description see Tobin (1992). However, the majority of observations were made with the SITe CCD chip of 1024×1024 24-μm pixels in the Photometrics Series 200 system (Barnes et al. 2000). This detector became available from 1997 July.

The wavelength range covered by the échelle spectrograph is between 5400 Å and 8600 Å, with some gaps due to the combination of the spectrograph and CCD detectors. This region includes three groups of spectral lines that are studied during the declines of RCB stars in this thesis: NaI D (5890 Å & 5896 Å), H_α (6562 Å) and two lines from the CaII IR triplet (8498 Å & 8542 Å). On the larger SITe CCD chip all three regions together can be recorded in a single exposure (orders 27–42). On the other hand, three separate exposures are needed in order to obtain the same spectra using the PM3000 CCD.

The wavelength region and other characteristics of the most frequently used configuration (i.e. with the SITe CCD detector) are given in Table 2.1 (together with the MRS parameters). The effective resolution of the échelle spectrograph has been obtained by measuring the FWHM (in pixels) of sharp emission lines from the thorium-argon spectra. A mean resolution of about 2.40 pixels has been found. The reciprocal dispersion (in Å pix^{-1}) is defined as the

---

[1] The actual blaze angle is somewhat larger ($\theta_B \approx 65.4°$, Skuljan 1999).

Table 2.1: *Instrumental set-up.*

Instrument	Order	Region (Å)	Reciprocal dispersion (Å pix^{-1})	Resolution (Instrumental profile)	
				(Å)	(km s^{-1})
échelle	42–27	5400–8600	0.08	0.2	10
MRS					
600 l mm^{-1}	1	8000–10000	1.90	3.4	130
	2	5200–7200	0.96	1.7	85
	3	3800–4200	0.64	1.0	72
300 l mm^{-1}	1	8000–10000	3.8	6.8	260
	2	5200–7200	1.90	3.2	160
	3	3800–4200	1.30	1.9	146
150 l mm^{-1}	2	5200–7200	3.8	7	350
	3	3300–4800	2.5	3.7	280

ratio between the wavelength interval and the corresponding number of pixels on the CCD chip. Around H$_\alpha$ ($\sim$ 6000 Å) this quantity is about 0.08 Å pix^{-1}. The resolution (in Å) is calculated by multiplying the mean FWHM value with the reciprocal dispersion, which gives a value of about 0.20 Å (or $\sim$ 10 km s^{-1}). This also defines the instrumental profile of the spectrograph. The resolving power ($R = \lambda/\Delta\lambda \approx 30000$) has been calculated by dividing the central wavelength ($\sim$ 6000 Å) by the mean resolution (0.20 Å).

Three high-resolution spectra of V854 Cen provided by D. L. Lambert were obtained at the W. J. McDonald Observatory (Texas, USA). The 2.7-m Harlan J. Smith reflector was used, equipped with the coudé cross-dispersed échelle spectrograph (Tull et al. 1995) and a Tektronix 2048 × 2048 CCD detector. The spectra are at a resolving power of $R \approx 60000$. The nominal wavelength range of the spectrograph is between 3800 Å and 10200 Å, with an incomplete coverage above 5500 Å. However, due to the fact that V854 Cen (with a declination of $\delta \approx -39°$) appears relatively low in the sky at McDonald Observatory (latitude $\sim$ +31°), most of the light in the blue is scattered by the Earth's atmosphere. The signal becomes usable only at wavelengths longer than about 4100 Å. The instrumental profile has been estimated from the atmospheric lines of OI and H$_2$O. In two spectra the sky lines around 6000 Å have a FWHM of about $\sim$ 0.1 Å ($\sim$ 5 km s^{-1}), while the third spectrum shows a slightly larger instrumental profile of about 0.2 Å ($\sim$ 9 km s^{-1}).

2.3.2 Medium-resolution spectrograph

The medium to low resolution spectrograph (MRS) was used for collecting spectra of RCB stars throughout the decline and maximum light phases over a wide wavelength range. The spectrograph was designed and built by Graeme Kershaw in the Department of Physics and Astronomy, University of Canterbury. The actual design was derived from an old B&C low-resolution spectrograph, which was used at MJUO for many years and was entirely manual in its operation. The MRS was developed to have a remote control of the observing process, which includes a control over the calibration lamps and guiding camera, as well as using a CCD as detector. The spectrograph was specifically designed for use with the 1-m or the 60-cm B&C telescope at MJUO in the f/13.5 configuration.

In this section a brief description of the MRS interior and its operation will be given. Also included are the configuration and settings used during the observing programme and some other characteristics of the MRS. A general overview of the MRS components, including a detailed description of the alignment procedure and an operations manual are available at the WEB page of the Department of Physics and Astronomy[2].

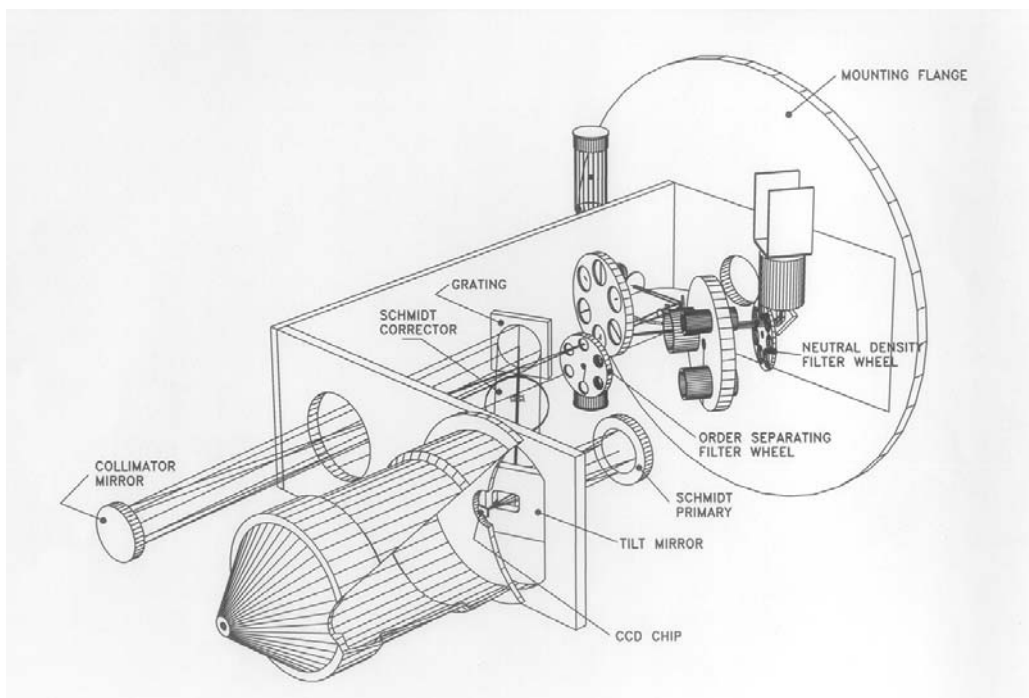Figure 2.1: *A schematic view of the medium-resolution spectrograph (kindly provided by G. Kershaw).*

A schematic view of the MRS spectrograph is shown in Figure 2.1. The light from an object being observed enters the spectrograph through a slit and an order-separating filter and falls onto the collimator. The parallel beam from the collimator gets dispersed by the

---

[2]http://www.phys.canterbury.ac.nz/ physplc/UPN.html

diffraction grating. Finally, the spectrum is focused onto the CCD chip by a Schmidt camera. The camera consists of a corrector plate, a fold mirror and a primary mirror which focuses the light onto the detector.

Six different slits are arranged on a rotating wheel and can be selected by the observer. Slit No. 1 of 150 μm $\times$ 30 mm ("long slit") was used most frequently, because it allowed the sky light to be collected simultaneously with the stellar spectrum. The full width of the slit image projected onto both the Thomson and SITe CCD detectors corresponds to ≈ 1.8 pixels or ≈ 43 μm. No eyepiece is used for the field and slit viewing. However, the entire slit is viewed by an additional Phillips CCD camera and an image intensifier. This system is equipped with three different lenses, producing three different fields of view, and with a variety of neutral density filters for bright stars. The whole system allows for the acquisition and guiding of stars down to a magnitude between $13^{\rm m}$ and $14^{\rm m}$.

The wavelength calibration of the MRS spectra was done using either a helium-argon (HeAr) or a helium-neon (HeNe) lamp. A tungsten lamp was used for the flat-field images. Typical exposure times for the lamps at various settings are given in Tables A.1–A.3 (Appendix A). The exposure duration has been chosen so that a sufficient number of well separated and not saturated lines is obtained for the wavelength calibration.

Most of the spectrograph functions can be controlled from the data room using the hand paddle. This includes operating the comparison and calibration lamps, selecting the field of view and choosing the filter for the guiding system. The hand paddle can also display all other settings of the spectrograph (the slit number, order-separating filter number, grating and collimator positions), although they have to be adjusted manually at the telescope.

Gratings and order-separating filters

Three different gratings are available for use with the MRS: 150 l mm^{-1}, 300 l mm^{-1} and 600 l mm^{-1}. They are all blazed at a wavelength of about 12000 Å in the first order, which corresponds to about 6000 Å, 4000 Å and 3000 Å in the second, third and fourth orders, respectively. This is shown in Figures A.1 and A.2 (Appendix A). The total wavelength range that can be covered by the CCD detector in each order (1–4), using the three MRS gratings, is represented in these figures by three different rectangles (Thomson CCD in Figure A.1 and SITe CCD in Figure A.2).

In order to change the wavelength region the grating tilt can be adjusted by rotating the corresponding knob on the outside of the spectrograph. The information on the grating tilt ("grating setting") is displayed digitally on the main case as a number between 0 and 1200.

Using the grating equation as: $n\lambda = 2d\cos\beta\sin(\phi_c - \beta)$, the theoretical curve $\lambda = f(\phi_c)$ can be obtained, where ϕ_c is the angle between a line perpendicular to the grating and the direction to the CCD (2β is the angle between the incident and reflected beams). This angle actually represents the grating tilt (grating setting). A similar relation can be obtained
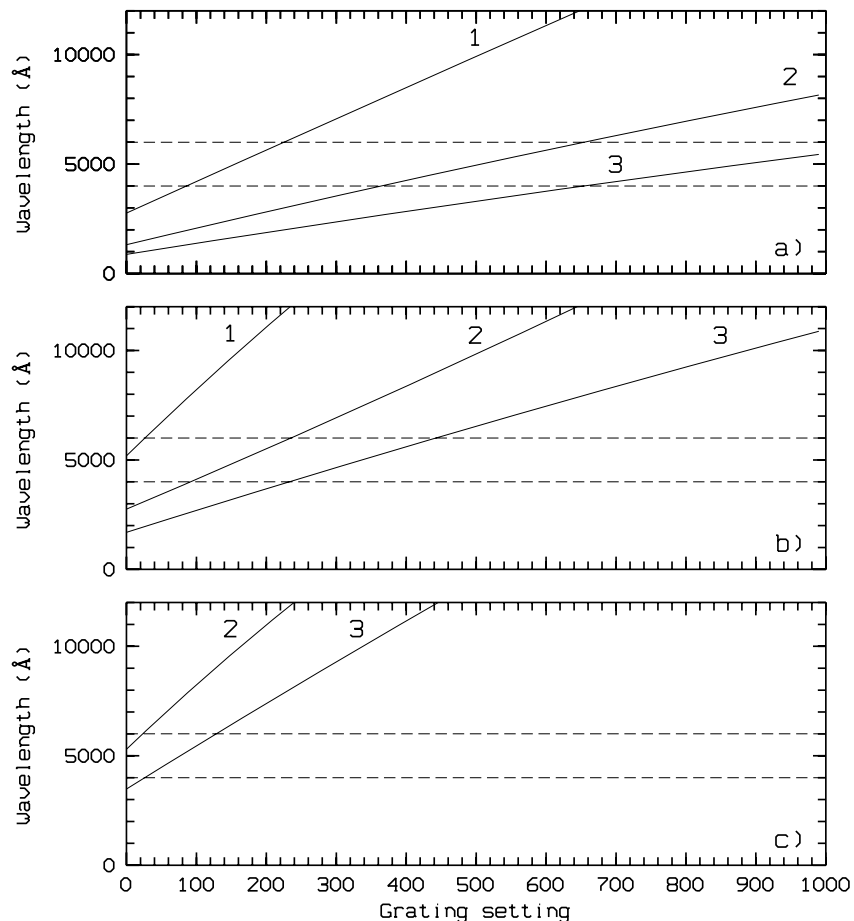
Figure 2.2: *Wavelength in the centre of the CCD versus grating setting for a) 600 l mm^{-1}, b) 300 l mm^{-1} and c) 150 l mm^{-1} gratings for different orders (1, 2 and 3). The horizontal dashed lines at 6000 Å and 4000 Å represent the blazing wavelengths in orders 2 and 3, respectively.*

experimentally by observing the pixel positions of a fixed spectral line (e.g. from helium-argon spectra) at different grating settings. This is shown in Figure 2.2. The available setting range in the cases of 600 l mm^{-1} and 300 l mm^{-1} gratings (Figures 2.2a&b) allows a comfortable access to the blazing wavelengths of 6000 Å in the second order, 3000 Å in the third order, as well as to longer wavelengths (above 9000 Å) in the first order. The wavelength region that can be obtained with 150 l mm^{-1} (Figure 2.2c) falls at the end of the grating setting scale in orders 2 and 3, while the first order cannot be used.

All diffraction orders produced by the grating appear overlapped in the focal plane of the spectrograph (see Figures A.1 and A.2, Appendix A). In order to separate different orders a set of standard filters is used. A list of currently installed filters (used during the observing programme) is given in Table 2.2. All filters are 2 mm thick, except filter No. 5, which is a combination of two 2-mm filters (GG420 and BG28). The filters have been carefully chosen according to their transparency curves (Schott 1989), so that they give the best coverage for

Table 2.2: *Filters available during the observing programme.*

Filter No.	Filter	Thickness (mm)
1	GG475	2
2	BG28	2
3	BG25	2
4	BG12	2
5	GG420+BG28	4
6	RG695	2

a given wavelength range. GG475 has been used in the red part of the spectrum (second order), RG695 in the infrared (first order) and BG12 and GG420+BG28 in the blue (third order). The other two blue filters (BG28 and BG25) can also be used for different parts of the blue region. However, they were not used in the present observations due to significant leakage of the red light (more than for BG12) from the first and second orders.

Tables A.1–A.3 (Appendix A) show the most frequently used settings for different gratings. For each wavelength range these tables give the corresponding filter name and grating setting, as well as the exposure time for the comparison (helium-argon and helium-neon) and flat-field (tungsten) lamps.

The resolution of the MRS spectrograph has been measured from the FWHM of the HeAr spectral lines in a similar way as for the échelle spectra. A summary of the observed wavelength regions in the first, second and third orders, for different gratings, are given in Table 2.1. The corresponding reciprocal dispersion and resolution are also included.

Focusing the spectrograph

The fine adjustment of the focus position of the spectrograph is done by moving the collimator. Although this way of focusing results in slightly non parallel light falling onto the grating, it is popular for adjusting spectrographs with Schmidt camera systems. The collimator mirror can be moved along the optical axis by rotating a knob at the bottom of the collimator tube. The reading is displayed on the main case of the spectrograph as a number between 0 and 2000.

This procedure has to be performed carefully before each observing night and sometimes also during the night, since it has been noticed that the focus depends strongly on the outside temperature. The focus adjustments were done by measuring the FWHM of some isolated lines from the comparison lamp spectra and finding the position of the collimator that gives the sharpest lines. A dependence of approximately 100 units of the collimator position per one degree Celsius has been detected, with higher values corresponding to
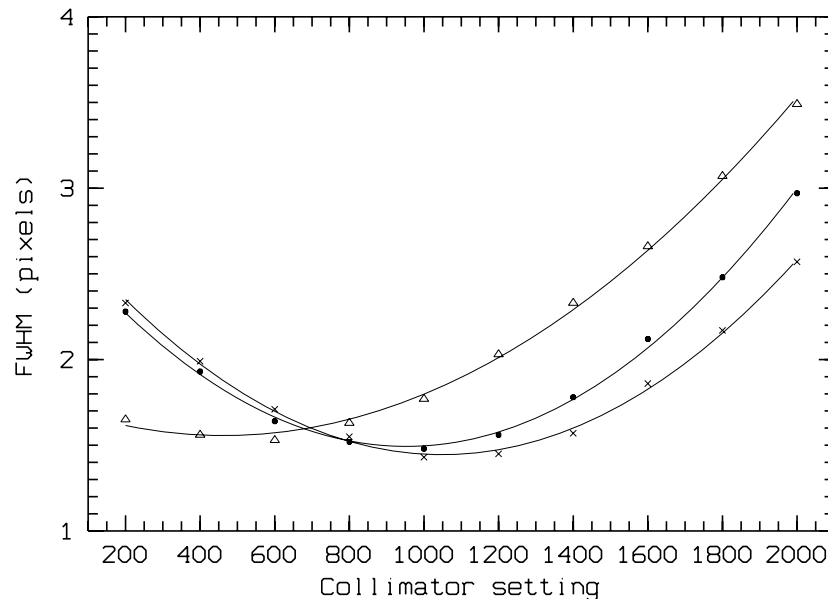
Figure 2.3: *The best collimator focus with the 300 l mm^{-1} grating at the stabilized dome temperature of about 10°C. Filled circles and crosses represent the lines measured at pixel numbers 380 and 120 respectively, while the triangles show the FWHM values of a line at the edge of the CCD (pixel ~ 550).*

higher temperatures. It is especially important that this is checked during the night when there are large temperature fluctuations. The optimum value for the collimator focus, at a stabilized temperature in the dome of about 10°C, was found at approximately 1600 for the 600 l mm^{-1}, and at 1000 for 300 l mm^{-1} and 150 l mm^{-1} gratings. Figure 2.3 shows the best collimator focus at ~ 1000 for the 300 l mm^{-1} as derived from the FWHM values of a few HeAr spectral lines. Some variations of the focus across the chip can also be noticed. The best collimator focus reading at the end of the CCD can differ from the middle of the chip by about 400 − 500 units. This results in slightly wider spectral lines around the edges of the CCD when the central parts are in focus. However, this variation (of only ~ 0.5 pixels) has not been regarded as significant for the medium-resolution spectrograph. Nevertheless, the instrumental profile in Table 2.1 was calculated by averaging the line widths of a number of lines across the CCD.

2.4   Reduction procedure

The reduction of both medium-resolution and échelle spectra was done using the MIDAS system (or ESO-MIDAS: the **E**uropean **S**outhern **O**bservatory − **M**unich **I**mage **D**ata **A**nalysis **S**ystem). The MIDAS package consists of a set of general tools for image processing and data reduction. The standard set of basic MIDAS commands was used, incorporated into several

```
                    Preparing images for reduction

                                                Forming quasi-echelle images
                                                     for the MRS spectra

                          Order definition and
                         offset of the stellar images

                            Background and
                          cosmic ray subtraction

                           Order extraction and
                               flat fielding

                                                  Sky lines subtraction
                                                   for some MRS spectra

                          Wavelength calibration

                             Normalization
```
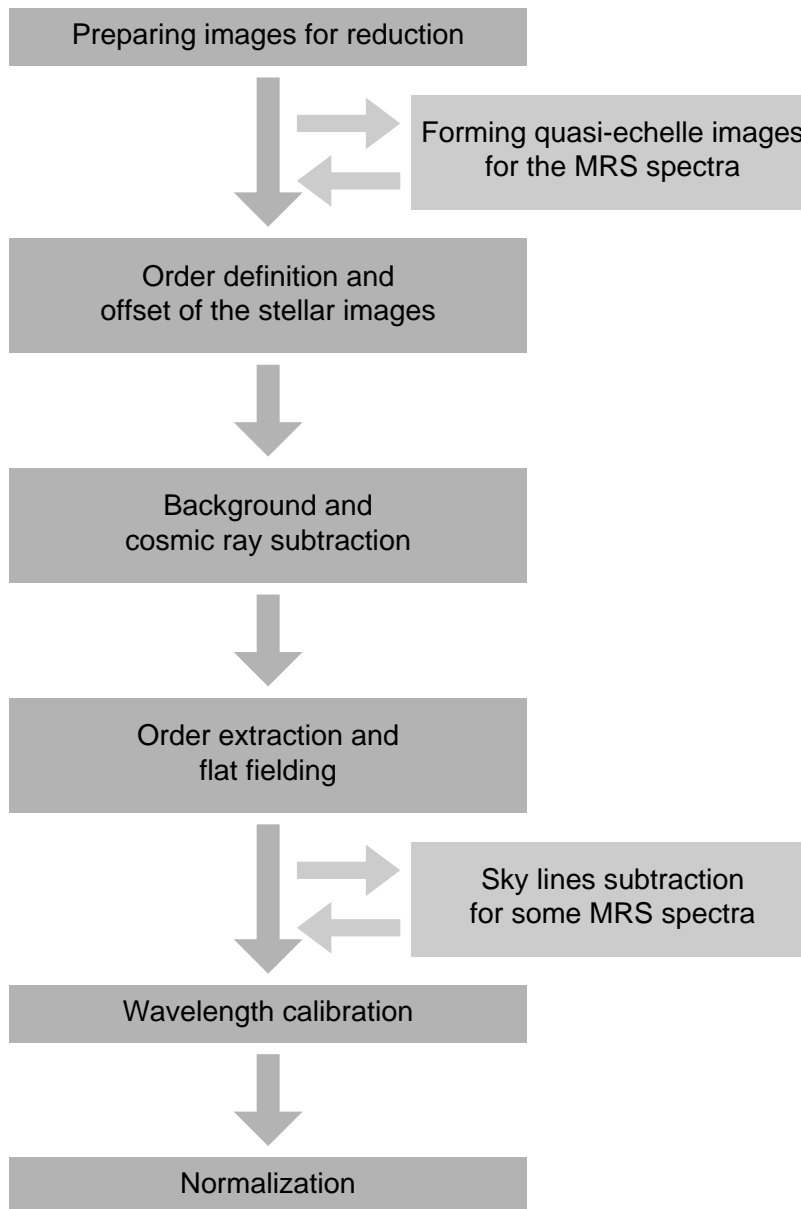
Figure 2.4: *Schematic diagram of the reduction procedure (échelle and MRS).*

complex procedures (MIDAS programs), written especially for this project so that the re-duction process can be performed more automatically. In addition, a number of C-programs were also developed to speed up some steps of the reduction procedure.

A typical échelle or MRS observation consists of several CCD exposures. A comparison spectrum (ThAr, HeAr or HeNe) is taken first and this is immediately followed by the stellar exposure and another comparison spectrum. A flat-field image (using the white light of a tungsten lamp) is usually taken only once during the observing night for a given setting. Three dark exposures (PM3000 system only) are also obtained at the beginning of the night and their median is automatically subtracted from all subsequent exposures. In the case

Figure 2.5: *Typical two-dimensional échelle CCD images of a star, thorium and white lamp.*

Figure 2.6: *Typical two-dimensional MRS CCD images of a star, helium-argon and white lamp.*

of the Photometrics Series 200 system, the bias is automatically recorded in pixel columns 1025–1058 and this has to be subtracted fro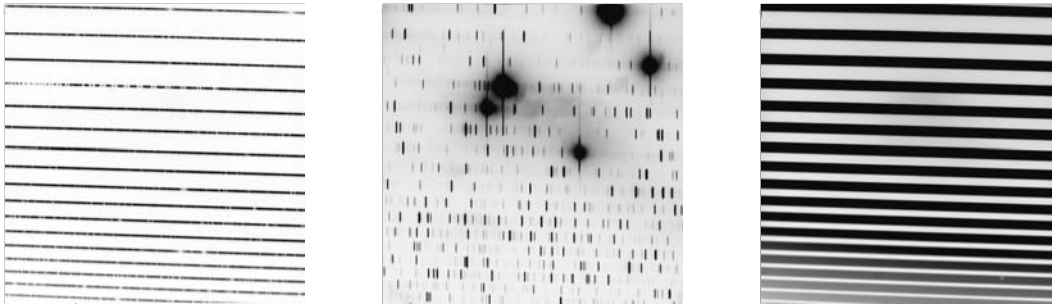m the image during the reduction procedure. In addition, a spectrum of a radial-velocity standard star is also collected for a given setting on every night.

A schematic diagram of the reduction procedure for the échelle and MRS spectra is shown in Figure 2.4. The standard MIDAS échelle routines have been used for the reduction of the échelle spectra. In the case of the MRS spectra the general reduction procedure is the same as for the échelle spectra, but with some additional steps and new programs developed. The échelle routines for order definition, cosmic ray and background subtraction and order extraction have been used for the single-order MRS spectra as well. These routines have significant advantages over the standard MIDAS procedures for single-order spectra. For all other reduction steps, including the flat-fielding, wavelength calibration and normalization, a number of complex MIDAS procedures have been developed.

The reduction procedure begins with the two-dimensional raw CCD images of the stellar, thorium (or helium-argon in case of the MRS) and white light spectra (Figures 2.5 and 2.6). The following reduction steps are performed:

- **Image preparation.** Before any other operation, the raw FITS images have to be converted into the standard MIDAS format (BDF). After that some other operations, such as dark or bias subtraction, cutting, flipping or rotating may also be performed. All images collected with the PM3000 system require a rotation, so that they are correctly

Figure 2.7: *Left: Two additional orders (above and below the central one) are added to the original single-order MRS spectrum, so that a new "quasi-échelle" image is obtained. A standard échelle order-tracing algorithm can then be used to extract the spectrum by taking the actual slope into account. Right: A typical MRS background image.*

oriented as expected by MIDAS. This means that the wavelength axis is horizontal, with the wavelength increasing from left to right and with the échelle diffraction order numbers increasing from top to bottom. The MRS images, with only one diffraction order, have been prepared for the échelle procedure by artificially adding two extra orders, one below and the other above the existing one. In this way, a so called "quasi–échelle" image is made (Figure 2.7). The two additional orders are actually *copies of the central one* and they are carefully placed so that the background level and sky emission lines are not disturbed around the main (central) order.

- **Order definition.** The échelle orders are defined by fitting a low-order two-dimensional polynomial to the central points at different pixel positions along the orders (method STANDARD in `define/echelle`). This procedure has also been used for tracing the orders in the "quasi-échelle" images (Figure 2.7). A slope of about 5 pixels (from one end of the CCD to the other) in the MRS spectra is taken into account in this way. In most cases, a bright stellar image, free of strong absorption lines, has been used for this purpose (the programme stars are usually too faint for a successful order tracing). Once the échelle orders have been traced, their position is recorded and this is used for all subsequent `extract/echelle` commands on images obtained on the same night and with the same spectrograph settings.

- **Background and cosmic ray subtraction.** The background and cosmic ray subtraction have been done using the `echkaren.prg` procedure (Pollard 1994), which is a slightly modified version of the standard MIDAS command `filter/echelle`. The modified procedure takes into account a possible vertical offset of the stellar spectrum with respect to the fixed échelle orders and can also accept higher values for the order widths. After the dark subtraction, the remaining background consists mainly of the scattered light in the spectrograph. This is estimated from the pixels found in the space between the orders. A two-dimensional spline interpolation has been used for modelling the background. The background is then subtracted from the raw image. A typical MRS background image is shown in the right panel of Figure 2.7. In addition,
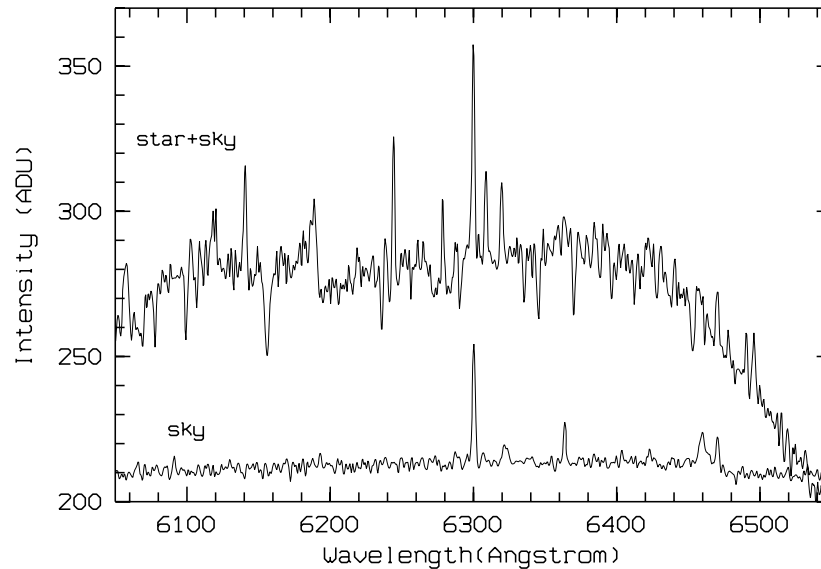
Figure 2.8: *A stellar image (star+sky) and the sky emission lines (sky) extracted from both sides around the stellar spectrum. The sky spectrum has been shifted vertically for convenience (the true sky continuum is about zero).*

the stellar image is usually contaminated with numerous cosmic rays, especially during longer exposures. The cosmic rays are detected and removed from the CCD image. In most situations, this process is done automatically and effectively. A difference image containing the cosmic rays only can be viewed at this stage to make sure that the filtering has been performed correctly. In the case of strong stellar emission lines, the parameters of the cosmic ray subtraction within the spectral orders have to be adjusted so that those lines are not removed from the spectra by accident.

The usual procedure for the background and cosmic ray subtraction is somewhat different for the long exposure MRS images of faint RCB stars in the deepest part of their declines. The strong sky lines are prominent features in these images, making the identification of the stellar emission lines more difficult. In order to obtain the correct position and intensity of the sky lines, an additional reduction step has been included in the standard procedure. The sky lines have been extracted from both sides of the stellar spectrum (immediately above and below) and these 'sky spectra' have been used to identify the sky emission lines in the stellar spectra (see Figure 2.8). For this procedure the parameters of the cosmic ray subtraction within and between the orders have been adjusted so that the sky lines are not removed.

- **Order extraction and flat-fielding.** After the positions of the spectral orders have been determined (usually from an image of a bright standard star), the offset of each stellar image, collected with the same settings, has to be determined. In addition,

the parameter SLIT must also be defined before the actual order extraction is done. This parameter defines the width of the échelle orders. A value of 2.2×FWHM (where FWHM is the full width at the half maximum) has been used. This produces spectra that have the largest signal-to-noise ratio (Skuljan 1999). The one-dimensional stellar spectrum (Figure 2.9b) is extracted by averaging a number of pixels above and below the central line, defined by the slit height. The same extraction procedure is used for the comparison lamp (ThAr or HeAr) and the white lamp spectra (Figures 2.9a and c). All extracted spectra are in pixel space (along the x-axis) and on a relative intensity scale (along the y-axis) derived from the original ADU counts. After the extraction procedure the flat-field correction is done by dividing the stellar spectrum with the white lamp spectrum (Figure 2.9d). Any possible pixel-to-pixel variations and shadows cast by dust spots, as well as all other combined light variations in the system, are eliminated in this way. After this step, as an option, the sky line subtraction procedure can be performed.

- **Wavelength calibration.** The wavelength calibration is done by using two comparison spectra collected immediately before and after the stellar exposure. The final dispersion solution is obtained by linear interpolation between the two solutions, using the exact times when the images were taken. Finding the dispersion solution for each échelle order means defining the relation between the pixel positions on the CCD images and the corresponding wavelengths. This is done by using the laboratory wavelengths of a set of known emission lines from the comparison spectrum. The *first* step in this procedure is the detection of the HeAr or ThAr lines, using the MIDAS thresholding algorithm. Two MIDAS parameters, WIDTH and THRESHOLD, are defined so that a sufficient number of isolated lines are found. The *second* step involves the identification of the spectral lines. The ANGLE method in MIDAS has been used during the initial identification of the ThAr échelle spectra for a given instrument set-up. This method requires a minimum of four ThAr spectral lines to be specified on input. The method GUESS has then been used for all subsequent spectra with the same settings. On the other hand, for the single-order HeAr MRS spectra, a similar procedure using the basic MIDAS commands has been developed, so that the initial identification requires only two spectral lines. A typical number of identified lines in every spectral order is about 10–15. In order to reduce the random errors in the dispersion solution, the same set of well separated and unblended spectral lines has always been used from the HeAr tables. Three different tables have been used for different gratings, due to the differences in the resolution. For example, some HeAr spectral lines are blended and consequently not suitable for the wavelength calibration in the case of the 300 l mm^{-1} grating, while they appear well separated in 600 l mm^{-1} spectra. The *third* step is computing the dispersion solution using the set of calibration lines. A parabolic fit is normally used
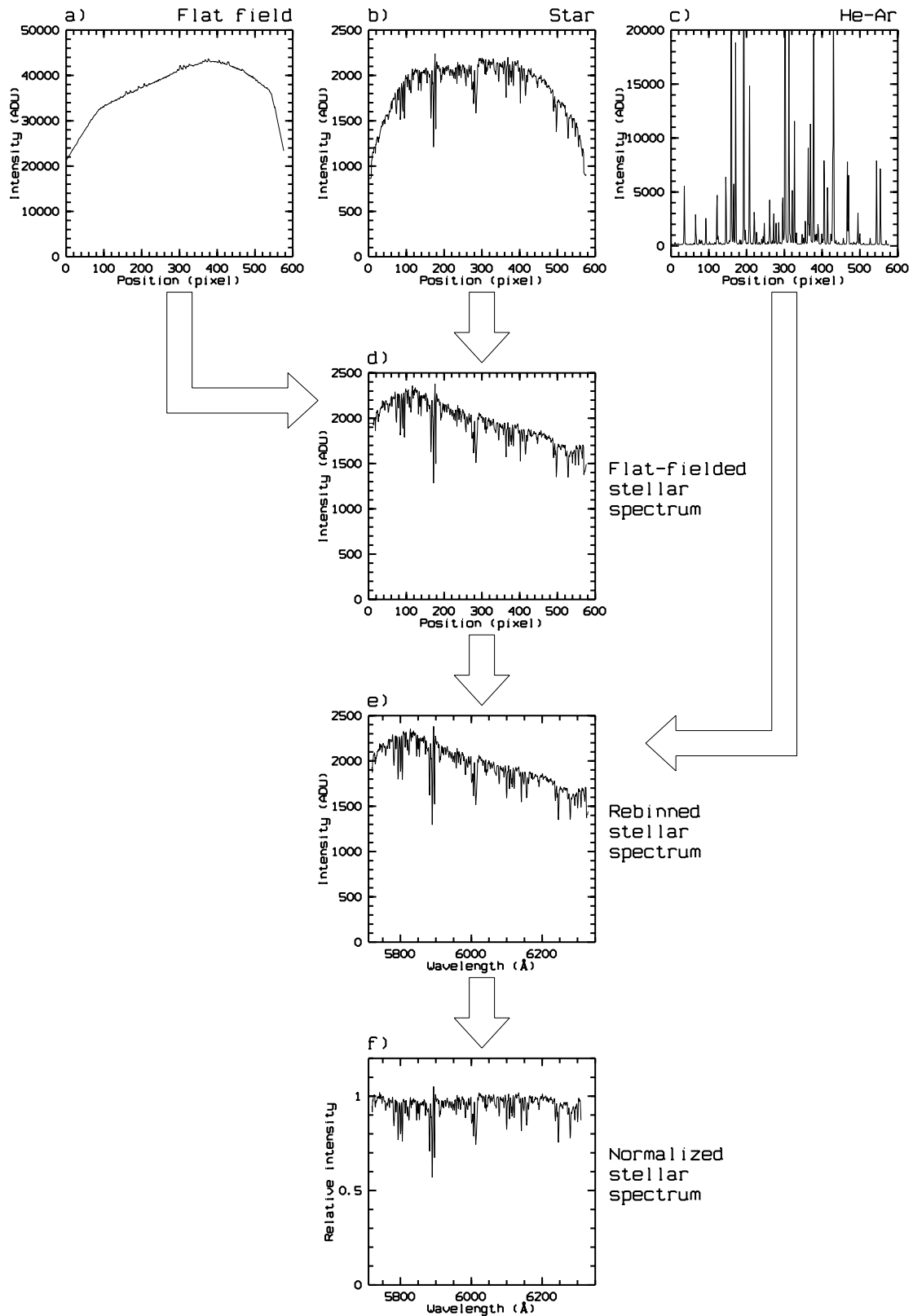
Figure 2.9: *Basic reduction steps after the one-dimensional spectra have been extracted. The stellar spectrum (b) is combined with the white lamp (a) and comparison spectrum (c) and a normalized stellar spectrum (f) is obtained in the end of the process.*

for the MRS spectra, while a two-dimensional low-order polynomial fit is performed for the échelle spectra, so that the solution is obtained for all orders simultaneously. A typical r.m.s. error of the dispersion solution for the échelle spectra is ~ 0.005 Å and for the MRS is ~ 0.05 Å for 600 $\mathrm{l\,mm^{-1}}$, ~ 0.1 Å for 300 $\mathrm{l\,mm^{-1}}$ and ~ 0.2 Å for 150 $\mathrm{l\,mm^{-1}}$. Finally, the *fourth* step is the actual rebinning of the stellar spectrum into the wavelength scale, using the coefficients of the dispersion solution.

- **Normalization.** The wavelength-calibrated spectra have to be normalized so that the stellar continuum takes an intensity equal to one. As a result, a spectrum with a relative intensity between 0 and 1 is obtained (Figure 2.9f). In the case of the MRS spectra, where the continuum is not well defined (due to line blending effects), some échelle spectra of the same star have been used to define the continuum level in some spectral regions. A second-order polynomial fit has then been used to define the shape of the continuum. For the normalization of spectra of cool RCB stars (e.g. S Aps and UW Cen), which are crowded with molecular bands, the continuum of some standard radial velocity stars of similar spectral types have been used. Due to these difficulties in the normalization procedure, some uncertainty in the continuum level can be expected in the normalized spectra.

2.5   Analysis techniques

Various analysis techniques have been used for examining the characteristics of the line profiles. A procedure for measuring the equivalent widths and line fluxes of the emission spectral lines will be explained in this section. A special technique developed for analysing the complex structure of the NaI D spectral lines will be also discussed.

2.5.1   Subtraction procedure

During the initial decline and recovery phases of RCB stars, when the photospheric continuum is still strong, the emission lines originating from the levels above the photosphere cannot be clearly resolved. In order to examine the line profiles of the emission features during these phases a maximum light spectrum has been subtracted from each decline and recovery phase spectrum. Figure 2.10 presents some examples of spectra before (b) and after (c) the subtraction of the maximum light spectrum (a). This procedure can be performed if we assume that the emission spectrum is superimposed on the photospheric continuum. This assumption is reasonable taking into account the likely origin of the emission lines (Clayton 1996), as well as the most commonly accepted theory of RCB declines, based on dust cloud formation (see Chapter 1). The subtraction procedure has not been performed on the deep decline spectra, when the emission is dominant and the photospheric continuum is already
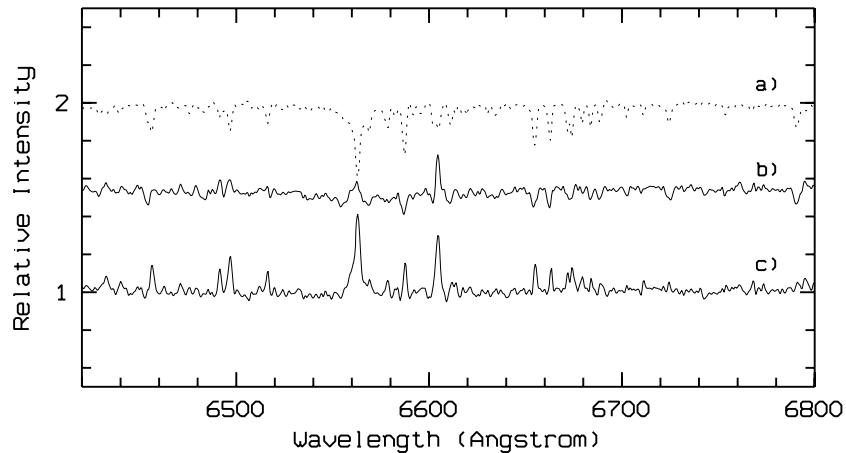
Figure 2.10: *An example of the maximum light subtraction procedure: (a) maximum light spectrum, (b) the decline spectrum, (c) the residual spectrum. The emission lines are clearly seen in the residual spectrum. The spectra are displaced vertically for convenience.*

weak.

For each wavelength region a pre-decline maximum spectrum has been chosen as a standard for all subsequent subtractions. The changes of the line depths in the light maximum spectra at different pulsation phases can be neglected in the MRS spectra, since the uncertainty due to the normalization and line blending effects is greater than the variations due to pulsation. In the case of the high resolution spectra, a spectrum from the stellar pulsation maximum has been taken as standard. After the normalized maximum spectrum has been subtracted, the residual spectra have been renormalized back to a mean continuum level of $I_c = 1$, so that the emission features all have intensities $I > 1$. The residual spectra are used to examine the equivalent widths and absolute fluxes of the emission spectral lines. The noise (σ_N) in the continuum of the residual spectra is in the range 2–8%, as estimated from portions free of spectral lines. Only the emission lines with intensities above $2\sigma_N$ have been analysed.

2.5.2 Flux calibration

Stellar spectra have been flux-calibrated using the observed *UBVRI* magnitudes brought to the standard Johnson-Cousins system (see Section 2.2). The magnitudes have been interpolated to the date of each spectrum. The observed flux $f_{\bar{\lambda}}$ of a star with a magnitude $m_{\bar{\lambda}}$ in a given filter characterized by a mean wavelength $\bar{\lambda}$ can be calculated as:

$$f_{\bar{\lambda}} = 10^{-0.4\,m_{\bar{\lambda}}} f_{\bar{\lambda},0} \qquad (2.1)$$

where $f_{\bar{\lambda},0}$ is the calibrated flux corresponding to $m_{\bar{\lambda}} = 0$, as derived from the standard photometry for Vega. The observed magnitudes ($m_{\bar{\lambda}}$) are corrected for the interstellar red-

Table 2.3: *Calibrated fluxes $(f_{\bar{\lambda},0})$ in units of $10^{-23}\,W\,m^{-2}\,Hz^{-1}$ for $m_{\bar{\lambda}} = 0$ for each bandpass (Bessell 1979).*

	$\bar{\lambda}(\text{Å})$	$f_{\bar{\lambda},0}$
U	3600	1.81
B	4400	4.26
V	5500	3.64
R	6400	3.08
I	7900	2.55
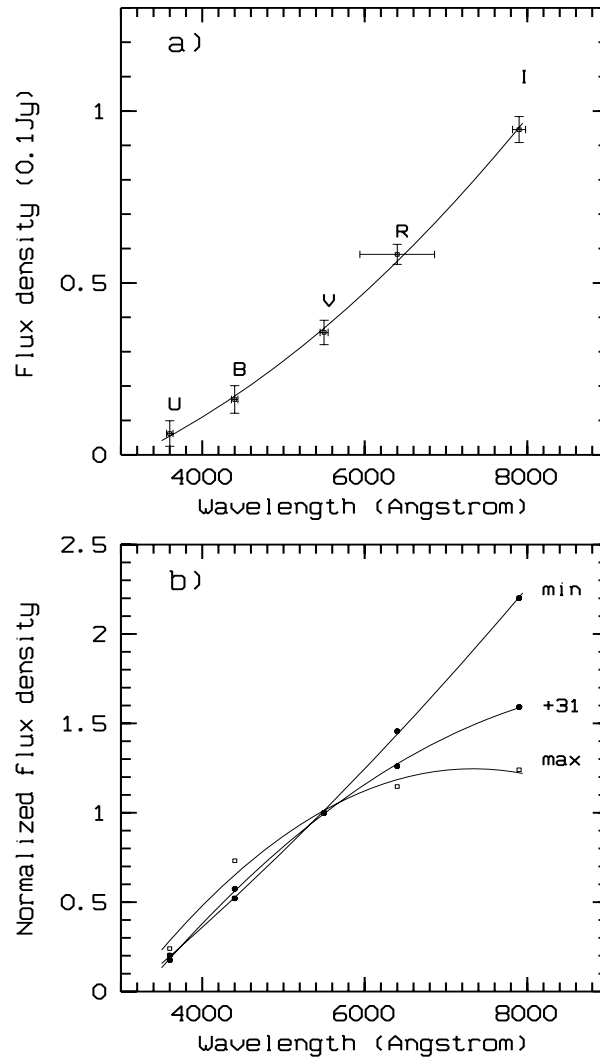
Figure 2.11: *a) Flux density distribution of V854 Cen in the deep minimum. b) Normalized flux distribution $(F_V = 1)$ at the maximum and during the decline (day number is shown).*
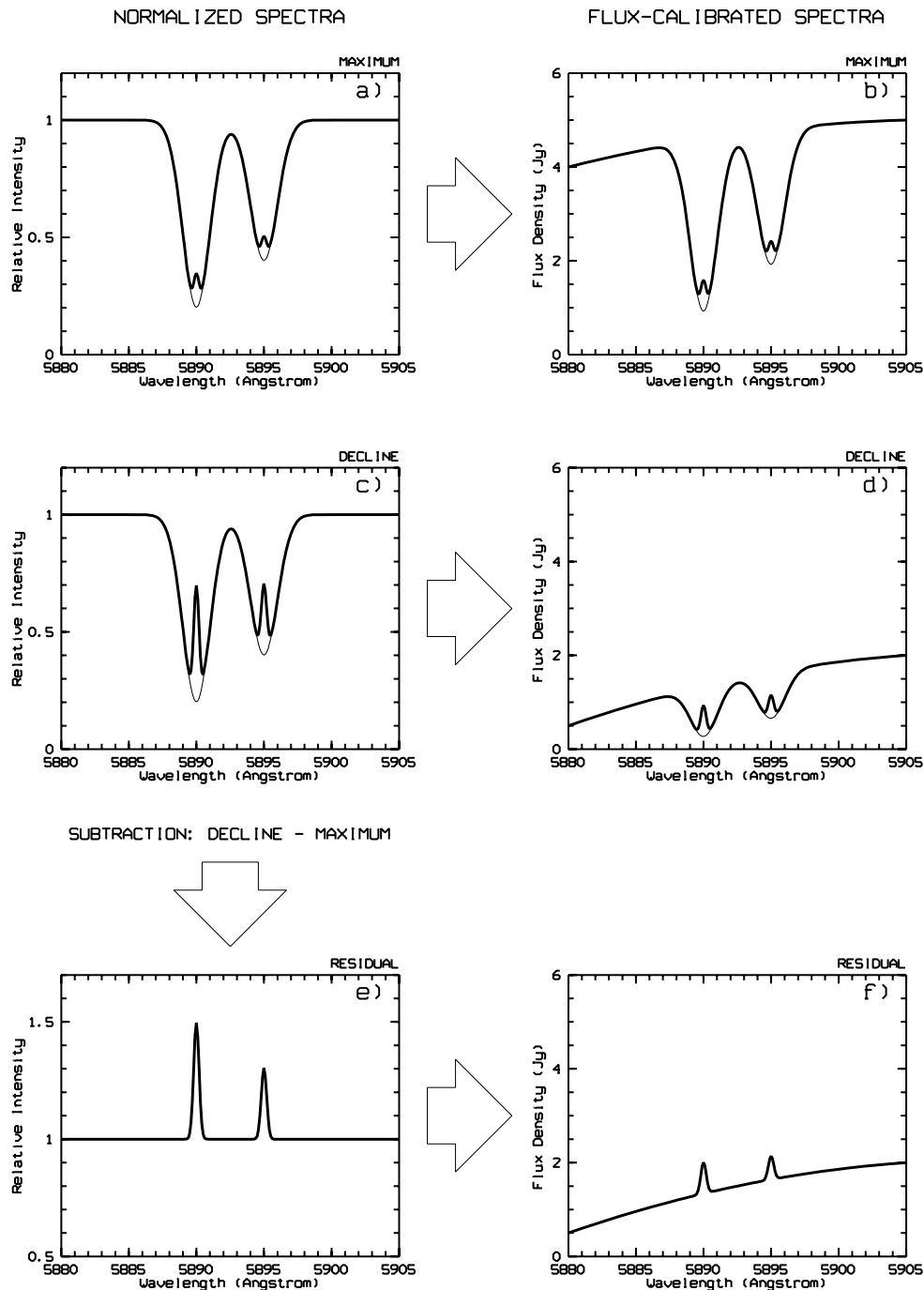
Figure 2.12: *Schematic diagram of the subtraction and flux calibration procedures: a) normalized maximum light spectrum with photospheric absorption perturbed slightly by a weak emission. b) flux calibrated maximum light spectrum, c) normalized decline spectrum with a typical emission in the core of absorption, d) flux calibrated decline spectrum, e) residual spectrum and f) flux calibrated residual spectrum.*
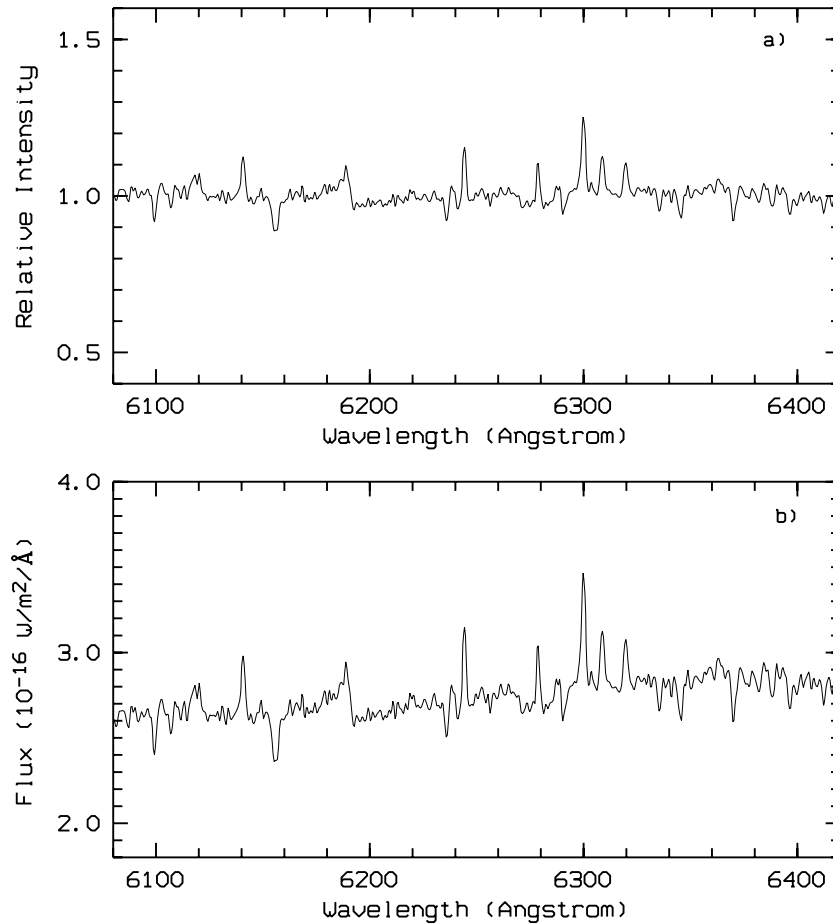
Figure 2.13: *An example of a stellar spectrum before (a) and after the flux calibration (b).*

dening (see Appendix B). The measured mean wavelengths of the bandpasses ($\bar{\lambda}$) and the calibrated fluxes for the standard system (Table 2.3) are taken from Bessell (1979).

The spectral flux distribution in the wavelength range from 4000 Å to 8000 Å has been obtained by fitting a second-order polynomial to the flux values obtained in the standard *UBVRI* filters. The flux distribution of V854 Cen in the deep minimum with the uncertainties in $\bar{\lambda}$ and $f_{\bar{\lambda}}$ is plotted in Figure 2.11a. The uncertainty along the wavelength axis is defined as the difference between the mean ($\bar{\lambda}$) and effective wavelengths (λ_{eff}) of the bandpasses. Since λ_{eff} depends on the spectral type, this difference will also vary from one spectral type to another. It has the largest value in the R filter ($\sim$ 130 Å, or 2%, for G0 and $\sim$ 800 Å, or 12%, for M0 spectral types), while it is less than 50 Å for the same spectral types in the other filters (Bessell 1979). The flux distribution in an RCB decline spectrum differs significantly from the distribution at the light maximum (Figure 2.11b). It is more similar to a distribution of a cooler star (K or M spectral types) for which λ_{eff} can differ from $\bar{\lambda}$ by about 12% for R filter and less than 2% for other filters. A typical uncertainty along the flux axis, due to the errors in measuring the magnitudes, has been estimated to be less than 8% for *U*, 6% for *I* and 3% for the other filters, depending on the stellar magnitude.

The use of the photometric magnitudes to calibrate the continuum fluxes assumes that the spectral lines in a photometric bandpass do not affect the total flux significantly. This is certainly the case for the V, R and I bandpasses, because the lines in these regions are relatively narrow and the bandpasses are broad. During some phases of RCB declines considerable variations in the $(U - B)$ and $(B - V)$ colour indices may be detected, corresponding to the appearance of broad line and continuum emission in the blue. This could significantly affect the stellar magnitude and therefore make the flux calibration less reliable. However, these fluctuations have been avoided in the majority of observations since most of the spectral lines analysed in this work do not fall in the blue region.

A schematic diagram of the whole procedure (including both the subtraction and flux calibration) is shown in Figure 2.12. The standard procedure includes obtaining the residual spectrum (Figure 2.12e), as well as the flux calibration of the maximum light, decline and residual spectra (Figure 2.12b, d, f). An example of a spectrum after the flux calibration is shown in Figure 2.13.

2.5.3   Equivalent widths and absolute fluxes of emission lines

In order to estimate the equivalent widths and absolute fluxes of emission lines, Gaussian fits to the lines have been used. A Gaussian function gives a reliable fit to most of the emission spectral lines. An example of a medium-resolution line with a single-gaussian fit is shown in Figure 2.14. In the case of the low-excitation sharp emission lines in the échelle spectra, where more line components can be resolved, a set of Gaussians is used (Figure 2.15).

The equivalent width (W_λ) of a Gaussian profile is proportional to the relative intensity (I_r) and the full width at the half maximum (FWHM). These parameters have been obtained using the MIDAS non-linear least square fitting procedure (Newton-Raphson method). Therefore, the equivalent width can be calculated as:

$$W_\lambda \, [\text{Å}] = \frac{\sqrt{\pi}}{2\sqrt{\ln 2}} \, I_r \times \text{FWHM}. \tag{2.2}$$

The absolute flux $F_l(\lambda)$ in a spectral line can then be expressed in a form:

$$F_l(\lambda) \, [\text{W m}^{-2}] = W_\lambda \, F_c(\lambda), \tag{2.3}$$

where $F_c(\lambda)$ $(\text{W m}^{-2}\,\text{Å}^{-1})$ is the interpolated value of the flux in the continuum at the central wavelength (λ) of the emission line. A typical uncertainty of the equivalent width measurements is about 2% (see Appendix C). For the line fluxes, the uncertainty ranges between 3% (in V) and 8% (in U).

It has been confirmed (by using the high resolution spectra) that the lines measured from the MRS spectra are not blended. All blended lines have been excluded from the measurement process, except in the case of strong emission lines such as NaI D, CaII H & K and the CaII IR triplet.
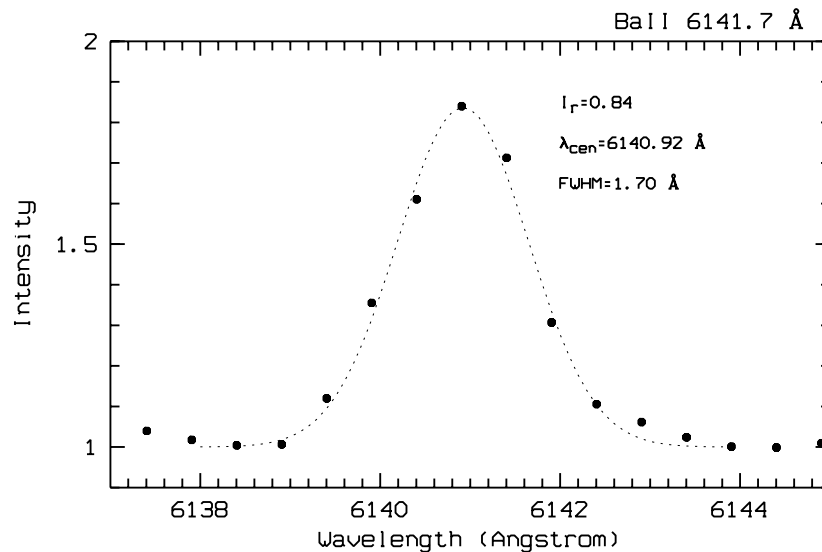
Figure 2.14: *The Gaussian fit to an emission spectral line and its parameters: I_r – relative intensity, λ_{cen} – central wavelength and FWHM – full width at the half maximum.*
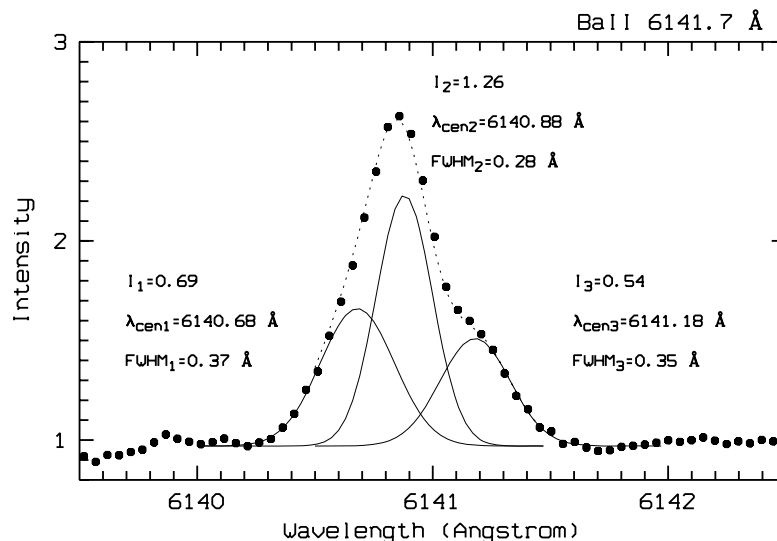
Figure 2.15: *Three Gaussians have been fitted to a multi-component low-excitation sharp emission line in the échelle spectrum. Solid lines represent each Gaussian, while the dashed line is their sum. Parameters of each Gaussian are displayed.*

High resolution profiles of low-excitation elements (observed in the 1998 decline of V854 Cen) show a complicated structure which can be decomposed into three components. The profiles of the components are assumed to be Gaussians (Figure 2.15). However, the three components are not completely resolved so that it is extremely difficult to obtain a unique solution. In such a case, obtaining the best fit for a given line does not necessarily mean that the actual solution has been found. Often, a set of three very different Gaussians (some

of them with the FWHM values even less than the instrumental profile) appear to give the best fit. In order to obtain a consistent solution for all sharp emission lines with similar structure, Gaussians with similar parameters have been used. As the first step of the fitting process, the initial values of the parameters of the three Gaussians are estimated using some of the strongest (or best resolved) examples. All parameters are defined relative to the central (strongest) component. They are varied until the minimum r.m.s. error for all three lines is obtained. It is assumed that all low-excitation sharp emission lines have the same three-component structure. As a result of this procedure, the equivalent widths and radial velocities of all line components have been obtained. The uncertainty in the equivalent width of each component ranges between 10% and 50%, depending on how well the components are separated. On the other hand, the total equivalent width and line flux are obtained with an uncertainty of a few per cent ($\leq 3\%$).

In principle, the absolute fluxes of emission lines can be measured directly from the flux-calibrated spectra (Figure 2.12f), since they are equal to the equivalent widths in this case. However, a possible slope of the continuum level can introduce some additional uncertainty (up to 10%) in the Gaussian parameters of emission lines. This is the reason why a different approach has been adopted in this thesis. The alternative procedure is based on Equation 2.3, where the equivalent widths are measured from the normalized spectra (Figure 2.12e).

2.5.4   Radial velocity measurements

The radial velocity of a spectral line is calculated as:

$$V_{\rm r} \, [{\rm km \, s^{-1}}] = \frac{\lambda_{\rm cen} - \lambda_{\rm lab}}{\lambda_{\rm lab}} \, c + V_{\rm bc}, \tag{2.4}$$

where $\lambda_{\rm cen}$ is the measured central wavelength of the line, as derived from the Gaussian fit, $\lambda_{\rm lab}$ is the laboratory wavelength of the line taken from Moore (1972) and $V_{\rm bc}$ is the barycentric correction, computed for the time of observation.

The radial velocity is also corrected for any systematic errors in the dispersion solution, as derived from the sky lines (assuming that their velocity is zero). The mean velocity of a number of sky lines from different échelle orders has been used. This correction can have a value of up to 1.5 km s^{-1} for the échelle spectra and about 3.5 km s^{-1} for the MRS spectra. For the single-order MRS spectra the correction has been calculated only for those regions where the sky lines are observed.

The total uncertainty in the radial velocity of one spectral line from the Gaussian fit is less than 3% (see Appendix C). In case of the low-excitation sharp emission lines, where three Gaussians have been fitted, the radial velocity of the central component is obtained with a similar uncertainty (less than 3%). The radial velocity of the other two weaker components is measured with a typical uncertainty of 15%.

2.5.5   Fitting the NaI D spectral lines

The NaI D spectral lines (D_2: 5890 Å and D_1: 5896 Å) show a complicated structure during RCB declines, with several different components. Although there are other lines that show similar features (e.g. CaII H&K, CaII IR triplet), the NaI D lines are the most prominent and easy to observe in all RCB declines. Since they have a multicomponent structure, with different components blending with each other (e.g., broad and sharp emission, high-velocity and photospheric absorption), they will be analysed separately.

Various NaI D components can have different parameters and appearance from one star to
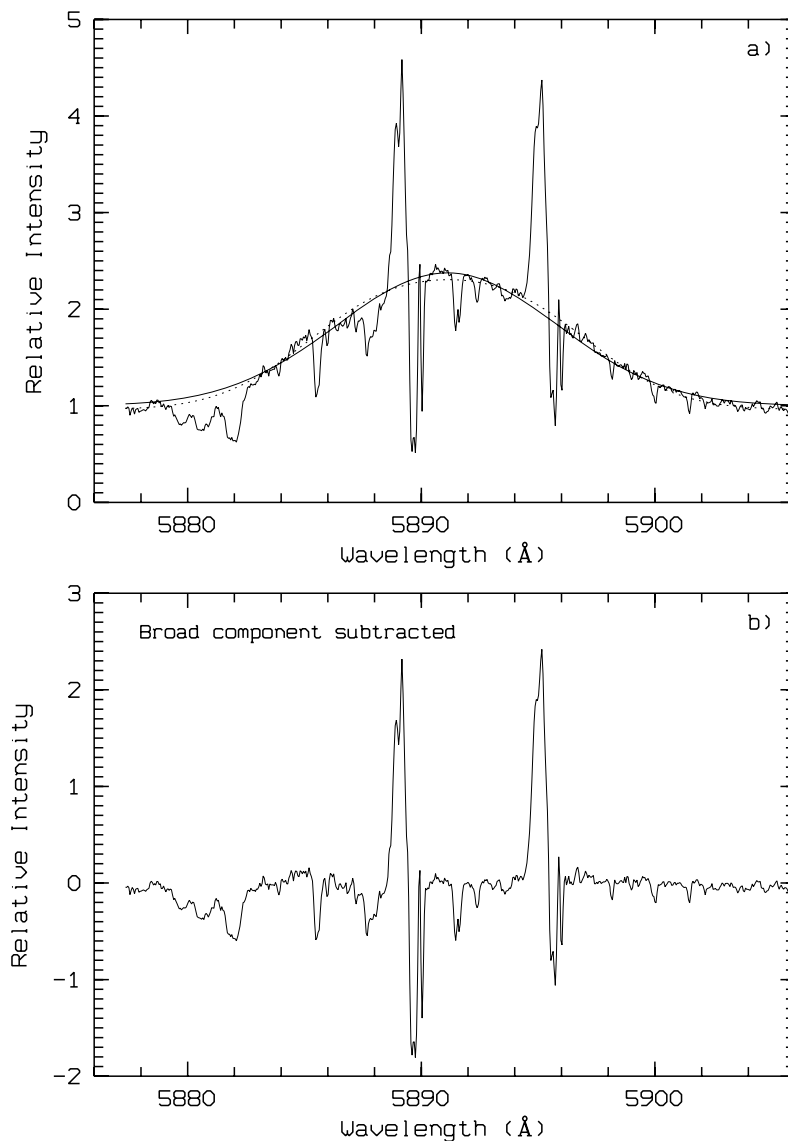
Figure 2.16: *a) A single Gaussian (solid line) and a pair of Gaussians (dotted line) fitted through the broad NaI D emission. b) The residual spectrum remaining after the broad emission (single gaussian fit) has been subtracted.*
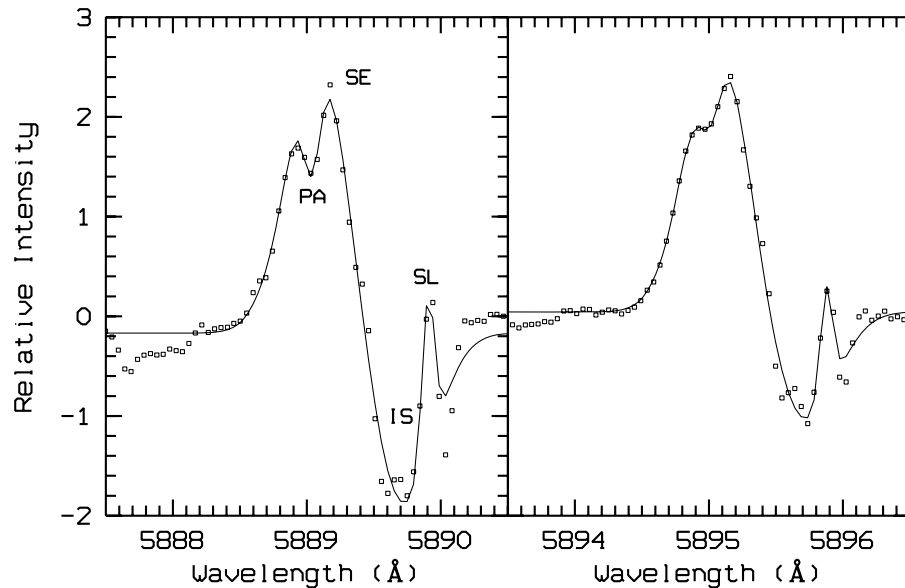
Figure 2.17: *An example of a multi-component Gaussian fit through the high resolution sharp NaI D emission lines (solid line). Four Gaussians have been used to fit the sharp emission (SE), photospheric absorption (PA), interstellar absorption (IS) and sky lines (SL).*

another, and even from one decline to another. The following procedure has been developed for the analysis of the high resolution spectra of NaI D lines from the 1998 decline of V854 Cen. This RCB star shows a strong underlying broad emission that can be fitted by a single (or double) Gaussian (Figure 2.16). Initially a number of points are set manually along the broad component, so that a preliminary Gaussian can be fitted. All points found outside 2σ of the fit are then rejected (this will include all sharp emission and absorption features). The remaining points represent the broad emission and are used for the final Gaussian fit. A single Gaussian gives a satisfactory fit, since the two emission lines are close and well blended. Figure 2.16a shows both the single and double Gaussian fits (both components of the double fit are of the same intensity and FWHM). The broad emission (single gaussian fit) is then subtracted from the observed spectrum, as shown in Figure 2.16b.

The fitting procedure for the other NaI D components (the sharp emission, high-velocity absorption and shell absorption) has been performed on the subtracted spectra (see Figure 2.16b). The sharp NaI D emission is blended with the photospheric and interstellar absorption, as well as the sky emission. The strongest of them are the interstellar and sky lines, while the photospheric absorption disturbs the profile only slightly. The deep decline spectra, where these components can be distinguished, have been modelled by three (sometimes four) Gaussians (Figure 2.17). The shell absorption has been approximated with a single Gaussian. The high velocity absorption, due to its complex structure, has not been modelled, but the total equivalent width has been estimated by numerical integration.

Modelling the NaI D lines

Numerous medium-resolution spectra of the NaI D region collected throughout the whole 1998 decline of V854 Cen (see Chapter 3) have enabled a detailed examination of various components of the NaI D lines and their evolution during the decline. However, many of these components are not resolved in the MRS spectra and their presence can be detected only indirectly, as they affect the overall profile of the spectral lines.

A special modelling procedure was developed as part of this thesis in order to examine the complex profiles of the NaI D lines during the decline. The model includes the strongest NaI D components that dominate the MRS spectra. These are the photospheric, shell, high-velocity and interstellar absorption, as well as the sharp and broad emission. The influence of the NaI D sky lines during the 1998 decline of V854 Cen can be neglected, due to the short exposure times and strong stellar emission. The NaI D model assumes that the broad and sharp emission components have a stable flux that does not depend on the photospheric continuum level. This is in agreement with the assumption that these two emission components are permanent features in RCB spectra (Rao et al. 1999). Their absolute fluxes (F_{b} and F_{se}) are therefore added to the stellar continuum flux (F_{c}). On the other hand, the NaI D shell and high-velocity absorptions are proportional to the stellar continuum. Therefore, the total stellar flux around the NaI D lines ($F^{\star}$), as received by the observer, can be expressed as:

$$F^{\star} = (F_{\mathrm{c}} * f_{\mathrm{ph}} * f_{\mathrm{sa}} * f_{\mathrm{hva}} + F_{\mathrm{b}} + F_{\mathrm{se}}) * f_{\mathrm{is}} \tag{2.5}$$

where F_{c}, F_{b} and F_{se} are the absolute fluxes of the stellar continuum, broad emission and sharp NaI D emission, respectively, while f_{ph}, f_{sa} and f_{hva} are the relative intensities of the photospheric, shell and high-velocity absorption. The schematic diagram of this process is shown in Figure 2.18.

Equation 2.5 can be normalized relative to the stellar continuum:

$$F^{\star}/F_{\mathrm{c}} = (f_{\mathrm{ph}} * f_{\mathrm{sa}} * f_{\mathrm{hva}} + F_{\mathrm{b}}/F_{\mathrm{c}} + F_{\mathrm{se}}/F_{\mathrm{c}}) * f_{\mathrm{is}} \tag{2.6}$$

so that all parameters are expressed in the relative scale and the result of the modelling ($F^{\star}/F_{\mathrm{c}}$) can be compared with the observed spectra.

The initial parameters of the spectral lines involved in the model described above have been determined from various high resolution spectra obtained during the light maximum, as well as at different decline phases. The total number of free parameters have been reduced by keeping the photospheric, shell and interstellar absorption constant. Their profiles are defined completely by their radial velocities, FWHM values, relative intensities of the D_1 component and flux ratios of the two components. A single pair of interstellar NaI D absorption lines has been considered. The parameters of the sharp emission lines also include their radial velocity, FWHM and flux ratio of the two components. A single broad component has
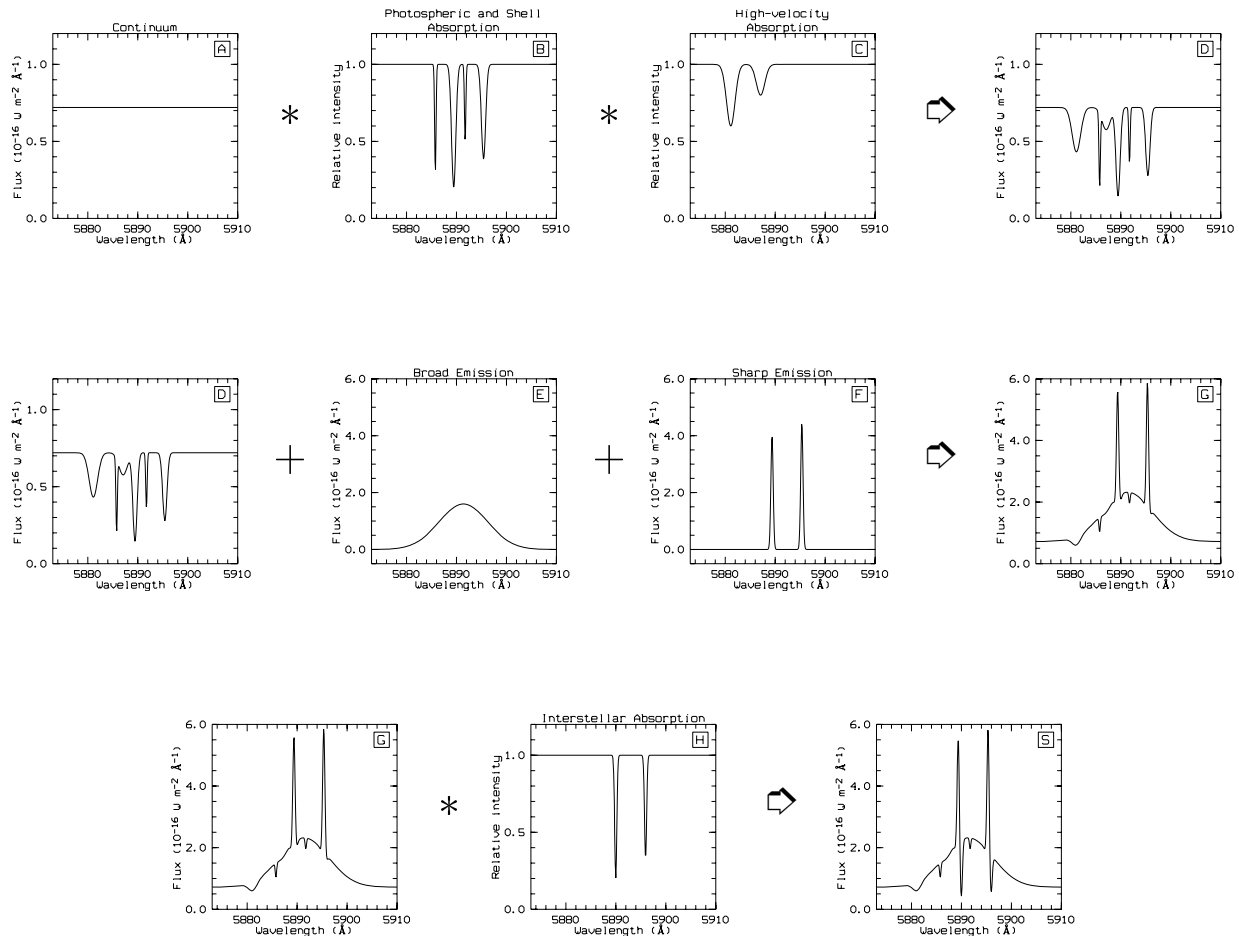
Figure 2.18: *Schematic diagram of the NaI D line modelling. The absolute flux of the stellar continuum (A) is multiplied by the normalized spectrum containing the photospheric and shell absorption (B) and by the high-velocity absorption (C). The result (D) is added to the broad and sharp emissions (E & F), both expressed in absolute flux units. The total stellar flux around NaI D lines (G) is absorbed by the interstellar medium (H) giving the final flux distribution (S) received by an observer.*

been used with a fixed radial velocity, FWHM and peak flux defined from the deep decline spectra. The parameters of the high-velocity absorption are treated as variables, since these lines change throughout the decline phase. They can be chosen at the beginning of the modelling process, so that the whole model gives the best match with the observed spectrum. The procedure allows some small variation of the photospheric flux in a given range and with a chosen step. The initial values of the flux are obtained from the flux calibrated spectra around the NaI D lines for the same day. Small variations of the sharp emission line fluxes have also been considered, due to the fact that their flux can decrease later during the decline. This is caused by the obscuration of the sharp emission region by the dust cloud. Using the parameters determined from each step, the model of the NaI D region is formed as a high-resolution spectrum which is then convolved to the lower resolution of the MRS
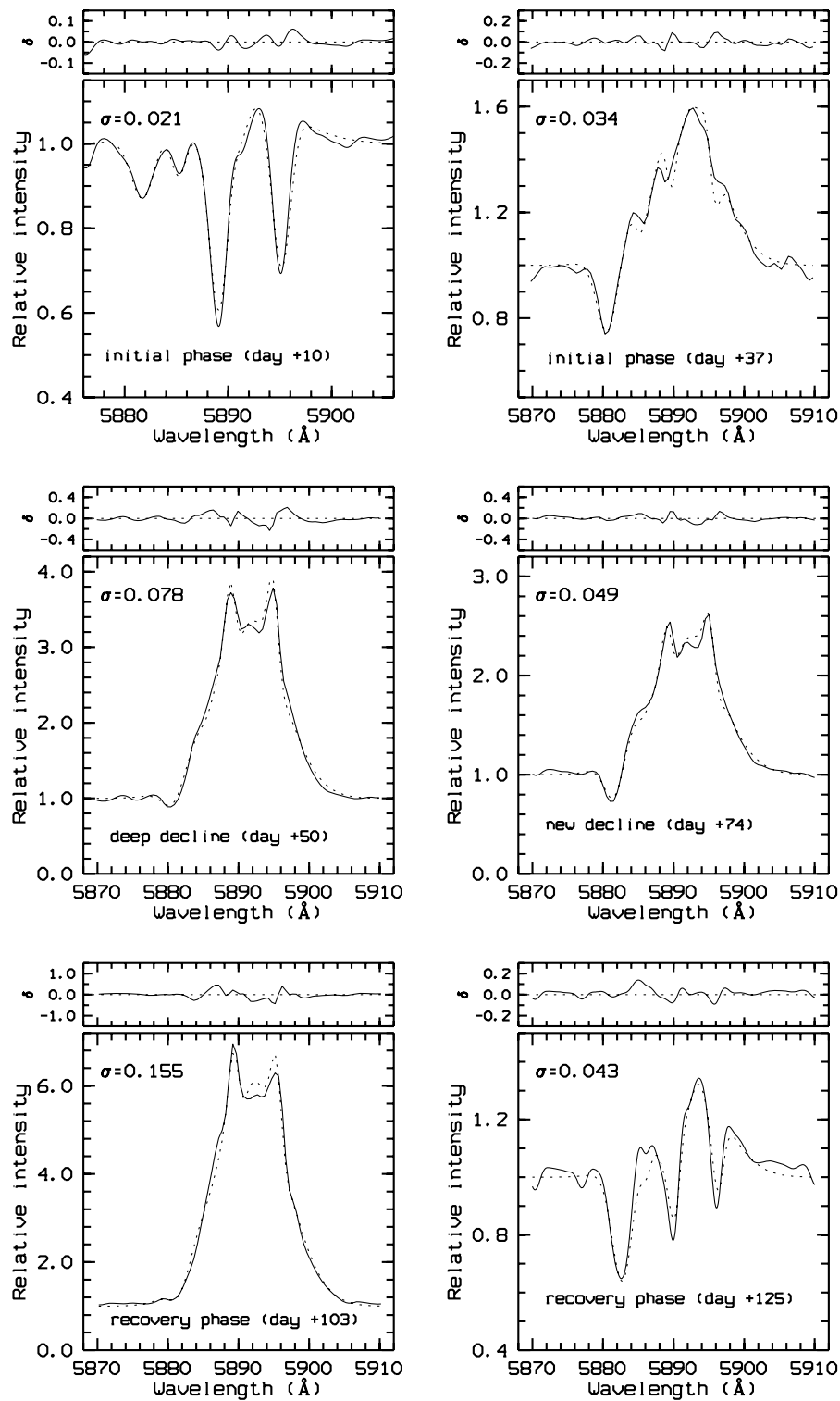
Figure 2.19: *Comparison between the NaI D model fit (dashed line) and the MRS spectra (solid line) at different phases of the 1998 decline of V854 Cen. The r.m.s. error (σ) is given for each model and the residuals (i.e. the difference between the spectral observations and the models) are plotted (δ).*

spectra. This is then compared with the observed MRS spectrum. The line parameters are varied until the smallest least squares deviation is achieved. Figure 2.19 gives a comparison between the models and the observed MRS spectra. As a final result, the procedure gives a set of equivalent widths for the broad and sharp emission lines, as well as the absolute fluxes for the sharp emission components.

The uncertainties of the parameters generated by the modelling process have been estimated by comparing the model values with those obtained from the high-resolution spectra. The following procedure has been used: First, the line parameters are measured from an échelle spectrum. Then the spectrum is convolved to the MRS resolution. Finally, this profile is modelled and the line parameters obtained. The difference between the measured and modelled parameters is about 10% for the broad and about 30% for the sharp emission. This is due to blending effects produced by the broad emission lines, introducing larger uncertainties in measuring the line parameters.

The above discussion on the analysis techniques of the NaI D spectral lines concludes this chapter on observations and data reduction. The following chapters will present the declines of some RCB stars included in the observing programme of this thesis.

Chapter 3

The 1998 decline of V854 Centauri

3.1   V854 Cen – current observational facts

V854 Cen (previously known as NSV 6708) is one of the most unusual of all R Coronae
Borealis stars. The star was discovered relatively recently by McNaught & Dawes (1986). It
is the third brightest RCB variable, after R CrB and RY Sgr, but distinguished from them by
a few characteristics. One is the presence of strong Balmer lines with a deep core and broad
shallow wings, typical for normal supergiants of the same effective temperature. These lines
are either weak, or not present in spectra of other RCB stars. The second characteristic is
the high frequency of declines, which is the reason why the star had not been discovered
earlier.

The abundance analysis at maximum light (Asplund et al. 1998) confirms that V854 Cen
has a somewhat unusual composition. V854 Cen is hydrogen-rich when compared to other
RCB stars. Its hydrogen abundance is about 10% of that in normal supergiants, compared
with < 1% in other RCB stars. V854 Cen is also one of the few metal-poor RCB stars
(Clayton 1996), together with three other RCBs with unusual compositions (V CrA, VZ Sgr
and V3795 Sgr). The basic stellar parameters for V854 Cen ($T_{\mathrm{eff}} \approx 7000$ K and $\log g \approx 0$)
were determined by Asplund et al. (1998). At light maximum V854 Cen shows fairly regular
pulsations of 43 days (Lawson et al. 1992), which appear to be correlated with the time of
the decline onset. This correlation suggests a connection between the stellar pulsations and
the dust cloud condensation.

Only a limited number of spectra of this peculiar RCB star during the declines are
available. From the low-resolution spectra of V854 Cen (Kilkenny & Marang 1989; Whitney
et al. 1992), the strongest emission lines were reported as: NaI D, H_{α}, H_{β} and lines of singly-
ionized metals (ScII, TiII, BaII, etc.). The molecular bands of the C_2 Swan system were also
found in emission in a deep decline (Whitney et al. 1992) and in absorption in a less deep
minimum (Kilkenny & Marang 1989). A key finding of the spectropolarimetry (Whitney
et al. 1992) is that the emission lines are unpolarized at the time when the continuum is

significantly polarized. The forbidden lines of [OI], [NII] and [SII] (Rao & Lambert 1993) were identified in the 1992 deep decline of V854 Cen. This was the first certain identification of these lines in an RCB star. From the 1998 decline spectra, Rao & Lambert (2000) also detected the absorption lines of the C_2 Phillips system, indicating the presence of a cold C_2 gas around V854 Cen. In the ultra-violet region V854 Cen shows the presence of some CII, MgI and CI lines not seen in other RCB stars (Clayton et al. 1992a; Lawson et al. 1999).

The current observations of the 1998 decline of V854 Cen obtained for this thesis represent the first almost complete coverage of a decline for this star. This includes simultaneous photometry (see Section 3.2) and medium to high-resolution spectroscopy (see Section 3.3) prior to and throughout the decline. The evolution and physical characteristics of various lines appearing during the decline are discussed in Sections 3.4–3.8. The photometric and spectroscopic data indicate similar decline characteristics as found in other RCB stars. These include the shape of the light curve, the behaviour of the colour indices and the appearance and evolution of various emission lines.

3.2   Photometry

The 1998 decline of V854 Cen was six magnitudes deep, with the initial phase about two times longer (~ 100 days) than the recovery phase (~ 60 days). The light fading was characterized by several successive declines, labelled as I, II and III in Figure 3.1, and separated by about 43 days corresponding to the pulsation cycle of the star (Cottrell et al. 1990). In each of these phases significant photometric and spectroscopic changes occurred.

The colour variations follow a typical decline pattern, reflecting the changes in the light curve (Figure 3.1). They indicate the actual fraction of the photosphere and of the emission regions being obscured by the dust cloud, as well as the optical depth of the cloud and the evolution of the emission spectrum. All colours, except $(U - B)$, are *reddened* at the very beginning of the decline, so that this can be classified as a "red-type" decline (Cottrell et al. 1990). Significant colour changes occur during the deepest decline (decline III, JD 2450950, day number +90), when all colours become bluer. This blueing is most prominent in $(U - B)$ and $(B - V)$, so that these colours get bluer even when compared with maximum light. The other two colours, although bluer locally, still remain redder than at the maximum. The blueing can be explained by the appearance of the broad-line emission (such as CaII H & K, NaI D and broad continuum emission[1]), as well as by the obscuration of the photosphere.

It is interesting to note that no obvious blueing in $(B-V)$ can be seen during the first two light fadings (I and II). This is supported by spectroscopy (see Section 3.5.3, Figure 3.36), showing that the CaII H & K lines went into strong emission only during the third decline (III), so that they could not contribute to the blue flux increase during the first two declines.

[1]A blend of numerous emission lines in the blue, causing an overall rise in the continuum level.
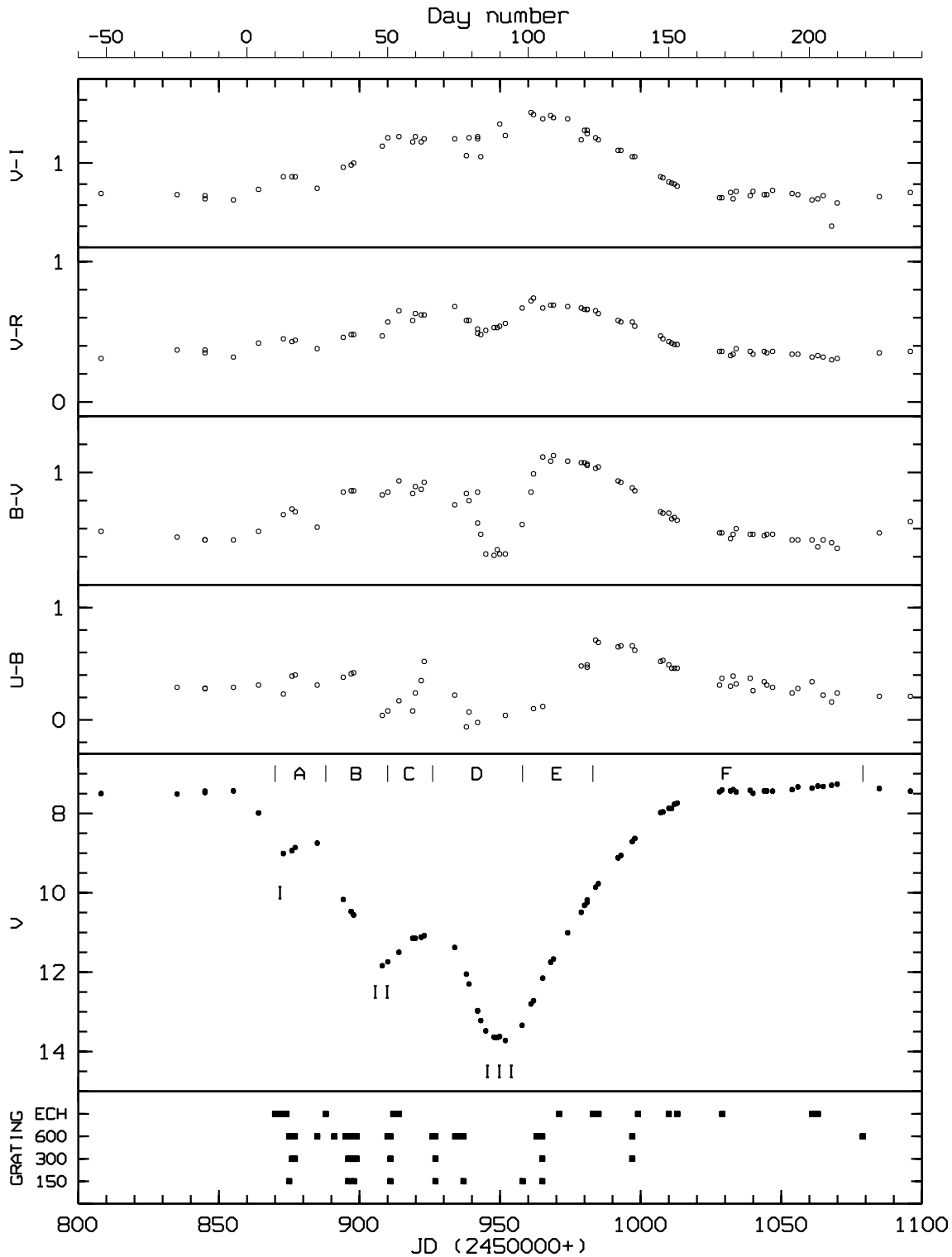
Figure 3.1: *The visual magnitude (V) and colours: (U − B), (B − V), (V − R) and (V − I) during the 1998 decline of V854 Cen. Day numbers (top axis) are measured from the beginning of the decline (JD 2450860). The times at which the spectroscopic observations were made are also marked (black squares in the lower panel). Phases A–F are marked as given in Tables 3.2 & 3.3.*

The fact that the third fading appears significantly bluer can also mean that the newly formed cloud obscures the photosphere, but not the chromosphere and regions where the strong broad emission originates.

3.3   Spectroscopy

Low, medium and high-resolution spectra of V854 Cen were obtained between 1996 April 20 and 1998 September 22 (Tables 3.1–3.3 and Figure 3.2). This includes the 1998 decline, as well as some time before and after it. In fact, the first spectra obtained originate from the very late recovery phase of the 1995/96 decline. They show no other changes except around the NaI D lines, which will be discussed later (see Section 3.7, Figure 3.44). All spectra were collected at MJUO, except for three obtained at McDonald Observatory (day numbers: +52, +54 and +111).
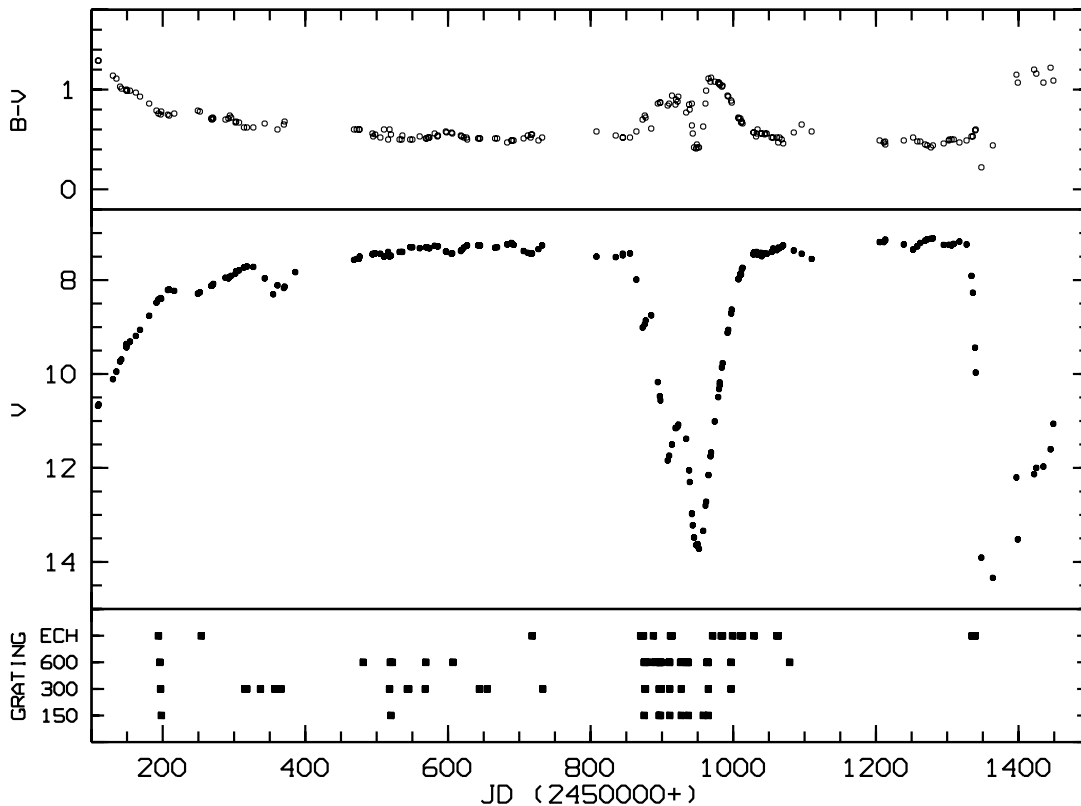
Figure 3.2: *Light curve, (B − V) colour and spectroscopic coverage during the observing programme of V854 Cen. Black squares in the lower panel represent the times at which the spectroscopic observations were made. Symbol ECH indicates the high-resolution spectra, while numbers 600 (medium-resolution) and 300, 150 (low-resolution) correspond to different gratings of the medium-resolution spectrograph.*

Table 3.1: *Summary of spectroscopic observations of the 1998 decline of V854 Cen: JD – Julian Day (2450000+), Day No. – number of days since* $JD_0 = JD\,2450860$ *(negative numbers are before* JD_0*),* m_V *– V magnitude, S/N – signal to noise ratio in the continuum in about the middle of the given wavelength range. Medium and low resolution is assumed for all spectra, except for the high-resolution échelle spectra, marked with (e).*

Date (UT)	JD 245...	Day No.	Spectral range (Å)	m_V	S/N	Comments
1996						
Apr 20	0194	−666	5430 – 8550	8.5	90	(e)**, recovery of the 1995/96 decline.
Apr 22	0196	−664	3800 – 6280	8.5	30	
Apr 23	0197	−663	3800 – 6800	8.5	67	HVA*
Apr 24	0198	−662	5200 – 7200	8.5	65	HVA
Jun 19	0254	−606	5430 – 8550	8.4	85	(e)
Aug 19	0315	−545	3800 – 6800	8.0	30	normal photosperic spectrum.
Aug 22	0318	−542	3800 – 6800	7.8	25	
Sep 10	0337	−523	5800 – 6800	8.0	50	
Sep 30	0357	−503	5800 – 6800	8.2	55	
Oct 09	0366	−494	5800 – 6800	8.2	42	
1997						
Feb 01	0481	−379	3800 – 6280	7.5	30	
Mar 10	0518	−342	5800 – 6800	7.5	75	
Mar 11	0519	−341	5200 – 9200	7.3	60	
Mar 12	0520	−340	3800 – 7200	7.3	45	
Mar 14	0522	−338	5750 – 6280	7.3	82	
Apr 04	0543	−317	5800 – 6800	7.3	54	
Apr 06	0545	−315	3800 – 4600	7.3	28	
Apr 29	0568	−292	5800 – 6800	7.3	55	
Apr 30	0569	−291	3800 – 6280	7.4	78	normal photospheric spectrum.
Jun 07	0607	−253	5750 – 6280	7.3	63	
Sep 26	0718	−142	4680 – 6280	7.3	106	(e)
Oct 11	0733	−127	5800 – 6800	7.3	53	

* high-velocity blue-shifted NaI D absorption.

** high-resolution échelle spectra.

Table 3.2: *Summary of spectroscopic observations of V854 Cen (continued).*

Date (UT)	JD 245...	Day No.	Spectral range (Å)	m_V	S/N	Comments
1998						Phase **A**
Feb 25	0870	+10	5430 – 8550	8.7	90	(e), HVA visible.
Feb 26	0871	+11	5430 – 8550	8.8	80	(e),
Feb 28	0873	+13	5430 – 8550	8.9	75	(e), broad NaI D emission.
Mar 01	0874	+14	5430 – 8550	9.0	84	(e)
Mar 02	0875	+15	5200 – 6800	9.0	72	weak HVA visible.
Mar 03	0876	+16	3800 – 9200	8.8	55	filling in of NaI D, H$_\alpha$, CaII IR triplet and
Mar 04	0877	+17	5200 – 6800	8.8	68	CI spectral lines.
Mar 12	0885	+25	3800 – 9200	8.7	65	
						Phase **B**
Mar 15	0888	+28	5430 – 8550	9.3	90	(e), HVA & broad NaI D emission.
Mar 18	0891	+31	5200 – 6800	9.5	65	
Mar 22	0895	+35	5200 – 6280	10.2	60	C$_2$ emission.
Mar 23	0896	+36	3800 – 6800	10.4	52	singly-ionized emission line increasing.
Mar 24	0897	+37	3800 – 9200	10.6	67	H$_\alpha$ broad emission.
Mar 25	0898	+38	5200 – 9200	10.8	58	CaII IR triplet and [CI] emission.
Mar 26	0899	+39	5200 – 6800	11.0	70	filling in of CaII H & K lines.
						Phase **C**
Apr 06	0910	+50	5200 – 9200	11.8	50	strong ionized & neutral atom emission.
Apr 07	0911	+51	3800 – 6280	11.7	45	CaII H & K lines in emission.
Apr 08	0912	+52	4200 – 10200	11.6	65	(e), MgI, NaI D, H$_\alpha$, CaII IR triplet,
Apr 10	0914	+54	4200 – 10200	11.5	50	(e), CI, [OI], C$_2$ emission.
						Phase **D**
Apr 22	0926	+66	5200 – 6800	11.2	32	emission decaying.
Apr 23	0927	+67	3800 – 9200	11.2	68	C$_2$ absorption.
Apr 30	0934	+74	5200 – 6800	11.4	72	
May 01	0935	+75	3800 – 9200	11.5	53	emission increasing.
May 02	0936	+76	3800 – 6800	11.8	43	no CI emission.
May 03	0937	+77	5200 – 9200	12.0	30	strong broad NaI D.

Table 3.3: *Summary of spectroscopic observations of V854 Cen (continued).*

Date (UT)	JD 245...	Day No.	Spectral range (Å)	m_V	S/N	Comments
1998						Phase **E**
May 24	0958	+98	3000 – 9000	13.4	15	
May 29	0963	+103	5200 – 6280	12.8	38	strong broad NaI D and CaII H & K.
May 30	0964	+104	5200 – 9200	12.5	42	ionized emission and
May 31	0965	+105	3800 – 7200	12.2	32	photospheric absorption.
Jun 06	0971	+111	4200 – 10200	11.5	60	(e), HVA increasing.
						Phase **F**
Jun 18	0983	+123	5430 – 8550	9.9	20	(e), weak broad NaI D.
Jun 20	0985	+125	5430 – 8550	9.8	54	(e), strong HVA
Jul 02	0997	+137	3800 – 9200	8.7	62	photosphere reappears.
Jul 04	0999	+139	5430 – 8550	8.5	69	(e), no emission.
Jul 15	1010	+150	5430 – 8550	7.9	65	(e), HVA decaying.
Jul 18	1013	+153	5430 – 8550	7.7	120	(e)
Aug 03	1029	+169	5430 – 8550	7.4	110	(e), weak HVA
Sep 04	1061	+201	5430 – 8550	7.3	97	(e), no HVA
Sep 06	1063	+203	5430 – 8550	7.3	100	(e), normal photospheric spectrum.
Sep 22	1079	+219	5200 – 6800	7.3	82	normal photospheric spectrum.

Most of the maximum-light spectra were recorded using the medium-resolution spectrograph. Figure 3.3 shows a low-resolution maximum-light spectrum in the interval 5200–7200 Å. The strongest absorption lines correspond to NaI D, CI and H_α. At this resolution, the variations in depth of the absorption lines with the stellar pulsations cannot be distinguished clearly. This is caused by line blending effects and the uncertainty in the continuum level fitting.

On the other hand, these stellar pulsation variations are seen in the high-resolution spectra. For example, a difference in the line depths of about 15% can be detected in the NaI D region (Figure 3.4) when comparing two high-resolution spectra, one from the pulsation minimum (day number −142) and the other from the pulsation maximum (day number +203). However, one should bear in mind that the photospheric NaI D lines are often blended with various interstellar and circumstellar components, which makes the identification and monitoring of the components that vary more difficult.

The main decline onset ($JD_0 = JD\ 2450860$) has been determined from the photometry (see Figure 3.1) as the moment of time when the visual magnitude fell below the minimum amplitude of the stellar pulsations. This zero point has then been used instead of the
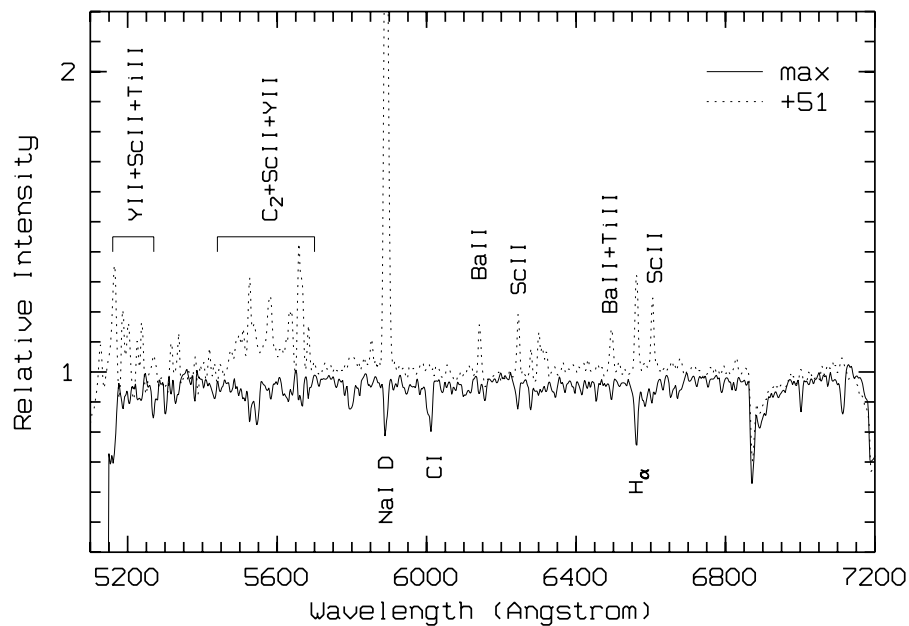
Figure 3.3: *A low-resolution maximum-light spectrum (solid line) and a deep decline spectrum (dashed line) between 5200 Å and 7200 Å. The strongest absorption and emission lines are marked.*
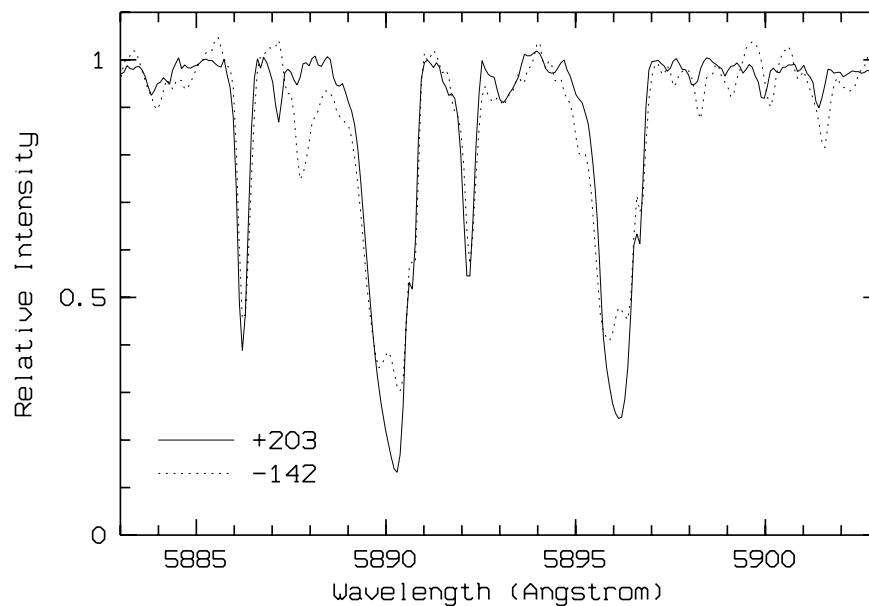

Figure 3.4: *High-resolution spectra of the NaI D region at the pulsation maximum (solid line) and minimum (dashed line). Various weak absorption lines correspond to the atmospheric H_2O.*

Julian Date to mark all spectra. The whole decline has been divided into several phases, demonstrating different photometric and spectroscopic characteristics (Tables 3.1–3.3).

The first set of spectra, marked as phase **A** in Table 3.2, is from the initial decline phase including a small recovery of about 0.5 magnitudes (decline I, day numbers +10 to +25). This small increase in brightness reflects the photospheric pulsations, probably triggering a new dust condensation causing a new light fading. The star was about 1.5 magnitudes below the average maximum ($7^{\mathrm{m}}.5$), showing reddening in all colours. The main spectroscopic changes are seen in the cores of the strongest spectral lines. A decrease in the line depths, indicating the appearance of line emission, can be noticed for NaI D, H_α, CaII IR triplet and CI spectral lines. The broad NaI D emission also rises above the noise in the continuum. An interesting feature of the NaI D lines is also the appearance of the high-velocity absorption (HVA) on day number +10.

The second successive decline (phase **B**, Table 3.2) occurs during the next stellar pulsation cycle (initial phase of decline II). The star declines by about four magnitudes relative to the mean maximum value in about 50 days from the first decline onset. Most of the emission lines appear or the absorption lines show filling in of their cores. The broad NaI D lines become dominant features blending with the other NaI D components. However, the strong high-velocity absorption can still be seen. The emission lines appear at the positions of most low-excitation singly-ionized elements (ScII, BaII, YII, TiII and FeII). Their emission increases as the star becomes fainter. Some other lines, such as the forbidden line of [CI] 8727 Å, CaII IR triplet and C_2 molecular bands, appear in emission as well. On the MRS spectra CI lines can be seen to further decrease in their depths. Similar changes are seen in the cores of the SiII 6371 Å and 6347 Å lines. At the end of this phase, CaII H & K lines show a decrease in their line depth, indicating the appearance of emission.

Phase **C** (day numbers +50 to +54) includes the spectra from the deepest part of decline II. The increase in reddening of all colours indicates further obscuration of the photosphere by the dust cloud. During this phase, the photospheric lines appear too weak (at the noise level in the continuum) due to broadening and filling in with emission. A low-resolution decline spectrum in the range 5200–7200 Å is shown in Figure 3.3. The strongest emission lines are the NaI D and H_α lines, as well as the low excitation lines of singly-ionized elements. The NaI D is the most prominent feature in the spectra of phase **C**, with strong broad and sharp emission blending with the high-velocity absorption. A complex profile, characterized by broad and sharp emission overlapping with the photospheric absorption, can be seen in the H_α, CaII H & K lines and CaII IR triplet. The CI spectral lines, as well as C_2 molecular bands, are in strong emission. The forbidden lines of [OI] (5577 Å and 6363 Å) are in emission, but are weak.

Phase **D** (day numbers +66 to +77, Table 3.2) includes the MRS spectra from the short recovery phase of decline II, as well as from the initial phase of decline III (which is about 2 magnitudes deeper than decline II). During this phase, the lines of NaI D, H_α, CaII H

& K and the Ca IR triplet, as well as the low-excitation lines of singly-ionized elements, remain in emission and their relative intensities change in time, due to the oscillations of the photospheric continuum. The broad NaI D emission increases further, almost completely blending with the weak high-velocity absorption. The CI lines decrease in strength gradually, while the forbidden lines (all except [CI]), are absent or very weak so that they cannot be identified. The C_2 Swan system appears in absorption for a short time during the recovery phase. As the star declines, the Swan bands possibly go into weak emission again.

Phases **E** and **F** (Table 3.3) are both from the recovery phase. The first one includes the MRS spectra from the early recovery phase (4 to 5 magnitudes below the maximum). The day numbers between +123 and +219 (phase **F**) correspond to the final recovery towards the maximum (3 magnitudes or less below the normal brightness), as well as a few maximum-light spectra. During the early recovery phase, the blueing of the $(B - V)$ and $(U - B)$ colours decreases slowly, until they again become significantly reddened (during the late recovery phase). First the sharp and then the broad emission decrease at this stage and the photospheric absorption reappears fully on day number +137. The most interesting feature of the recovery phase is the appearance of the high-velocity NaI D absorption (HVA), composed of several different components gradually changing their strength and position. The HVA components disappear completely between day numbers +169 and +201, when only the normal photospheric spectrum remains.

A graphical presentation of all identified spectral lines during the 1998 decline of V854 Cen is given in Figures E.1–E.7 (Appendix E). In these diagrams the date of observation is given for each spectral line, as well as an indication of whether the line was seen in absorption or emission or both.

All spectral lines from the 1998 decline of V854 Cen have been classified in the following qualitative way:

- sharp emission lines,

- broad emission lines,

- molecular bands,

- high-velocity absorption and

- photospheric absorption.

In addition, the NaI D lines demonstrate a complicated, multi-component structure. This structure has not been seen in other spectral lines. Before the actual analysis of each of the groups introduced above, the components of the NaI D lines will be classified.

Components of NaI D lines

During the 1998 decline of V854 Cen, the NaI D lines (D_2: 5890 Å and D_1: 5896 Å) were monitored throughout the whole phase using both the medium- and high-resolution spectrographs. These are the resonance lines of NaI (transitions from the ground state $3^2S_{1/2}$ to the second excited states $3^2P_{3/2}$ and $3^2P_{1/2}$, as shown in Figure 3.5). The NaI D emission is the most prominent feature in the entire visible spectrum during the decline (see Figure 3.3). The other NaI lines were not seen in emission, except for two relatively weak ones at 8183 Å and 8195 Å.
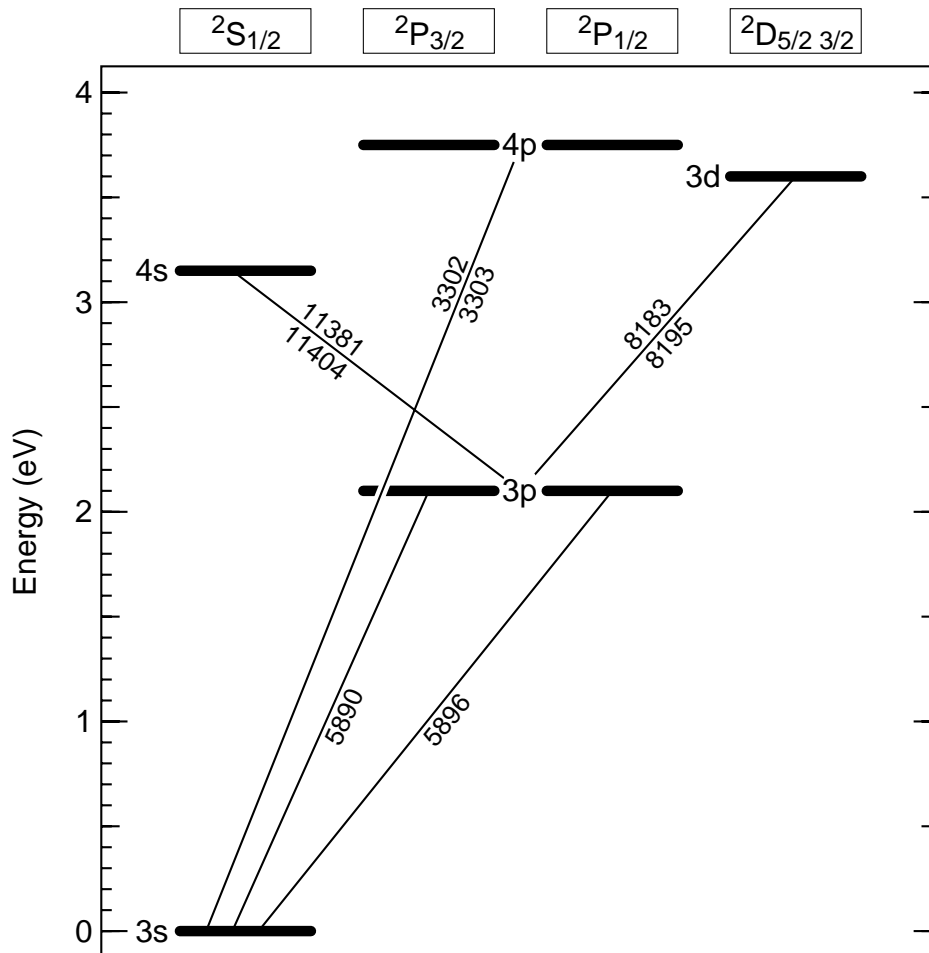
Figure 3.5: *Simplified energy diagram showing the transitions in the NaI atom. Wavelengths in angstrom units are shown along the lines representing the transitions. Energies in eV are given relative to the ground state.*

Four main NaI D components can be seen during this decline (Figure 3.6): sharp emission (SE), broad emission (BE), high-velocity blue-shifted absorption (HVA) and shell absorption (SA). In addition, the interstellar components (IS), photospheric absorption (PA) and sky components (at long exposures) can also be seen. Each of these features will be dis-
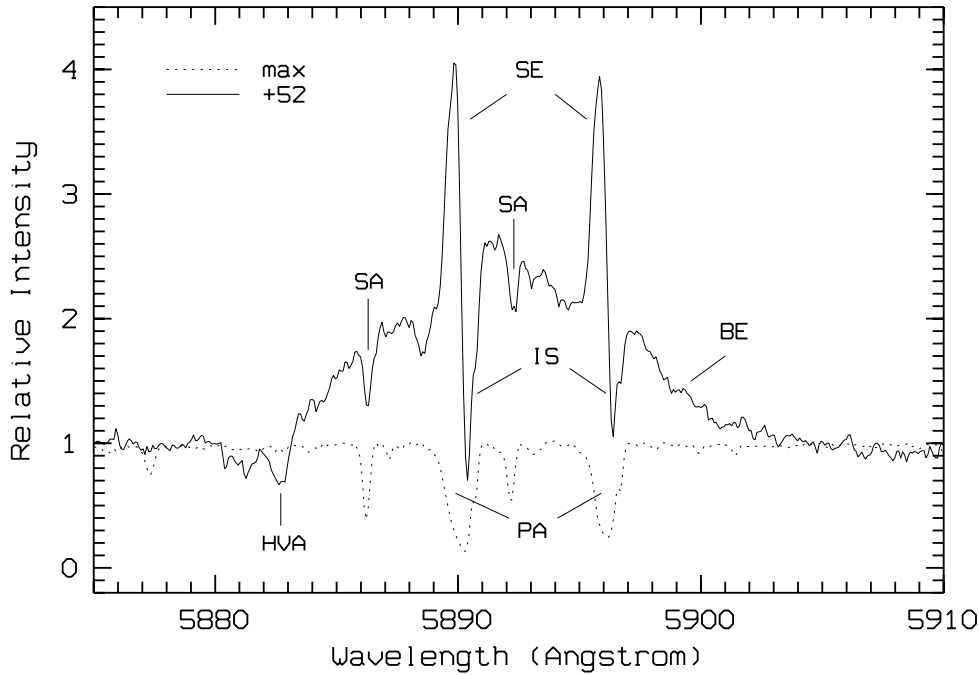
Figure 3.6: *Components of the NaI D lines: SE – sharp emission, BE – broad emission, HVA – high-velocity absorption, IS – interstellar absorption, SA – shell absorption and PA – photospheric absorption. Many of the weak, narrow absorption lines at other wavelengths are telluric H_2O lines.*

cussed and analysed separately later, with the appropriate group of similar spectral lines (see Sections 3.4–3.7).

The NaI D lines exhibit an interesting evolution during the decline phase (Figures 3.7 and 3.8). At the very beginning of the decline (phase A, Figure 3.7), the high-velocity absorption can be seen, as well as a weak broad emission (day numbers +10, +14). In the core of the photospheric absorption, a weak emission can also be identified. As the decline progresses (phase B), the photospheric continuum and absorption decrease and the broad and sharp emissions become obvious. In the deep decline (phase C) all three main components (SE, BE and HVA) become prominent. During the small recovery phase of decline II (phase D, Figure 3.8) the broad emission remains strong, while the sharp emission becomes weaker relative to the temporary continuum. As the star declines again, the broad and sharp emissions are clearly visible. Phase E corresponds to the early recovery phase: the broad emission is still strong, while the SE decreases. The HVA is also getting stronger. As the star returns to its normal brightness (phase F), both the broad emission and sharp absorption become weak and the normal photospheric spectrum reappears. Only the HVA remains visible close to light maximum (day numbers +125 to +169).
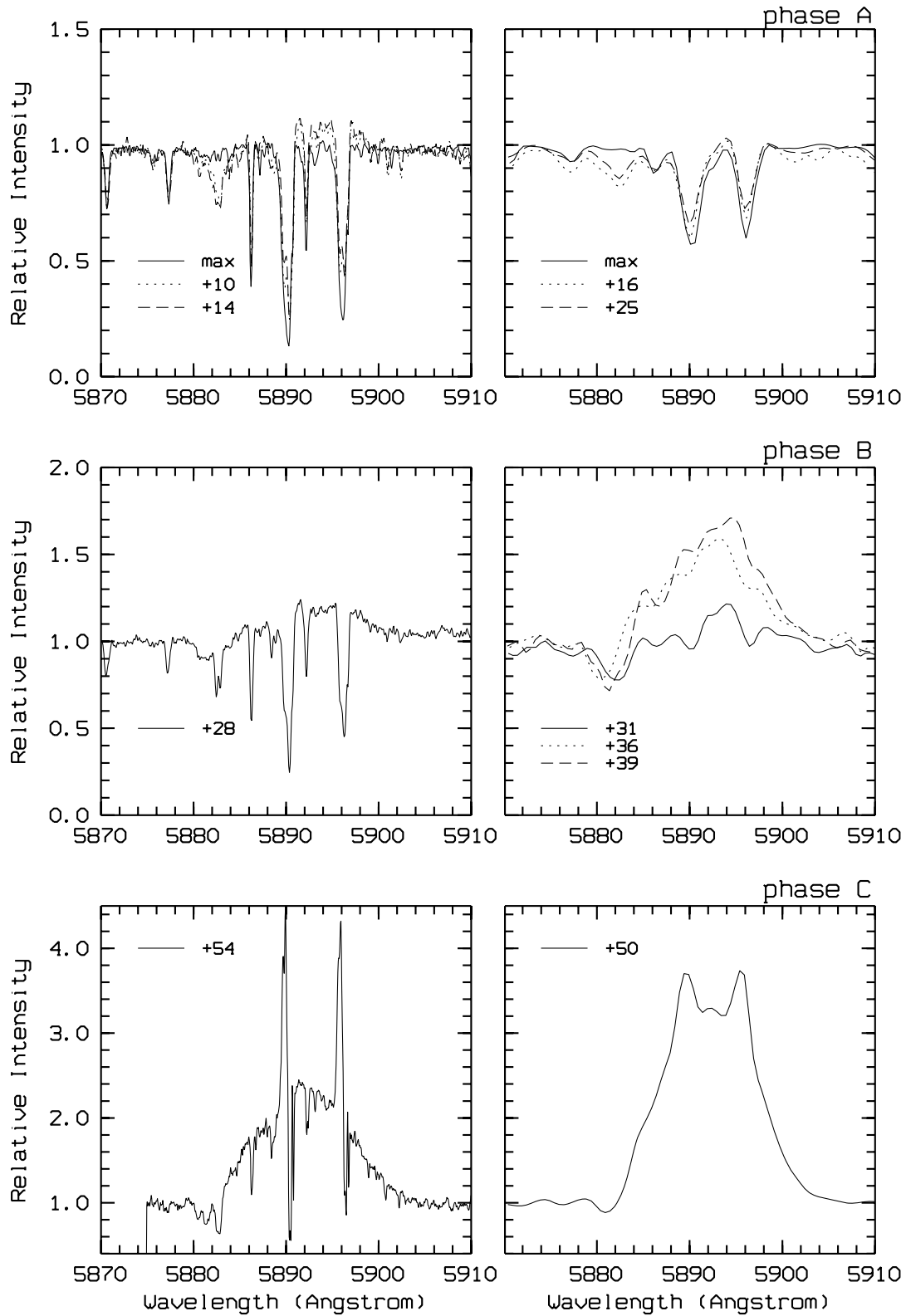
Figure 3.7: *The evolution of the NaI D lines throughout the decline (phases: A, B, C). Left: high-resolution spectra. Right: medium-resolution spectra. Day numbers are used to mark the spectra.*
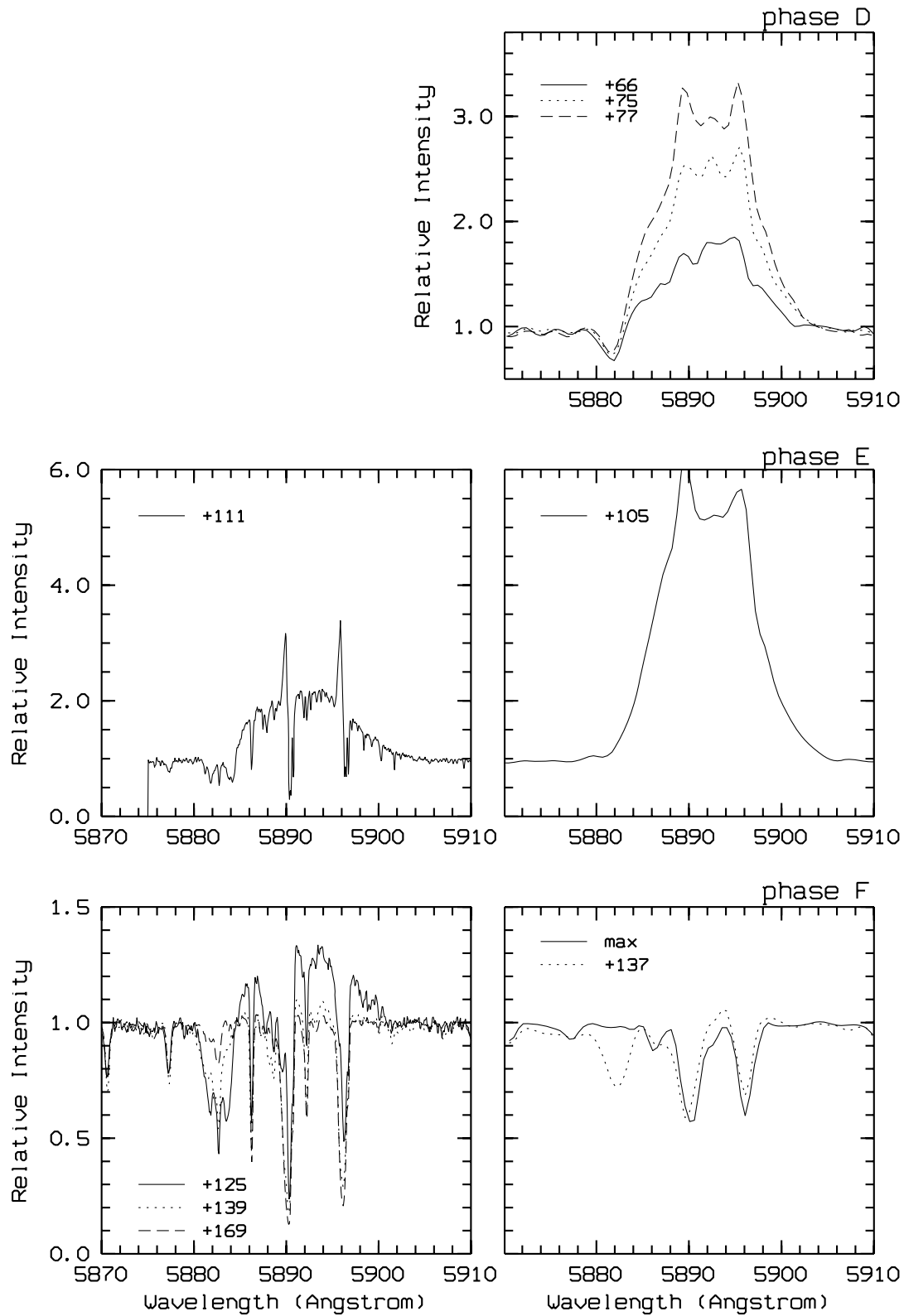
Figure 3.8: *The evolution of the NaI D lines throughout the decline (phases: D, E, F). Left: high-resolution spectra. Right: medium-resolution spectra. Day numbers are used to mark the spectra.*

3.4   Sharp emission lines

The sharp emission lines which appeared during the 1998 decline of V854 Cen included both *permitted* and *forbidden* lines. The lines appeared slightly broader (FWHM$\sim 10 - 20$ km s^{-1}) than the instrumental profile ($5 - 10$ km s^{-1}) in the high-resolution spectra, while they are not resolved in the MRS spectra (instrumental FWHM ~ 100 km s^{-1}).

The majority of the permitted sharp lines are low-excitation lines ($\chi_U \sim 3$ eV) of singly-ionized species, such as: BaII, ScII, TiII, YII, FeII. In addition, some lines of neutral atoms, particularly CI ($\chi_U \sim 10$ eV) and FeI ($\chi_U \sim 4$ eV), as well as lines of the C_2 Swan system, show similar widths. These sharp emission components can also be identified as part of complex profiles of the NaI D, the MgI triplet, H$_\alpha$ and the CaII IR triplet. These profiles usually include a number of different features, such as the broad and sharp emission and high-velocity absorption. The only forbidden lines identified belong to [OI], [CaII] and [CI].

Although all sharp emission lines have similar widths, various groups of lines can be distinguished. The lines demonstrate different evolution throughout the decline and can be classified, according to Alexander et al. (1972), into two major groups: E_1 and E_2 (see Chapter 1). In this chapter the basic physical parameters of lines belonging to these two groups, as well as their evolution, are discussed.

3.4.1   Low-excitation lines

The lines of low-excitation ions (BaII, ScII, TiII, YII and FeII) were observed throughout the whole decline using the MRS spectrograph and, at some phases, the high-resolution spectrograph.

The emission in the core of the photospheric absorption for the strongest lines was first noticed around day number +30, during the second light fading (decline II). At that time the star was at about 10^m, or 2.5 magnitudes below the maximum. On the other hand, during the first small decline of 1.5 magnitudes below the maximum (decline I), no emission was observed in the high-resolution spectra from 5000 Å to 7000 Å. The emission was still visible in the recovery phase (day number +111), when the star was between 10^m and 11^m. The evolution of the BaII, ScII and FeII lines is shown in Figure 3.9.

Some lines of FeI, NiI, LaII, ZrII and SrII ($\chi_U \leq 5$ eV) were also identified in emission during the 1998 decline of V854 Cen (see Tables E.1–E.7, Appendix E). Since they also exhibit the same line profile and evolution as the low-excitation lines throughout the decline, they have been analysed together with the most prominent lines of BaII, ScII and others. However, most of these lines have only been identified, but not measured, because they are extremely weak (practically at the noise level). In addition, the sharp emission components of the NaI D lines have also been analysed with the other low-excitation lines.

Using some of the high-resolution spectra from decline II (day numbers +52 and +54),
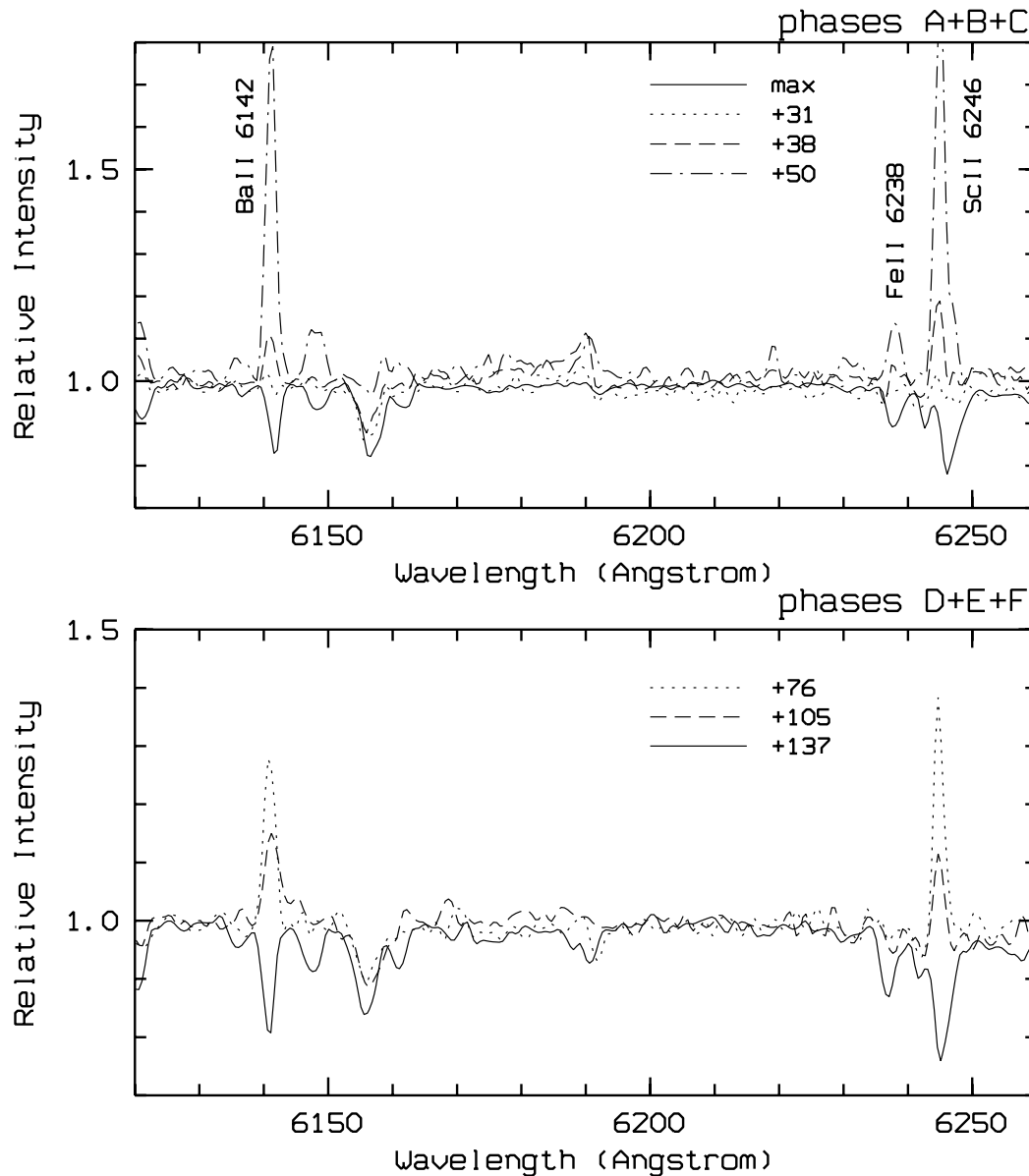
Figure 3.9: *Medium-resolution spectra of BaII 6141.7 Å, ScII 6245.6 Å and FeII 6238.4 Å throughout the decline.*

the structure of the low-excitation lines can be recognized. The lines do not consist of one emission component, but rather two, or three (Figure 3.10). The components will be referred to as 'blue', 'central' and 'red' in this thesis. The blue and red components are found at lower and higher velocities, respectively, with respect to the central one. The high-resolution spectra have been used for more precise measurements of the radial velocities and equivalent widths of the line components. On the other hand, the MRS spectra provide a more detailed coverage throughout the decline, so that they have been used in combination with the échelle spectra for monitoring the equivalent width and absolute flux evolution of these lines.
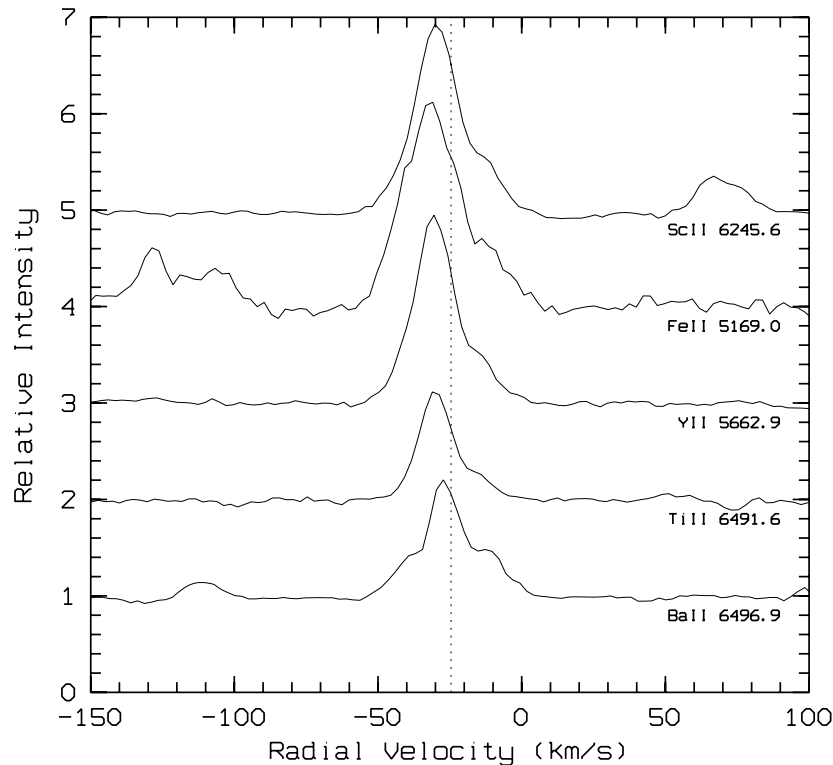
Figure 3.10: *Selected sharp emission lines of singly-ionized elements (day number +54), blue-shifted relative to the systemic velocity (dashed line). All lines exhibit a multicomponent structure.*

Radial velocity and FWHM

Using the procedure described in Chapter 2, precise measurements of radial velocities and FWHM values were made of the three components (blue, central, red) of the sharp emission lines. Two of the three high-resolution spectra (day numbers +52 and +54) obtained at McDonald Observatory (and provided by David Lambert) were used for this purpose.[2] It has been assumed that all lines have the same structure and that they are coming from the same region around the star.

The mean velocities of the three components of spectral lines for different elements are listed in Table 3.4 and plotted in Figure 3.11. The average value for the central (and dominant) component, as derived from six elements, is $-(28.1 \pm 0.1)$ km s^{-1}. This is blue-shifted by about 3 km s^{-1} relative to the stellar photospheric velocity of $-(25.1 \pm 0.9)$ km s^{-1}. The photospheric radial velocity has been taken from Lawson & Cottrell (1989).

The velocity separation of the other two components relative to the central one (in an absolute amount) is (8.2 ± 0.4) km s^{-1} for the blue component and (12.0 ± 0.2) km s^{-1} for the red one. The arithmetic mean of the blue and red velocities, $-(26.5 \pm 0.6)$ km s^{-1}, is

---

[2]The third spectrum (day number +111) was not used because the emission was blended with strong photospheric absorption.
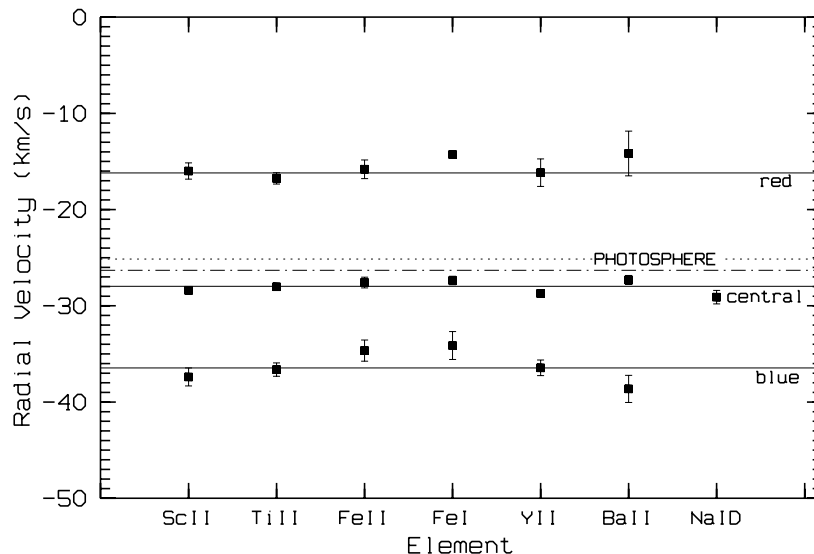
Figure 3.11: *Radial velocities of different atomic species (day number +52) derived from a number of sharp emission lines (see Table 3.4). Three different components (blue, central, red) have been identified in every spectral line, and their velocities have been averaged for each element (filled squares). The three horizontal solid lines represent the mean velocity of each component derived from all elements. The systemic velocity is marked by a dotted line (PHOTOSPHERE) and the average velocity of the blue and red components by a dashed-dotted line.*

closer to the systemic velocity than to the velocity of the central component. This asymmetry in the velocity distribution of the red and blue components with respect to the central one provides some information on the position of the corresponding emitting regions. It is possible that these lines originate from two different shells surrounding the star and expanding with different velocities. The blue and red components may belong to the outer shell (expanding faster), so that they are coming from the regions moving towards and away from the observer, respectively. On the other hand, the central component may originate from a slower-moving inner shell, so that the corresponding two components cannot be resolved.

The radial velocities of the three components do not change between days +52 and +54. The medium-resolution spectra also show that the total velocity of the combined profile stays approximately constant (within the uncertainty) throughout the decline.

Apart from the spectral lines of low-excitation ions, Figure 3.11 also includes the velocity of the sharp NaI D components (see Table E.14, Appendix E) for comparison. The mean radial velocity of $-(30.3 \pm 2)$ km s^{-1} (including both D_2 and D_1 components) is close to the velocities of the other sharp emission lines, indicating that they probably originate from the same region. However, the systematic error in measuring the NaI D lines is larger than for the other species, due to blending effects by other components (e.g. broad emission and

Table 3.4: *Mean radial velocity (V_r) and FWHM of sharp emission lines (red, central and blue components) of various elements, for day numbers +52 and +54. The total number of lines used for each element is given as N. The last entry (Average) represents the average velocity derived from all elements.*

Element	N		Comp.	V_r [km s^{-1}]		FWHM [Å]	
	+52	+54		+52	+54	+52	+54
ScII	22	14	red	-16.0 ± 0.8	-15.4 ± 0.9	20.4 ± 1.3	18.3 ± 1.4
			central	-28.4 ± 0.2	-28.8 ± 0.2	15.1 ± 0.8	12.9 ± 0.6
			blue	-37.4 ± 0.9	-36.9 ± 1	17.9 ± 1	14.3 ± 1
TiII	44	26	red	-16.8 ± 0.6	-18.3 ± 0.7	19.5 ± 1	16.5 ± 0.9
			central	-28.0 ± 0.2	-29.2 ± 0.2	13.3 ± 0.5	11.1 ± 0.6
			blue	-36.6 ± 0.7	-37.2 ± 0.9	15.9 ± 0.7	15.7 ± 1
FeII	16	14	red	-15.8 ± 0.9	-15.2 ± 0.9	16.9 ± 1	15.3 ± 1
			central	-27.6 ± 0.6	-28.1 ± 0.4	12.8 ± 0.8	12.1 ± 0.9
			blue	-34.7 ± 1	-34.1 ± 1	14.9 ± 2	12.8 ± 2
FeI	4	3	red	-14.3 ± 0.3	-15.8 ± 0.9	20.6 ± 4	11.5 ± 2
			central	-27.4 ± 0.4	-27.4 ± 0.9	10.9 ± 0.8	9.7 ± 1
			blue	-34.1 ± 1	-32.6 ± 1	16.6 ± 5	15.2 ± 7
YII	18	15	red	-16.8 ± 1	-17.3 ± 0.7	18.0 ± 1	16.5 ± 1
			central	-28.5 ± 0.2	-29.4 ± 0.2	13.5 ± 0.5	11.8 ± 0.6
			blue	-37.6 ± 1	-38.2 ± 1	16.7 ± 1	14.6 ± 1
BaII	4	4	red	-14.2 ± 2	-12.9 ± 1	18.8 ± 3	15.9 ± 2
			central	-27.3 ± 0.5	-27.6 ± 0.4	15.6 ± 3	13.8 ± 2
			blue	-38.6 ± 1	-38.4 ± 1	17.0 ± 0.7	16.2 ± 3
Average:	108	76	red	-16.3 ± 0.4	-16.6 ± 0.4	19.1 ± 0.7	16.4 ± 0.6
			central	-28.1 ± 0.1	-28.8 ± 0.1	13.6 ± 0.3	11.8 ± 0.3
			blue	-36.6 ± 0.4	-36.6 ± 0.5	16.3 ± 0.5	14.7 ± 0.7

photospheric and interstellar absorption). This is also the reason why the three-component structure of the NaI D sharp lines cannot be resolved. In fact only one sharp component of each of the two D lines (D$_2$ and D$_1$) has been resolved. Their mean FWHM (see Table E.14, Appendix E) is about (27 ± 2) km s^{-1} (uncorrected for the instrumental broadening), which is significantly broader than the central component of other sharp emission lines, $\sim (13.6 \pm 0.3)$ km s^{-1}. This indicates that the NaI D sharp lines may indeed include three different
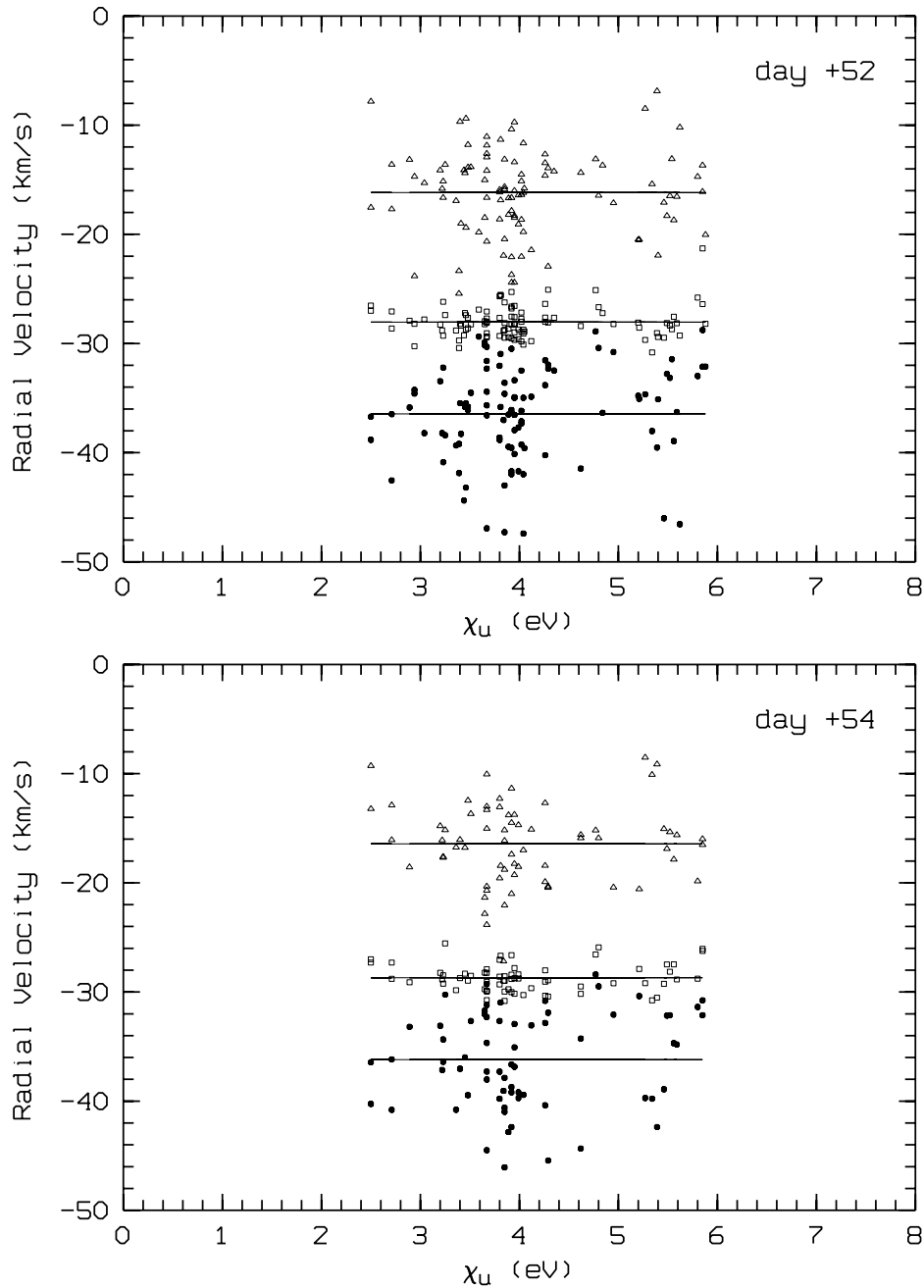
Figure 3.12: *Radial velocity versus upper excitation potential* (χ_{U}) *for the three components of the sharp emission lines. Straight lines are the least-squares fits through the data.*

components, similar to the other sharp emission lines. According to their flux ratio ($D_2/D_1 \sim 1$) the lines are optically thick (Asplund 1995).

Returning to the radial velocity distribution of the low-excitation lines, Figures 3.12 and 3.13 demonstrate the behaviour of the velocities with respect to the excitation potential and FWHM of the three components. On both days +52 and +54 the radial velocities of the three components are clearly independent of the upper excitation potential χ_{U} (Figure 3.12). There is also no evidence of any systematic difference between the neutral atoms and ions.
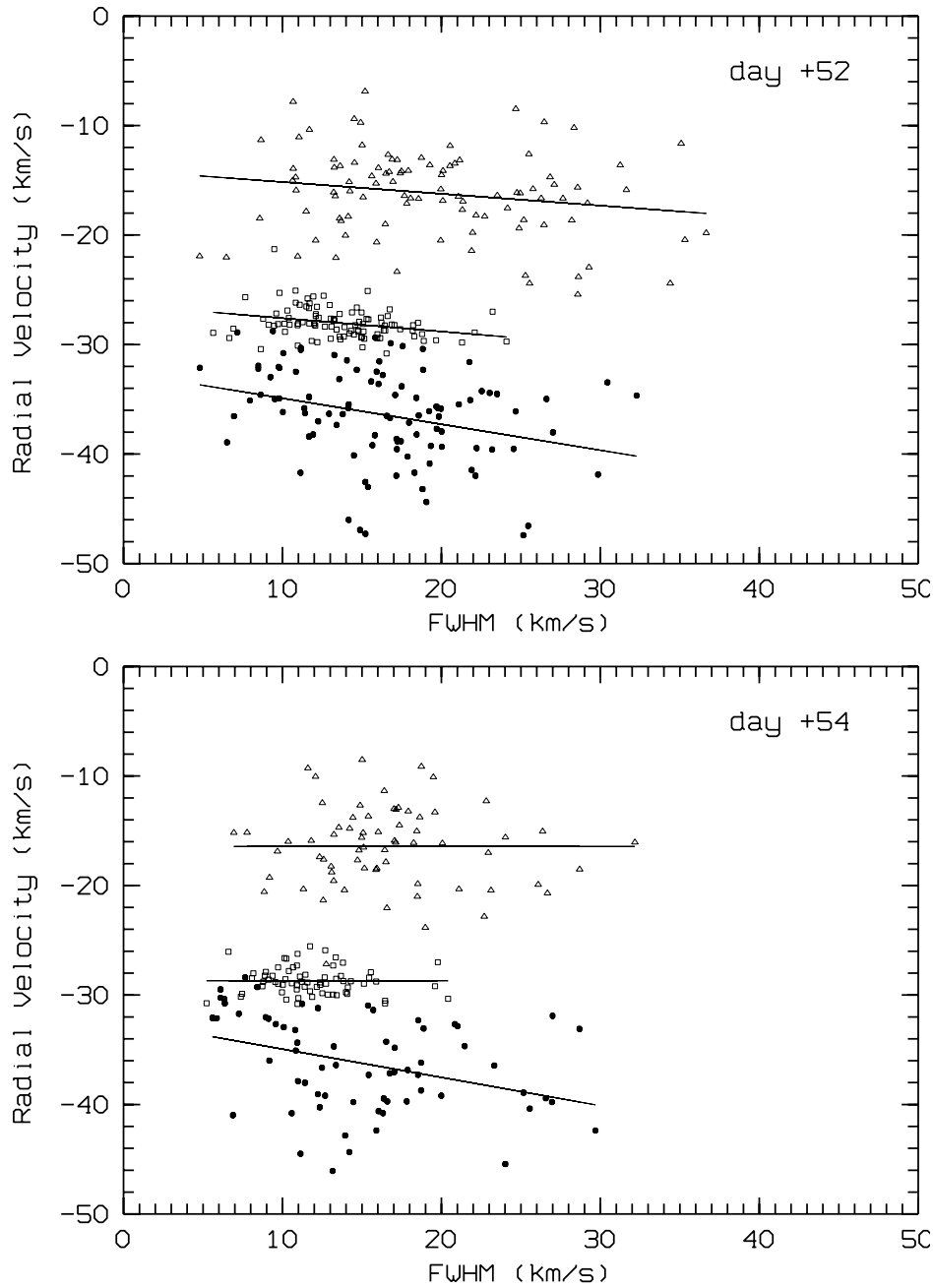
Figure 3.13: *Radial velocity as a function of FWHM for the three components of the sharp emission spectral lines.*

In addition, the mean flux ratios (blue to central and red to central) do not depend on the atomic species. The same value of about 0.6 ± 0.1 has been obtained for both ratios.

Finally, Figure 3.13 demonstrates that the radial velocity is not correlated with the FWHM values of the low-excitation emission lines. Some information on the distribution of the FWHM values for each component can also be obtained from this figure. The mean FWHM of the central component is about (13.6 ± 0.3) km s^{-1}, uncorrected for the instrumental broadening of ~ 5 km s^{-1}. The other two components show slightly broader distributions, with a mean value of about 20 km s^{-1}. The uncertainties in these cases are significantly larger

due to more severe blending of these weaker components. The radial velocities and FWHM values of sharp emission lines presented in this section will be compared with other existing observations of RCB stars in Chapter 5, where various characteristics of their emitting regions will also be discussed.

Line reddening

While the photospheric continuum is obscured and reddened by the dust causing the decline, the emission lines appear to be unaffected by this reddening (Clayton 1996). The influence of the interstellar and circumstellar reddening on the sharp emission lines can be neglected in the case of V854 Cen, due to the very low value of the colour excess of $E_{B-V} \approx 0$ (Lawson et al. 1990).

It is possible to check whether the sharp emission lines are affected by the reddening due to the dust cloud obscuration. This can be done by examining the flux ratio of a pair of lines originating from the same upper level. In an optically thin region, the line flux (F_{line}) can be expressed (see e.g. Pandey et al. 1996) as:

$$\log F_{\text{line}} = \log gf - 3 \log \lambda + \log N_{\text{U}}/g_{\text{U}} + \log C, \tag{3.1}$$

where N_{U} is the population of the upper level, g_{U} is the corresponding statistical weight and C is a constant. On the other hand, from the Boltzmann equation it can be obtained that:

$$\frac{N_{\text{U}}}{g_{\text{U}}} = [\text{constant}] \times 10^{-\theta \chi_{\text{U}}}, \tag{3.2}$$

where χ_{U} is the excitation potential of the upper energy level, and $\theta = \log e/kT = 5040/T$, so that Equation (3.1) can be rewritten in the following form:

$$\log F_{\text{line}} = \log gf - 3 \log \lambda + \log C - \theta \chi_{\text{U}}, \tag{3.3}$$

with a new value for the constant C.

Using Equation (3.3) the flux ratio of a pair of optically thin spectral lines, F_1 and F_2, becomes:

$$\frac{F_1}{F_2} = \frac{gf_1}{gf_2} \left(\frac{\lambda_2}{\lambda_1}\right)^3 10^{-\theta(\chi_1 - \chi_2)}. \tag{3.4}$$

It is interesting to note that the flux ratio from Equation (3.4) approximately reduces to the ratio of gf values for spectral lines within a single multiplet, since $\lambda_1 \approx \lambda_2$ and $\chi_1 - \chi_2 \approx 0$. This means that the line fluxes within a multiplet should stay approximately proportional to the gf values, as demonstrated in Figure 3.14, where a sample of BaII spectral lines is shown, as obtained from the high-resolution deep decline spectra of V854 Cen.

On the other hand, if the two lines are coming from the *same upper level*, then the energy difference $\chi_1 - \chi_2$ in Equation 3.4 is equal to zero, so that the flux ratio is given by:

$$\frac{F_1}{F_2} = \frac{gf_1}{gf_2} \left(\frac{\lambda_2}{\lambda_1}\right)^3. \tag{3.5}$$
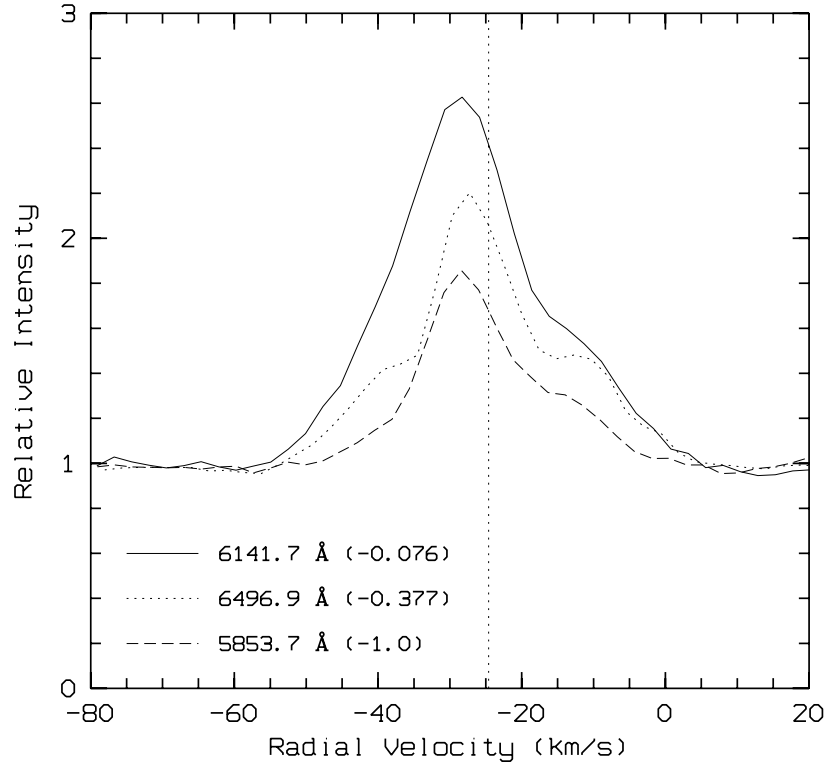
Figure 3.14: *BaII spectral lines of the multiplet 2 on a velocity scale. The* $\log gf$ *values (in brackets) have been taken from Kurucz & Bell (1993). The line flux is approximately proportional to the* gf *value.*

This relation can be expressed in terms of the line transition probabilities for spontaneous emission (A_1, A_2), taking into account:

$$gf = [\text{constant}]\, \lambda^2\, g_{\text{U}}\, A. \tag{3.6}$$

Then the flux ratio of a pair of optically thin spectral lines coming from the same upper level is proportional to the ratio of their transition probabilities:

$$\frac{F_1}{F_2} = \frac{A_1 \lambda_2}{A_2 \lambda_1}. \tag{3.7}$$

A set of TiII spectral lines has been chosen for the investigation, because a relatively large number of these lines has been identified over a wide wavelength range and because they have reliable transition probabilities. Accurate transition probabilities of TiII spectral lines have been taken from Martin et al. (1988). The predicted flux ratios for the unreddened optically thin lines (Table 3.5) have been calculated using Equation (3.7). The observed flux ratios for the same set of lines (red, central and blue components) have been estimated using the equivalent width and the continuum flux at the line position. The results are shown for day number +52. Similar ratios have been found for the spectra obtained two days later (day number +54). The same test turned out to be unreliable later during the decline, either

Table 3.5: *Predicted and observed flux ratios (red, central and blue components, day number +52) of selected TiII emission lines originating from the same upper level (χ_{U}).*

λ_1/λ_2	χ_{U} (eV)	Flux ratio (F_1/F_2) Predicted	Observed red	central	blue
5381/4708	3.85	0.90	1.22	1.10	1.70
4708/4450	3.85	0.15	0.73	0.27	0.28
6492/4544	3.95	0.99	1.12	1.70	1.75
6492/5189	3.95	0.096	0.29	0.49	0.45
8979/6492	3.95	0.24	0.55	0.48	0.80
8979/4544	3.95	0.24	0.66	0.93	0.38
5189/4544	3.95	10.4	8.1	4.0	5.7
7214/5129	4.29	0.20	0.7	0.36	0.30
7214/4529	4.29	0.50	0.53	0.67	1.2

due to the incompleteness of the list of identified spectral lines, or due to severe blending effects (emission blended with absorption).

As can be seen from Table 3.5, the observed flux ratios for all three components are close to the predicted ones, assuming no reddening. Taking into account a typical uncertainty for the measured flux of about 0.05 10^{-16}W m^{-2}, the uncertainty of the flux ratios can range between 10% and 20%. Therefore, the reddening of the observed emission lines by the dust causing the decline can be considered very small on day number +52.

Excitation temperature of the emitting region

The line flux ratio of appropriately chosen spectral lines can also provide an estimate of the physical parameters (i.e. the excitation temperature T_{exc} and electron density N_{e}) of the emitting gas region. The forbidden lines are usually used for this purpose. However, the permitted lines can be used as well. In this case, T_{exc} can be found using the observed fluxes and the line transition probabilities. This procedure, adopted by Pandey et al. 1996, is straightforward for lines emitted by an optically thin gas. Returning to Equation (3.3), a new quantity G can be defined as:

$$G = \log F_{\mathrm{line}} - \log gf + 3 \log \lambda, \tag{3.8}$$

so that one obtains:

$$G = \log C - \theta \chi_{\mathrm{U}}. \tag{3.9}$$
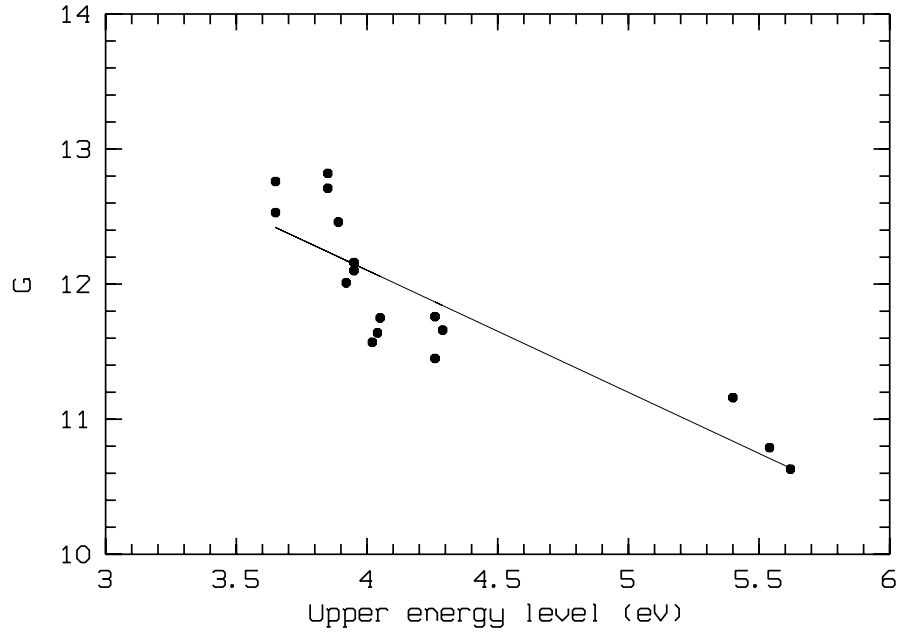
Figure 3.15: *A Boltzmann plot for the central component of the TiII spectral lines (day number +52).*

Therefore, the quantity G is a linear function of χ_{U}, so that the excitation temperature T_{exc} can be obtained from the line slope $\theta = 5040/T_{\mathrm{exc}}$.

In accordance with the conclusions made in the previous section dealing with line reddening, it is reasonable to assume that the low-excitation sharp emission lines are optically thin. It has also been assumed that the gas is homogeneous and that all sharp emission lines originate from the same region. Therefore, the estimates obtained for some elements can be applied to all other low-excitation sharp lines as well. In order to get the excitation temperature of the emitting region, a set of TiII spectral lines of different upper excitation potential and with reliable transition probabilities (Martin et al. 1988) has been used. The G values have been calculated from Equation (3.8) using the observed line fluxes (F_{line}) for the central component on day +52. Instead of the gf values, the transition probabilities A_{UL} have been used, in accordance with the following relation:

$$gf = 1.499 \times 10^{-8} \, \lambda^2 \, g_{\mathrm{U}} \, A_{\mathrm{UL}}, \qquad (3.10)$$

where λ is given in Å and A_{UL} is in $10^8 \ \mathrm{s}^{-1}$.

The results are plotted in Figure 3.15. The line slope of $\theta = 0.904$ corresponds to the excitation temperature of $T_{\mathrm{exc}} = (5600 \pm 800)$ K. A similar temperature of $T_{\mathrm{exc}} \sim (5700 \pm 1000)$ K fits the red and blue components as well. The excitation temperature stays at about the same value for the spectra obtained on day number +54. Unfortunately, it has not been possible to estimate the electron density (N_e) of the emitting region using Saha's equation and T_{exc}. The identified FeI lines, used for deriving the ratio $N(\mathrm{FeII})/N(\mathrm{FeI})$, were

too weak and not in a sufficient number for any reliable measurement.

Distribution of the line fluxes throughout the decline

The integrated fluxes of the sharp lines do not decline in step with the photospheric flux (Figure 3.16). All sharp emission lines show a constant flux (day numbers between +30 and +40) until the star reaches a brightness of about four magnitudes below the maximum. After that, the line fluxes decrease slowly, indicating that the emission line regions probably become obscured by the dust cloud. While the continuum flux between days +50 and +70 is changing in accordance with the stellar pulsations, the line flux stays constant, or decreases slowly, and is not affected by the pulsations.

The slope of the line flux curve (ΔFlux/ΔDay) ranges from -0.01×10^{-16} to -0.027×10^{-16} W m^{-2} per day for different spectral lines. This indicates a similar behaviour for all these lines, with a mean slope of -0.018×10^{-16} W m^{-2} per day. At the same time, the continuum is decaying about ten times faster (-0.15×10^{-16} W m^{-2} per day).

While the line flux variations do not seem to be obviously correlated with the changes in the photospheric continuum, the equivalent widths of the lines clearly reflect these changes (Figure 3.17b). This is due to the fact that the equivalent widths are actually measured relative to the local continuum, which decays as a result of the dust cloud obscuration. If
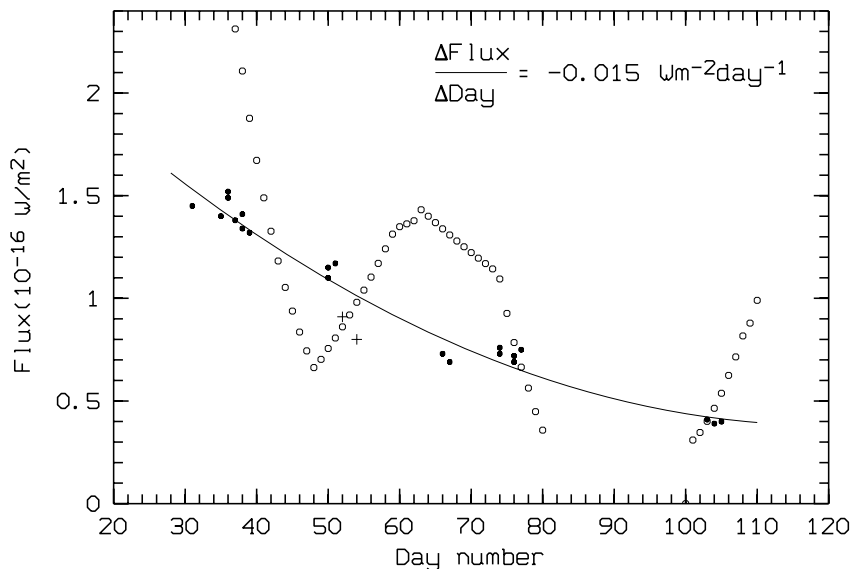
Figure 3.16: *Line fluxes (filled circles) of a sharp emission line, BaII 6141.7 Å, exhibiting a steady decay throughout the decline. A few measurements from the high-resolution spectra are presented as crosses. The shift between days +50 and +52 could be either due to the systematic difference between the two instruments (MRS and échelle), or a real decrease in the line flux. The continuum flux (open circles, arbitrary units) is modulated by stellar pulsations, which do not affect the line fluxes.*
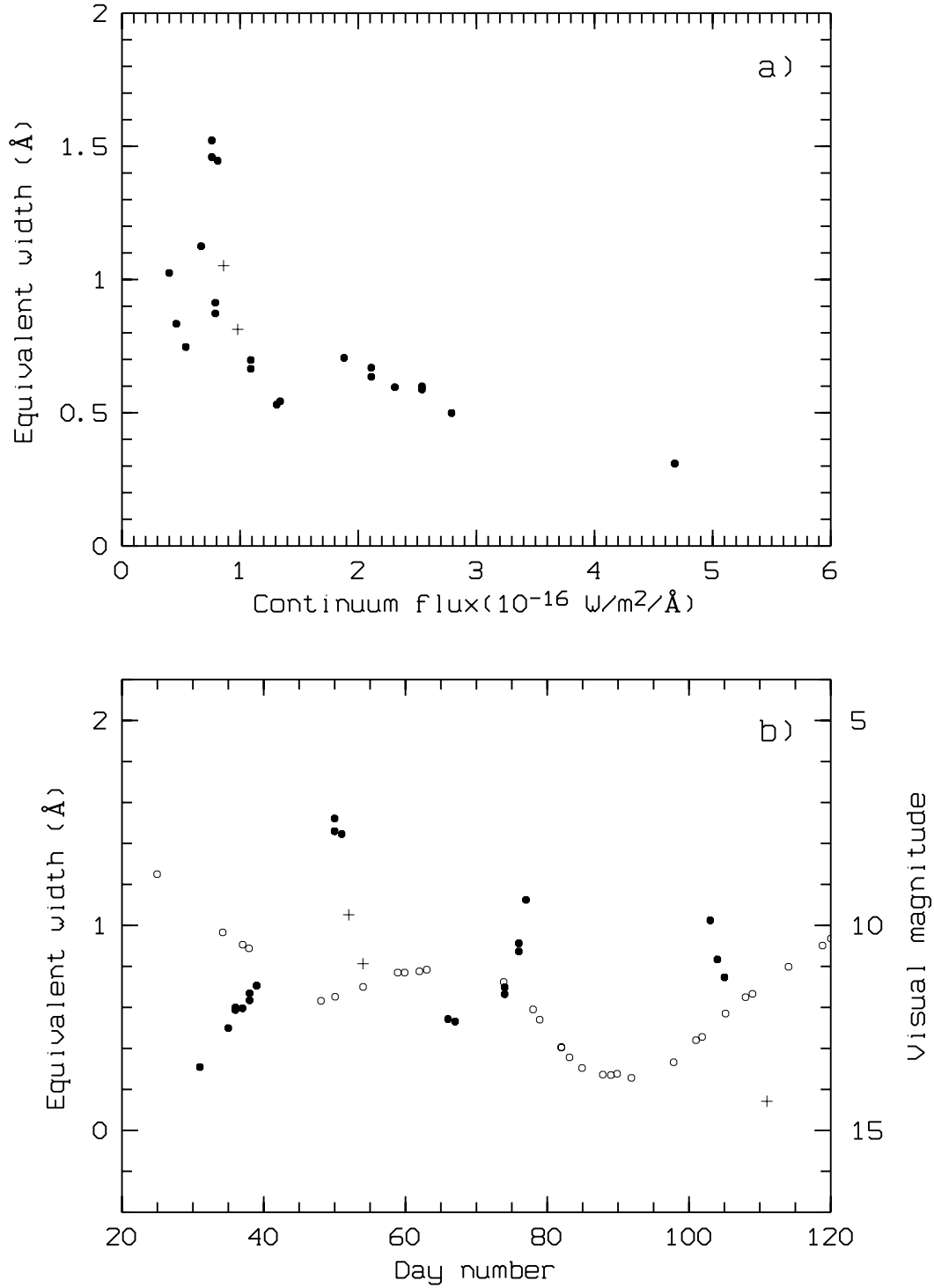
Figure 3.17: *The equivalent width (filled circles) of a sharp emission line, BaII 6141.7 Å, versus (a) the continuum flux and (b) day number. The crosses represent the measurements obtained from the high-resolution spectra (including all three components). The light curve (open circles) is also shown in (b).*
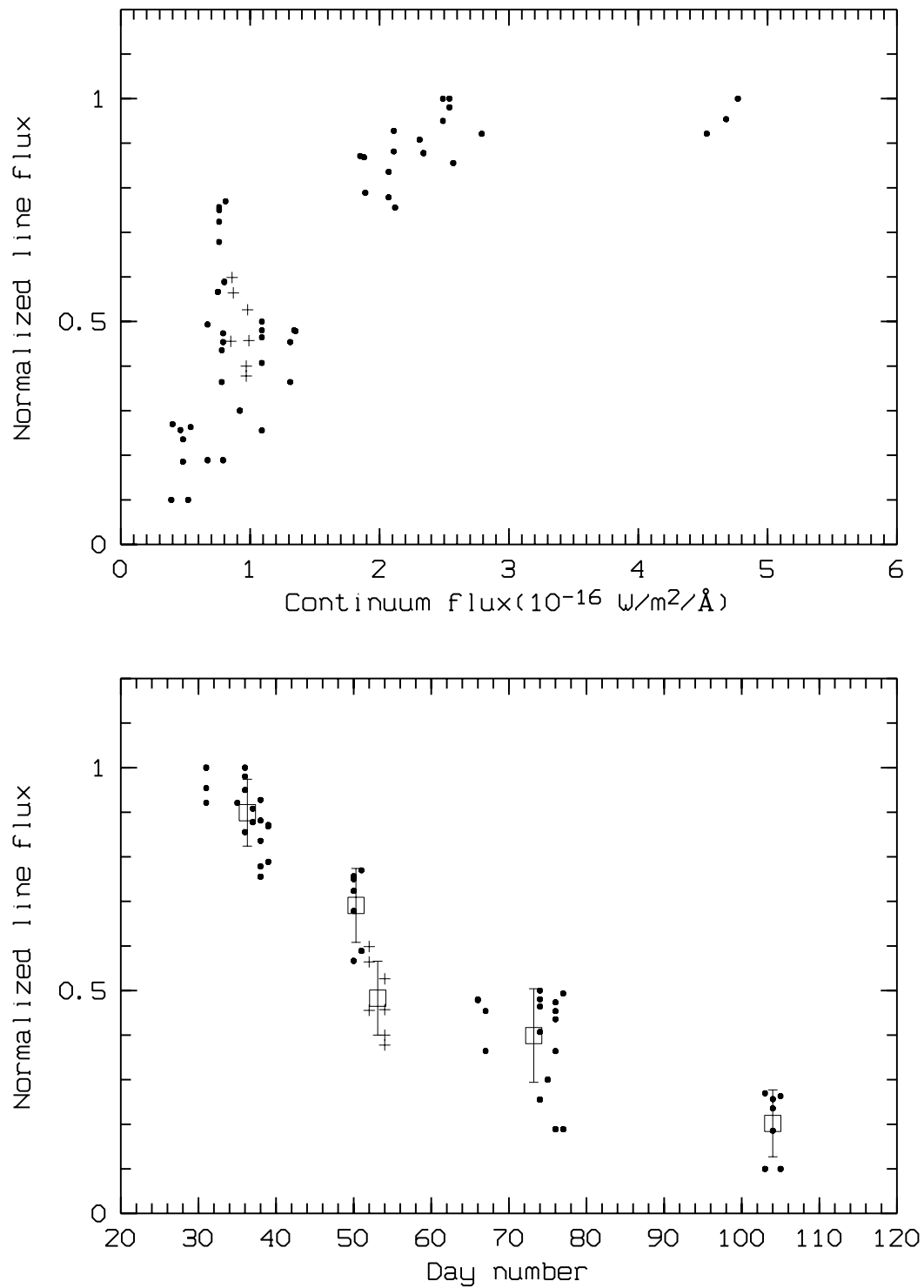
Figure 3.18: *Normalized fluxes (filled circles) of all observed BaII spectral lines versus continuum flux and day number. The crosses represent measurements from the high-resolution spectra (including all three components). Five groups of measurements are seen in the bottom plot. Open squares, with uncertainty estimates, are used to represent the mean flux for each group.*
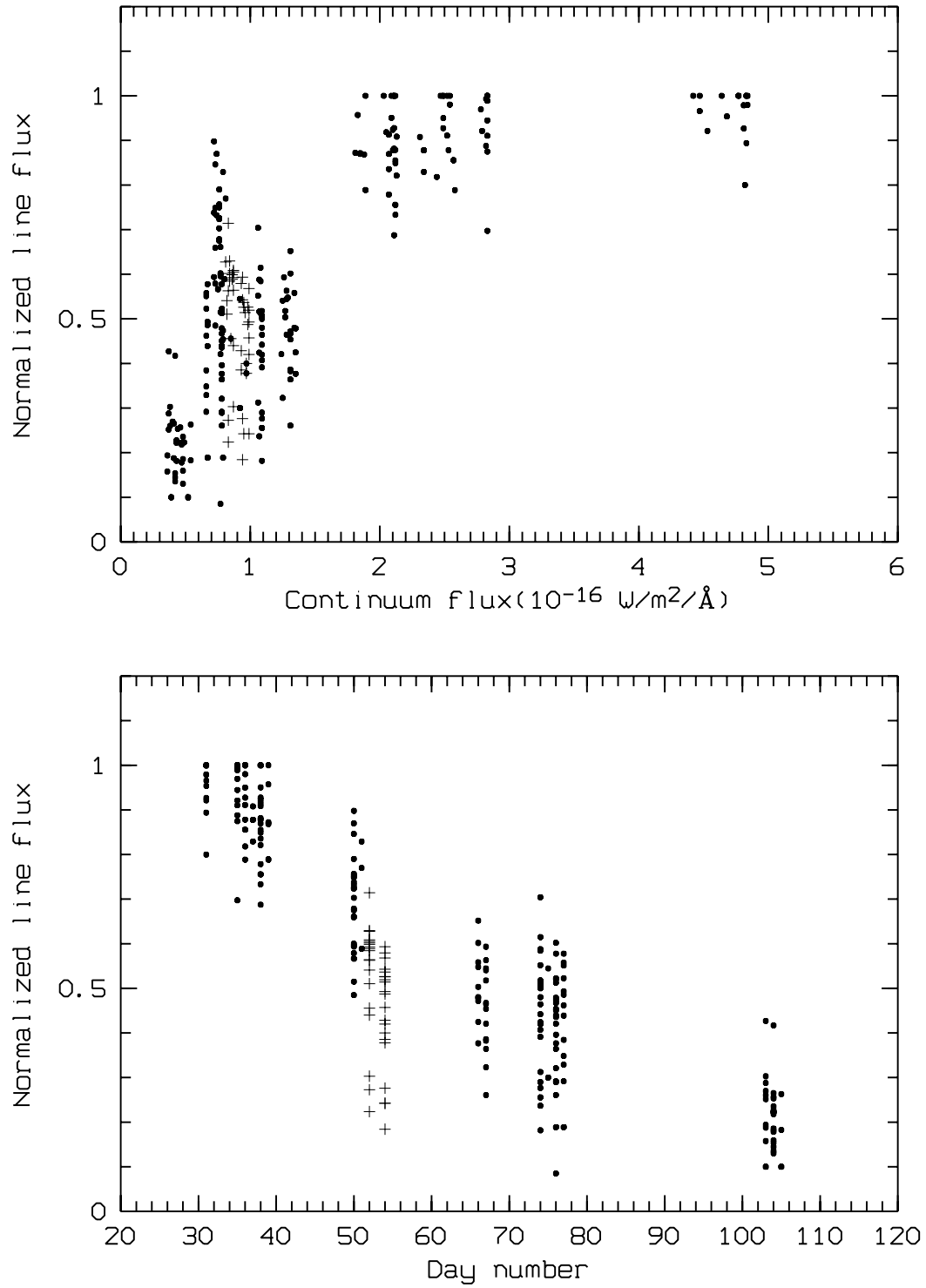
Figure 3.19: *Normalized fluxes of BaII, ScII, YII and TiII emission lines versus continuum flux and day number. Filled circles and crosses have same meaning as in Figure 3.18.*

the emission lines were of the same constant flux throughout the decline (i.e. not affected by the dust), their equivalent widths would show a perfect mirror image of the photospheric variations (the lower the continuum, the larger the equivalent widths, and vice versa). This is the case in the very beginning of the decline (declines I and II, up to day number about +60). After that, the equivalent widths start decreasing slowly. During the initial phase of decline III (day +70), and also during its early recovery phase (day +100), the equivalent widths appear significantly smaller than around day +50, although the continuum flux has almost the same value at these times. This is also seen in Figure 3.17a, where a wide range of equivalent widths is found in a small interval of the continuum fluxes between $(0.5-1.0)\times 10^{-16}\,\mathrm{W\,m^{-2}\,\mathring{A}^{-1}}$. Considering only the MRS spectra (filled circles in Figures 3.18 and 3.19), a similar line flux increase is observed around day number +50. This can be a result of the multiple decline pattern of V854 Cen, where several dust clouds are formed in subsequent declines. The first dust cloud may have dispersed significantly by day number +50, allowing the sharp-line emission region to become visible when a newly formed dust cloud obscures the photosphere.

In order to compare the flux distributions of different BaII spectral lines (see Tables E.1–E.13, Appendix E), the measured flux of each line on a given day has been normalized relative to its maximum value during the decline (the actual procedure for obtaining the line fluxes is explained in Sections 2.5.3 and 2.5.2, Chapter 2). The line fluxes have then been plotted as a function of the continuum flux and day number (Figure 3.18). A similar diagram (Figure 3.19) can be obtained for all observed low-excitation sharp emission lines (BaII, ScII, YII and TiII).

Similar flux and equivalent width distributions throughout the decline have been obtained for the sharp NaI D lines. These lines can be detected at the very beginning of the decline, and also during the late recovery phase, since they are stronger than the other lines. However, the uncertainty in measuring their parameters is larger than in other sharp emission lines, due to blending effects with other components. In order to get reliable equivalent widths of the NaI D components, a special procedure has been developed in this thesis (see Chapter 2). Using this procedure, the line fluxes have been estimated for the first 30 days of the decline, which was not possible for other spectral lines (Figure 3.20). Taking into account the estimated uncertainty of about 20%, the NaI D lines show a constant flux until the star reaches a brightness of about two magnitudes below the maximum (crosses in Figure 3.20). After this, the line fluxes increase by about 50% and stay constant for the next 30 days (triangles and asterisks in Figure 3.20). A slow decrease starts between days +50 and +70 (crossed squares in Figure 3.20) and continues to day number +120 (filled circles in Figure 3.20), after which the flux stays constant. During the late recovery phase the flux values are roughly the same as during the initial phase. The decrease in line fluxes between day numbers +60 and +70 may indicate that the NaI D emission region also becomes obscured by the dust cloud.
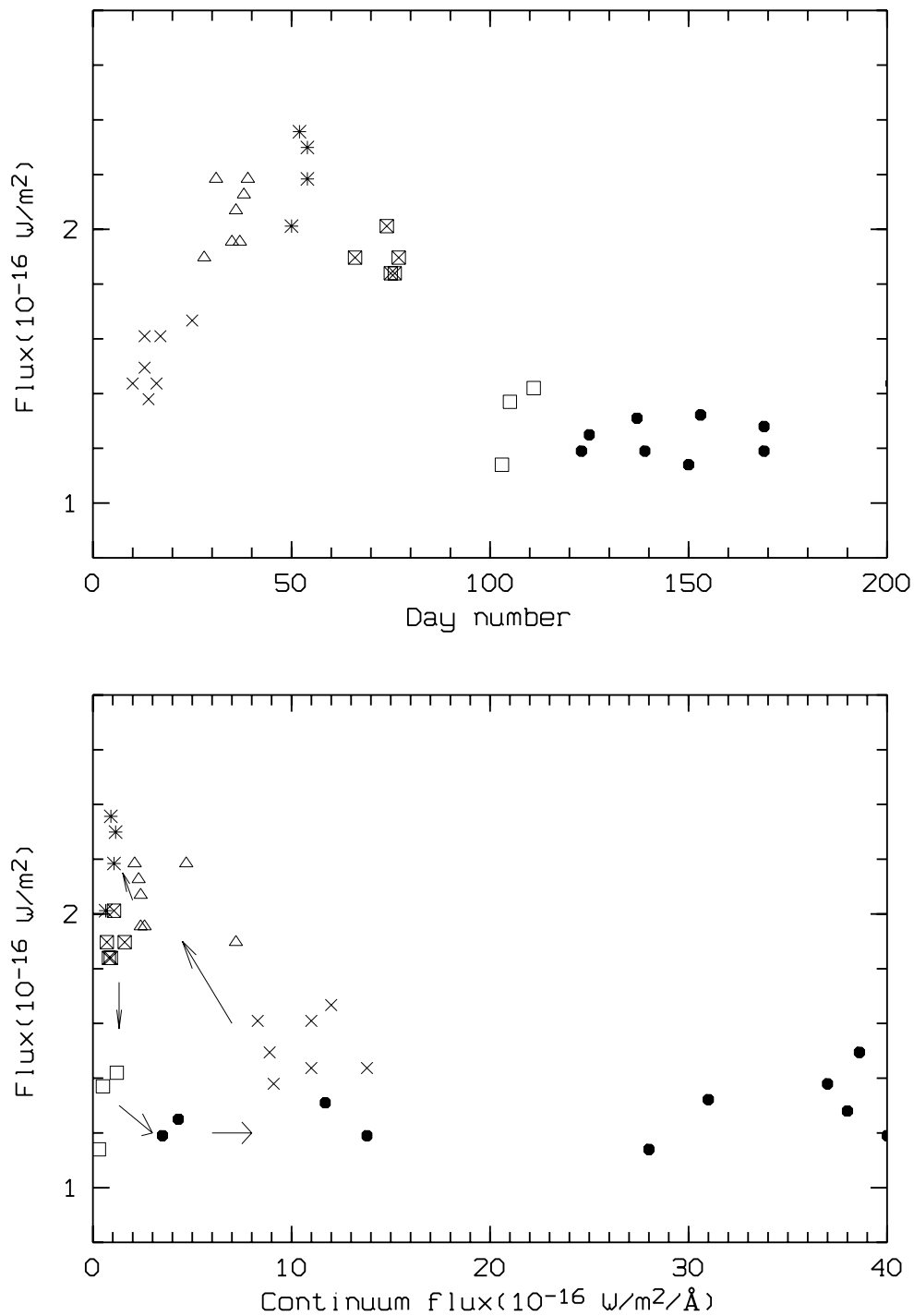
Figure 3.20: *Line fluxes of the NaI D_2 spectral line versus continuum flux and day number. Different symbols represent different phases of the decline: crosses ($\times$) – up to day number +30, triangles – between days +30 and +40, asterisks – around day number +50, crossed squares – between days +66 and +77, squares – early recovery phase (day numbers +103 to +111) and filled circles – recovery phase (day numbers +123 to +169). The arrows indicate the direction of the flux changes from the initial decline (crosses) to the recovery phase (filled circles).*
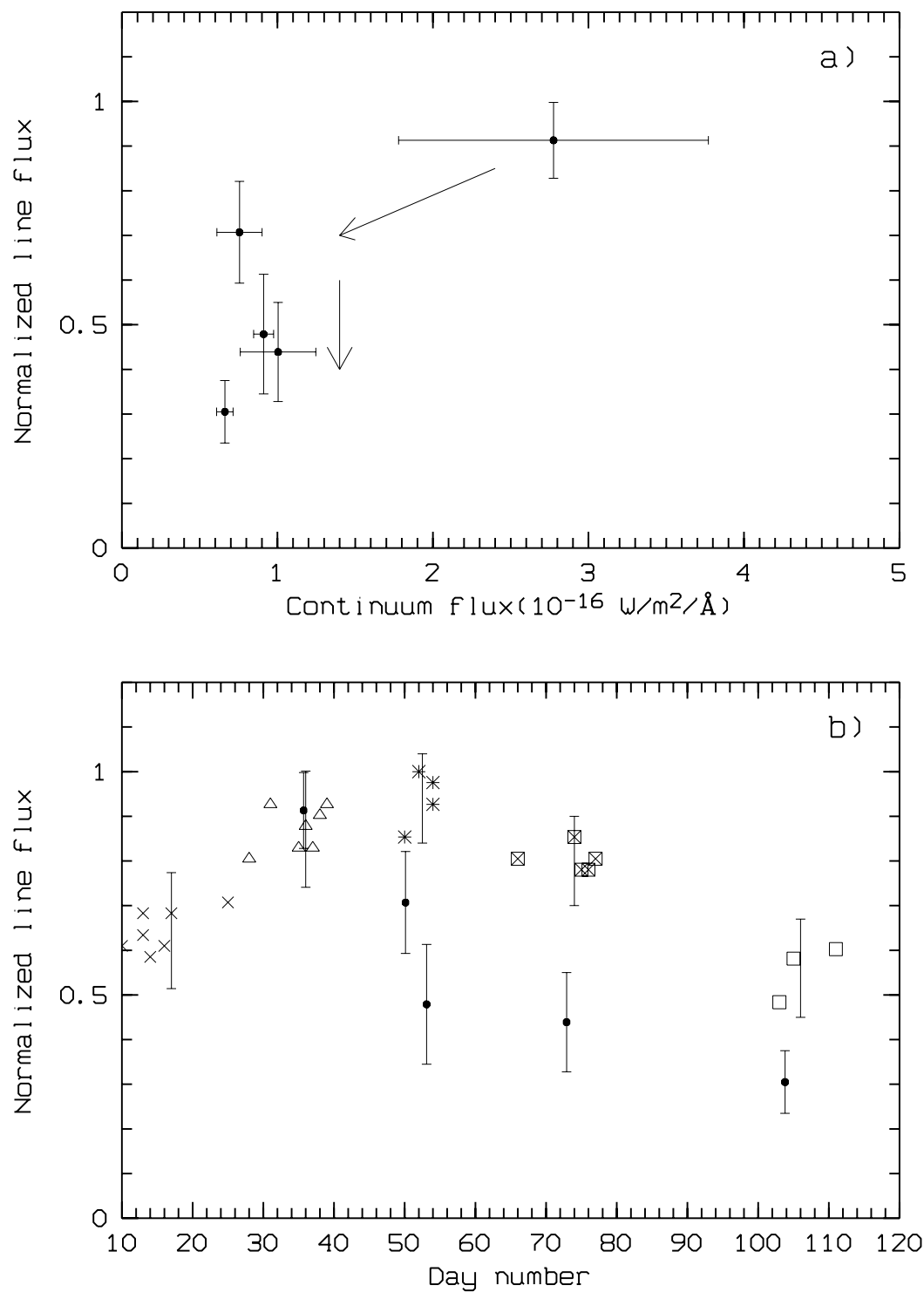
Figure 3.21: *Mean values of normalized line fluxes of low-excitation sharp emission lines (filled circles) versus (a) continuum flux and (b) day number. The arrows in (a) indicate the direction of the line flux decrease, during which time the continuum flux stays approximately constant. The other symbols in (b) represent the fluxes of the NaI D_2 spectral line (same as in Figure 3.20), with their uncertainties.*

The mean values of the normalized line fluxes for the low-excitation sharp emission lines are plotted in Figure 3.21. As can be seen from Figure 3.21a, the line fluxes decrease while the continuum flux stays mainly constant. Figure 3.21b shows the NaI D and other low-excitation sharp emission lines. The distributions are similar. The NaI D lines change their fluxes by $\sim 40\%$ during the whole decline phase, while for the other spectral lines the change is larger ($\sim 70\%$). This noticeable difference can be due to the larger uncertainty in measuring the NaI D_2 sharp emission line fluxes. In both cases, all sharp emission lines show a decrease of the line flux, starting on about day number +50 and continuing during the deepest decline and recovery phase.

3.4.2 CI, OI and MgI emission lines

It can be seen from the MRS spectra that the CI absorption lines ($\chi_{\mathrm{U}} \sim 10$ eV) begin to fill in with emission on day number +17 (Figure 3.22). They do not stay in emission as long as the low-excitation sharp emission lines. After day number +50, they do not show any
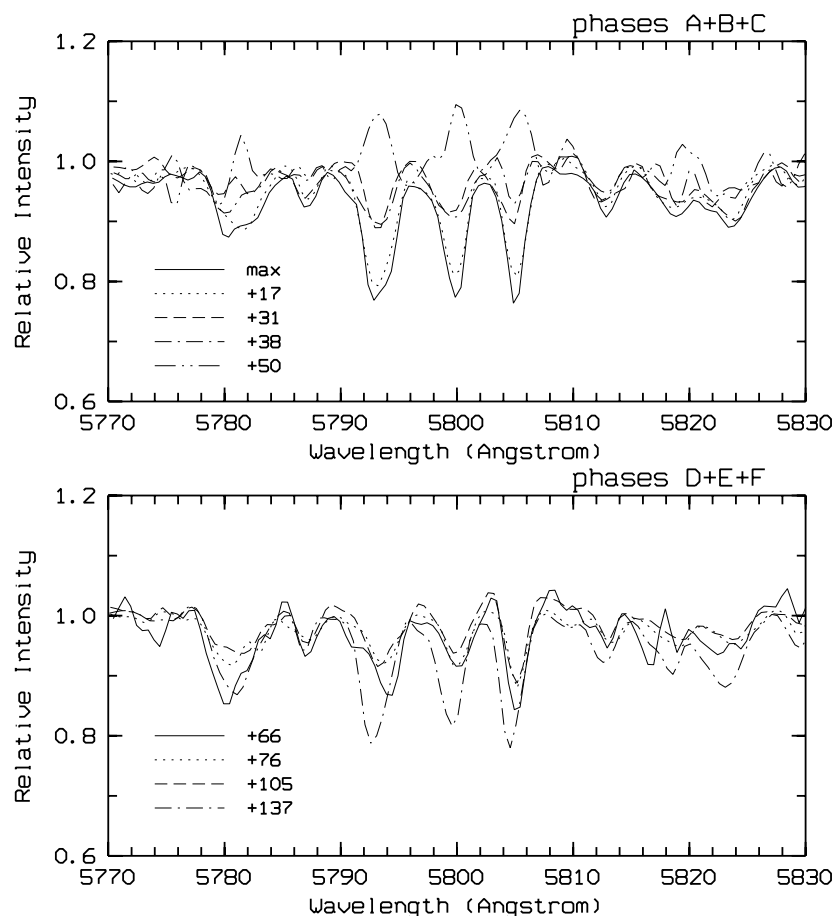
Figure 3.22: *Medium-resolution spectra around the CI 5793.1 Å, 5800.6 Å and 5805.2 Å lines (multiplet 18) throughout the decline.*
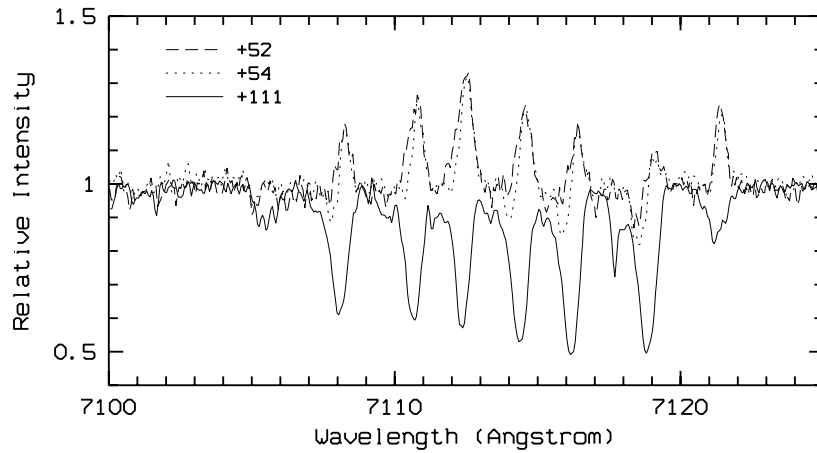
Figure 3.23: *The CI spectral lines (multiplet 26) during decline II (day numbers: +52 and +54) and recovery phase (+111).*
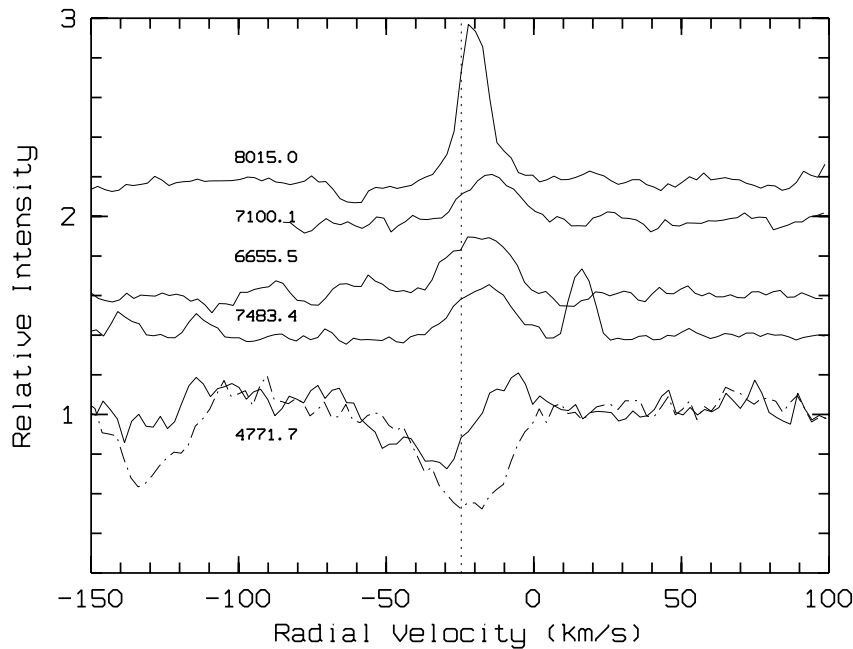
Figure 3.24: *The CI emission spectral lines on day number +52. The dash-dot spectrum shows the absorption profile of 4771.7 Å during the early recovery phase. A red shift of the emission components relative to the stellar velocity (dotted line) is noticeable.*

clear emission, in spite of the fact that the star is fainter ($12^{\text{m}}2$) on day number +105 than on day +50 (Figure 3.22). By day number +137 they return to their normal photospheric absorption profile.

There are only two sets of high-resolution spectra covering the CI lines, the first one from decline II (day numbers 50–54), and the second one from the early recovery phase (day +111). The lines are seen in emission on day number +52 and in absorption on day number

Table 3.6: *Radial velocity (V_r) and equivalent width (W_λ) of the CI lines in emission (day number +52) and absorption (day number +111).*

λ [Å]	Multiplet	V_r [km s^{-1}] +52	V_r [km s^{-1}] +111	W_λ [Å] +52	W_λ [Å] +111
5969.326	17.20	-21.6	-23.0	0.10	0.09
5793.116	18	-17.6	-22.3	0.12	0.21
6828.117	21	-20.2	-20.3	0.44	0.19
6711.291	21.01	-17.9	-24.2	0.06	0.09
6655.509	21.03	-18.5	-23.3	0.20	0.24
6587.608	22	-11.1	-20.7	0.10	0.32
7108.935	25.02	-14.6	-22.8	0.12	0.28
7100.124	25.02	-14.6	-24.1	0.12	0.25
7116.990	25.02	-11.0	-21.4	0.11	0.33
7113.180	26	-16.0	-20.5	0.23	0.24
7115.186	26	-12.9	-20.3	0.16	0.31
7111.475	26	-16.7	-20.3	0.18	0.25
7132.112	26	-20.2	-25.6	0.13	0.08
7122.196	26	-19.2	-25.8	0.11	0.14
7022.129	26.03	-17.2	-21.4	0.08	0.04
7692.495	29.01	-19.0	-23.2	0.14	0.16
7483.436	29.03	-17.2	-22.7	0.16	0.20
7476.178	29.03	-15.7	-22.0	0.15	0.19
7473.303	29.03	-19.1	-23.4	0.07	0.16
8014.998	31	-20.4	-20.9	0.24	0.12
8018.564	31	-21.7	-24.9	0.14	0.09
7840.270	32	-16.7	-25.4	0.08	0.14
7852.862	32	-15.9	-23.2	0.20	0.10
7837.105	32	-16.9	-23.0	0.11	0.15
7848.246	32	-18.8	-23.4	0.16	0.12
7832.629	32	-17.8	-23.1	0.12	0.16
Mean value:		-17.3	-22.7		
Standard error:		0.6	0.3		

+111 (Figure 3.23). On day number +54, the lines show a P Cygni profile, with a blue-shifted absorption component. Some weaker CI lines show this profile even on day number +52 (Figure 3.24). The appearance of the P Cygni profile in this case can be due to the red-shifted emission filling in the photospheric absorption, as demonstrated by two different
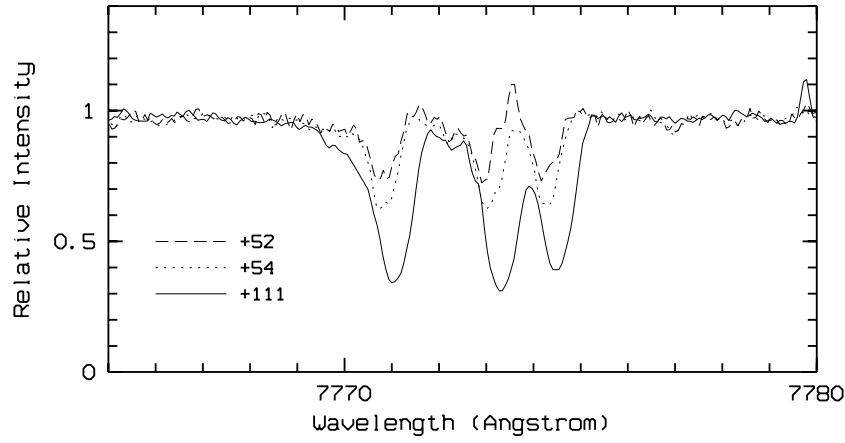
Figure 3.25: *Filling in of the photospheric spectral lines of OI (7771.9 Å, 7774.2 Å and 7775.4 Å) throughout the deep decline.*
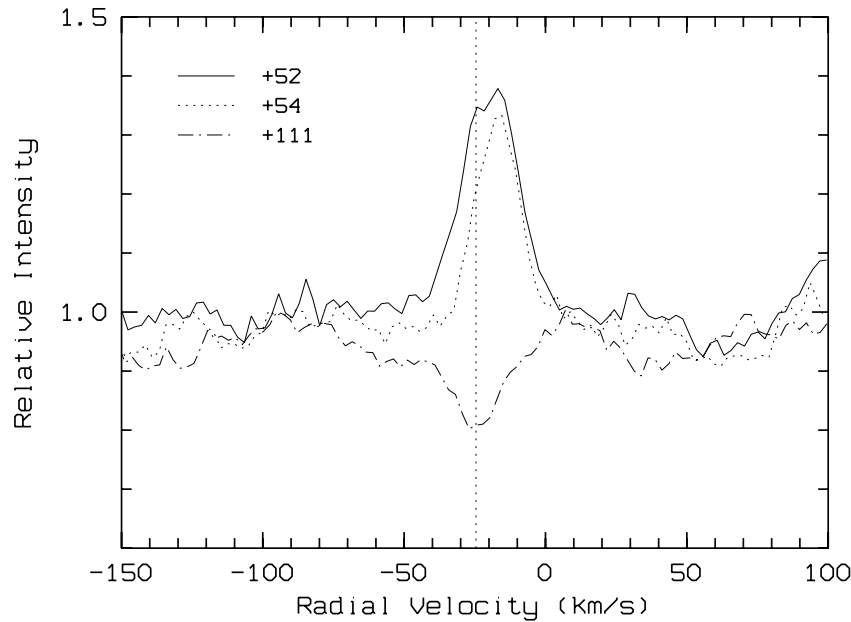
Figure 3.26: *The MgI 8806.8 Å spectral line red-shifted by about 5 $km\,s^{-1}$ relative to the photospheric absorption.*

profiles of the CI 4771.7 Å line in Figure 3.24. The mean radial velocity of CI emission lines, $-(17.3 \pm 0.6)$ $km\,s^{-1}$ on day number +52, exhibits a red shift of about 5 $km\,s^{-1}$ relative to the photospheric velocity. The radial velocities and equivalent widths of a number of CI lines are given in Table 3.6. The strongest CI emission lines from the same multiplet do not scale with their gf-values (Figure 3.23) indicating that they are optically thick. This is opposite to the case of the low-excitation sharp emission lines discussed above.

The OI high-excitation lines ($\chi_U \sim 10.7$ eV) at 7771.9 Å, 7774.2 Å and 7775.4 Å, show a profile similar to the CI lines (Figure 3.25). Even if they do not go into clear emission,

they show more filling in of the red part of the absorption profile. Similar profiles have been recorded for the prominent SiII 6347.1 Å and 6371.4 Å lines with the upper excitation potential of $\chi_U \sim 10$ eV (Figure 3.48). These lines will be discussed in more detail later, together with other photospheric lines (see Section 3.8).

In addition to this, some lines with the upper excitation potential of about 5 eV, such as the MgI triplet and MgI 8806.8 Å line, show a red-shifted emission as well (Figure 3.26). The MgI 8806.8 Å line has also been identified in the MRS spectra. It is a short-lived line and has not been seen after day number +54. The MgI triplet will be discussed later (see Section 3.5.4), since these lines are a blend of a few different components.

Alexander et al. (1972) found that many CI absorption lines fill in, but never go into emission. The present observations show that these lines (as well as some other high-excitation spectral lines, such as MgI and OI) go into emission that lasts for a few weeks. Given the time scale of their emission, these lines seem to belong to the group of E_1 lines defined by Alexander et al. (1972). The origin of these lines will be discussed in Chapter 5.

3.4.3 Forbidden lines

Apart from the low and high-excitation emission lines observed in some RCB stars, the forbidden spectral lines of [OI], [CI], [CaII] and [FeII] have also been classified as sharp (Rao & Lambert 1993; Asplund 1995; Vanture & Wallerstein 1995; Pandey et al. 1996; Rao et al. 1999). These lines play a significant role in revealing information on the physical conditions in the emitting gas.
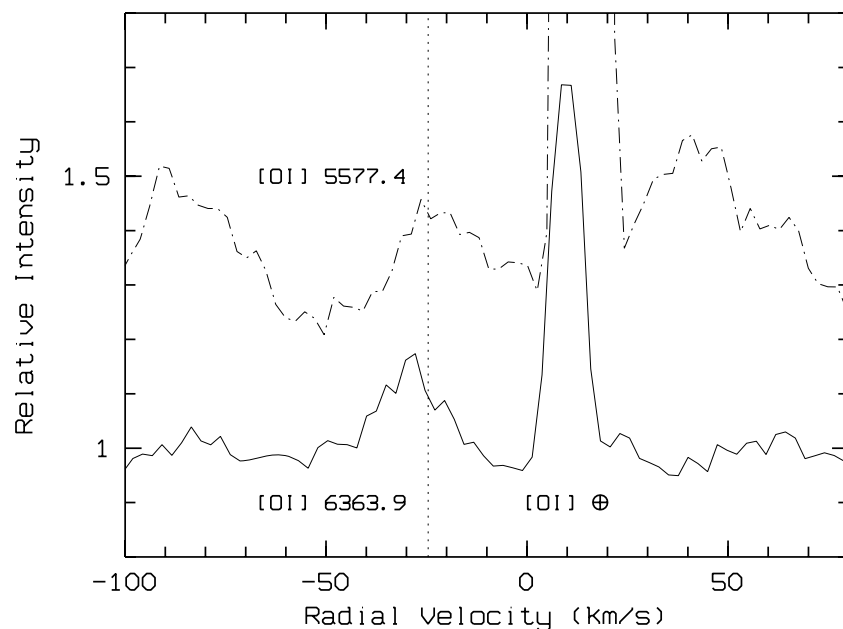
Figure 3.27: *Forbidden lines of [OI].*
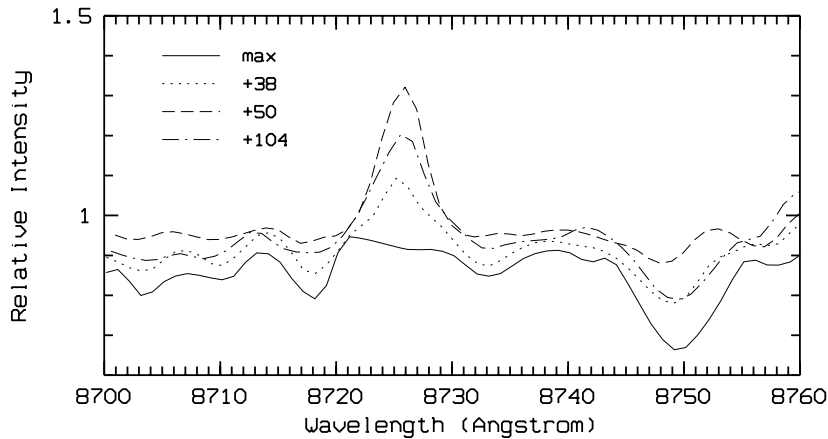
Figure 3.28: *Medium-resolution spectra around [CI] 8727.1 Å throughout the 1998 decline of V854 Cen.*

During the 1998 decline of V854 Cen, only the forbidden lines of [OI], [CI] and [CaII] were identified. They are all at the same velocity as the permitted low-excitation sharp lines. The detailed line profile is not easy to recognize in the case of the forbidden lines, since all the lines are relatively weak. There is an indication, however, of the existence of a very weak broad component in some of these lines.

The [OI] lines 5577 Å and 6363 Å were identified in the high-resolution spectra during decline II (day number about +50). The line 6300 Å falls outside the observed spectral region. The [OI] lines are not seen during the early recovery phase (day number +111). No spectra are available from the deepest minimum (decline III). However, the medium-resolution spectra from the phase close to the minimum (day numbers +104 and +105) indicate the existence of a broad 6300 Å line. Due to the poor resolution and blending with strong sky and other lines, the parameters of these lines cannot be reliably measured.

At its base, the 6363 Å line profile (Figure 3.27) extends to about ± 25 km s^{-1} from the central position. The line centre, at a velocity of -29.5 km s^{-1}, is blue-shifted by about 5 km s^{-1} relative to the stellar velocity. The equivalent width of ~ 0.1 Å indicates that this nebular line is very weak. If it had been observed, the 6300 Å line would have been three times stronger than the 6363 Å line, according to the predicted fluxes for an optically thin region (see Equation 3.7).

The 5577 Å line (which is not the same transition as the other two lines), with an equivalent width of ~ 0.5 Å, appears to be stronger, but also blended with some other spectral lines. However, the existence of the [OI] emission lines indicates the presence of a nebula surrounding the star. Since the forbidden lines are most probably optically thin, their profiles reflect the velocity distribution of the emitting gas.

From other declines of V854 Cen it is known that this star shows strong emission from the CII] 2325 Å semi-forbidden line in the UV region, which is not seen in other RCB stars

(Clayton et al. 1992b; Clayton et al. 1993a). However, in the present spectra, lines of [CI], not [CII], have been identified. The [CI] lines (9850.3 Å, 9824.1 Å and 9808.3 Å, transition: $2^3P - 3^1D$) appear quite weak (just above the noise level) in the high-resolution spectra. They do not fall inside the observed portion of the MRS spectra. On the other hand, the [CI] 8727.1 Å line (transition: $3^1D - 2^1S$) was monitored throughout the whole decline phase in the MRS spectra (Figure 3.28). The line appears during the initial phase (day number +38) and stays visible through to the early recovery phase (day number +104). The mean radial velocity of the line throughout the decline is: $-(28 \pm 5)$ km s^{-1}. The [CI] 8727.1 Å line appears to be blue-shifted relative to the stellar velocity of $-(25.1 \pm 0.9)$ km s^{-1}. The line flux stays constant throughout the decline, similar to the broad emission lines. The [CaII] lines will be discussed later (see Section 3.5.3), together with other CaII lines.

3.5   Broad emission lines

The list of broad emission lines identified during the 1998 decline of V854 Cen includes: NaI D, H$_\alpha$, CaII H & K, CaII IR triplet and MgI triplet. The HeI emission lines (3889 Å, 5876 Å and 7065 Å), observed as broad in some other RCB declines (Rao et al. 1999), were not seen during this decline. The 5876 Å line is not found within the observed region in the high-resolution spectra. The 3889 Å line, normally expected to be the strongest one, was not identified, or was very weak, in either the échelle or the MRS spectra.

The observed broad lines belong to a wide range of the excitation potential: the high-
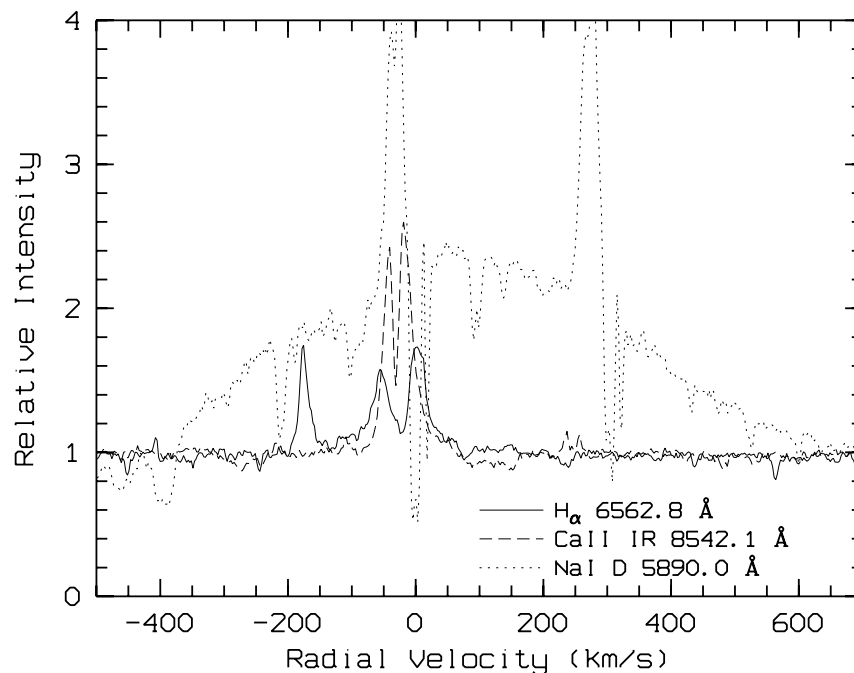
Figure 3.29: *The H$_\alpha$ line and the CaII IR triplet compared to the broad NaI D emission.*

excitation lines, such as H_α ($\chi_U \sim 12$ eV), as well as the low-excitation lines, such as CaII IR triplet ($\chi_U \sim 3.1$ eV), and the resonance lines of NaI D ($\chi_U \sim 2$ eV) and CaII H & K ($\chi_U \sim 3.1$ eV). In contrast with the sharp emission lines, different broad lines have different intensities and widths. In fact, apart from the resonance CaII H & K and NaI D lines, the other broad lines appear significantly weaker and narrower (Figure 3.29). The CaII IR triplet and H_α lines exhibit a full width at the base of about 300 $\mathrm{km\,s^{-1}}$, while the NaI D lines have a base width of about 1000 $\mathrm{km\,s^{-1}}$. The MgI lines ($\chi_U \sim 5$ eV) also show a narrower base (~ 70 $\mathrm{km\,s^{-1}}$).

The difference in the base width between the resonance lines (NaI D, CaII H & K) and the other low-excitation lines can be due to the high optical depth of the resonance lines. It is also known that the high-excitation lines form close to the star, while the low-excitation ones (both resonance and forbidden) form at greater distances.

In the following subsections various broad lines will be discussed. Most frequently these features appear as parts of more complex profiles. In such cases they will not be analysed separately, but as part of the entire profile.

3.5.1   NaI D broad emission

All declines of V854 Cen are characterized by a very strong broad NaI D emission, in contrast with other RCB stars. This was observed during the 1998 decline as well. The broad NaI D emission appeared first at an early stage, around day number +10 (Figure 3.7), and was still visible during the recovery phase (day number +125, Figure 3.8). The strong broad NaI D emission indicates the presence of a significant amount of gas (and dust) around the star, probably due to very frequent declines.

Both the MRS and the high-resolution spectra have been used and compared to each other, in order to get the parameters of the broad components throughout the whole decline. First, the parameters of the broad lines have been obtained from several high-resolution spectra taken around the minimum of decline II (Table E.14, Appendix E). These parameters have then been used for modelling the MRS spectra. The procedure is explained in detail in Chapter 2. As a result the equivalent widths of the broad component have been obtained throughout the decline (see Table E.15, Appendix E). It turns out that a single gaussian provides a sufficiently good fit to the entire profile consisting of two broad NaI D components (D_2 and D_1), as shown in Figure 2.16, Chapter 2. The average FWHM of a single broad component is about (600 ± 20) $\mathrm{km\,s^{-1}}$. On the other hand, if a pair of gaussians of the same intensity and FWHM is fitted to the same profile, a width of about (400 ± 26) $\mathrm{km\,s^{-1}}$ is obtained for each component. From numerous examinations of the high-resolution spectra during the deep decline, the broad NaI D emission has been found to extend at its base to ± 500 $\mathrm{km\,s^{-1}}$ on the either side of the assumed photospheric velocity (-25.1 $\mathrm{km\,s^{-1}}$).

The variations of the equivalent width of the NaI D broad emission during the decline are
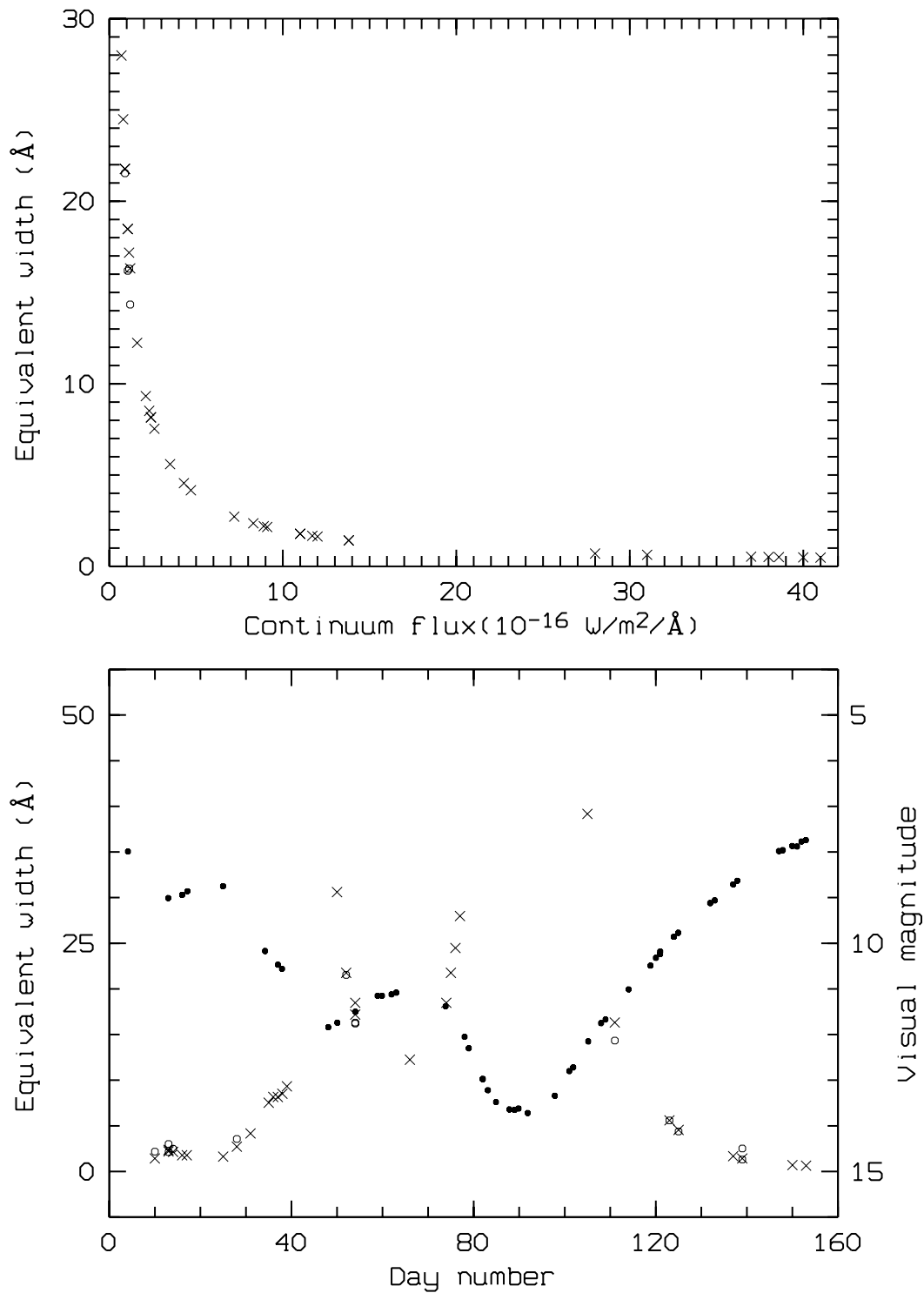
Figure 3.30: *The equivalent width of the broad NaI D emission versus the continuum flux and day number. The crosses (×) represent the MRS measurements, while the open circles correspond to the data obtained from the high-resolution spectra. The filled circles represent the light curve.*

presented in Figure 3.30, as a function of time and the continuum flux. The equivalent width follows the changes in the continuum, so that it becomes larger when the continuum flux is weaker, and vice versa, throughout the whole decline. This behaviour is clearly different from what has been found for the sharp emission lines (see Figure 3.17).

In spite of the fact that the two NaI D components are blended, the whole profile is symmetric (Figure 3.6), which is consistent with a symmetric, expanding circumstellar shell with the same amount of gas in front of the star and behind it. In addition, the flux of the entire broad component stays constant to within 12%, from its first appearance (day number +10), up to its disappearance (day number +139). This is in contrast with the sharp emission lines, whose fluxes have been found to decrease during the decline. This difference in behaviour between the broad and sharp emission lines indicates that the corresponding emitting regions are well separated. It can also be noticed that the relative intensities of the NaI D broad emission in 1998 and 1999 (Figure 3.46) are approximately the same when the star is at about the same magnitude in both declines. This is consistent with the idea that the broad emission is a permanent feature, whose visibility depends only on the photospheric brightness.

3.5.2   H$_\alpha$ emission

The H$_\alpha$ emission was observed during the initial phase of the 1998 decline, around day number +28. It stayed visible throughout the whole decline (Figure 3.31) up to the early recovery phase (day number +111). The absorption maximum-light profile has a sharp core superimposed on the broad wings. The core (at a velocity of ~ -24 km s^{-1}) is asymmetric, indicating that its blue part might be filled by emission (Figure 3.32).

The H$_\alpha$ emission profile during the decline also shows broad wings and a sharp core, disturbed by the photospheric absorption, or self absorption. This absorption, as a mirror image of the photospheric absorption, remains visible throughout the whole decline (Figure 3.31). Both the broad and sharp H$_\alpha$ emission components seem to be centred at the photospheric velocity. However, around day number +54 (the dashed and dotted spectra in Figure 3.33), the central absorption profile exhibits some noticeable asymmetry. This could be due to a displacement of both the broad and sharp emission profiles with respect to the photospheric absorption. In addition, the combined profile at medium resolution shows a noticeable blue shift, in spite of the fact that the medium-resolution H$_\alpha$ emission is blended with a TiII spectral line. When a pair of gaussians is fitted to the data the centre of the emission becomes blue-shifted by about 5 km s^{-1} relative to the mean photospheric velocity (~ -23 km s^{-1}), which was obtained from a few medium-resolution spectra. During the recovery phase (day number +111), the broad wings cannot be distinguished, while the sharp emission is superimposed on the absorption profile (Figure 3.31).

The broad H$_\alpha$ emission is considerably narrower than the much stronger NaI D profile.
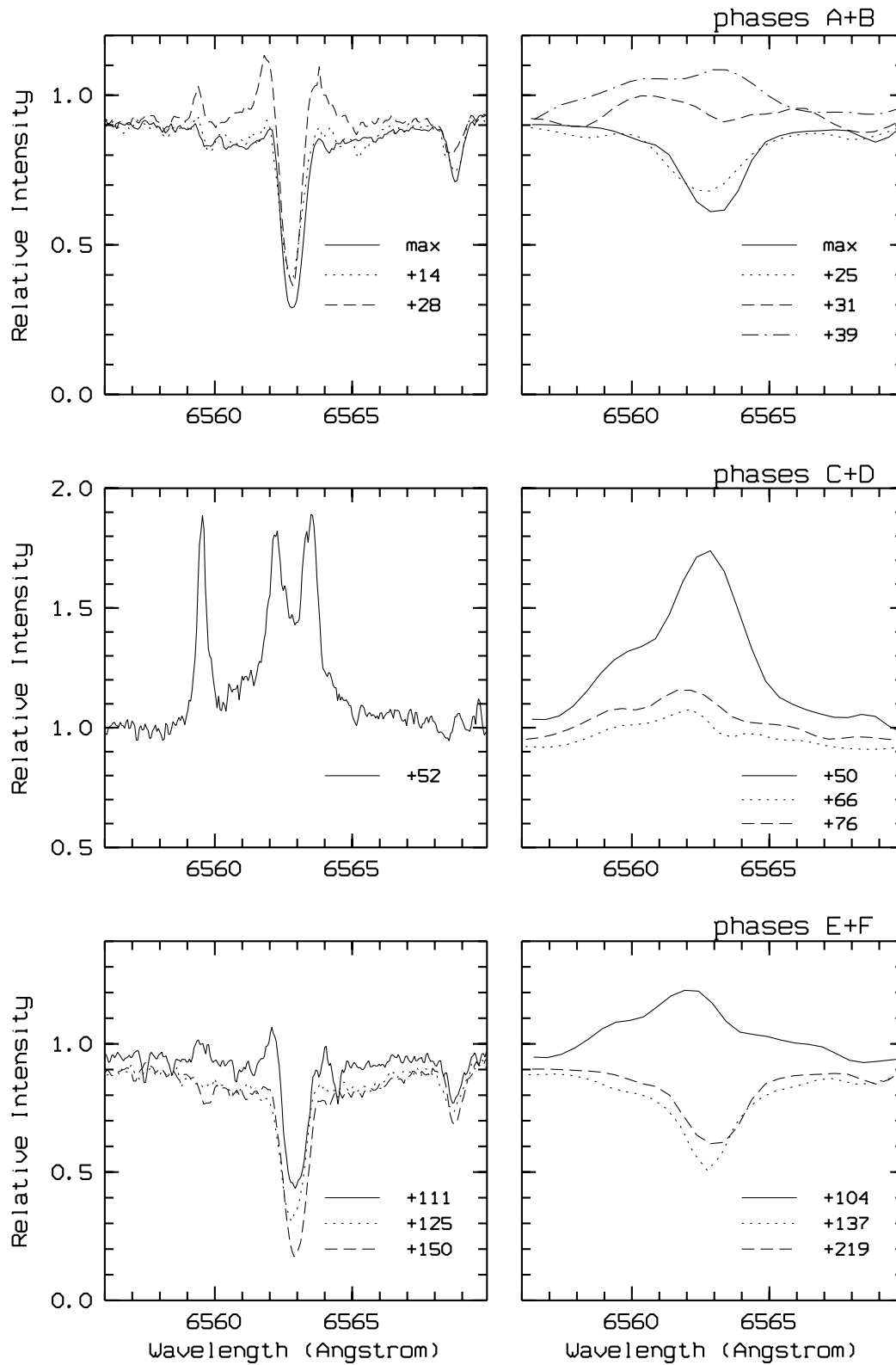
Figure 3.31: *The evolution of the* H_α *line throughout the decline phase. Left: high-resolution spectra. The strong emission line on day number* +52 *is the TiII 6559 Å. Right: medium-resolution spectra.*
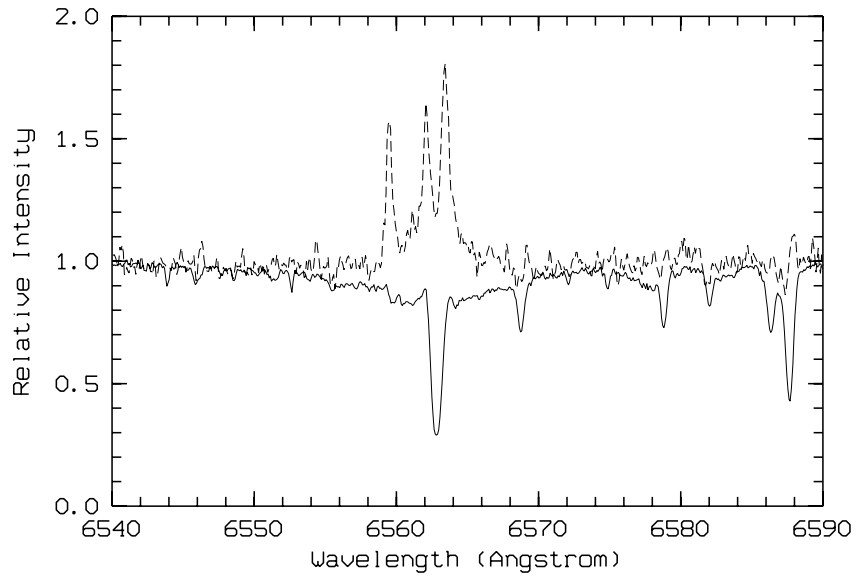
Figure 3.32: *The H$_\alpha$ profile at the light maximum (solid line) and during the deep minimum of the 1998 decline (dashed line).*
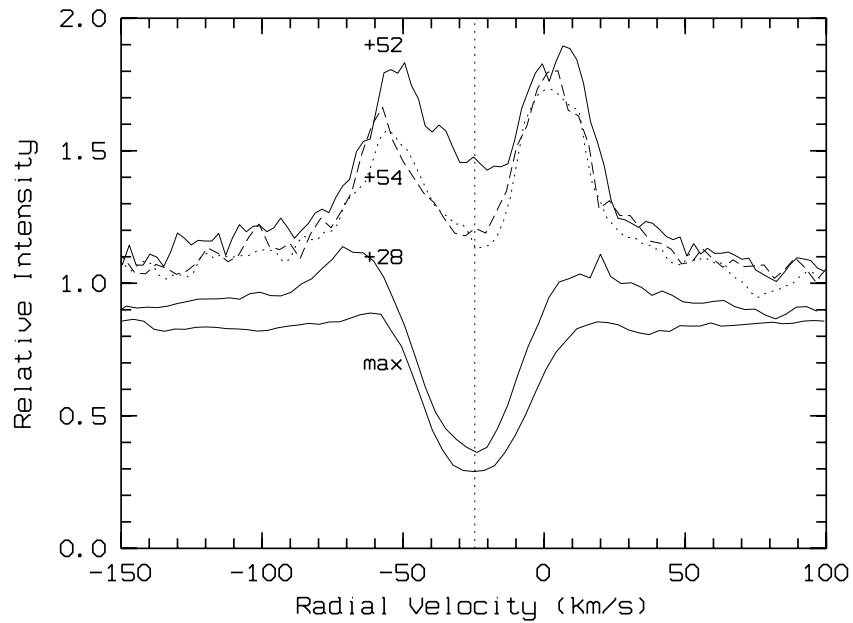
Figure 3.33: *The H$_\alpha$ line at the light maximum and during the initial decline phase (decline II, day numbers +28, +52 and +54). The stellar velocity is marked by a vertical dotted line.*
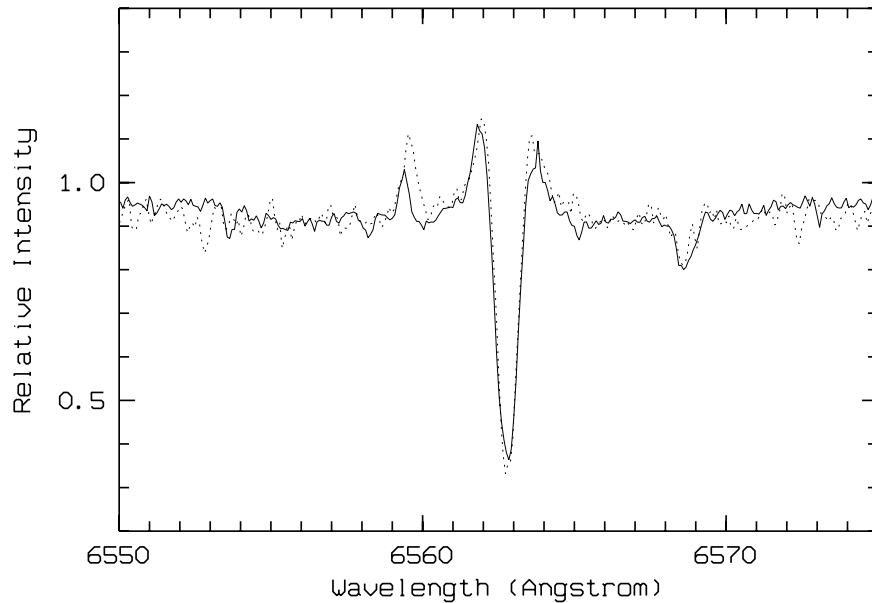
Figure 3.34: *The H$_\alpha$ line from the 1998 (solid line) and 1999 (dotted line) declines.*

The H$_\alpha$, at its base, extends to about ± 150 km s^{-1} from the line centre. This broad emission is also much weaker (with a central intensity of about 15% above the continuum) than the broad NaI D profile. It has been confirmed that the whole H$_\alpha$ emission appears identical during the subsequent (1999) decline. When two spectra from both declines (corresponding to the same photospheric brightness) are compared, the H$_\alpha$ emission shows identical width and overall structure (Figure 3.34). This is similar to the behaviour of the NaI D emission.

3.5.3   CaII lines

The CaII ion was detected during the decline in the H & K lines (3968 Å and 3934 Å), the infrared triplet (8662 Å, 8542 Å and 8498 Å) and two forbidden lines (7291 Å and 7324 Å). These lines form a closed loop between the ^{2}P, ^{2}D and ^{2}S levels. The H & K resonance lines correspond to the transition from the 4^2S$_{1/2}$ ground state to the second excited state (4^2P$_{3/2}$ or 4^2P$_{1/2}$), which serves as the upper state of the infrared lines (Figure 3.35). The lower state of the infrared lines, 3^2D, and the ground state are connected by the forbidden lines.

By comparing the similarities and differences between the permitted and forbidden CaII lines, one can draw some important conclusions concerning the density and the optical depth of the emitting region. The following observational and theoretical facts can help understand the relationship between these lines. First, the upper level (4p) has a lifetime of 0.8 s for spontaneous deexcitation (Wiese et al. 1969), leading to the existence of H & K and IR triplet in emission. Since these lines originate from the same upper level, then their flux ratio can be expressed as $F_1/F_2 = A_1\lambda_2/A_2\lambda_1$ (Equation 3.7), if one assumes that the emitting region is optically thin. Therefore, the H & K lines should appear much stronger than the lines
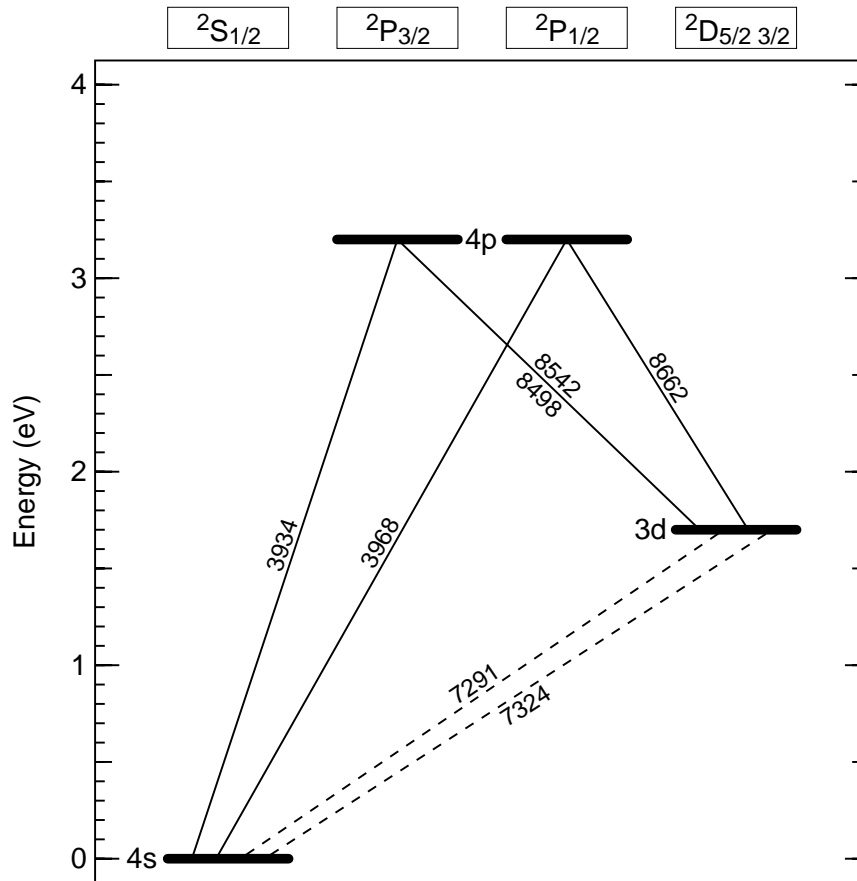
Figure 3.35: *A simplified energy diagram showing the transitions in CaII. The wavelengths in angstrom units are shown along the lines representing the transitions. Energies in eV are given relative to the ground state.*

from the IR triplet.

Considering the relationship between the IR triplet and the two forbidden lines in a low density gas optically thin to the IR triplet, the number of photons emitted in the IR triplet is equal to the number of photons emitted in the forbidden lines (Rao et al. 1999). On the other hand, the forbidden lines are usually formed due to collisional deexcitation. In order to have the collisional deexcitations as frequently as the radiative deexcitations, one must have a certain critical density of the ^{2}D level. According to Asplund (1995), this critical density has to be at least $\sim 9 \times 10^6$ cm^{-3}. From the broad HeI lines, observed during the 1995 decline of R CrB, Rao et al. (1999) found densities of $N_e \sim 10^{11}$ to 10^{12} cm^{-3} (i.e. well above the critical value) for the HeI broad line emitting region. It can be assumed that this is the same region as for the CaII lines. Therefore, one can expect that in an optically thin, low-density gas the strength of the CaII IR triplet is similar to the strength of the [CaII] forbidden lines.

Broad CaII H & K lines and IR triplet

The H & K lines were first seen in emission on day number +51, when the star was at a magnitude of about 11^{m}7. They went into emission later than the other spectral lines (e.g. NaI D) and became strongest when the other lines had already begun to decay (day number +105, Figure 3.36). Since they form quite high in the chromosphere (Noyes & Avrett 1987), they are probably not obscured by the dust cloud at the same time as the other spectral lines.

From the medium-resolution spectra it is not possible to distinguish clearly between the sharp and broad emission profiles. Similar to the broad NaI D lines, the CaII H & K extend at the base to about ±600 km s^{-1}. The broad CaII IR component underlying the sharp feature is seen only during the deep minimum of decline II (day number ∼ +50), bearing in mind that no spectra from the deepest minimum are available. This component is very
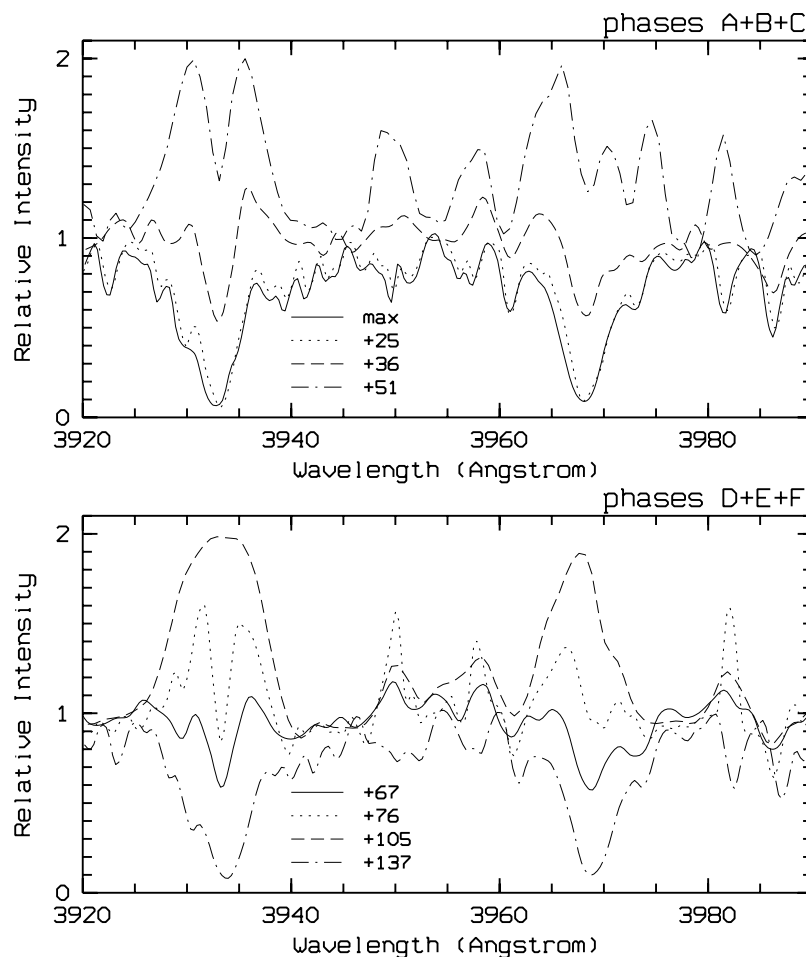
Figure 3.36: *Medium-resolution spectra around the CaII H & K lines throughout the decline. The spectra on days +36, +51, +67 and +105 are of low resolution (using the 300 l/mm grating). The absorption, present on some deep decline spectra, is photospheric.*

weak (only about 10% above the continuum).

Due to the poor resolution, the flux of the CaII H & K lines was only roughly estimated and compared with the IR triplet. The flux ratio, F_K/F_{IR}, between the broad K line (3934 Å) and the IR triplet line 8542 Å, both originating from the same upper excitation level, is about 26. This is very close to the value obtained by using Equation (3.7), which suggests that the gas emitting these lines is optically thin.

Sharp emission in the IR triplet

The sharp emission in the IR triplet lines can be seen at the very beginning of the decline (day number +14, Figure 3.37) and it stays visible until the recovery phase (day number +125), when it appears superimposed on the photospheric absorption line.

The red peak of the sharp 8542 Å line is stronger than the blue one. This fact, together with a noticeable asymmetry in the underlying broad emission (Figure 3.37) suggests that both the sharp and broad CaII IR emission components are shifted relative to the photospheric absorption. The measurements of the emission IR profile from the MRS spectra,
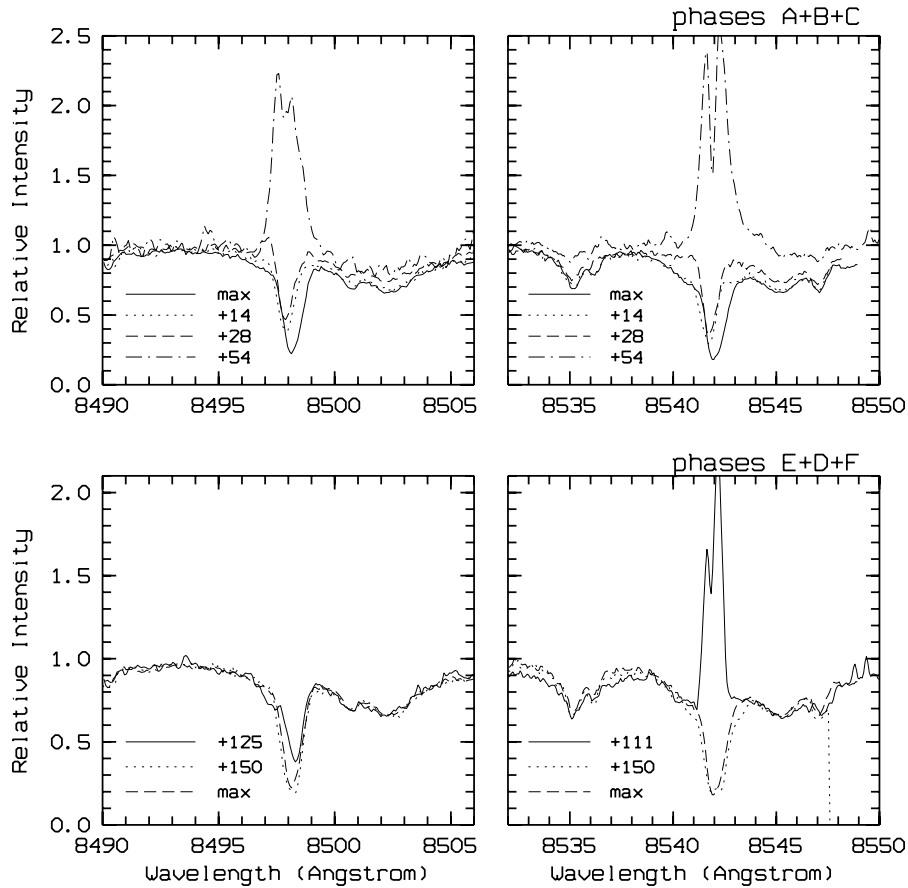
Figure 3.37: *High-resolution spectra around CaII 8498 Å (left side) and 8542 Å lines (right side) throughout the decline phase.*
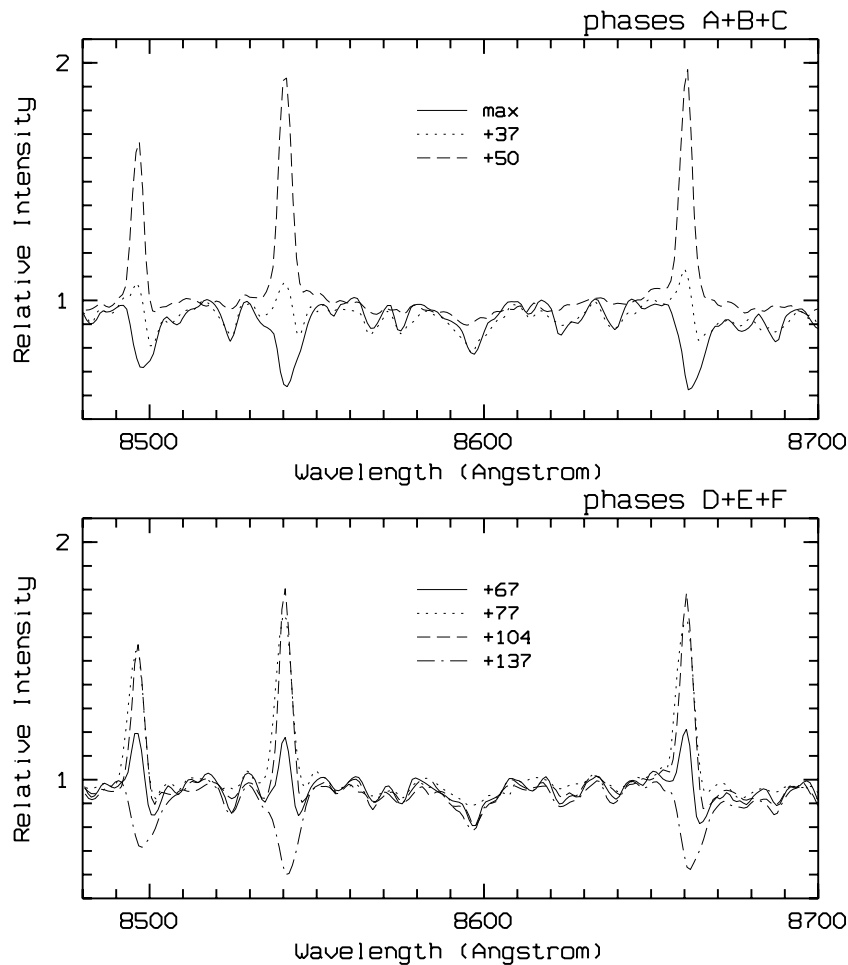
Figure 3.38: *Medium-resolution spectra of the CaII IR triplet (8498 Å, 8542 Å and 8662 Å) throughout the decline.*

including the sharp emission features, also show a blue-shift of about 7 $\mathrm{km\,s^{-1}}$ relative to the photospheric absorption (Figure 3.38). The flux ratio of the IR triplet (including the sharp emission lines) measured from several MRS spectra is 8498:8542:8662=1:1.5:1.5, with an uncertainty of about 15%. This is closer to an optically thick ratio of 1:1:1, than to an optically thin one of 1:9:5 (Asplund 1995). The changes of the flux ratio throughout the decline are within the uncertainty.

The emission in the forbidden [CaII] lines falls out of the observed region in the MRS spectra. In the high-resolution spectra, the 7323 Å line was observed only during the deep minimum of decline II (day numbers +52 and +54). This line extends at the base to about ± 25 $\mathrm{km\,s^{-1}}$ and can be classified as a sharp line. In fact it is only slightly wider than the instrumental profile. The line is at a velocity of about 4 $\mathrm{km\,s^{-1}}$, blue-shifted relative to the stellar velocity and similar to other sharp emission lines. The flux in the sharp IR triplet is about 12 times larger than in the sharp [CaII] forbidden lines. This suggests that collisional deexcitation of the ^{2}D level is taking place.

3.5.4   MgI triplet

The MgI triplet (5184 Å, 5173 Å and 5167 Å, transitions from 4^3S to 3^3P) was identified in the high-resolution spectra around the deep minimum of decline II (day numbers +52 and +54). It was not detected during the early recovery phase (day number +111). The lines show a structure similar to the H_α and CaII IR, with a sharp, bimodal emission profile, and a weak broad emission. This can be seen in Figure 3.39. The broad components extend at the base to about ± 35 km s^{-1} from the photospheric velocity, which is less than in other broad lines. The MgI triplet lines also show some redward asymmetry and are displaced more towards the red than the other broad emission lines. This could be a result of a complex profile including both the red-shifted (lines from the E_1 region) and blue-shifted E_2 emission, as well as the photospheric absorption and broad emission. It is interesting to note that another MgI line (8806.8 Å) also exhibits a red-shifted emission component.

The flux ratio of the two strongest MgI triplet lines (5184 Å/5173 Å) has been estimated and compared with the theoretical predictions for an optically thin region (see Equation 3.7). The MgI triplet lines appear to be originating from an optically thin region. A more detailed discussion on the origin of the broad emission lines and the physical conditions characterizing the emitting regions will be given in Chapter 5.
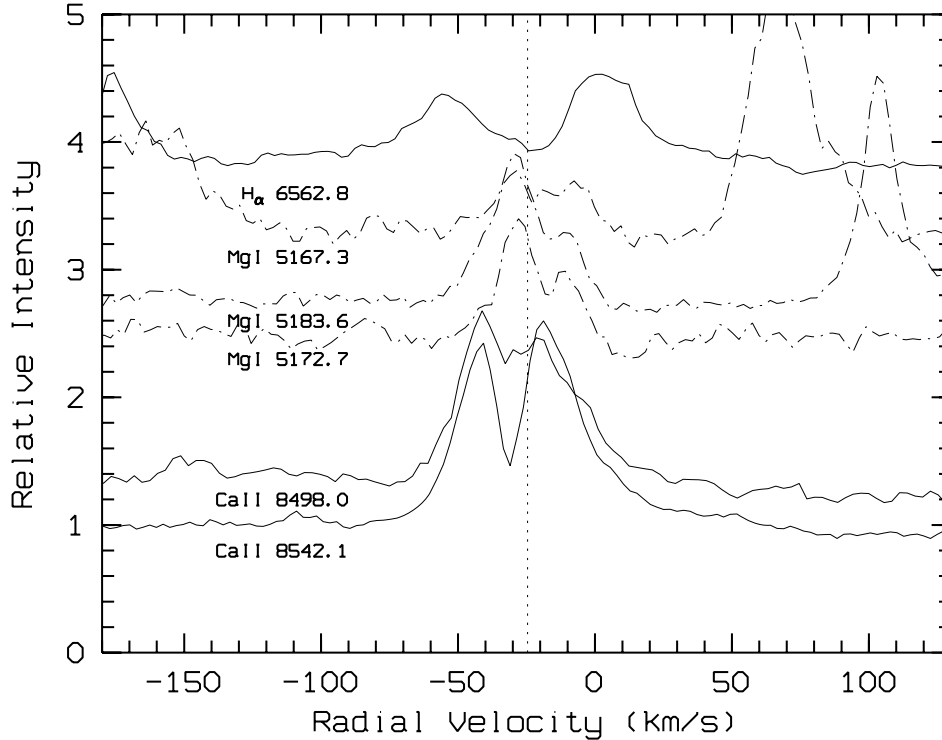
Figure 3.39: *Various broad emission lines, including the MgI triplet, CaII IR triplet and H_α. The vertical dotted line represents the stellar velocity.*

3.6 Molecular bands

During the 1998 decline of V854 Cen, the molecular bands of the C_2 Swan system were identified. The CN red system, previously found in V854 Cen by Whitney et al. (1992), is absent in this decline. In some deep declines of RCB stars, in particular V854 Cen (Rao & Lambert 1993) and R CrB (Rao et al. 1999), the Swan system has been found to exhibit a broad emission displaced towards shorter wavelengths. In the present observations only the sharp lines of this molecular band have been identified throughout the whole decline phase. The broad emission, if at all exists, must be at a very low level.

The absorption bands of the C_2 Swan system are very weak at the light maximum. The emission appears at the very onset of the decline (day number +25, Figure 3.40) and stays visible through the minimum of decline II (day number +50). During the small recovery phase of decline II (day number +67), the bands are seen in absorption for a short time. The
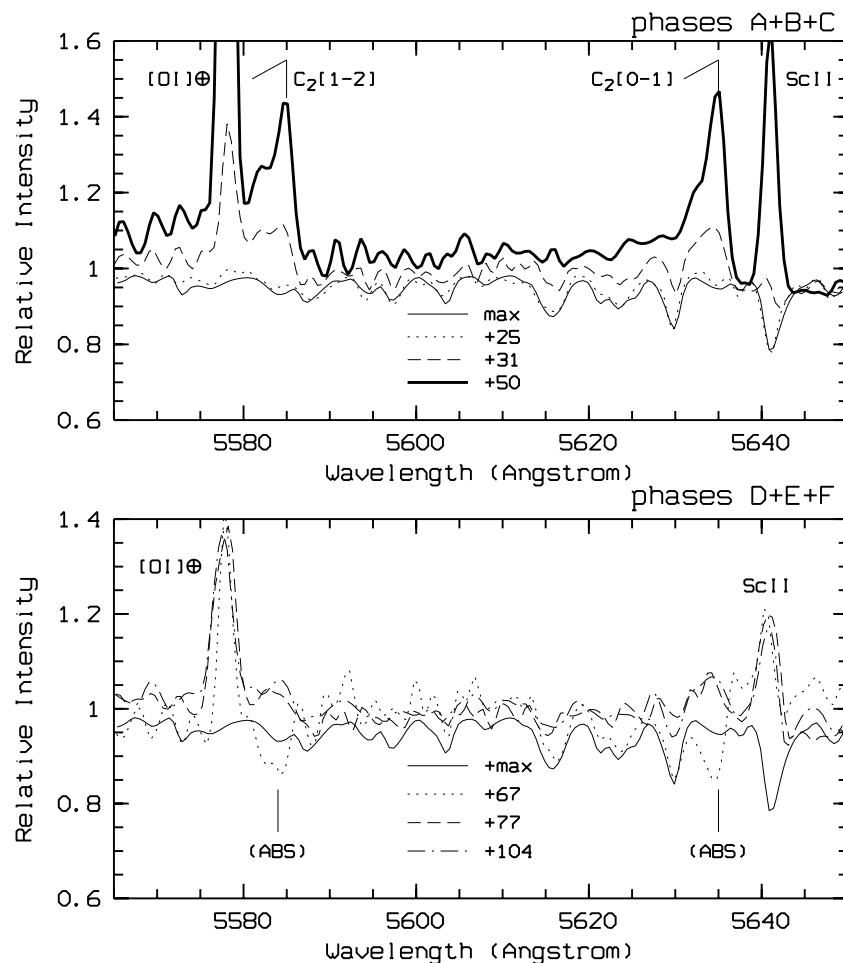
Figure 3.40: *Medium-resolution spectra of the C_2 Swan system (transitions (0–1) and (1–2)) during the 1998 decline. A noticeable absorption (ABS) in the bands on day number +67 is seen. A strong telluric line of [OI], as well as a sharp stellar emission line of ScII are marked.*
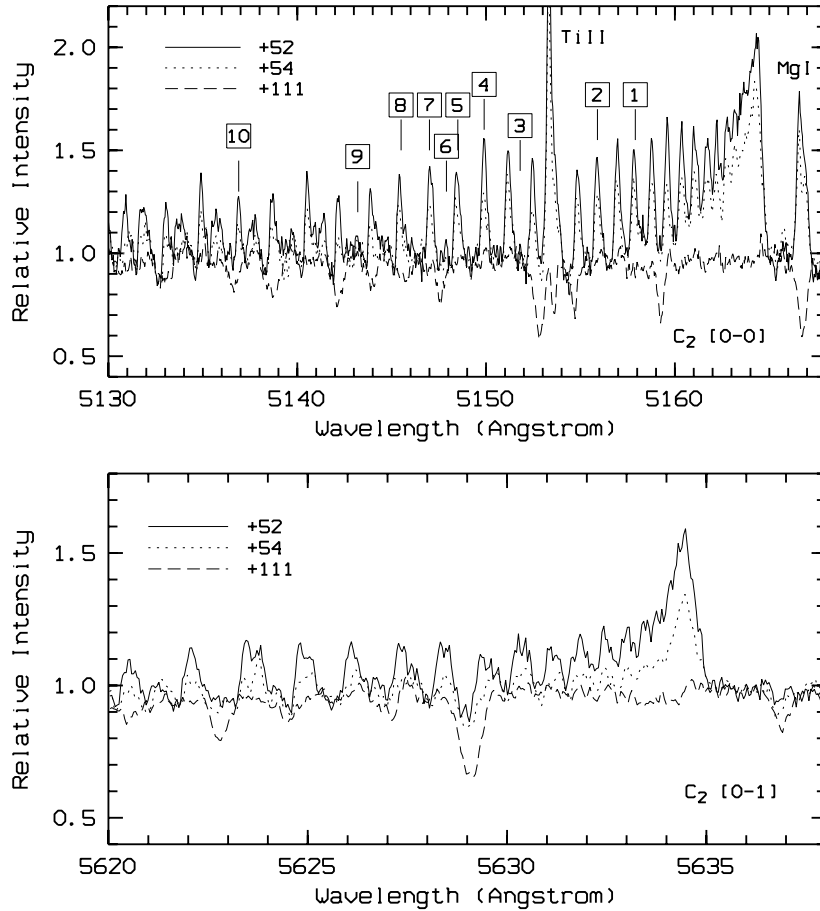
Figure 3.41: *High-resolution spectra of the C_2 Swan system (transitions (0–0) and (0–1)) during the deep minimum of decline II (day numbers +52 and +54) and the early recovery phase (+111). A few molecular lines of the (0–0) band (including the blended ones) are marked as:* $\boxed{1}$ $P_1(29) + P_2(28) + P_3(27)$, $\boxed{2}$ $P_1(31) + P_2(30) + P_3(29)$, $\boxed{3}$ $R_2(5)$, $\boxed{4}$ $P_1(36) + P_2(35) + P_3(34)$, $\boxed{5}$ $P_1(37) + P_2(36) + P_3(35)$, $\boxed{6}$ $R_3(7)$, $\boxed{7}$ $P_1(38) + P_2(37) + P_3(36)$, $\boxed{8}$ $P_1(40) + P_2(39) + P_3(38)$, $\boxed{9}$ $R_3(10)$ *and* $\boxed{10}$ $P_1(44) + P_2(43) + P_3(42)$.

emission might be appearing again during the new light fading (decline III), but only at a very low level (day number +77, Figure 3.40). During the recovery phase, no emission was detected (Figure 3.41). The strongest main bandhead identified is (0–0) (sequence $\Delta v = 0$) with well separated sets of P and R lines (Figure 3.41). The bandheads (0–1), (1–0), (1–1) and (1–2) are twice as weak as (0–0), while the (2–3) and (3–4) are at a very low level. The (4–5), (1–3) and (2–4) bandheads are just detectable.

The rotational structure in the Swan system (0–0) band is resolved in the high-resolution spectra and shown in Figure 3.41. The strongest identified lines are from the lowest level (P branch), while the lines from the next to the lowest level (R branch) are much less prominent. Some of these lines with measured radial velocities are listed in Table E.16, Appendix E. A cool environment for the majority of the C_2 molecules is confirmed by the weakness of all

but leading bands of each Δv sequence. The mean velocity measured from the strong (0–0) lines is $-(26.6 \pm 0.8)$ km s^{-1}. These lines are blue-shifted by about 1.5 km s^{-1} with respect to the stellar velocity of -25.1 km s^{-1}. This is slightly less than in the case of the sharp E_2 emission lines. The FWHM values are also similar to that of the central component of the low-excitation sharp emission lines and are slightly larger than the instrumental profile. The rotational and vibrational temperatures of the (0–0) band for this decline have been estimated by Rao & Lambert (2000) to be about 5000 K. A comparison of these results with other observations of RCB declines will be given in Chapter 5.

3.7 High-velocity NaI D absorption

The high-velocity absorption (HVA) was observed throughout the whole 1998 decline of V854 Cen using both the high-resolution and medium-resolution spectrographs. The evolution of the HVA profile during the initial and recovery phases exhibits some interesting characteristics (Figure 3.42).

At least three HVA D_2 components can be recognized during the initial phase (day number +10). The strongest of them remains visible throughout the whole decline. During the
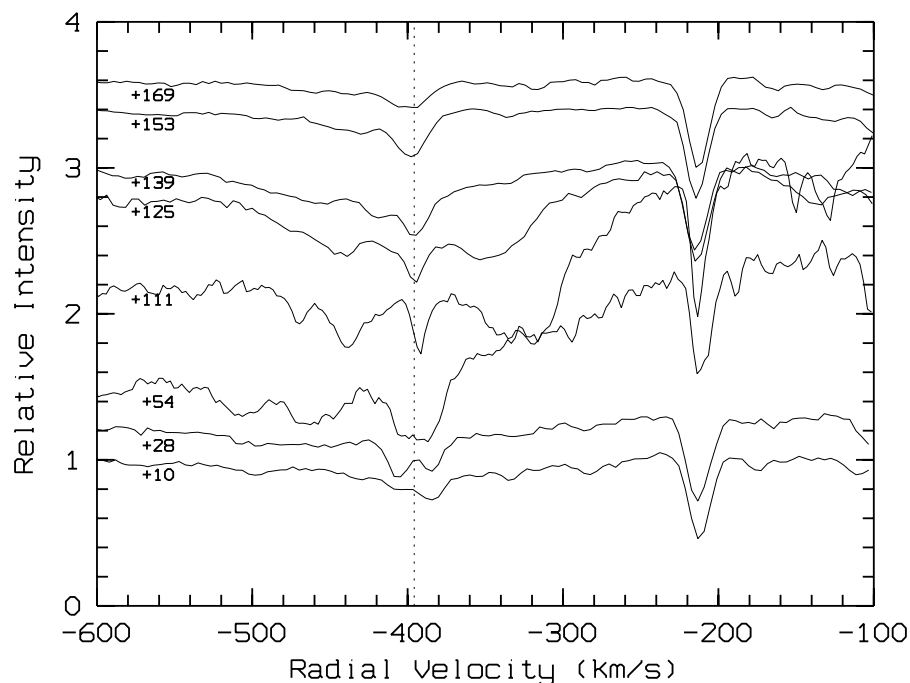
Figure 3.42: *The evolution of the NaI D_2 high-velocity absorption throughout the decline. The vertical dashed line is placed at the position of the central component of the recovery phase spectra. The strongest component of the initial phase (day number +10) appears red-shifted with respect to this line.*
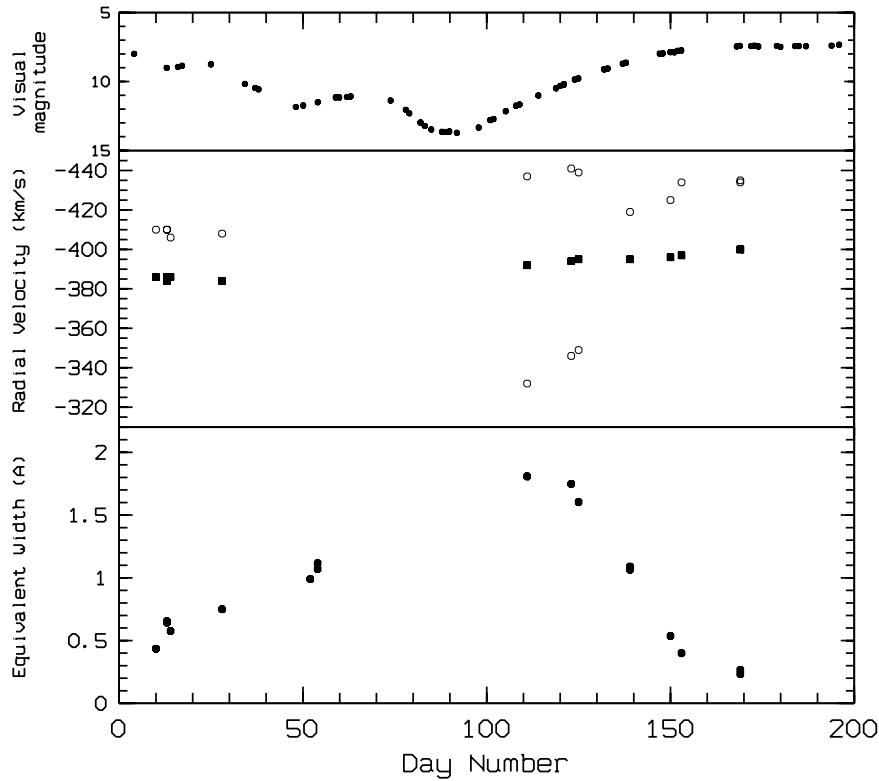
Figure 3.43: *The equivalent width and radial velocity of the NaI D$_2$ high-velocity absorption versus day number. The equivalent width is given for the total D$_2$ profile. Filled squares represent the radial velocity of the central component, while empty circles correspond to the other two components on each side of the central one.*

deepest minimum, the HVA profile becomes quite extended, so that the components become difficult to recognize (day number +54, Figure 3.42). During the recovery phase (from day number +111), the HVA exhibits a sharp and well distinguished central component, with a few broad absorption profiles on both sides. The blue-shifted component is visible only for about 15 days during the recovery phase. After that, it disappears, leaving the HVA profile with a shape similar to that of the initial phase. However, the whole profile is shifted more towards the blue than at the beginning of the decline. If one assumes that the same material is responsible for the HVA profile on days +10 and +169, then the material has to be moving with a small acceleration of ~ 0.1 cm s^{-2}, or ~ 0.1 km s^{-1} day^{-1}. In general, the total extent of the HVA profile is similar during the initial and late recovery phases, while it is larger during the deep decline and early recovery phase (Figure 3.45). The profile can be considered as asymmetric, with the red wing steeper than the extended blue one. Therefore, the weaker components at higher velocities probably originate from the less dense clouds farther away from the central star.

The radial velocities and equivalent widths of various HVA components are plotted in Figure 3.43. The equivalent widths include all components. The estimated flux ratio of
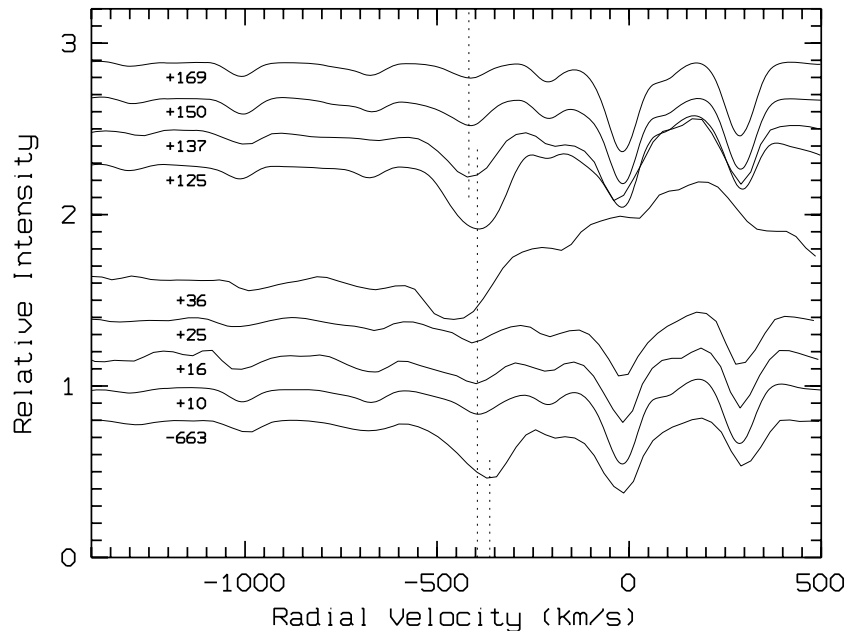
Figure 3.44: *Medium-resolution spectra of the NaI D_2 high-velocity absorption from the initial (day numbers +10, +16, +25, +36) and recovery (day numbers +125, +137, +150, +169) phases. The spectrum marked as −663 is from the recovery phase of the 1996 decline. Note the velocity shifts throughout the recovery phase and relative to the previous decline.*

the two HVA profiles (D_2/D_1), when they are not blended by other spectral lines, is about $D_2/D_1 \sim 1.9$. Using the 'doublet-ratio' method developed by Wilson & Merrill (1937), the column density[3] (N) of the absorbing gas can be estimated. The method is based on the assumption that the velocity distribution within the cloud is gaussian. In such a case, the theoretical curve of growth for the NaI D absorption lines can be obtained by integrating Equation (18) of Strömgren (1948):

$$\frac{W_\lambda}{b_\lambda} = \int \left(1 - e^{-(a_\lambda/a_0)\,\tau_0}\right) dv. \tag{3.11}$$

This gives a relationship between W_λ/b_λ and τ_0, where W_λ is the equivalent width, b_λ is the Doppler constant, describing the velocity distribution within the cloud in terms of both the thermal and internal turbulent motions, and τ_0 is the optical thickness corresponding to the line centre (τ_0 is proportional to N). Table 2 of Strömgren (1948) gives the values of W_λ/b_λ as a function of τ_0 for the D_1 component. In addition, the doublet flux ratio (D_2/D_1) is also tabulated, as well as the quantity N/W_λ. Using the measured flux ratio of $D_2/D_1 \approx 1.9$, one finds $\log(N/W_\lambda) = 12.98$, which gives a column density of $N \sim 9 \times 10^{12}$ cm^{-2} (for a measured equivalent width of $W_\lambda \approx 0.92$ Å). Therefore, the high-velocity NaI D absorption is optically thin. It should be pointed out that the doublet-ratio method can be applied

---

[3]Number of atoms, or ions, in a column of unit cross section along the line of sight (usually measured in cm^{-2}).
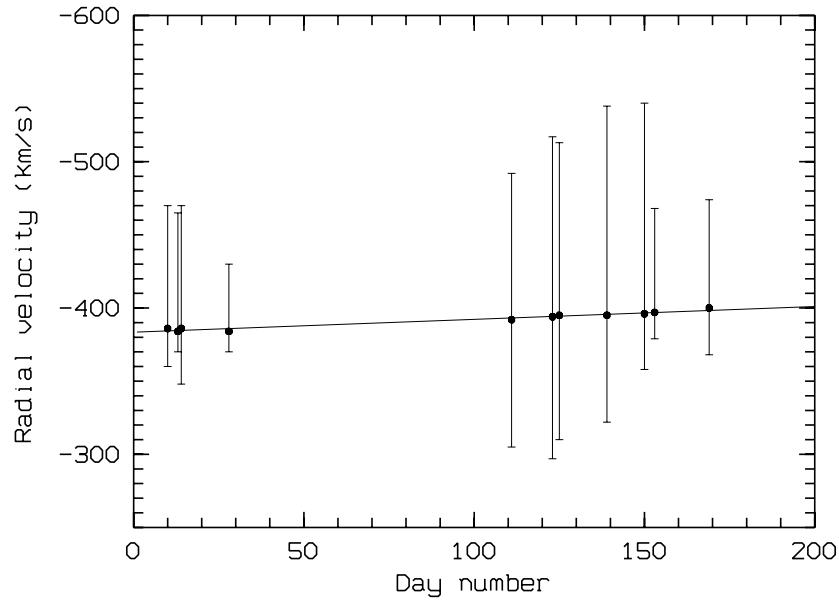
Figure 3.45: *The radial velocity of the central high-velocity NaI D$_2$ absorption component versus day number. The vertical bars show the total extent of the absorption.*
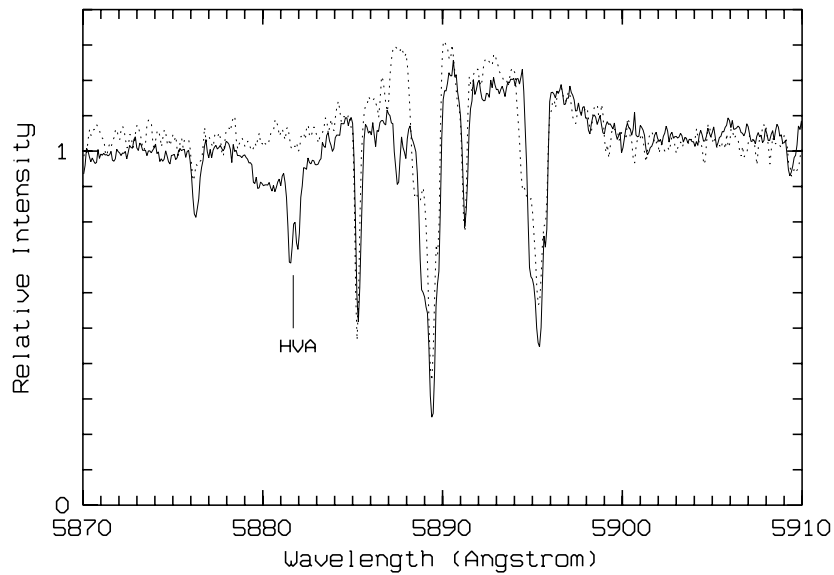
Figure 3.46: *The NaI D lines from the 1998 (solid line) and 1999 (dashed line) declines. The broad emission is similar, while the high-velocity absorption (HVA) cannot be seen in the 1999 spectrum.*

only in the case when the lines are not saturated, so that their strengths are sensitive to the variations in N and b_λ.

From the medium-resolution spectra (Figure 3.44), the centre of the D_2 component appears to be shifted by an amount ranging from about $-393\,\mathrm{km\,s^{-1}}$ (day $+123$) to $-418\,\mathrm{km\,s^{-1}}$ (day $+169$). This can be interpreted as a motion of the obscuring material away from the star with an acceleration of about $0.5\,\mathrm{km\,s^{-1}\,day^{-1}}$ ($\sim 0.6\,\mathrm{cm\,s^{-2}}$). During this time the dust cloud would pass a distance of at least $1.2\,R_*$ ($R_* \approx 57\,R_\odot$). Using this acceleration, the position of the sharp emission lines region (E_2) can be estimated. Assuming that the dust cloud was formed at $2\,R_*$, and taking into account that the sharp emission lines start decaying around day number $+50$, the position of the E_2 region can be found at about $3.5\,R_*$ (the dust cloud moves a distance of $1.5\,R_*$ in 50 days). A somewhat larger distance, of $3.5\,R_* - 5.3\,R_*$, can be obtained from the sharp NaI D components, which start decaying between days $+50$ and $+75$.

By extrapolating the velocity of the central HVA component (Figure 3.45) one can come to a conclusion that the corresponding shell was created about 12 years prior to the 1998 decline. However, this result probably does not reflect the true moment of the shell's creation, due to the following reasons. The very small acceleration of the central HVA component, of only $0.1\,\mathrm{km\,s^{-1}\,day^{-1}}$ throughout the decline indicates that the shell might already be moving as a result of previous interactions. In addition, the star exhibits frequent declines, producing new dust shells every time, so that it becomes difficult to identify the shell belonging to the current decline. It is possible that the main HVA components originate from a few gas clouds associated with some previous declines, or even from some clouds that were originally formed off line-of-sight, and then drifted (or expanded), coming slowly into the line-of-sight.

The red-shifted broad HVA component, at a velocity of $-340\,\mathrm{km\,s^{-1}}$ (Figure 3.42), appearing during the early recovery phase (between day numbers $+111$ and $+125$), may have a different origin than the central one. It can either be associated with the dust formed during the 1998 decline, or it can be produced by a shock wave acting on the material responsible for the central HVA component. It disappears quickly (within 15 days) after passing the shock wave.

To complete this analysis of the high-velocity NaI D absorption, the spectra from the 1998 decline have been compared with those from the late recovery phase of the previous (i.e. 1996) decline and the initial phase of the following (i.e. 1999) one. The HVA radial velocity of $-370\,\mathrm{km\,s^{-1}}$ from the 1996 decline (Figure 3.44) indicates that this absorption probably does not originate from the same material as that of the 1998 one. This velocity falls well off the extrapolated line corresponding to the central HVA component of the 1998 decline (Figure 3.45). On the other hand, the HVA was absent during the initial phase of the 1999 decline. This is illustrated in Figure 3.46, where two spectra (from different declines) of the NaI D region are presented, both corresponding to the same magnitude of the star. The 1999 decline was of a similar depth as the 1998 one, but with a sharp and sudden initial

phase. Other reports of the HVA components in V854 Cen are from the 1992 decline (Rao & Lambert 1993), at a velocity of -83 km s^{-1} and also weak HVA from the 1993 decline (Clayton et al. 1993b), at -390 km s^{-1}.

Shell absorption

The two absorption NaI D components (see Figure 3.6), at velocities $V_{r1} = -(213.0 \pm 0.3)$ km s^{-1} and $V_{r2} = -(213.9 \pm 0.6)$ km s^{-1}, probably originate from an expanding circumstellar shell. They are present at the light maximum, as well as during the decline, with no significant changes in the equivalent width. Their position also seems unchanged during the whole observing period of almost two years.

Figure 3.47 shows the flux ratio of the two absorption components, both at the light maximum and during the minimum. The mean flux ratio of $D_2/D_1 = (1.35 \pm 0.05)$ indicates that these lines are forming in a region which is between being optically thin and optically thick. On the other hand, several measurements from the deep decline spectra (crosses in Figure 3.47) suggest an optically thin region. However, the question is whether this difference can be regarded as significant, since the uncertainty in the flux measurements is larger due to the strong underlying broad emission. Using the doublet-ratio method (as explained above) the estimated column density is about $N \approx 2.6 \times 10^{11}$ cm^{-2}.

These shell components were also recorded during the 1992 decline (Rao & Lambert 1993), as well as during the 1989 one (with a spectrum close to the light maximum). They
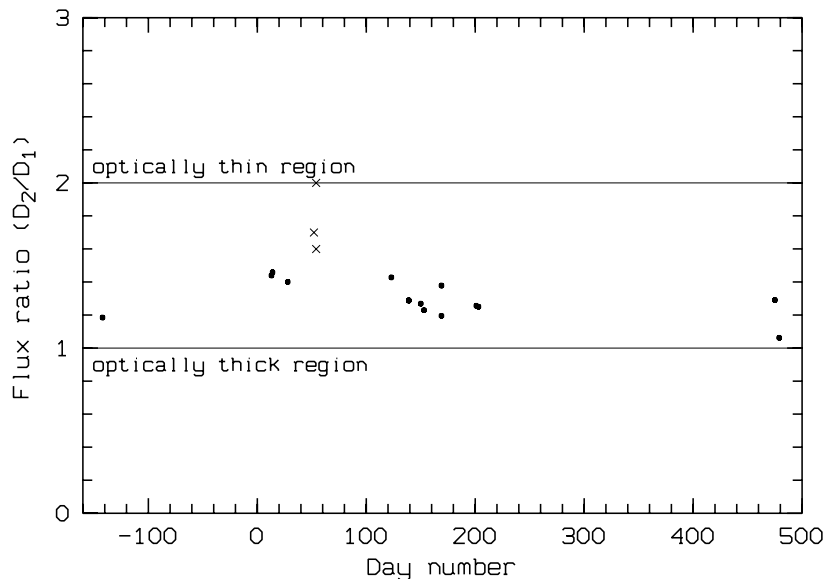
Figure 3.47: *Flux ratio of two NaI D shell absorption components at the light maximum and throughout the decline phase. Horizontal solid lines correspond to purely optically thin and thick environments. Crosses represent the measurements from the deep decline spectra.*

were identified as approximately optically thin lines with a column density of $N \approx 6 \times 10^{11}$ cm^{-2}. During the 1992 decline they were at a velocity of about -209 km s^{-1}. The velocity difference between the present observations and those of the 1992 decline might be due to systematic errors, or due to a slow acceleration of the shell. If one assumes that both the 1992 and 1998 shell absorption lines originate from the same material, then between these two years the shell would extend to a distance of $1000\,R_*$, which far exceeds the assumed position of the dust shell ($\sim 100\,R_*$).

3.8   Photospheric absorption

Some previous observations of RCB stars in deep declines (Herbig 1949; Payne-Gaposchkin 1963; Cottrell et al. 1990; Rao et al. 1999) have reported a weakening of the photospheric absorption lines. The weakening is attributed to the 'veiling', or dilution, of the photospheric spectra by an overlying continuum or line emission. Alternatively, the same effect can be explained by processes of light scattering from the material surrounding the star. After the decline onset, the photosphere becomes obscured by the newly-formed dust cloud. A significant contribution to the photospheric absorption can come not only from the light that penetrates the material causing the decline, but also from the light scattered by the circumstellar dust moving away from the star. When the stellar photosphere is blocked completely (during the deep decline) only the scattered light from the shell's far side (i.e. behind the star) can be detected. The scattered line profile can be red-shifted, broadened and it can have extended red wings (Rao et al. 1999), so that it differs from the normal photospheric absorption. A red shift of a few km s^{-1} with respect to the photospheric velocity was first recorded by Payne-Gaposchkin (1963).

The evolution of the majority of strong photospheric absorption lines during the 1998 decline of V854 Cen was difficult to follow using the MRS spectra, due to blending with other lines. The low-excitation lines are significantly blended with strong sharp emission components (E_2). Only the high-excitation lines, such as SiII, OI and SI, with the excitation potential of the upper level of $\chi_{\mathrm{U}} \geq 10$ eV can be monitored, after the disappearance of their short-lived emission (E_1). This emission was observed in high-resolution spectra of some well isolated spectral lines of SiII. The high-resolution spectra of SiII 6347.1 Å and 6371.4 Å lines during the initial phase and the minimum of decline II (day numbers: $+28$, $+52$ and $+54$, Figures 3.48 and 3.49) show a weak emission superimposed on the absorption profile. The emission disappears after a few weeks and is probably responsible for the filling in of some of the photospheric absorption lines at the initial decline phase. Since the present coverage does not include any spectra from the deepest minimum of decline III, no red-shift of the photospheric absorption lines, previously noticed in some other RCB declines (Payne-Gaposchkin 1963; Rao et al. 1999), nor any significant broadening, has been observed.
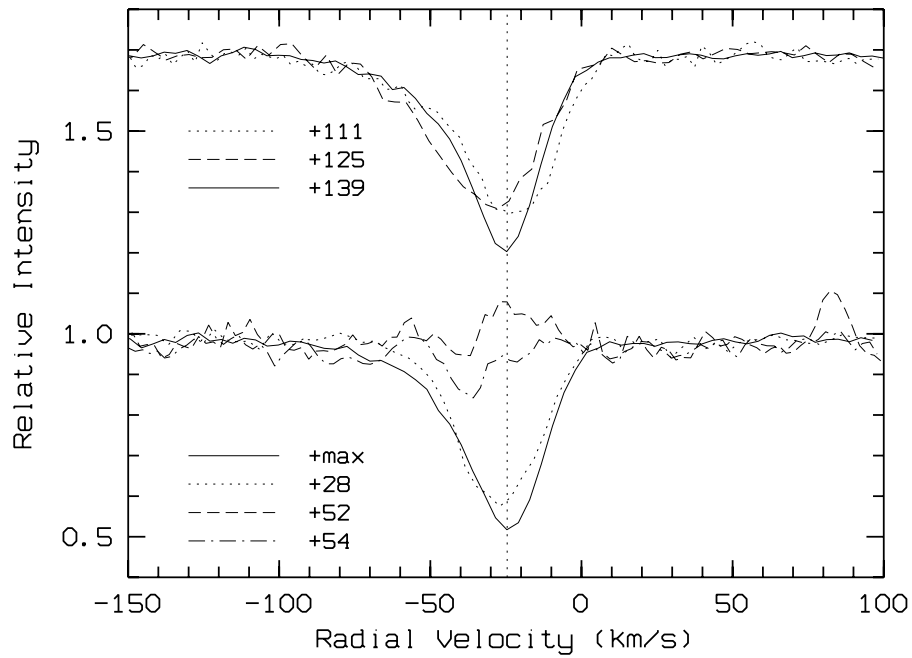
Figure 3.48: *High-resolution spectra around SiII 6347.1 Å throughout the initial and deep decline phases (day numbers +28, +52 and +54) and recovery phase (+111, +125 and 139).*
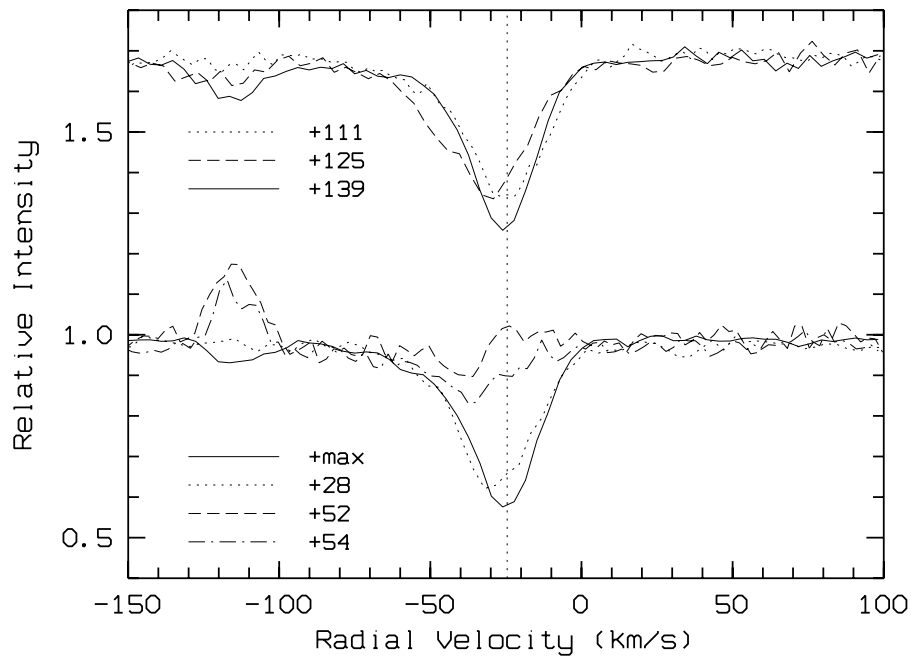
Figure 3.49: *High-resolution spectra around SiII 6371.4 Å throughout the initial and deep decline phases (day numbers +28, +52 and +54) and recovery phase (+111, +125 and 139).*

The MRS spectra from the early recovery phase (day number +104), when the star was at a magnitude of about $12^{\text{m}}.5$, show that the equivalent widths of the same two SiII spectral lines (6347.1 Å and 6371.4 Å, $W_\lambda = 0.20$ Å and 0.16 Å respectively) were at a level of about 55% of the corresponding maximum photospheric equivalent width ($W_\lambda = 0.36$ Å and 0.29 Å). A small weakening of the spectral lines can also be noticed during the recovery phase (day numbers: +111 and +125, Figures 3.48 and 3.49). By day number +139 the normal photospheric lines reappear. The radial velocity of both lines throughout the observed part of the decline remains at approximately the photospheric velocity: $-(25 \pm 2)$ km s^{-1}. This does not include the +52 and +54 spectra, when the lines are blended with emission.

A similar evolution was observed for the OI 6158.2 Å line and OI triplet (Figure 3.25), although the temporal coverage of these lines throughout the decline was not complete. Also, the filling in of SI lines (6743.5 Å, 6748.8 Å and 6757.1 Å) can be noticed, in spite of blending by some CI spectral lines.

This analysis of various groups of spectral lines appearing in spectra of V854 Cen concludes the discussion of the 1998 decline of this star, involving the observations made for this thesis. A presentation of the declines of other RCB stars is given in the next chapter.

Chapter 4

Declines of some other RCB stars

Apart from the three brightest RCB stars (R CrB, RY Sgr and V854 Cen), there have not been many observations in the literature covering the decline phases of these stars. The majority of RCB stars are fainter then 9^m at light maximum, so that they are relatively difficult to observe spectroscopically, especially during the deepest decline phase. Most of the papers published on the fainter RCB stars are on their chemical composition (Bond et al. 1979, Lambert & Rao 1994) and photometric characteristics (Lawson et al. 1990) at light maximum. However, some sporadic observations of faint RCB declines can be found. One such observation is a high-resolution spectrum of S Aps during the 1993 decline (Goswami et al. 1997). The spectrum shows a number of emission features, including the NaI D and HeI 7065 Å lines.

In this chapter spectroscopic observations of a cool RCB star, S Aps, and a number of typical RCB stars (RZ Nor, RS Tel, UW Cen and V CrA) during their recent declines will be presented. All stars are between 9^m and $10\overset{m}{.}5$ at light maximum. During the observing programme of this thesis, a number of declines of these stars were observed. They all differed in their depth and duration. However, a similar spectroscopic behaviour, especially around the NaI D lines, was detected. The results on the 1996/97 decline of S Aps and 1997 decline of RZ Nor have already been published (Skuljan & Cottrell 1999).

4.1   S Apodis

S Aps had not fully recovered (to its normal maximum brightness of $V \sim 9.8$) from its previous decline when it went into decline on JD 2450300 from a magnitude of $V \sim 11$ (1996 August). It reached a minimum magnitude of $V \sim 15$ ($\Delta V \sim 6$) about 40 days after decline onset and recovered to its maximum light magnitude ~ 300 days later.

Medium, medium-low and low resolution spectra of S Aps were obtained between 1996 April 23 and 1997 September 12, covering its latest deep decline (see Figure 4.1 and Tables 4.1–4.2). Five échelle spectra were obtained on 1997 August 29, 30 and 31 when the
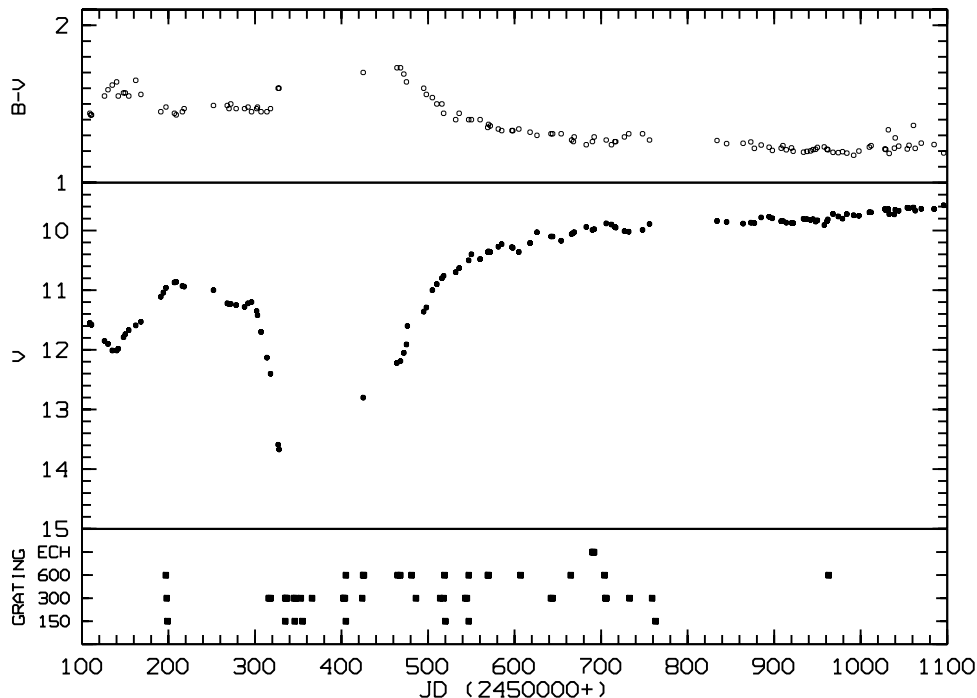
Figure 4.1: *V magnitude and colour changes of S Aps and the times at which spectroscopic observations were obtained.*

star was close to its light maximum. The observations continued until 1997 November with no change in the spectrum.

Figure 4.2 shows MRS spectra of S Aps at its light maximum, as well as a high resolution échelle spectrum. Strong C_2 Swan system bands are the main feature of the S Aps spectra at light maximum.

This cool RCB star has lots of molecular bands, which make the determination of the continuum very difficult. To normalize the spectra of S Aps the continuum of some standard radial velocity stars (of similar spectral types) have been used. However the continuum level (set to 1 on the intensity scale) cannot be defined well, especially with higher resolution spectra covering relatively short wavelength regions. In this case the maximum flux within the order has been taken as the unit continuum level.

The main decline onset (JD 2450300 is defined as day number 0) has been determined from the photometry (see Figure 4.1). This zero point has been used instead of Julian Dates to mark spectra and compare them to each other. At the beginning of the main decline the brightness was already $1^m\!.4$ below the average maximum of $\sim 9^m\!.8$. In fact the brightness was slowly decreasing (from $10^m\!.8$ to $11^m\!.2$) over a period of about 90 days prior to the main decline.

Low resolution spectra of S Aps throughout the decline phase are shown in Figure 4.3. Compared to the light maximum (+247d), the pre-decline spectrum (−102d) shows no major

Table 4.1: *Summary of spectroscopic observations of the 1996/97 decline of S Aps: JD –*
Julian Day (2450000+), Day No. – number of days after JD 2450300, m_v – V magnitude,
S/N – signal to noise ratio in the continuum. MRS spectra are used, unless noted otherwise.

Date (UT)	JD	Day No.	Spectral range (Å)	m_v	S/N	Comments
1996						
Apr 23	0197.1	−103	5750 − 6270	10.9	67	recovery phase of the small predecline.
Apr 24	0198.0	−102	5800 − 6800	10.9	90	HVA* can be noticed.
Apr 24	0198.1		3800 − 4500	10.9	20	weak CaII H & K emission remains.
Apr 25	0199.1	−102	5000 − 7200	10.9	65	normal photospheric spectrum (except NaI D lines).
Aug 20	0315.9	16	5650 − 6700	12.2	75	NaI D emission appears. filling in of molecular bands (30%).
Sep 08	0334.9	35	5200 − 7200	15.0	9	C_2 molecular bands visible.
Sep 18	0345.1	45	5700 − 6700	15.0	4	strong NaI D emission.
Sep 19	0346.1	46	5200 − 7200	15.0	10	C_2 molecular bands visible.
Sep 20	0347.0	47	5700 − 6700	15.0	20	C_2 molecular bands visible.
Oct 10	0366.0	66	5700 − 6700	15.0	5	NaI D emission decaying.
Nov 15	0403.0	103	5700 − 6700	13.5	32	NaI D emission visible.
Nov 17	0405.0	105	5750 − 6250	13.5	27	HVA ($\sim -250\ \mathrm{km\,s^{-1}}$) appears.
Nov 17	0405.1	105	5200 − 7200	13.5	40	photosphere reappears ($\sim 100\%$).
Dec 06	0423.9	123	5700 − 6700	12.7	150	normal photospheric absorption.
Dec 08	0425.9	126	5250 − 6250	12.7	80	weak NaI D emission, strong HVA.
1997						
Jan 16	0465.1	165	5750 − 6250	12.1	50	weak NaI D emission, strong HVA.
Jan 19	0467.9	168	5250 − 5750	12.1	50	normal photospheric absorption.
Feb 01	0480.9	181	5750 − 6250	11.7	90	HVA decaying, no NaI D emission.
Mar 06	0512.2	212	5750 − 6700	10.8	90	normal stellar absorption.
Mar 10	0517.9	218	3800 − 4500	10.8	38	weak CaII H & K emission remains.
Mar 11	0519.0	219	5250 − 7250	10.8	60	HVA ($\sim -300\ \mathrm{km\,s^{-1}}$) decaying.
Apr 06	0544.9	245	3800 − 4500	10.5	35	normal stellar CaII H & K absorption.
Apr 08	0547.0	247	5200 − 7200	10.5	150	normal photospheric spectrum.
Apr 08	0547.1	247	5750 − 6250	10.5	43	HVA weakening.
Apr 30	0568.9	269	3800 − 4200	10.4	16	as for Apr 6.
Apr 30	0568.9	269	5750 − 6250	10.4	100	stellar NaI D absorption only, no HVA.
Jun 07	0606.9	307	5750 − 6250	10.3	150	normal photospheric spectrum.

* High-velocity blue-shifted NaI D absorption.

Table 4.2: *Summary of spectroscopic observations of the 1996/97 decline of S Aps (continued).*

Date (UT)	JD	Day No.	Spectral range (Å)	m_v	S/N	Comments
1997						
Jul 12	0641.9	342	5750 – 6700	10.1	150	as for Jun 7.
Aug 04	0665.2	365	5750 – 6250	10.0	90	as for Jun 7.
Aug 29	0689.9	390	5430 – 8500	9.9	55	high resolution échelle spectra.
Aug 30	0691.1	391	5430 – 8500	9.9	60	as for Aug 29.
Aug 31	0691.9	392	5430 – 8500	9.9	85	as for Aug 29.
Sep 12	0704.0	404	5250 – 7250	9.8	110	as for Jun 7.
Sep 14	0706.0	406	3800 – 4500	9.8	32	as for Apr 6.
Nov 6	0758.9	459	5750 – 6700	9.8	60	as for Jun 7.
Nov 10	0763.0	463	5200 – 7200	9.8	80	as for Jun 7.

difference. On the other hand extremely strong NaI D emission lines dominate the deep decline spectrum (+46d). A time series of the rise and decay of NaI D emission lines can be seen in Figure 4.4.

Compared to the maximum light spectrum the C_2 Swan molecular bandheads show filling in by about 30% on day +16. However some of the main band heads (0-2 and 1-3) were visible in absorption even at the deepest minimum (Figure 4.4, spectrum +47d). Some changes in the structure of deep decline bandheads (+47d spectrum), compared to the maximum light spectrum, can be noticed as well. Unfortunately, the Swan system 0-0 (5165 Å) and 0-1 (5636 Å) cannot be seen due to the low S/N in the spectra obtained for this study. They have been reported in emission during the deep declines of V854 Cen (Whitney et al. 1992; Rao & Lambert 1993). On the other hand the 0-2 and 1-3 heads are not seen in emission in our deep decline spectra. However, S Aps is a cool RCB star with T_{eff} ~5000 K (Lawson et al. 1990) and this may mean that the Swan system's upper vibrational states are not sufficiently populated for these weak bands to be seen in emission. Normal strength photospheric molecular bands and continuum had reappeared by the +103d spectrum (Figure 4.4).

Because of the lower S/N and resolution of the deep decline spectra no narrow line emission features (e.g. BaII and ScII) are seen. A similar argument can be applied to the broad emission. These lines in S Aps can only be at a low level as with the strong molecular absorption bands, our low resolution and low S/N deep decline spectra do not clearly show that these lines exist.
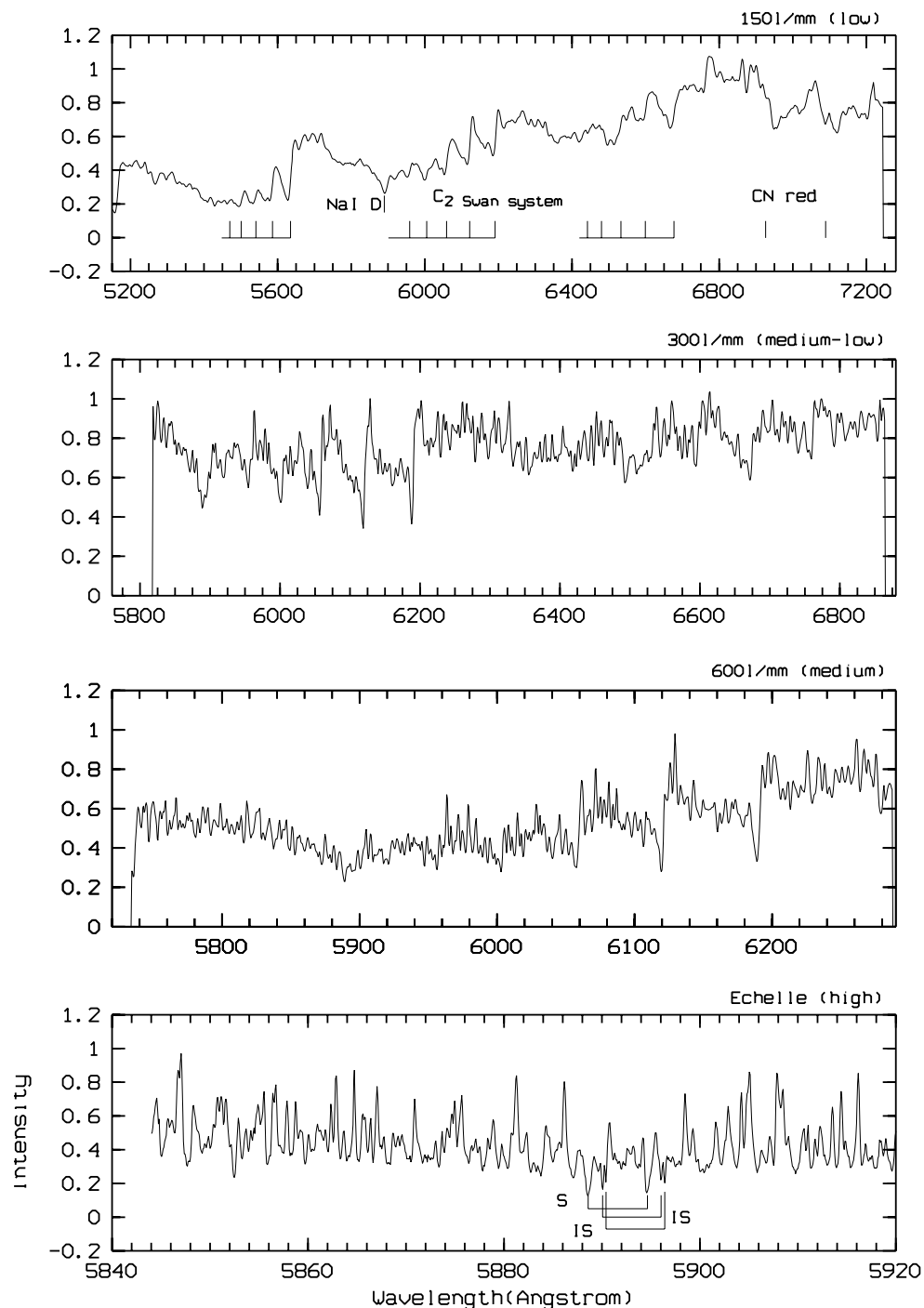
Figure 4.2: *Comparison between the MRS (150, 300, 600 l mm^{-1}) and échelle maximum light spectra of S Aps in the wavelength region 5200 Å to 7200 Å. First spectrum on the top shows the C_2 Swan molecular bands and some components of the CN red system. Note the multi-component structure in the NaI D lines in the échelle spectrum: S (stellar components) and IS (interstellar components).*
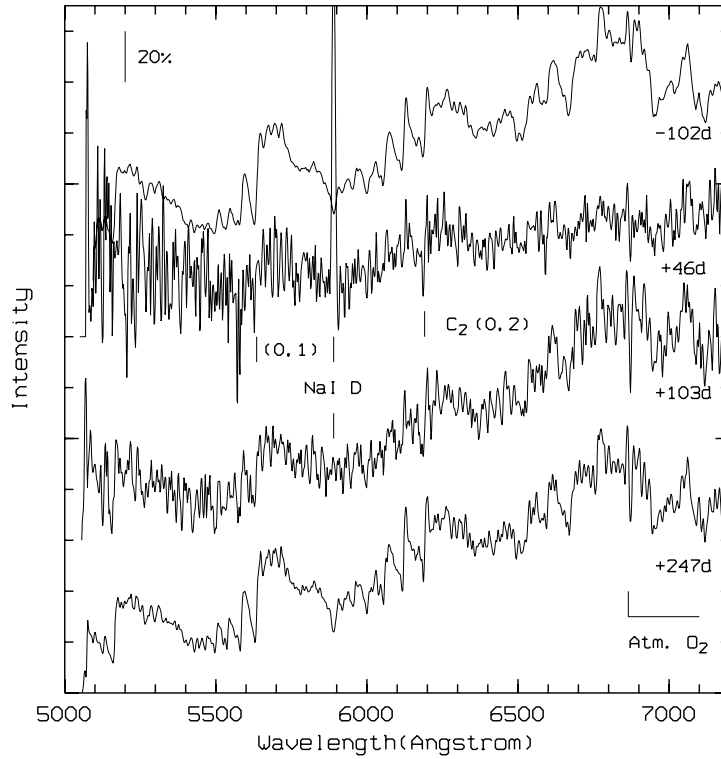
Figure 4.3: *Low resolution spectra of S Aps. NaI D emission lines from the deep minimum (+46d) and recovery phase (+103d) are marked. The main bandheads of C_2 (0,2) can be seen. The position of the (0,1) bandhead is also marked, but its identification is uncertain due to the low S/N for wavelengths less than 5700 Å. The strong atmospheric O_2 region is marked at about 7000 Å.*
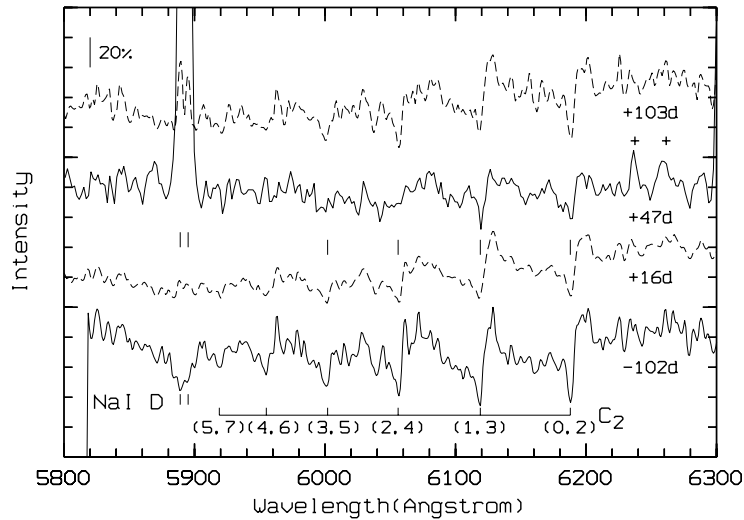
Figure 4.4: *The medium-low resolution S Aps spectra show time series of the spectral evolution of region between 5800 Å and 6300 Å. The positions of the NaI D lines, C_2 molecular bands and sky lines (+) are marked.*

NaI D lines during the decline

The most prominent features in the deep decline spectra (days 35–66) are the NaI D emission lines. We assume that our NaI D profiles are similar to those in the high resolution spectra of S Aps (Goswami et al. 1997) and other RCB stars (Cottrell et al. 1990; Rao & Lambert 1993). Unfortunately broad and narrow emission features of the NaI D lines cannot be separated in our MRS spectra at the deepest minimum. Our estimate of any broad NaI D emission is less than 10% of the continuum.

In our study the peaks of the NaI D emission lines have about the same radial velocity as the star itself (-75 ± 2) km s^{-1} (see Table 4.3) and they probably correspond to chromospheric emission lines. Given the resolution of our spectra we are not able to measure any small scale ($\sim$ few km s^{-1}) blue shift in these lines compared to the photospheric components.

The equivalent width of these emission features is approximately (25 ± 4) Å for the D_2 (5890 Å) and (17 ± 2) Å for D_1 (5896 Å) components on day +47. The flux ratio of D_2 to D_1 is 3:2 (with a relative error of about 20%), similar to that obtained by Asplund (1995) for RY Sgr. Due to this uncertainty it is not possible to distinguish between whether these lines are forming in a purely optically thin (2:1) or optically thick (1:1) environment.

It is not clear when the weakening of NaI D emission features started. However, it is obvious that the NaI D emission flux was approximately half its peak flux by day +66 ($W_\lambda \sim 15$ Å and 11 Å for D_2 and D_1 respectively). Day +103 spectra show the reappearance of the normal photospheric spectrum (Figure 4.4), but NaI D emission features are still visible out to day +160.

In order to emphasize the changes around the NaI D lines a standard spectrum (+404d) has been subtracted from all the other spectra as shown in Figure 4.5. Before the subtraction all normalized spectra were lined up so that they all have the same radial velocity as the maximum light spectrum. A pair of high velocity blue-shifted absorption components can be seen in the residual spectra even in the -102d spectrum. The -102d residual spectrum appears to be the same as those from the main recovery phase when the star has a similar magnitude (spectra +219d and +247d).

The high-velocity absorption (HVA) first appears on about day +105, when the chromospheric emission components have decayed and the photospheric spectrum has reappeared (Figure 4.5). They are not seen in the +16d spectrum, at least not at the position of about -200 km s^{-1}. The high-velocity absorption has disappeared by day +269.

The equivalent width of the stronger blue shifted NaI D component (D_2) shows that the line decays by a factor of approximately three between days +165 and +247 ($W_\lambda \sim 0.6$ Å and 0.2 Å respectively). The line ratio D_2/D_1 shows that these components are formed in an approximately optically thin region.

The centre of the D_2 component appears to be shifted from about -250 km s^{-1} (day +105) to -300 km s^{-1} (day +219) assuming that these lines originate from the same material.
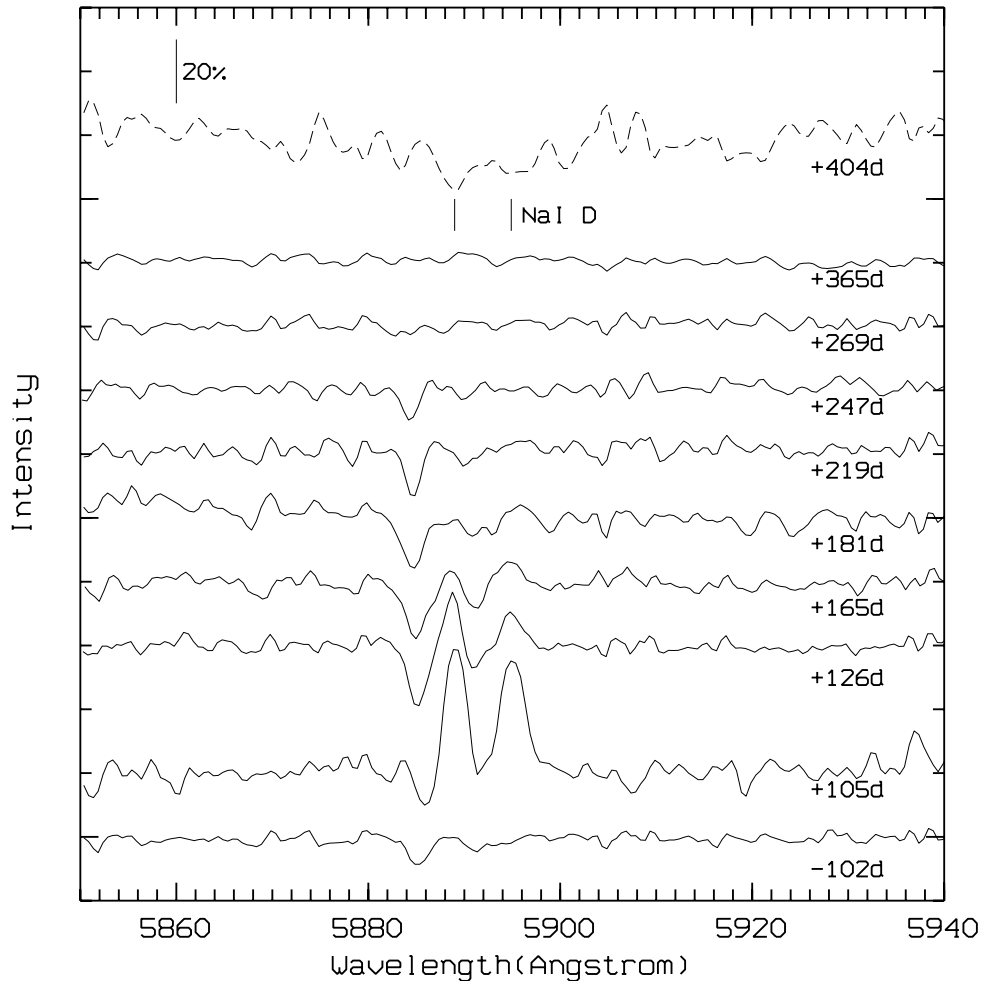
Figure 4.5: *The evolution of the residual spectra of S Aps around the NaI D lines throughout the decline. The high-velocity blue-shifted absorption and the emission are visible. The dashed spectrum (+404d) is the maximum light spectrum which has been subtracted from all the other spectra. Positions of the absorption NaI D lines are marked. Note a shift of the high velocity absorption between day +105 and +219.*

This material moves away from the star with an acceleration of about 50 km s^{-1} in 120 days ($\sim 0.5 \text{ cm s}^{-2}$). If we assume a constant acceleration, the material would have moved a distance of at least $5 R_*$ ($R_* \approx 80 R_\odot$) at this latest time (+219d) relative to the position on day +105, depending on the starting velocity. The high velocity component on day +105 is blended with emission lines causing more uncertainty in the determination of its line centre. Taking into account this blending, it is possible that the absorption is less blue-shifted than it appears on the spectrum and this would lead to a bigger acceleration. Assuming that the strongest NaI D emission peak decays from about day +55, the position of the emitting region has been estimated to be about $3 R_*$, taking into account that the dust cloud was formed at about $2 R_*$.

High resolution spectra

Radial velocities for some of the absorption lines in the high-resolution spectra of S Aps are presented in Table 4.3. The wavelengths have been taken from Moore (1972), Moore et al. (1966) and Reader & Corliss (1980). Gaussian profiles have been fitted to the spectral lines in order to find the line centres. The NaI D lines are blended with C_2 Swan and CN red system lines causing a larger uncertainty (~ 3 km s^{-1}) in measuring the velocity of these lines. The radial velocity of stellar and interstellar NaI D components are the mean velocity from five S Aps échelle spectra with $\sigma \sim \pm 1$ km s^{-1}, but mean stellar radial velocity determined from other lines (Table 4.3) is $-(75 \pm 2)$ km s^{-1}. The cause of the discrepancy (~ 10 km s^{-1})

Table 4.3: *Radial velocities for some absorption lines of S Aps at maximum using the échelle spectra.*

Line (multiplet)	λ [Å]	V_r km s^{-1}	Comments
CaI (21)	5588.757	-75.3	
CaII (2)	8498.018	-76.7	
CaII (2)	8542.089	-77.9	
FeI (62)	6219.290	-77.3	
FeI (168)	6393.605	-75.0	
FeI (816)	6336.835	-77.1	
FeI (1001)	7418.674	-75.7	
NiI (84)	7385.24	-73.2	
NiI (139)	7422.30	-73.1	
NiI (292)	7381.94	-75.4	
TiI (97)	7357.74	-72.4	
TiII (91)	6559.580	-74.6	
	Mean:	-75 ± 2	
NaI D (1)	5889.97	-10.7	interstellar*
NaI D (1)	5889.97	$+4.8$	interstellar*
NaI D (1)	5889.97	-86.8	stellar*
NaI D (1)	5895.94	-10.5	interstellar*
NaI D (1)	5895.94	$+7.7$	interstellar*
NaI D (1)	5895.94	-83.6	stellar*

* Blended with C_2 Swan system.

between the NaI D lines and other metallic lines is uncertain, but it could be due to the existence of some chromospheric NaI D components distorting the absorption line profile.

4.2   RZ Normae

The 1997 decline of RZ Nor was of relatively short duration and depth (110 days and two magnitudes, respectively), compared to the S Aps decline. The decline began on about JD 2450485 and reached its minimum magnitude about 40 days later.

MRS spectra of RZ Nor were obtained between 1996 April 23 and 1997 November 6, covering its latest shallow decline (see Table 4.4 and Figure 4.6).
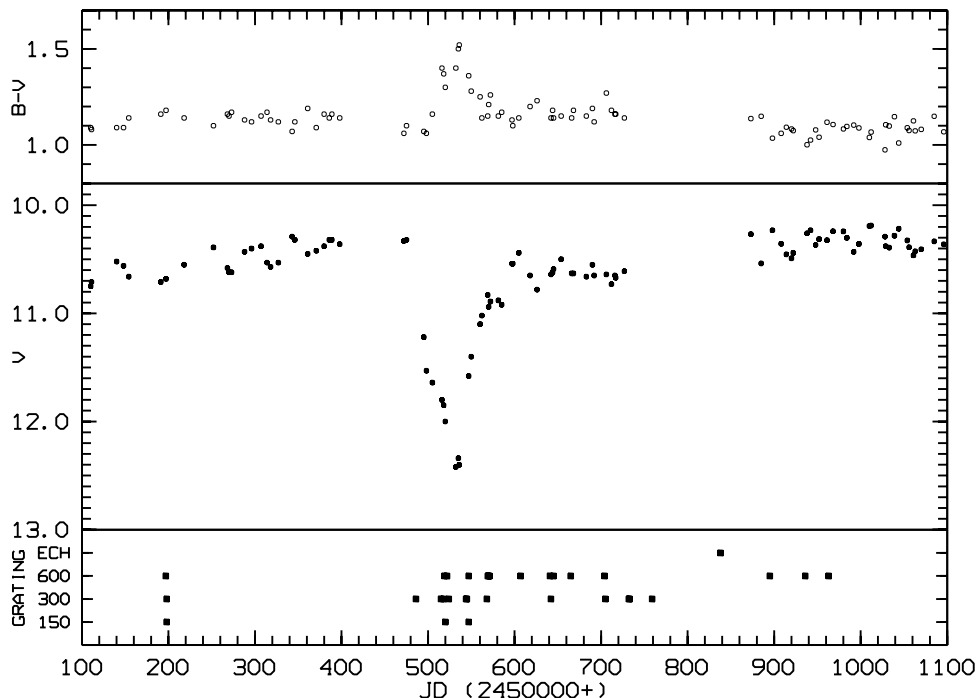
Figure 4.6: *V magnitude and colour changes of RZ Nor and the times at which spectroscopic observations were obtained.*

High resolution échelle spectra were collected when the star was already at the light maximum, about 353 days after the beginning of the decline. A total of three spectra of one-hour exposure duration each on 1998 January 24 were combined to increase the signal-to-noise ratio.

Decline onset time has been estimated using available photometry. Initial decline photometry was obtained when the star was already $0\overset{m}{.}6$ below the average pulsation minimum $(10\overset{m}{.}6)$ on JD 2450495. The star was still around the maximum light 22 days earlier, on JD 2450473, so the decline must have started somewhere in between these two dates. According to some previous well covered initial decline light curves of RZ Nor it takes approximately

Table 4.4: *Summary of spectroscopic observations of the 1997 RZ Nor decline: JD – Julian Day (2450000+), Day No. – number of days after JD 2450485, m_v – V magnitude, S/N – signal to noise ratio in the continuum. MRS spectra are used, unless noted otherwise.*

Date (UT)	JD	Day No.	Spectral range (Å)	m_v	S/N	Comments
1996						
Apr 23	0197.2	−287	5750 − 6270	10.7	50	predecline spectrum.
Apr 24	0198.1	-288	5000 − 7200	10.7	55	normal photospheric spectrum.
1997						
Feb 06	0486.1	+1	5800 − 6800	10.9	37	normal photospheric spectrum.
Mar 07	0514.1	+29	5800 − 6800	11.8	33	NaI D emission lines.
Mar 10	0518.1	+33	5800 − 6800	11.8	50	HVA* (~ -280 km s^{-1}) visible.
Mar 11	0519.0	+34	5750 − 6270	11.9	51	weaker NaI D emission, strong HVA.
Mar 12	0520.0	+35	5200 − 7000	11.9	80	no filling in of spectral lines.
Mar 14	0522.1	+37	5750 − 6270	12.0	110	strong HVA.
Mar 16	0523.9	+39	5800 − 6800	12.1	40	faint NaI D emission.
Apr 05	0544.2	+59	5800 − 6800	11.8	103	strong HVA, weak NaI D emission.
Apr 08	0547.1	+62	5750 − 6270	11.6	65	strong HVA.
Apr 08	0547.1	+62	5000 − 7200	11.6	65	normal photospheric spectrum (except NaI D lines).
Apr 30	0569.1	+84	5750 − 6270	11.0	114	HVA (~ -330 km s^{-1}) decaying.
Jun 07	0607.0	+122	5750 − 6270	10.5	110	no HVA normal photospheric spectrum.
Jul 11	0641.1	+156	5750 − 6270	10.6	40	normal photospheric spectrum.
Aug 04	0665.2	+180	5750 − 6270	10.6	110	↓
Sep 12	0703.9	+219	5750 − 6270	10.7	45	↓
Oct 10	0731.9	+247	5800 − 6800	10.7	110	↓
Nov 06	0758.9	+274	5800 − 6800	10.5	75	↓
1998						
Jan 24	0838.0	+353	5430 − 8500	10.5	50	high resolution échelle spectra.

* High-velocity blue-shifted NaI D absorption.

10 days for the star to fade by 0^{m}6. Therefore, we define day number 0 as JD 2450485 with an uncertainty of about 5 to 10 days for this 'red' type decline (Cottrell et al. 1990).

MRS spectra of RZ Nor during this shallow decline show no major differences compared to the maximum light spectrum, except for the NaI D lines. All decline spectra have been compared with those from the light maximum taken before and after the decline. Low resolution spectra of RZ Nor on days −287, +34 and +62 are shown in Figure 4.7. These
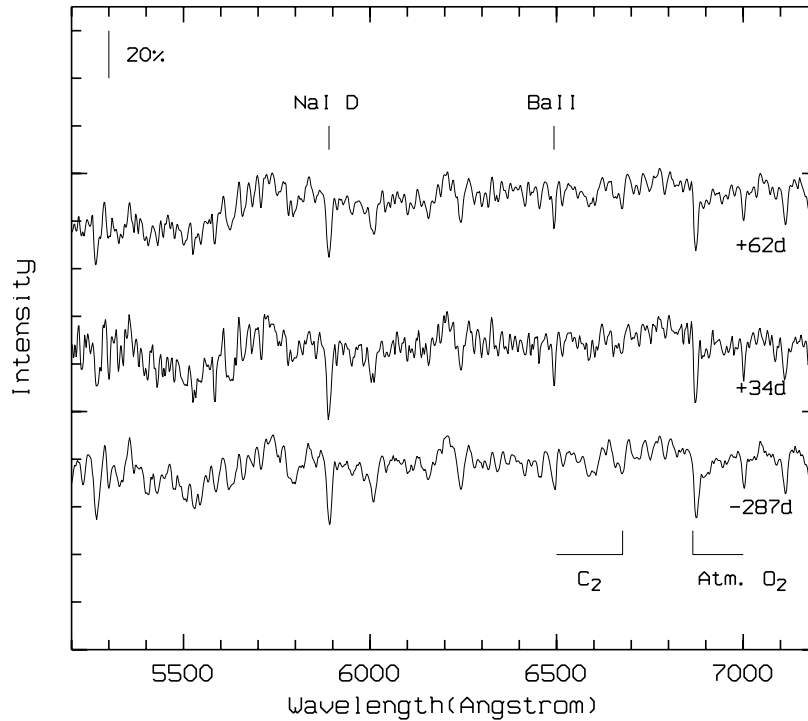
Figure 4.7: *Low resolution spectra of RZ Nor before and during the decline. The positions of the C_2 Swan system bandheads, as well as the NaI D and BaII lines, are marked.*

spectra do not show filling-in of the spectral lines during the decline phase. In fact, BaII spectral lines (6141.7 Å and 6496.9 Å) have been identified in the medium resolution spectra and monitored during the decline. They do not show any changes.

NaI D lines during the decline

The evolution of NaI D lines in RZ Nor spectra throughout the decline is shown in Figure 4.8.

No visible NaI D emission (as seen in the deep decline S Aps spectra) can be noticed here due to the strong photospheric absorption. However, it is obvious that the depth of the NaI D lines is changing, as well as the depth of a line at 5883.8 Å (a feature on the left side of the NaI D lines). In order to emphasize these changes the same procedure used for S Aps has been performed on these RZ Nor spectra. The residual spectra are shown in Figure 4.9.

After subtraction of the NaI D photospheric absorption lines, NaI D emission and blue-shifted absorption remain. They are obvious in the +34d and +62d spectra. Some medium-low resolution spectra on day +29 (not shown in Figure 4.9) indicate that the emission lines on day +34 are already decaying. They may still remain on day +62, although the two broad bumps on the spectrum could correspond to the NaI D broad emission components as well.

It should be mentioned that the high resolution spectra show very complicated structure
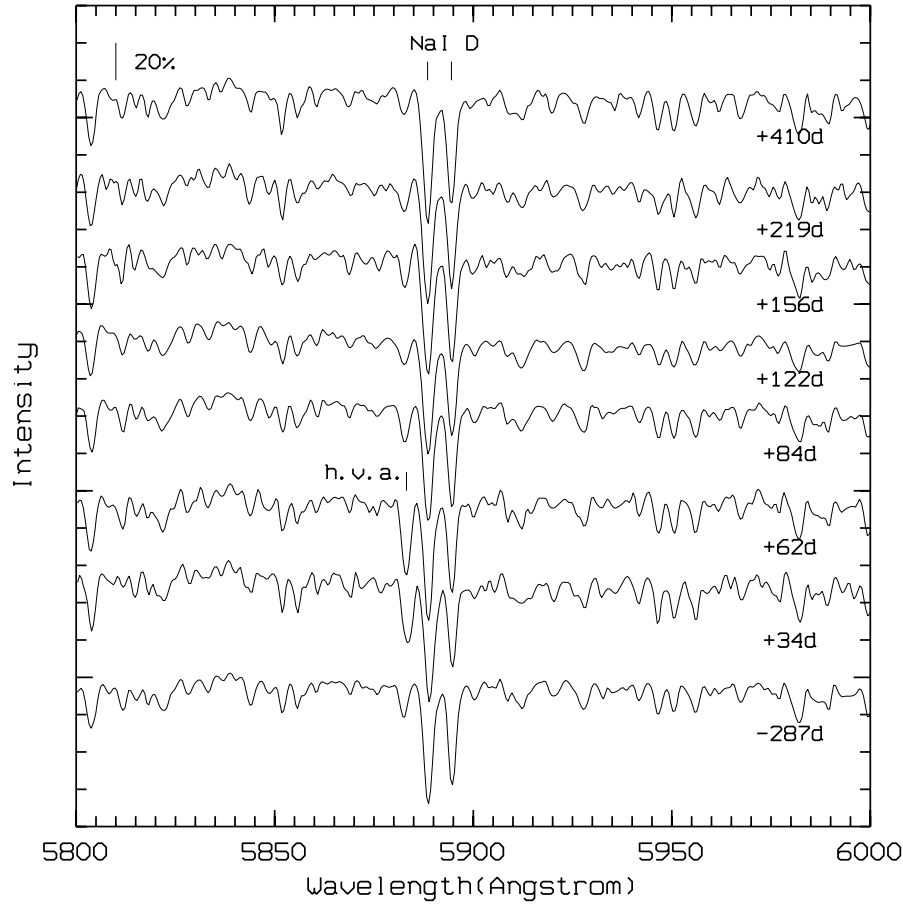
Figure 4.8: *The medium resolution RZ Nor spectra show the evolution of NaI D lines throughout the decline. Positions of NaI D absorption lines and the high-velocity absorption (HVA) components are marked.*

around the NaI D lines. Because of the strong NaI D interstellar components at -46 km s^{-1}, the NaI D peaks in the medium resolution spectra do not correspond to the stellar components exactly. In fact, an average radial velocity derived from medium resolution spectra using the NaI D lines is $-(47 \pm 5)$ km s^{-1}, which is closer to the interstellar component. This is the reason why any relative shifts between the emission and absorption NaI D lines, visible in Figure 4.9, do not represent a real velocity difference between the chromospheric emission and photospheric absorption.

A high-velocity blue-shifted NaI D absorption (HVA) component is found in the RZ Nor decline (Figure 4.9), similar to that seen in S Aps (Figure 4.5). It is seen on day $+29$ and disappears by day $+122$. The equivalent width of the stronger HVA component (D_2) shows that the line is about constant between the days $+34$ and $+62$ and then decays by a factor of two between days $+62$ and $+84$ ($W_\lambda \sim 0.9$ Å and 0.4 Å respectively). The centre of the D_2 component appears to be shifted from about -280 km s^{-1} (day $+34$) to -330 km s^{-1} (day $+84$). This indicates that the obscuring material is moving away from the star with
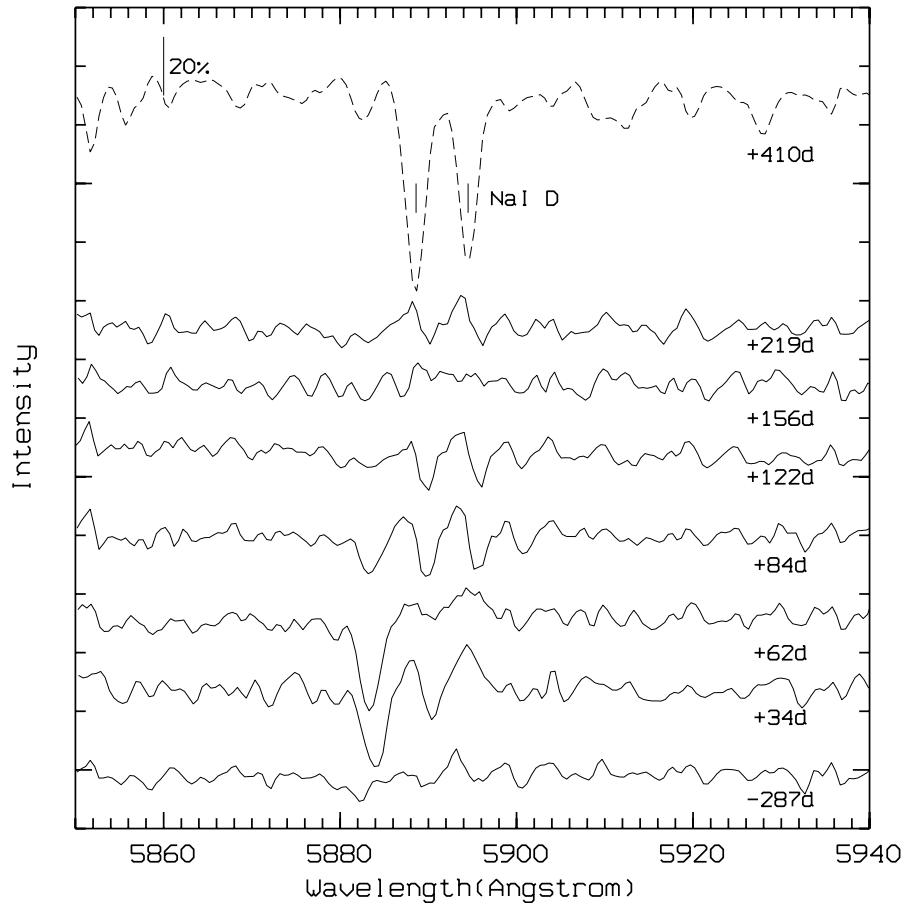
Figure 4.9: *The evolution of the residual spectra of RZ Nor around NaI D lines throughout the decline. The high velocity blue shifted absorption and the emission are visible. The dashed spectrum (+410d) is the maximum light spectrum which has been subtracted from all the other spectra represented in Figure 4.8. Positions of the absorption NaI D lines are marked. Note a shift of the high velocity absorption between day +34 and +84.*

an acceleration of about 50 $\mathrm{km\,s^{-1}}$ in 50 days (~ 1 $\mathrm{cm\,s^{-2}}$). During that time a dust cloud would move a distance of at least $3\,R_*$ ($R_* \approx 60\,R_\odot$) by day +84 relative to its position from the day +34. The significant interstellar reddening for RZ Nor (Lawson et al. 1990) has been taken into account in calculating R_*. Using the acceleration of ~ 1 $\mathrm{cm\,s^{-2}}$, and the fact that the NaI D emission decays from day +30, the position of the emitting region has been estimated to be about the same as for S Aps ($\sim 3\,R_*$).

Some additional red-shifted absorption features are seen in spectra from day +84 and +122. They can hardly be explained by noise since they appear on both spectra with a relatively low noise level in regions surrounding the NaI D lines. They could be as a result of broad emission distorting the normal photospheric spectrum.

High resolution spectra

Radial velocities for some of the absorption lines in the high-resolution spectra of RZ Nor are presented in Table 4.5. Gaussian profiles have been fitted to the spectral lines in order

Table 4.5: *Radial velocities for some absorption lines of RZ Nor at maximum using the échelle spectra.*

Line (multiplet)	λ [Å]	$V_{\rm r}$ $\mathrm{km\,s^{-1}}$
CI	6006.061	−73.9
CI	6010.650	−71.4
CI	6013.199	−71.6
CI	6014.842	−72.8
CaI (21)	5588.757	−75.1
CaI (21)	5594.468	−74.2
CaI (21)	5598.487	−75.1
BaII (2)	5853.675	−70.6
MgI (8)	5711.091	−72.2
SI (8)	6743.580	−73.4
SI (8)	6748.790	−74.1
SI (8)	6757.160	−73.2
MnI (27)	6021.802	−73.2
FeI (15)	5434.527	−69.9
FeI (62)	6213.438	−72.6
FeI (111)	6750.152	−72.0
FeI (168)	6393.605	−72.0
FeI (816)	6232.661	−73.7
FeI (1018)	6027.057	−73.5
FeI (1178)	6024.066	−73.7
FeI (1180)	5862.357	−70.8
FeI (1181)	5859.608	−74.3
FeI (1260)	6170.492	−70.3
NiI (57)	6767.778	−73.9
NiI (127)	6772.360	−72.6
Mean:		−73 ± 1

Table 4.6: *Radial velocities for various components of NaI D lines of RZ Nor at maximum using the échelle spectra.*

Line (multiplet)	λ [Å]	V_r km s^{-1}	Comments
NaI D (1)	5889.97	-16.4	interstellar
NaI D (1)	5889.97	$+1.4$	interstellar
NaI D (1)	5889.97	-46.4	interstellar
NaI D (1)	5889.97	-79.5	stellar
NaI D (1)	5895.94	-17.4	interstellar
NaI D (1)	5895.94	$+0.9$	interstellar
NaI D (1)	5895.94	-46.3	interstellar
NaI D (1)	5895.94	-77.1	stellar
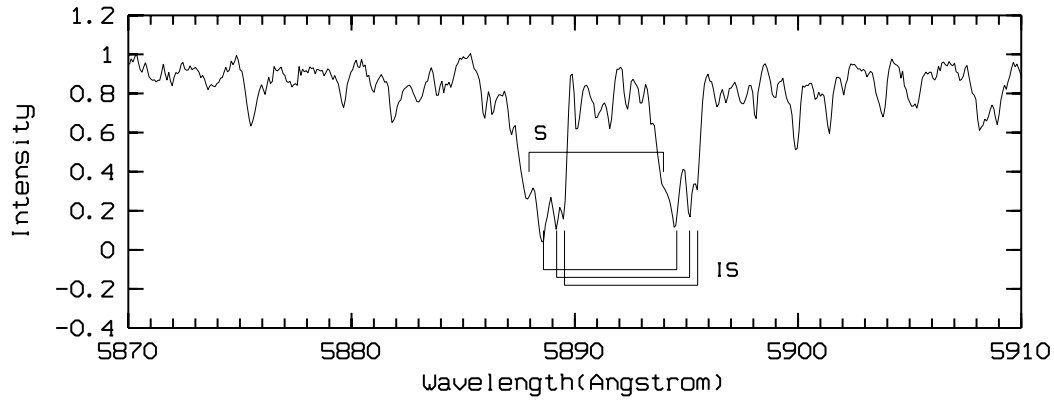
Figure 4.10: *The high resolution échelle spectrum of RZ Nor around the NaI D lines. Note the three interstellar (IS) and one stellar (S) NaI D components.*

to find the line centres.

Radial velocities of the NaI D components are given in Table 4.6. According to the galactic position of RZ Nor ($l = 332°$ and $b = -4°$) it is expected that the NaI D lines are blended with a number of interstellar components (see Figure 4.10).

Several Gaussian profiles have been fitted to the NaI D lines in order to find more precise positions of the stellar components. They give a radial velocity of about -78 km s^{-1}, which is blue shifted relative to the velocity determined from other spectral lines (the other lines give a mean value of -73 ± 1 km s^{-1}, as found from Table 4.5). A similar disagreement was also found in S Aps spectra and may indicate the existence of some additional NaI D components with a strong blending effect.

4.3   RS Telescopii

RS Tel was observed partially throughout two of its declines (1996 and 1997). The 1996 decline was about two magnitudes deep. Some maximum-light spectra were collected prior to this fading, as well as some decline spectra during the late recovery phase. The 1997 decline was only about one magnitude deep and was covered completely (Figure 4.11). The decline began on about JD 2450600 (as estimated from the photometry) and finished about 160 days later.

Figure 4.11: *V magnitude and colour changes of RS Tel and the times at which spectroscopic observations were obtained.*

Medium-resolution spectra of RS Tel were obtained between 1996 April 24 and 1998 October 23 (see Table 4.7 and Figure 4.11). A high-resolution échelle spectrum was collected when the star was already close to the light maximum during the late recovery phase of the 1997 decline. A low resolution spectrum at the light maximum is shown in Figure 4.12.

All decline spectra have been compared with those from the light maximum taken before and after the decline. They do not show any significant differences from the maximum-light spectra. Similar to the shallow decline of RZ Nor, no filling in of spectral lines was noticed during the 1997 decline, except for the NaI D lines. The NaI D components exhibit some changes in the line depths during the 1997 decline (Figure 4.13), but no visible emission. On the other hand, the high-velocity blue shifted absorption was not seen either in the recovery phase of the 1996 decline, or during the entire 1997 decline. These lines could

Table 4.7: *Summary of spectroscopic observations of the 1996 and 1997 declines of RS Tel:*
JD – Julian Day (2450000+), Day No. – number of days after JD 2450600, $m_{\rm v}$ – V magnitude,
S/N – signal to noise ratio in the continuum. MRS spectra are used, unless noted otherwise.

Date (UT)	JD	Day No.	Spectral range (Å)	$m_{\rm v}$	S/N	Comments
1996						
Apr 24	0199.2	−402	5000 – 7200		60	predecline spectrum.
Sep 19	0345.8	−254	5700 – 6700	11.3	75	recovery phase of the 1996 decline.
Sep 20	0346.8	−253	5700 – 6700	11.0	65	
Sep 28	0354.2	−245	5000 – 7200	10.7	70	
1997						
Mar 10	0518.5	−82	5700 – 6700	10.3	45	predecline spectrum.
Mar 12	0520.1	−80	5000 – 7200	10.3	80	
Mar 14	0522.1	−78	5750 – 6270	10.3	63	
Apr 06	0545.1	−55	5700 – 6700	10.4	72	
May 02	0570.9	−29	5700 – 6700	10.2	55	
Jun 06	0606.2	+6	5750 – 6270	10.2	70	
Jul 14	0644.1	+44	5700 – 6700	10.9	68	minimum phase of the 1997 decline.
Jul 15	0645.0	+45	5000 – 7200	11.0	55	filling in of NaI D spectral lines.
Jul 24	0654.2	+54	5750 – 6270	11.0	63	
Aug 31	0691.9	+92	5430 – 8500	10.6	30	high-resolution échelle spectrum.
Sep 12	0703.9	+104	5700 – 6700	10.5	74	recovery phase of the 1997 decline.
Sep 13	0704.9	+105	5700 – 6700	10.5	70	
Oct 11	0732.9	+133	5700 – 6700	10.4	85	
Nov 06	0758.9	+159	5700 – 6700	10.2	65	
Nov 10	0762.9	+169	5000 – 7200	10.2	80	
1998						
Mar 04	0877.1	+277	5750 – 6270	10.2	65	maximum-light spectrum.
May 02	0936.2	+336	5750 – 6270	10.1	75	
Sep 22	1078.9	+479	5750 – 6270	10.1	64	
Oct 22	1108.9	+509	5750 – 6270	10.1	72	
Oct 23	1109.9	+510	5750 – 6270	10.1	55	

still be present but very weak (at the noise level in the continuum), or with a smaller blue shift (≤ -100 km s^{-1}), so that they cannot be resolved from the photospheric absorption. Also, the residual spectra of the NaI D lines in both declines do not show any blue-shifted absorption that can be distinguished from the noise.

The radial velocity of RS Tel ($V_{\rm r} = -(3 \pm 1)$ km s^{-1}) has been determined from some of
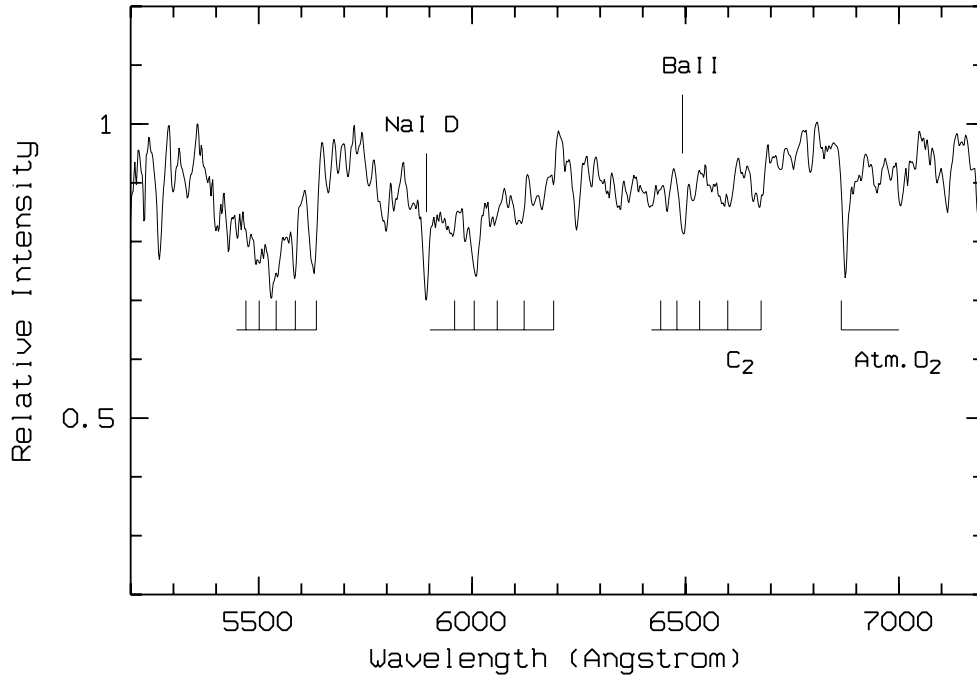
Figure 4.12: *A low resolution spectrum of RS Tel. The positions of the C_2 Swan system as well as of the NaI D and BaII lines are marked.*
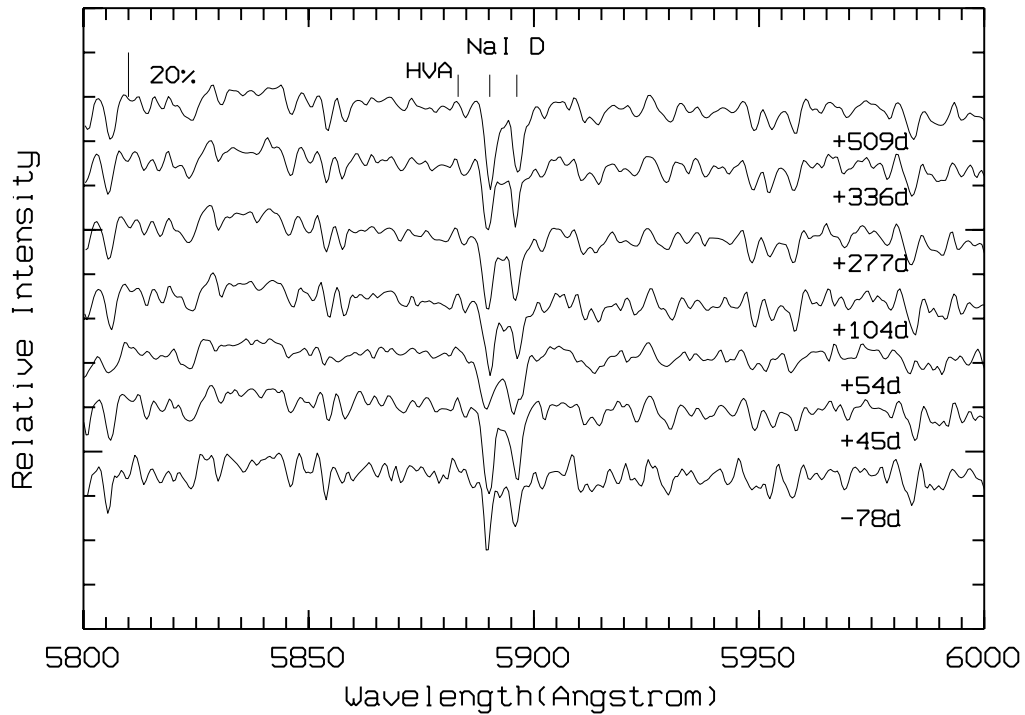
Figure 4.13: *The medium-resolution spectra of RS Tel show the characteristic evolution of the NaI D lines throughout the 1997 decline. The positions of the NaI D absorption lines are marked. The expected position of the high-velocity absorption (HVA) is also indicated (as found from the declines of other RCB stars).*
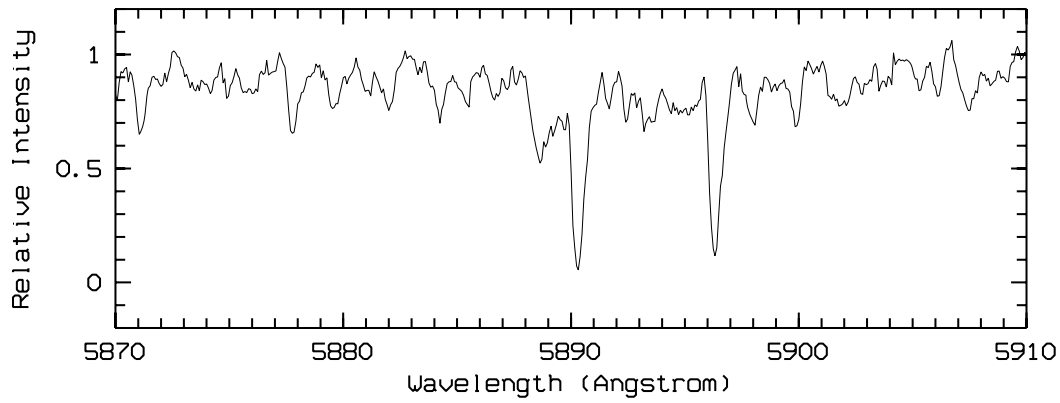
Figure 4.14: *The high-resolution échelle spectrum of RS Tel around the NaI D lines.*

Table 4.8: *Radial velocities of some absorption lines of RS Tel using the échelle spectra.*

Line (multiplet)	λ [Å]	$V_{\rm r}$ $\rm km\,s^{-1}$
CI	6006.061	-4.9
CI	6010.650	-2.4
CI	6013.199	-0.4
CI	6014.842	-2.5
CaI (21)	5594.468	-2.8
BaII (2)	5853.675	-2.6
SI (8)	6743.580	-3.5
SI (8)	6748.790	-5.3
SI (8)	6757.160	-4.9
SiII (14)	6347.091	-3.7
SiII (14)	6371.359	-1.3
TiII (91)	6559.580	-2.5
FeI (111)	6750.152	-3.2
FeI (168)	6393.605	-2.6
FeI (1001)	7418.674	-2.8
FeI (1018)	6027.057	-1.3
FeI (1178)	6024.066	-4.2
NiI (57)	6767.778	-5.3
NiI (139)	7422.300	-3.9
Mean:		-3 ± 1

the absorption lines in the high-resolution spectra (Table 4.8). The NaI D lines give a radial velocity of about -6 km s^{-1}, which is blue shifted relative to the velocity determined from other spectral lines, probably due to blending effects. The NaI D lines do not show any clear interstellar components (Figure 4.14), although some might be present due to the star's low galactic latitude ($b = -14°$). The disagreement between the radial velocities of the NaI D and other spectral lines can also indicate presence of some other NaI D components, such as permanent emission, but this is also not resolved in the spectra.

4.4 UW Centauri

During the entire observing programme, UW Cen was mainly in a deep decline, as faint as about 16^m. Spectroscopic observations of this star cover various decline phases, as shown in Figure 4.15. The last maximum-light photometry was obtained on JD 2450343 and this has been taken as day number 0 for labelling the spectra (Table 4.9). The star went into decline during the following 150 days. The first decline photometry was collected around JD 2450500.
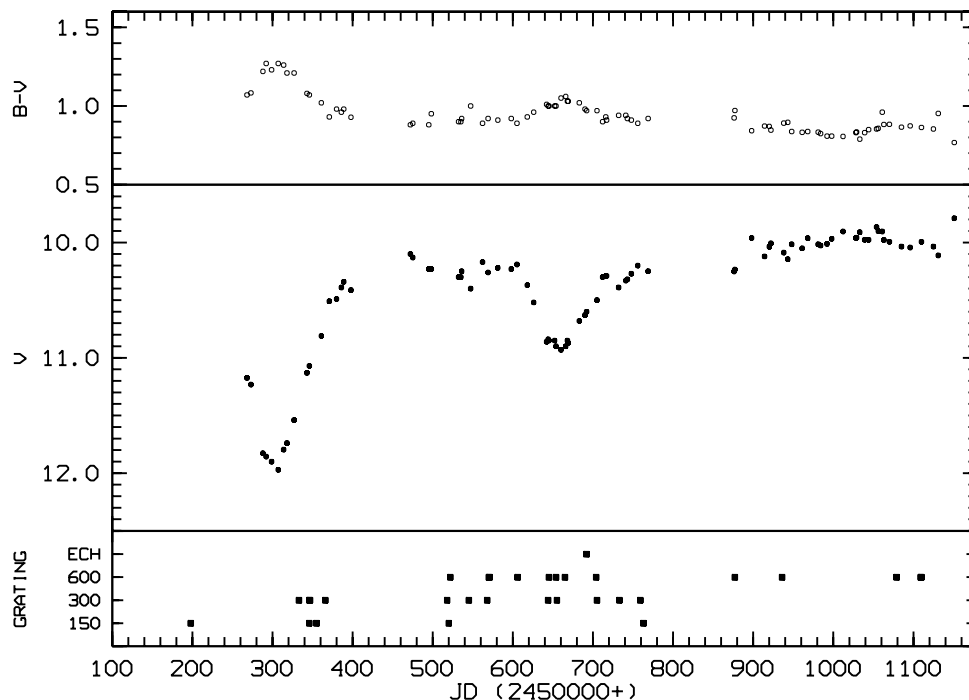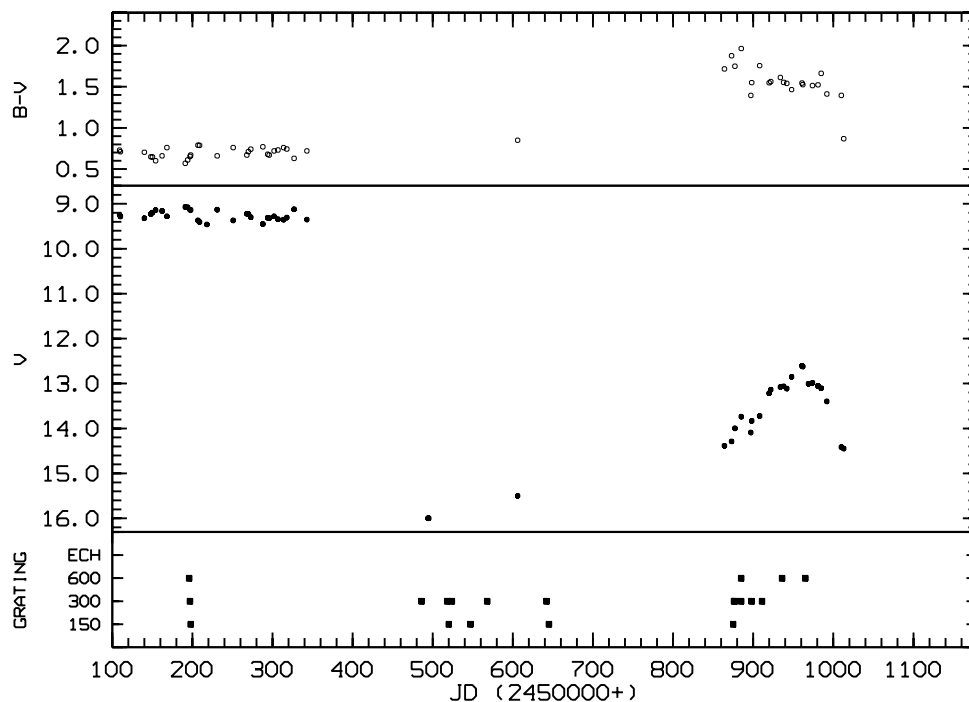

Figure 4.15: *V magnitude and colour changes of UW Cen and the times at which spectro-scopic observations were obtained.*

UW Cen was observed with the MRS spectrograph between 1996 April 22 and 1998 May 31 (see Table 4.9 and Figure 4.15). The maximum-light spectra were collected prior to the 1997/98 decline. The first low-resolution spectra from the deep decline reveal the NaI D

Table 4.9: *Summary of spectroscopic observations of the 1997/98 decline of UW Cen: JD – Julian Day (2450000+), Day No. – number of days after JD 2450343, m_v – V magnitude, S/N – signal to noise ratio in the continuum. MRS spectra are used, unless noted otherwise.*

Date (UT)	JD	Day No.	Spectral range (Å)	m_v	S/N	Comments
1996						
Apr 22	0196.9	−147	5750 – 6270	9.4	60	maximum light spectrum.
Apr 23	0197.9	−146	5700 – 6700	9.4	80	
Apr 24	0199.0	−145	5000 – 7200	9.4	85	
1997						
Mar 10	0517.9	+175	5700 – 6700	∼ 16	15	deep decline spectrum.
Mar 12	0519.9	+177	5000 – 7200		20	NaI D emission lines.
Mar 16	0523.9	+181	5700 – 6700		8	↓
Apr 08	0546.9	+204	5000 – 7200	∼ 16	10	↓
Apr 29	0567.9	+225	5700 – 6700	∼ 16	5	↓
Jul 15	0645.2	+302	5000 – 7200		5	↓
1998						
Mar 02	0874.9	+532	5000 – 7200	14.0	45	recovery phase.
Mar 03	0875.9	+533	5700 – 6700	14.0	30	NaI D HVA* (~ -220 km s^{-1})
Mar 04	0876.9	+534	5700 – 6700	14.0	50	NaI D emission.
Mar 12	0884.9	+542	5700 – 6700	13.8	48	
Mar 25	0897.9	+555	5700 – 6700	13.6	55	emission decaying.
Apr 07	0911.1	+568	5700 – 6700	13.2	60	HVA (~ -285 km s^{-1})
May 02	0935.8	+593	5750 – 6270	13.0	50	emission increasing.
May 31	0964.8	+622	5750 – 6270	13.0	55	new fading; HVA present.

* High-velocity blue-shifted NaI D absorption.

emission lines. The identification of other spectral lines is not reliable due to the low signal in the continuum. The second set of observations covers a partial recovery phase up to $12^m_.4$ and the beginning of a new fading. No other changes in the spectra, except around the NaI D lines, have been noticed. During the temporary recovery phase ($\sim$JD 2450900) the stellar continuum appears almost fully recovered. Low resolution spectra at light maximum and during the recovery phase are shown in Figure 4.16.

The evolution of the residual spectra around the NaI D lines is shown in Figure 4.17. Similar to other RCB declines, the NaI D lines include the sharp emission components, as well as the high-velocity absorption. The sharp emission lines observed in the MRS spectra are at about the same velocity as the photospheric absorption ($V_r \sim -(25\pm5)$ km s^{-1}). These
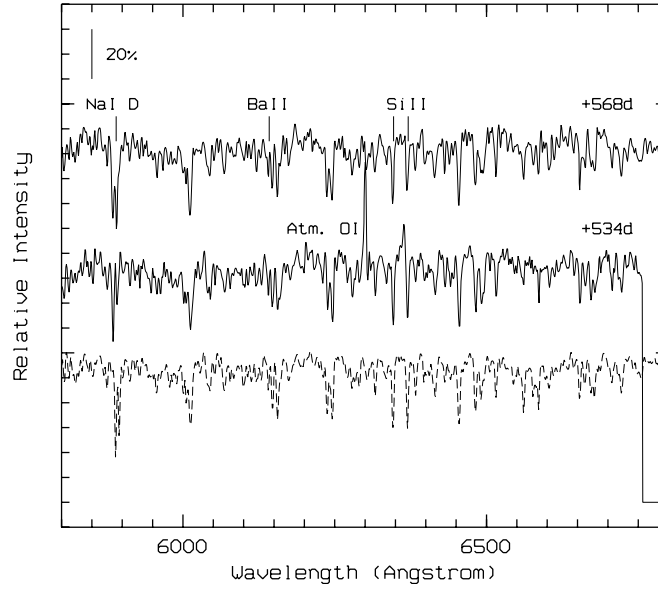
Figure 4.16: *Low resolution spectra of UW Cen at light maximum (dashed line) and during the temporary recovery phase (solid lines). The positions of some stellar and sky spectral lines are marked.*
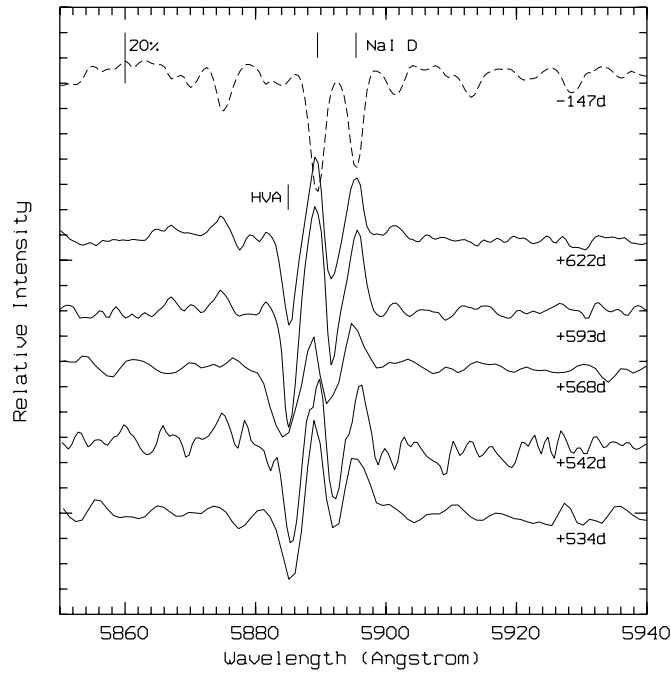
Figure 4.17: *The evolution of the residual spectra of UW Cen around the NaI D lines throughout the decline. The high-velocity blue shifted absorption (HVA) and the emission are visible. The first three spectra (+534d, +542d and +568d) are from the recovery phase, while the following two (+593d and +622d) correspond to the new light fading. The dashed spectrum (−147d) is the maximum-light spectrum. The positions of the absorption NaI D lines are marked. Note a shift of the high velocity absorption between days +534 and +568.*

lines decay during the partial recovery and then they strengthen again at the beginning of the new fading. Broad NaI D lines are not noticeable, indicating that they are probably at the noise level in the continuum. Similar to the declines of S Aps and RZ Nor, the high-velocity absorption during the recovery phase appears to be shifted from about -220 km s^{-1} (day $+534$) to -285 km s^{-1} (day $+568$). This material moves away from the star with an acceleration of about 64 km s^{-1} in 34 days (~ 2 cm s^{-2}). Assuming a constant acceleration, the material would have moved over a distance of at least $2\,R_*$ ($R_* \approx 61 R_\odot$) during this time.

4.5   V Coronae Australis

V CrA went into decline in 1994 February. Over the following four years (until early 1998) the star was undergoing various partial recovery and fading phases, never reaching its maximum brightness. During the observing programme of this thesis, V CrA was observed at the initial stage of the small 1997 fading, as well as during its final recovery phase to the light maximum (see Figure 4.18 and Table 4.10). The decline onset, JD 2449432 (day number 0), has been estimated from the photometry and used for labelling the spectra (Table 4.10).
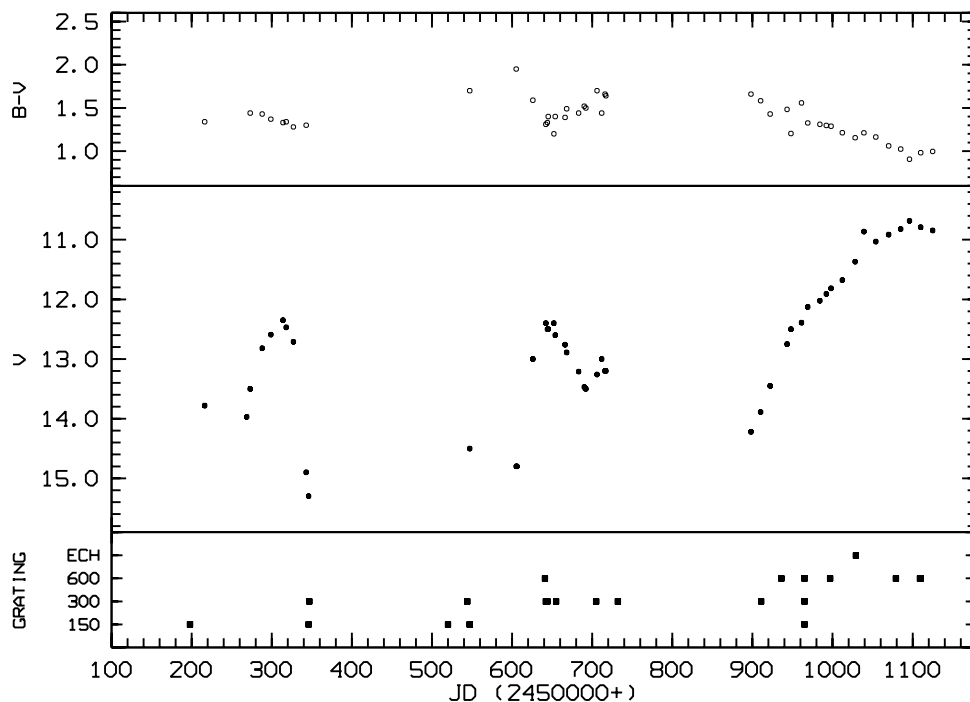
Figure 4.18: *V magnitude and colour changes of V CrA and the times at which spectroscopic observations were obtained.*

V CrA was observed intermittently between 1996 April 24 and 1998 October 23 (see Table 4.10 and Figure 4.18). The maximum-light spectra were collected after the decline

Table 4.10: *Summary of spectroscopic observations of the 1994–98 decline of V CrA: JD –*
Julian Day (2449432+), Day No. – number of days after JD 2449432, $m_{\rm v}$ – V magnitude,
S/N – signal to noise ratio in the continuum. MRS spectra are used, unless noted otherwise.

Date (UT)	JD	Day No.	Spectral range (Å)	$m_{\rm v}$	S/N	Comments
1996						
Apr 24	0199.1	+766	5000 – 7200	13.8	25	decline spectrum; NaI D emission.
Sep 20	0345.9	+915	5000 – 7200	15.0	5	NaI D emission.
1997						
Mar 12	0520.2	+1088	5000 – 7200	14.4	10	NaI D emission.
Apr 08	0547.2	+1115	5000 – 7200	14.4	8	NaI D emission.
Jul 11	0641.1	+1209	5750 – 6270	12.4	35	HVA*; weak NaI D emission.
Jul 12	0641.9	+1210	5700 – 6700	12.4	40	normal photospheric spectrum, except for NaI D lines.
Jul 25	0654.1	+1223	5700 – 6700	12.6	34	HVA decaying; filling in of spectral lines.
Sep 13	0705.1	+1273	5700 – 6700	13.2	52	HVA increasing; photospheric absorption.
Oct 10	0731.9	+1300	5700 – 6700	> 13.2	30	NaI D emission increasing.
1998						
Apr 07	0911.2	+1479	5700 – 6700	13.8	60	HVA; strong NaI D emission.
May 02	0936.1	+1504	5750 – 6270	12.8	55	HVA;NaI D emission; photospheric absorption.
May 31	0965.0	+1533	5000 – 7200	12.1	60	strong HVA; NaI D emission decaying.
Jul 2	0997.1	+1565	5750 – 6270	11.8	56	strong HVA; normal photospheric spectrum.
Aug 3	1029.0	+1597	5430 – 8500	11.4	40	high resolution échelle spectra; strong HVA
Sep 22	1078.9	+1647	5750 – 6270	10.8	70	weak HVA.
Oct 22	1108.9	+1677	5750 – 6270	10.8	63	no HVA; normal photospheric spectrum.
Oct 23	1109.9	+1678	5750 – 6270	10.8	55	normal photospheric spectrum.

* High-velocity blue-shifted NaI D absorption.
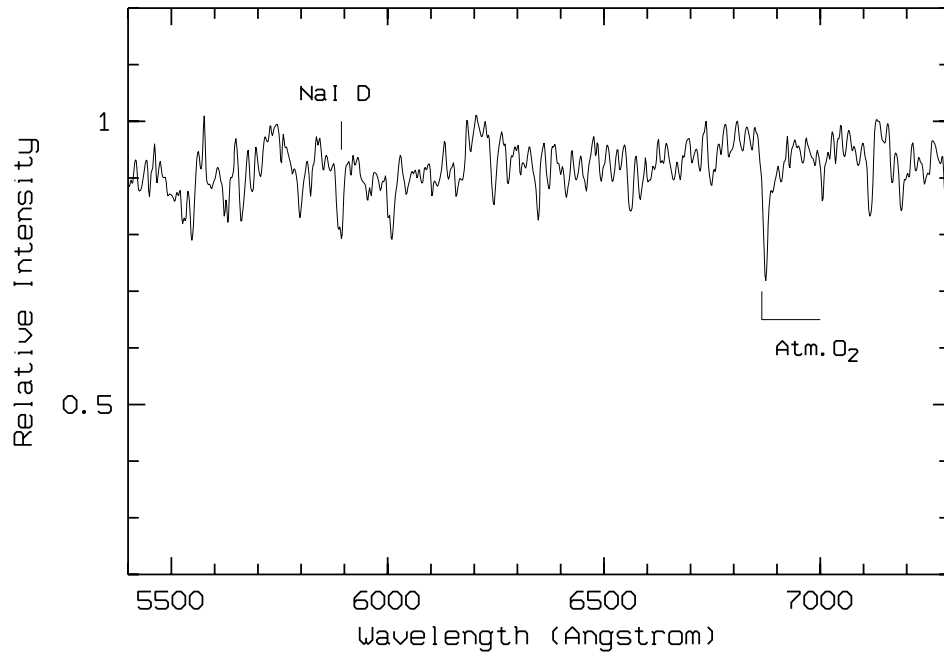
Figure 4.19: *A low-resolution spectrum of V CrA close to the light maximum. Position of the NaI D lines is marked.*
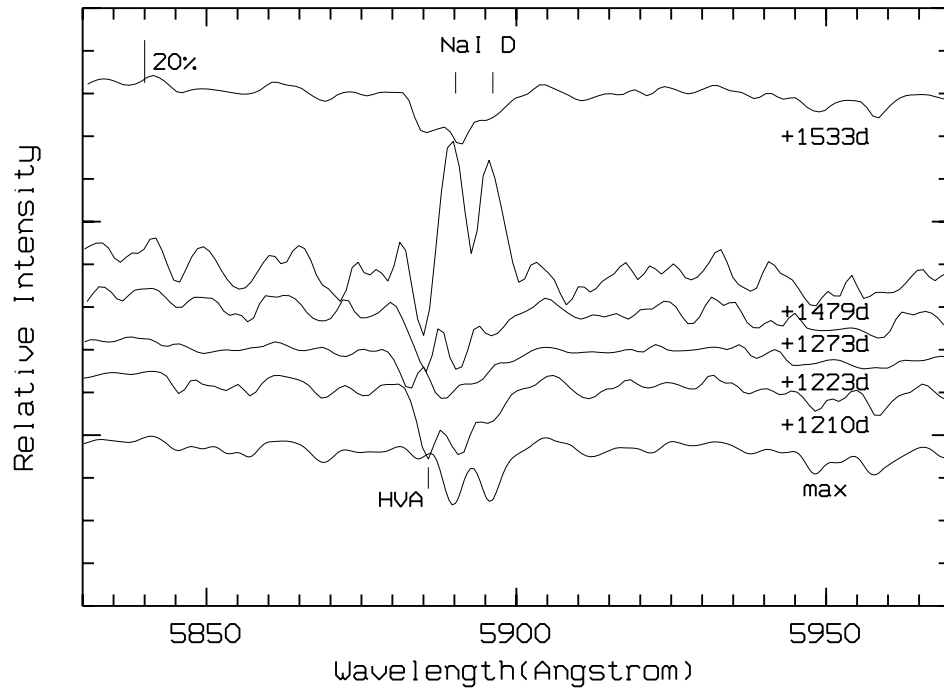
Figure 4.20: *Low-resolution spectra of V CrA show the evolution of the NaI D lines throughout the decline. Positions of the photospheric and high-velocity absorptions (HVA) are marked.*
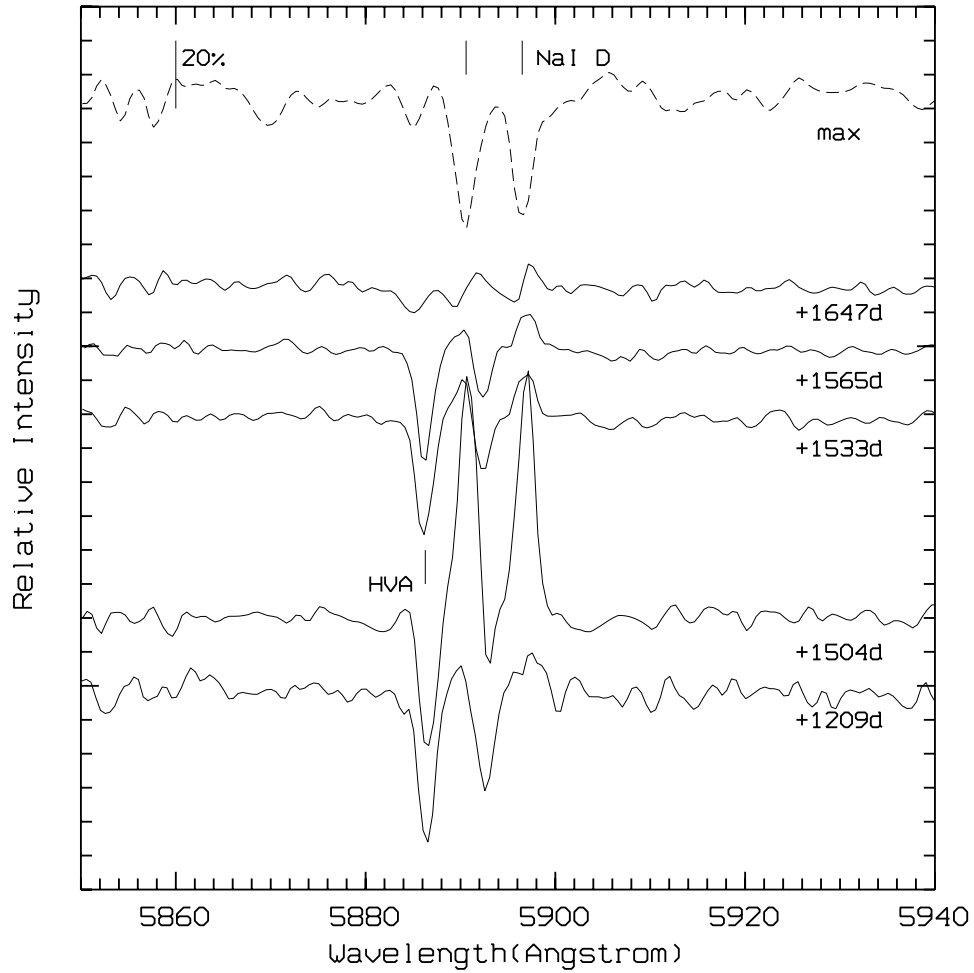
Figure 4.21: *The evolution of the residual spectra of V CrA around the NaI D lines through-out the recovery phase. The high-velocity blue shifted absorption (HVA) and the emission are visible. The dashed spectrum ("max") represent the maximum light. Positions of the absorption NaI D lines are marked.*

(Figure 4.19). The decline spectra from 1996 and 1997 (until 1997 July) were collected when the star was quite faint. These spectra show a clear NaI D emission at a level above the NaI D sky lines, while the identification of other emission lines is not reliable, due to the low signal-to-noise ratio in the continuum.

   Spectra obtained between 1997 July and 1997 October are from a small fading phase. Filling in of strong low-excitation spectral lines (such as BaII, ScII and TiII) can be noticed, as well as changes around the NaI D spectral lines. Compared to the light-maximum spectra, the NaI D components show a disturbance of the profile due to the emission and high velocity absorption (see Figure 4.20). Spectra marked as +1210d and +1223d are from the beginning of this fading phase. The +1223d spectrum shows filling in of the profile due to the increase in the strength of the emission components and decaying of the high-velocity absorption components. The NaI D emission increases further on days +1273 and +1479. The high-

Table 4.11: *Radial velocities for some absorption lines of V CrA measured from the échelle spectra.*

Line (multiplet)	λ [Å]	V_r km s^{-1}
CI	6006.061	-11.1
CI	6010.650	-8.6
CI	6013.199	-10.0
CI	6014.842	-8.7
CI	6711.291	-12.0
CI	5720.779	-11.9
CI	7132.112	-13.0
CI	6962.310	-12.9
CaI (21)	5588.757	-12.2
CaI (21)	5594.468	-10.7
BaII (2)	5853.675	-10.7
SI (8)	6743.580	-12.8
SI (8)	6748.790	-15.5
SI (8)	6757.160	-11.9
SiII (14)	6347.091	-5.2
SiII (14)	6371.359	-7.0
FeI (1178)	6024.066	-11.9
Mean:		-11 ± 2
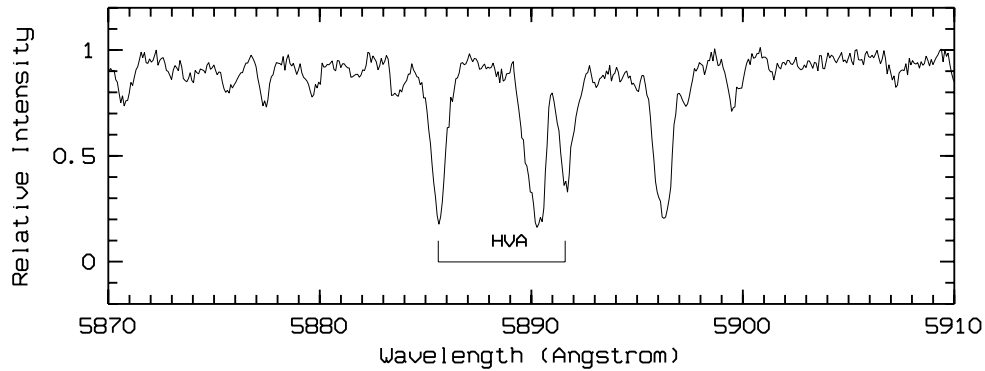
Figure 4.22: *The high-resolution échelle spectrum from the late recovery phase (close to the light maximum) of V CrA around NaI D lines. High-velocity absorption (HVA) is prominent.*

velocity components also become stronger. The spectrum marked as +1533d is from the final recovery phase, still showing the presence of the HVA at about a similar position as in the previous decline phases.

The 1998 observations are from the final recovery phase. They mainly show changes in the NaI D components and a slow recovery of the normal photospheric spectrum. In order to emphasize these changes, the residual spectra relative to the maximum light have been examined (Figure 4.21). The NaI D emission lines are still present during the recovery phase and they decay slowly. The high-velocity absorption remains at almost the same position (within the measurement error) throughout the whole decline (day +1209 to +1647). It is interesting to note that both the +1209d and +1504d spectra were collected when the star was at about the same magnitude ($\sim 12^{m}5$). The first one originates from the early initial phase and the other one is from the recovery phase. The high-velocity absorption components are found in both spectra, indicating the presence of numerous dust clouds generated in previous decline phases.[1]

The high-resolution spectrum from the late recovery phase (see Figure 4.22) gives a velocity of $-(234 \pm 2)$ km s^{-1} for the high-velocity absorption. The velocity of the photospheric absorption components of $-(0.5 \pm 2)$ km s^{-1} differs from the value obtained from other spectral lines (see Table 4.11), due to blending with the interstellar components. The mean stellar velocity measured from various photospheric absorption lines in the high-resolution spectra is $-(11 \pm 2)$ km s^{-1}.

4.6 Summary of the declines

Although the observed declines of different RCB stars had different durations and depths, a number of common photometric and spectroscopic characteristics could be noticed. In this section some of the most important of these characteristics will be summarized for the six RCB declines presented in this thesis (see Chapters 3 and 4).

The following are the common photometric features:

- Most of the declines show complex light curves with a number of successive fadings and partial recoveries. In general, the multiple fadings are correlated with the stellar pulsation cycle.

- By examining the colour changes during the decline, a significant reddening can be seen, especially during the recovery phase.

The most important spectroscopic features include:

---

[1] The whole decline is characterized by a complex pattern of alternate fadings and partial recoveries. A significant amount of material can be formed and accelerated in each of these phases.

- The photospheric spectrum exhibits various changes during the decline, characterized by weakening (filling in) of the absorption lines as the star gets fainter. However, the spectroscopic changes are not uniquely determined by the change in the stellar magnitude. In the relatively shallow declines of RS Tel and RZ Nor the changes are seen only around the NaI D lines, while various additional features (around H_α, CaII IR triplet and CI lines) are detected in the initial decline of V854 Cen (of a similar depth). In a similar way, the photospheric spectrum appears fully recovered at the 4^m-deep partial recovery phase of UW Cen, while it is still filled in during the similar 2^m-deep recovery phase of V CrA.

- All decline spectra exhibit a strong NaI D emission with a complex profile including various sharp and broad components. The only exception is the shallow decline of RS Tel, where the NaI D emission was not detected.

- The sharp NaI D components, visible throughout the decline phase, behave as other sharp lines from the E_2 group, with a characteristic blue shift and flux distribution.

- The broad NaI D components vary in strength from one RCB star to another. They appear about two times stronger in V854 Cen than in the other stars.

- The high-velocity NaI D absorption (HVA), blue-shifted by a value ranging from ~ -230 km s^{-1} for V CrA to ~ -400 km s^{-1} for V854 Cen can be seen in various decline phases, from the initial phase of V854 Cen, throughout the declines of most of the RCB stars.

- Various emission features were observed during the 1998 decline of V854 Cen, including the low-excitation sharp emission lines of BaII, TiII, ScII and other elements, the high-excitation lines of CI, OI and MgI, the broad emission lines of the NaI D, H_α, CaII IR triplet, CaII H & K and MgI triplet and the forbidden lines of [OI], [CI] and [CaII]. While the low-excitation lines exhibit typical characteristics of the E_2 region (blue-shifted by a few km s^{-1} and visible throughout the decline), the high-excitation lines lines belong to the E_1 group, are red-shifted and disappear during the initial phase of the decline.

- The C_2 molecular bands, blue-shifted by a few km s^{-1}, were observed in emission during the decline of V854 Cen. The lines were seen in absorption during the deep decline of S Aps and partial recovery phase of V854 Cen.

A more detailed discussion of the spectroscopic characteristics of different RCB declines will be given in Chapter 5.

Chapter 5

Discussion

Over the last three decades, since the first extensive spectroscopic coverage of an RCB decline was obtained (Alexander et al. 1972), attempts have been made to explain the origin of various features commonly found in the decline spectra. However, neither of the models (see below) have provided a complete and satisfactory explanation of all essential characteristics of the spectral lines that appear and evolve during the decline phase.

The first classification of the spectral lines in an RCB decline (Alexander et al. 1972, see Chapter 1) was based on their evolution throughout the decline phase. This model introduced three distinct regions, E_1, E_2 and BL, responsible for different emission features. However, additional observations have revealed new characteristics of the decline spectra and a large variability in the line behaviour between different declines (Lawson et al. 1999), as well as between different RCB stars. These new characteristics, such as line structure, precision radial velocities, line fluxes and the relative flux ratio of spectral lines, give information on the physical conditions (temperature and electron density) of the emitting regions. They indicate different physical conditions characterizing each region, which is a clue to their relative location and size. In general, two possible models of the spectral line formation regions are considered, depending on their position with respect to the star. The first one places the E_1 region close to the star, at about $2R_*$, while the E_2 and BL regions are at somewhat larger distances, starting at about $10R_*$ (Clayton 1996). According to the other idea, the line emitting regions are found quite far from the star, between $15R_*$ and $35R_*$ (Rao et al. 1999).

In this thesis all emission spectral lines are classified as either *sharp* or *broad* (according to their widths), rather than involving the three line regions mentioned above. Also, the sharp lines can be classified into a number of sub-groups, depending on their different evolution and origin. In addition to this, the high-velocity absorption, being a typical feature of all RCB declines, is distinguished from the other lines and is treated separately.

In this chapter the most important characteristics of the observed decline spectra of various RCB stars will be compared with other observations and models. In particular, the

parameters of the emission and absorption lines obtained mainly from the 1998 decline of
V854 Cen will be discussed and compared with the E1/E$_2$/BL emission line region model.
Special attention will be paid to the analysis of the high-velocity NaI D components, which
are important indicators of the time-scale of the dust cloud dissipation.

5.1 Sharp emission lines

Sharp emission lines identified in this thesis include:

- the low-excitation lines of singly-ionized and neutral elements (BaII, ScII, TiII, YII,
  FeII and FeI),

- emission lines of CI, OI and MgI,

- sharp components of complex profiles of NaI D, H$_\alpha$, CaII IR triplet and MgI triplet,

- forbidden lines of [OI], [CI] and [CaII] and

- molecular lines of the C$_2$ Swan system.

These lines all appear slightly broader (between 10 and 30 km s^{-1}) than the instrumental
profile (5–10 km s^{-1}). They show different evolution and characteristics, which suggests
different an origin as well.

Low-excitation lines

The most prominent sharp emission lines, also observed in some other RCB declines (R CrB:
Payne-Gaposchkin 1963, Cottrell et al. 1990 and Rao et al. 1999; RY Sgr: Alexander et al.
1972 and V854 Cen: Rao & Lambert 1993), are the low-excitation ($\chi_{\rm U} \sim 3$ eV) emission
lines of ions and neutral atoms. According to their evolution and general behaviour, they
can be classified as E$_2$ lines. However many details concerning their origin and position with
respect to the dust cloud (and the star) still remain unexplained.

In this thesis the low-excitation emission lines were observed during the 1998 decline of
V854 Cen (see Chapter 3). In addition the sharp emission lines of NaI D were observed
during the declines of other stars (Chapter 4). These lines were found to exhibit a similar
behaviour as in R CrB during its 1995/96 decline (Rao et al. 1999). In V854 Cen these lines
appeared shortly after the onset of the decline and disappeared before the full return to light
maximum. They all seem to be composed of three components. The central component is
the strongest and the two side ones are weaker and slightly broader. The side components
are shifted by -8 km s^{-1} ('blue' component) and $+12$ km s^{-1} ('red' component) with respect
to the central one, which is, in turn, slightly blue shifted (by about 3 km s^{-1}) relative to
the stellar systemic velocity. During the 1992 decline of the same star, a blue shift of

about 1 km s^{-1} was measured for these lines (Rao & Lambert 1993). This blue shift means that the gas is slowly flowing out, with a velocity comparable to the speed of sound in the chromosphere (Cottrell et al. 1990).

The arithmetic mean of the two velocities of the 'red' and 'blue' components is closer to the stellar velocity than to the velocity of the central component. This asymmetry in the velocity distribution indicates that the side components might be coming from an outer shell expanding faster, while the central one originates from the slower-moving inner parts of the same region, so that the corresponding two components cannot be resolved. Similar structure was observed in the 1995/96 decline of R CrB with a slightly larger blue shift of about 4 km s^{-1} for the central component and with the side components at -11 km s^{-1} and $+15$ km s^{-1} with respect to the central one. The region emitting the central component was found to be optically thin (see Chapter 3). In some RCB declines (Pandey et al. 1996) the sharp emission lines were seen as double-peaked, which suggests that they originate from an optically thick region, either from a rotating envelope of gas surrounding the star, or from a bipolar flow.

Present observations show that the mean flux ratios between the blue and central (or red and central) components do not depend on the atomic species. The central component is about twice as strong as either of the other two, indicating a higher population of the region producing the central component. However, the excitation temperature of all three components was found to be similar ($T_{exc} \sim 5600$ K). Some estimates of the excitation temperatures of forbidden and sharp lines from the 1992 decline of MV Sgr (Pandey et al. 1996) give similar values. In the same paper, the lower and upper limits for the electron density and excitation temperature are given as $2 \times 10^5 \leq n_e \leq 9 \times 10^7$ cm^{-3} and $5000 \leq T_{exc} \leq 7300$ K. Observations in the UV region (Clayton et al. 1992a) suggest a temperature of ~ 5000 K for the neutral and singly ionized species composing the inner E_1 and E_2 regions, but a much higher temperature for the outer BL region. Some earlier papers (Payne-Gaposchkin 1963) indicate also that the temperature of the emitting region may be a bit lower than the stellar temperature, but the pressure is significantly lower than the photospheric value.

The radial velocity of the sharp emission lines appears to stay unchanged from the decline onset to the recovery phase. It seems that the lines are not affected by the decline. In addition, there is a difference between the continuum and line flux distributions. As shown in Chapter 3, the integrated flux of the sharp lines does not decline in step with the photospheric flux. The photospheric continuum is obscured by the dust causing the decline, while the emission lines are not (or are very little) reddened and affected by the dust cloud during the initial decline phase.[1] A similar behaviour was observed during the 1993 decline of RY Sgr (Asplund 1995) and 1995/96 decline of R CrB (Rao et al. 1999). The line flux distribution

---

[1]The same lines can be reddened later during the decline, when their emitting region becomes obscured by the dust cloud.
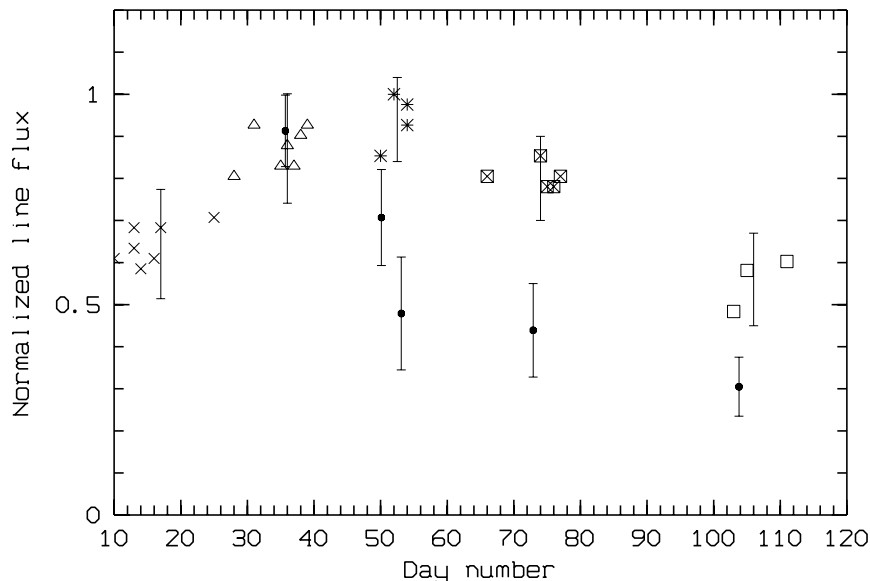
Figure 5.1: *Mean values of normalized line fluxes of low-excitation sharp emission lines (filled circles) versus day number. The other symbols represent the fluxes of the NaI D_2 spectral line (as for Figure 3.21b).*

derived from the present observations indicates a flux decrease between days +40 and +50 (measured from the beginning of the decline), probably due to the obscuration of this region by the dust cloud. The sharp components of the NaI D spectral lines also show a similar flux distribution, but decaying between days +50 and +70 (see Figure 5.1, which is a repetition of Figure 3.21, Chapter 3).

This significant difference between the distributions of the continuum and line fluxes provides information on the relative position of the sharp line emitting region with respect to the dust cloud. Taking into account the acceleration of the dust cloud of ~ 0.6 cm s^{-2}, as obtained from the high-velocity absorption (see Chapter 3), the position of the line emitting region can be calculated. Assuming that the dust cloud was formed at $2R_*$ and taking into account that the low-excitation sharp emission lines decay around day number +50, the position of the emitting region can be determined to be $\sim 3.5 R_*$. For the sharp components of the NaI D lines the position of the emitting region is about the same (from $3R_*$ for S Aps and RZ Nor up to $\sim 5R_*$ for V854 Cen). If one assumes that the dust cloud is formed at about $20 R_*$, then the emitting regions also have to be placed farther from the star ($21 R_* - 23 R_*$). The main problem with this model is finding a suitable heating mechanism for the line excitation and also a source of the acceleration of the chromosphere. One possible mechanism of the line excitation is *photoionization* by stellar radiation. Another possibility is that the lines are formed by the compressed gas behind a shock produced during the decline. In this scenario the emission line spectrum should not be seen during the recovery phase (as with the E_1 lines). However, the observations clearly show the presence of the

emission during this phase.

If one considers the physical processes causing the emission, then the fact that the emission lines are not affected by the dust cloud can also mean that the emission region is still exposed to the photospheric radiation during the decline (i.e. without any obscuration). This can lead to some alternative models of the RCB declines, different from the simple model involving a dust cloud condensating in the stellar vicinity and gradually obscuring the photosphere, with the $E_1/E_2/BL$ structure of the emission regions. One of these alternative models, which attempts to explain the nature of the RCB stars and their declines, assumes that these objects are bipolar nebulae with a high-velocity bipolar wind and a dusty equatorial torus (Rao & Lambert 1993; Clayton et al. 1997). In this case, the sharp emission lines that are not reddened can be explained by the extended chromosphere, with a diameter larger than that of the dusty torus, so that some parts of the chromosphere are not obscured by the dust. A small blue shift of the sharp emission lines (between ~ 3 $km\,s^{-1}$ for V854 Cen and 10 $km\,s^{-1}$ for R CrB, Cottrell et al. 1990) can be explained by the bipolar flow approximately perpendicular to the line of sight.

In addition to the low-excitation lines of singly-ionized elements, the lines of the NaI D, CaII IR triplet, H_α and MgI triplet also show sharp emission components, with similar evolution. However, the low-excitation lines of the NaI D and CaII IR triplet can be seen during the recovery phase, while the higher-excitation H_α and MgI triplet fade earlier. The first two lines originate from the highest regions of the chromosphere, while the other two are from deeper parts (H_α forms mainly high in the photosphere). Therefore, their evolution is consistent with the gradual blocking of the emitting regions by the expanding dust cloud.

From the observations made for this thesis, no spectroscopic changes were noticed before the star began to decline. The gradual filling-in of the the absorption spectrum is noticed in all observed declines. This phase is followed by a transition to a chromospheric emission spectrum. However, the E_2 lines have been identified as permanent features, present at all times. Obvious doubling was seen in the absorption cores of some lines (ScII 4246 Å, NaI D and CaII IR triplet) by Payne-Gaposchkin (1963) and confirmed from high-resolution spectra by Lambert et al. (1990b) and Rao et al. (1999). This is considered to be due to the superposition of an emission component on the photospheric absorption core.

Other permitted and forbidden atomic sharp lines

The CI, OI and MgI emission spectral lines that were observed during the 1998 decline of V854 Cen were all short-lived features and appeared only during the initial decline phase. A similar behaviour of the CI and OI spectral lines was observed during the 1995 decline of R CrB (Rao et al. 1999). In the same paper these lines were classified as the *transient* emission lines and their relationship with the disturbed photospheric absorption prior to the decline onset was established. In the present spectra of V854 Cen, the CI, OI and MgI

emission lines were seen only in the first initial phase, but not in the subsequent ones. A similar behaviour in the UV region was also noted by Clayton et al. (1992b) in the case of several local minima separated by relatively short time intervals.

According to their evolution, the CI, OI and MgI emission lines could be classified as E_1. However, the original list of E_1 spectral lines includes mainly short-lived lines (10 to 30 days from the decline onset) of neutral and singly ionized metals (see Chapter 1). All of these lines show a characteristic blue shift (Clayton 1996). The list has then been extended by including the high-excitation lines of CI, OI and other elements (Rao et al. 1999). These lines have been identified as an indicator of a shock and related to the decline onset. In the spectra collected for this thesis the CI emission lines were observed to be optically thick and red-shifted by about $5 \, \mathrm{km \, s^{-1}}$. This red shift supports the idea that the lines are connected with the shock triggering the decline onset. The shock causing the disturbance of the photospheric profile can move outwards to initiate emission in lower density regions. In this scenario, the red shift can be explained assuming that the lines originate from the gas heated immediately behind the shock and subsequently sinking from the shallower photospheric layers.

The onset-related lines have been found to have a large range of excitation potentials, from the lower excitation lines, such as LaII, FeII, LiI, CaI and NiI, to the high-excitation lines of CI, OI and MgI (Rao et al. 1999). Some of the lower-excitation spectral lines (e.g. FeII) can also belong to the emission lines of the E_2 group, which are dominated by lines of singly-ionized metals (ScII, BaII, TiII, YII, FeII).

The existence of the forbidden lines of [OI], [CI] and [CaII] in the observed spectra is strong evidence of a nebula surrounding the star. The lines show a similar blue shift of about $5 \, \mathrm{km \, s^{-1}}$ as the low-excitation sharp emission lines, but a slightly broader profile ($\pm 25 \, \mathrm{km \, s^{-1}}$ at the base). The broader profile can be due to the weak broad emission that has been seen in some forbidden lines (Rao & Lambert 1993). In addition, the line flux of the [CI] lines was found to remain constant throughout the decline (similar to the other broad emission lines), indicating that the lines are not affected by the decline and are probably permanent features. If one considers the physical processes that are responsible for the excitation of the forbidden lines, it is found that they are quite different from the low-excitation emission lines. Excitation of the forbidden lines is achieved by electron collisions, which means that a different region must be involved compared to the sharp emission lines. However, during the 1995/96 decline of R CrB (Rao et al. 1999), a similar excitation temperature ($T \sim 4000$ K) and electron density ($n_e \sim 3 \times 10^7 \, \mathrm{cm^{-3}}$) were found for both groups of lines.

C_2 molecular bands

Spectral lines from the molecular bands (C_2 in particular) have been observed in some declines (Rao & Lambert 2000) to have sharp emission components, while in other declines (Rao & Lambert 1993, Rao et al. 1999) only broad features have been seen.

During the observing programme of this thesis, the C_2 Swan system has been detected in emission and absorption in the 1998 decline of V854 Cen and the 1996/97 decline of S Aps. The sharp emission components of the C_2 band were identified during the decline of V854 Cen, while the broad emission was not detected. During the small recovery phase of V854 Cen (decline II, Chapter 3) and the deep decline phase of S Aps the main C_2 bandheads (0–0, 0–1, 0–2) were observed in absorption. The rotational structure was resolved for the main bandheads in the 1998 decline of V854 Cen. A blue shift of about 1.5 $\mathrm{km\,s^{-1}}$ (slightly smaller than for the low-excitation sharp emission lines) was measured from the molecular lines of the (0–0) bandhead.

Existing observations of the C_2 molecular band in emission during the RCB declines is a clear indicator of a cool emitting region. Otherwise, the molecules would dissociate. In addition to the C_2 Swan system, Rao & Lambert (2000) found the low-excitation absorption lines of the C_2 Phillips molecular bands using the high-resolution spectra from the 1998 decline of V854 Cen. The Phillips system actually belongs to the singlet-singlet transition ($^1\Pi - ^1\Sigma$). On the other hand, the Swan system is due to the triplet-triplet transition ($^3\Pi - ^3\Pi$). This might appear unusual, since the Swan bands represent the strongest C_2 molecular system, and one would expect that its lower electronic level corresponds to the ground molecular state. Although the Swan system's lower level is the *lowest triplet* state (X $^3\Pi_u$), it is still found slightly above the ground (singlet) state of the C_2 molecule (X $^1\Sigma_g^+$), which is, in fact, the lower electronic level of the Phillips system (Pearse & Gaydon 1976).

Observations of the Swan and Phillips molecular systems can provide important information on the excitation temperature of the molecules, and hence the location of the molecular gas. By measuring the (2–0) and (3–0) absorption lines of the Phillips system, Rao & Lambert (2000) found about the same velocity (blue-shifted by about 5 $\mathrm{km\,s^{-1}}$ relative to the stellar photosphere) as for the Swan emission lines. The mean rotational temperature of ~ 1150 K (Rao & Lambert 2000) for the Phillips system also suggests that these absorption lines originate from a cold gas below the condensation temperature (~ 2000 K) of the carbon dust grains. Therefore, the lines can be related to the initial phase of the decline and the dust cloud condensation.

When the present observations of the C_2 Swan system for the 1998 decline of V854 Cen are compared with the results of the Phillips system obtained by Rao & Lambert (2000) for the same decline, the following conclusions can be drawn. Since both systems have similar velocities (blue-shifted relative to the photospheric one), they probably originate from the same region which is moving away from the star. The low-excitation lines, classified as E_2, also show similar velocities and profile widths as the molecular C_2 bands. On the other hand, the difference in the rotational temperature (~ 5000 K for the Swan system and ~ 1100 K for the Phillips system, Rao & Lambert 2000) suggests that they originate from different parts of the same gas. The Phillips system indicates a cold gas, while the Swan system is related to the warmer part and also associated with the low-excitation E_2 spectral lines. A
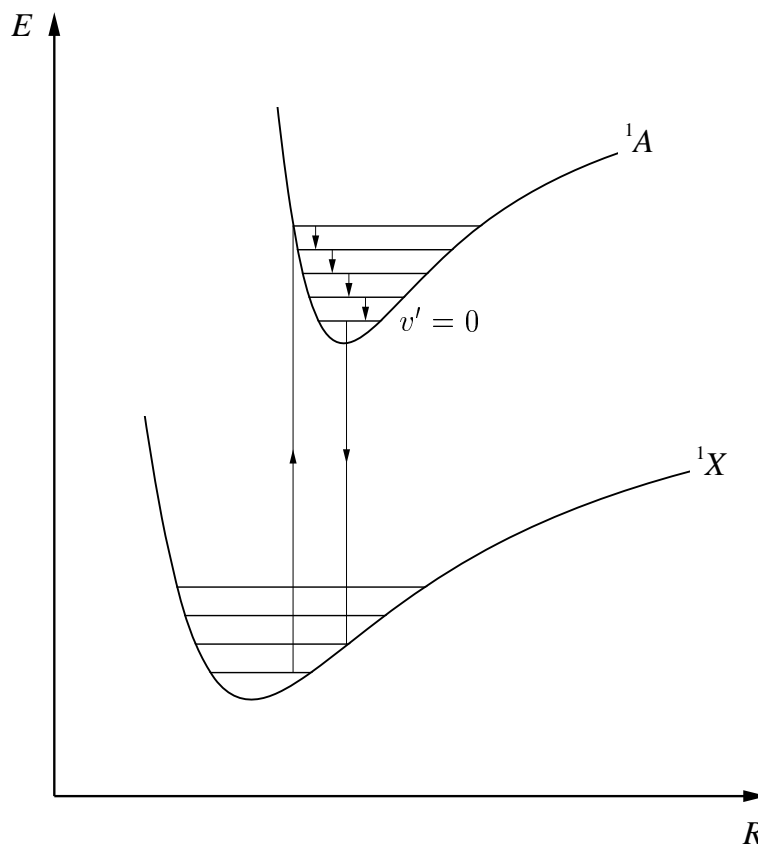
Figure 5.2: *Schematic diagram of fluorescence in molecules. Energy (E) of two electronic states (in arbitrary units) is plotted against the inter-nuclear separation (R). The absorption transitions occur from a lower electronic state (^1X) to an excited vibrational level of an upper electronic state (^1A). The molecule may then lose the vibrational energy through collisions with other molecules and reach the lowest vibrational state $v' = 0$, re-emitting radiation at a wavelength longer than the incident one. The subsequent emission from the selected vibrational levels may give an emission spectrum of an abnormal vibrational intensity distribution.*

similar gas temperature (~ 5000 K) has been obtained from the Boltzmann plot of the sharp emission lines (see Chapter 3).

The evolution of the C_2 Swan system is also similar to the evolution of the E_2 spectral lines. They both start decaying around day number $+50$, when the dust cloud obscures the emitting region. The emission in the Swan system is also visible during the early recovery phase, but at a very low level (Chapter 3, Figure 3.41). The only difference is that the Swan system appears in absorption for a short time after day number $+50$. This absorption can be explained by processes of resonance fluorescence. The mechanism of fluorescence can also be responsible for the excitation of the molecules. The absorption of the stellar radiation in

the resonance transitions of the molecules can lead to re-emission at a wavelength different from the incident radiation (Figure 5.2).

On the other hand, the evolution of the Phillips system in RCB stars has not been observed in all details. During the 1998 decline of V854 Cen, the system is visible around day number +50, but not during the recovery phase. These lines could be more related to the E_1 lines, and the decline onset.

Finally, one should emphasize that there are large differences in the appearance of molecular bands in declines of different RCB stars. The bands have been observed both in emission and in absorption. These variations are probably due to different physical conditions and chemical compositions of the upper atmospheres from one RCB star to another.

5.2 Broad emission lines

The broad emission lines are typical features of an RCB decline, observed in a number of RCB stars (see Chapter 1). They include a wide range of spectral lines from the high-excitation lines (e.g. HeI) to the low-excitation ones (such as NaI D and CaII H& K), as well as the forbidden lines of [OI], [SII], [NII], [SII], [CaII] and [CI]. Different broad emission lines (NaI D, H_α, CaII lines and MgI triplet) have been monitored during the declines of selected RCB stars in this thesis. In this section a common characteristic behaviour of these lines will be discussed.

The existence of the broad emission lines certainly indicates a presence of a hot, dense, high-velocity gas in the region surrounding RCB stars. The strongest of the broad emission lines (and also the easiest to observe, even during the faintest declines), are the broad NaI D lines. While the appearance of the underlying NaI D broad feature is typical for all declines, the strength and the width of the profile vary from one star to another. The strongest NaI D broad components appear during the declines of V854 Cen. At the deepest minimum, the entire profile can have a relative intensity of about 2.4 (140% of the continuum) with a mean base width of about 1000 $\mathrm{km\,s^{-1}}$ and a FWHM of one component of ~ 400 $\mathrm{km\,s^{-1}}$. On the other hand, the other RCB stars observed (S Aps, RZ Nor, V CrA and UW Cen), with less frequent declines, show the NaI D broad feature at a level less then 10% of the continuum. This strong NaI D emission for V854 Cen is expected, since the star has experienced many declines in recent years. In each of them a significant amount of dust is condensed. Assuming an expansion velocity of about 300 $\mathrm{km\,s^{-1}}$ (as derived from the high-velocity NaI D absorption), the gas dragged by the dust cloud after about 10 years would extend to about 2500 R_*. Therefore, the gas responsible for the broad emission would, after some time, be very extended and diluted in the case of stars with less frequent declines.

The base width of the other broad spectral lines (except CaII H & K lines, whose width of about 1200 $\mathrm{km\,s^{-1}}$ is similar to the broad NaI D components) is much lower: about
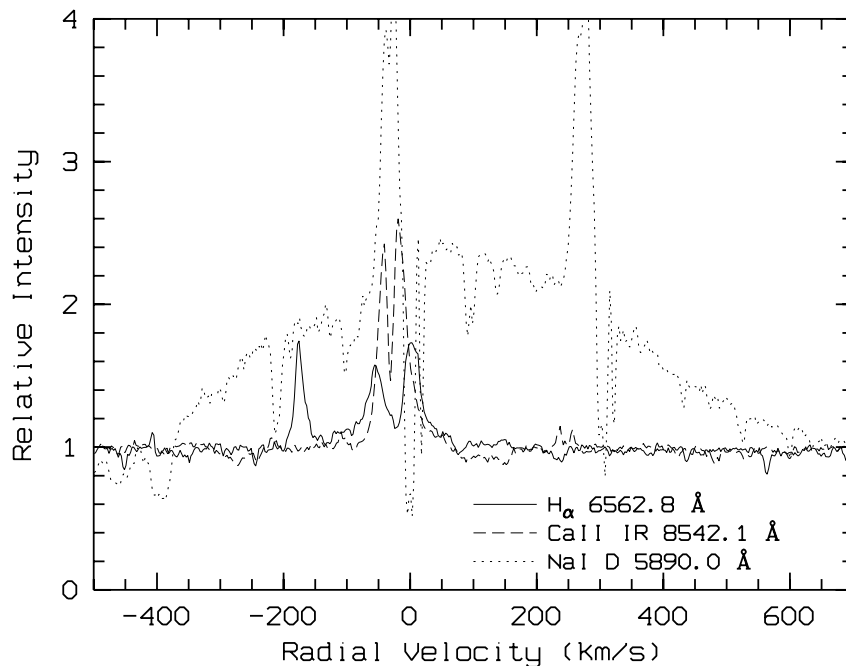
Figure 5.3: *The H_α line and the CaII IR triplet compared to the broad NaI D emission (as for Figure 3.29).*

300 km s^{-1} for the CaII IR triplet and H$_\alpha$ lines and about 70 km s^{-1} for the MgI triplet (Figure 5.3, which is a repetition of Figure 3.29). These lines are also much weaker (less than about 15% of the continuum) compared with the strong NaI D lines.

The large differences between the widths of the NaI D, or CaII H & K, lines and the other low-excitation broad lines can be due to different optical depths (higher for the NaI D and CaII H & K). It is also known that the high-excitation lines form closer to the star than the low-excitation lines. The estimated flux ratio between the broad CaII H & K lines and the IR triplet lines suggests that the gas emitting these lines is optically thin. It should be mentioned that the low-excitation broad lines are also blended with sharp components, originating probably from a different region.

Even if the two NaI D components are blended, the whole profile (in all observed RCB stars) seems to be symmetric around the stellar velocity. This is consistent with a symmetric expanding circumstellar shell with the same amount of gas in front of the star as behind it. However, from the 1998 decline of V854 Cen there are some indications (from H$_\alpha$ and the CaII IR triplet) of a slight blue shift relative to the stellar velocity. This suggests an expanding shell with slightly more gas in front of the star than behind it.

In addition, the relative intensities and fluxes of the broad lines observed throughout the decline reveal some interesting characteristics of the emitting region. First, the relative intensities of the broad NaI D and H$_\alpha$ emissions from two subsequent declines of V854 Cen at about the same visual magnitude are at the same level (see Figures 3.46 and 3.33,

Chapter 3). This supports an idea that the broad emission is a permanent feature, whose visibility depends on the photospheric brightness. However, only a detection of this emission at light maximum would be real proof of the hypothesis of its permanent nature. This is extremely difficult, since these lines are much fainter than the photosphere. There is a possibility of observational detection of the broad emission in the UV, where the photospheric continuum is fainter. For example, the CII 1335 Å emission line (probably a broad line) is visible at all times (Clayton 1996).

Another characteristic of the broad emission lines (as measured from the NaI D lines) is that their absolute flux stays mainly constant[2] compared to the sharp emission lines, whose flux decreases during the decline. The difference between the broad and sharp lines suggests that the corresponding emitting regions are well separated. The broad emission region is probably not obscured by the same dust cloud responsible for the decaying of the sharp lines. An additional observational fact that supports the idea that the broad line emission region is not directly affected by the dust cloud is the line polarization. It was observed that the broad NaI D and H_α lines are *not* polarized (Whitney et al. 1992) and, therefore, not significantly reddened. They could originate from regions outside those parts with a high dust concentration.

One should also discuss different physical processes leading to the excitation of various broad spectral lines, as well as the characteristics of their emitting regions. The existence of different broad emission lines implies different possibilities for the source of their excitation. This can even include the existence of different emitting regions. The presence of high-excitation HeI lines, identified as broad lines in the 1995/96 decline of R CrB (Rao et al. 1999), means that their source is probably not the same as for the NaI D broad components, even if the lines give the same radial velocity. The source of HeI excitation cannot be radiative and is probably collisional (Rao et al. 1999). On the other hand, the NaI D lines are excited by radiative processes. Other possibilities for spectral line broadening is scattering by dust and broadening by turbulent winds (Rao et al. 1999). For example, it is known that broadening of the H_α line, in general (not only in RCB stars), can be due to turbulent winds at the base of the chromosphere. In the case of RCB stars this means that the broad H_α component can be obscured by the dust cloud at an earlier phase of the decline than is the case for the sharp lines. From the present observations it cannot be seen clearly whether this is the case for the H_α line. It has also been shown (Rao & Lambert 1993) that hydrogen in the broad-emission gas is photoionized, since the calculated luminosity needed for the photoionization of the Balmer lines is similar to the observed one.

In some RCB declines the forbidden lines have also been observed as broad features (Herbig 1949; Rao & Lambert 1993; Asplund 1995; Vanture & Wallerstein 1995; Pandey et al. 1996). From the present observations the forbidden lines of [OI] and [CI] have been

---

[2]Some variations of the broad emission line fluxes have been reported by Herbig (1949) and Lawson et al. (1999).

classified as sharp, although with a slightly broader profile than the other sharp emission
lines. This might be due to the weak underlying broad emission. However, even with a
similar broad profile, the forbidden lines do not necessarily originate from the same region
as the other broad emission lines. A very low electron density, of only $n_e \sim 50$ cm^{-3} for
the region producing the forbidden lines, has been obtained for V854 Cen (Rao & Lambert
1993). On the other hand, higher values for the density ($n_e \sim 10^9$ cm^{-3}) and fairly high
temperatures ($1 - 2 \times 10^4$ K) have been obtained for the other broad lines (Asplund 1995,
Lambert et al. 1990b). This can be an indicator that the forbidden lines originate from the
low-density nebula, while the other broad lines are coming from a different, denser region.
In such a case, the nebula is located at a larger distance than the high-density region.

In addition to the standard, spherically symmetric model of RCB stars (Loreta 1934),
in which the broad emission originates from a large nebula surrounding the star, some
alternative models have also been considered. One of them is based on a bipolar nebula
(Rao & Lambert 1993; Clayton et al. 1997), as already mentioned above. The broad spectral
lines are attributed to the bipolar flow. Both arms of the flow will contribute to the broad
emission, so that the lines will be approximately centred on the photospheric velocity. The
width of the emission lines will increase as the bipolar flow is more nearly aligned with the
line of sight. This is supported by optical polarization measurements of R CrB (Clayton
et al. 1997) indicating a preferred direction for ejection or accumulation of dust.

Another model, suggested by Rao et al. (1999), assumes that the broad emission lines
in R CrB originate from the accretion disk of a spectroscopic binary system. From an RCB
star gas can flow through the accretion disk towards a compact white dwarf companion. The
broadening of the spectral lines is due to the velocity of gas in the disk close to the white
dwarf. The broad optically thick lines (such as HeI) are emitted by the inner regions of the
disk, while the lower-excitation lines (such as NaI D and the forbidden lines) originate from
the disk's cooler outer regions. However, there is no proof for the radial velocity variations
of the star itself and/or of the broad line emitting region.

5.3   High-velocity NaI D absorption

The high-velocity NaI D absorption (HVA) has been observed in several RCB declines (Van-
ture & Wallerstein 1995; Clayton et al. 1993b; Rao & Lambert 1993; Cottrell et al. 1990;
Skuljan & Cottrell 1999). It is one of the most interesting decline features with a velocity of
about a few hundreds km s^{-1} and a quite extended and asymmetric profile. In some declines
the HVA has been observed only during the recovery phase (Rao et al. 1999), while in the
others it has been seen during the initial phase as well (Cottrell et al. 1990).

In most of the RCB declines observed in this thesis (V854 Cen, S Aps, RZ Nor, UW Cen
and V CrA) the high-velocity absorption has been monitored. The lines appeared even

during the shallow decline of RZ Nor (two magnitudes deep), when the stellar photospheric absorption spectrum was still dominant.

The HVA lines have been found at different decline phases: from the early initial phase until the late recovery phase of V854 Cen (see Chapter 3), during the decline minimum and recovery phase of RZ Nor, as well as throughout the complex decline patterns of UW Cen and V CrA and during the recovery phase of S Aps (see Chapter 4). The lines were not identified in the two shallow declines of RS Tel (one and two magnitudes deep). This can mean that the lines were either weak, or with a very small blue shift (≤ -100 km s^{-1}) so that they could not be resolved from the photospheric absorption. A similar line profile and line evolution has been observed during the recovery phases of all declines. The profile is quite strong and extended around the decline minimum and at the beginning of the recovery phase (with at least one blue and one red component relative to the central one). As the star becomes brighter, the red-shifted component disappears first, leaving the central and the blue ones visible until light maximum. However, the whole profile seems to be shifted towards the blue more than at the beginning of the recovery phase. This type of profile is not clearly recognized in the case of the stars with multiple declines (UW Cen and V CrA). During the observing programme these two stars were undergoing various fadings and partial recovery phases. In each of them a strong HVA was present, blended with the sharp emission components. The shape of the HVA profile and its evolution are typical for shell absorption.

The highest velocity of the HVA was detected during the 1998 decline of V854 Cen (~ -400 km s^{-1}), while it is somewhat smaller for the other stars: RZ Nor (~ -330 km s^{-1}), S Aps (~ -300 km s^{-1}), UW Cen (~ -280 km s^{-1}) and V CrA (~ -230 km s^{-1}). The fact that the radial velocity of HVA is relatively high means that the gas associated with these lines has circumstellar origin with a velocity far exceeding the escape velocity (an escape velocity of ~ 73 km s^{-1} has been calculated for V854 Cen). If the HVA is analysed as a single profile, then the blue-shift throughout the recovery phase can be interpreted as an acceleration of the cloud. A range of accelerations have been measured, between 0.5 cm s^{-2} for S Aps and 2 cm s^{-2} for UW Cen. A similar acceleration of ~ 1 cm s^{-2} was predicted for the gas in a spherically symmetric flow, forming at about $20R_*$ (Fadeyev 1988). According to this prediction, the gas has to be at about $20R_*$ from the star at the time the HVA components appear. The observational parameters of the HVA components (velocity and acceleration) can also be used to calculate the location of the line emitting regions and are important elements of a model of an RCB star.

The flux ratio of the two NaI D components ($D_2/D_1 \approx 2$) found in all RCB declines observed indicates that these lines originate from an optically thin region. A column density of $N \sim 10^{12}$ cm^{-2} has been estimated (using the doublet-ratio method) in the case of the decline of V854 Cen.

This high-velocity feature of the NaI D lines has not been seen in any other spectral lines. One could expect that the KI resonant spectral lines (7664 Å and 7699 Å) would show

a similar feature, since NaI and KI atoms have similar structures. However, the KI lines were not observed during the 1998 decline of V854 Cen. The sodium is probably far more abundant in RCB stars (Lambert & Rao 1994). The HVA has not been identified in CaII H & K lines either, which indicates that the gas producing the HVA components is primarily neutral.

The problem of the origin of the high-velocity absorption still remains unsolved. The HVA has only been observed during the decline (i.e. never at light maximum), which means that processes responsible for the decline and HVA are probably linked in some way. An analysis given by Rao & Lambert (1997) supports the idea that the origin of the HVA is in the gas being accelerated during the process of dust cloud formation. In that case, a dust cloud of carbon grains condenses at about $2R_*$ (Woitke et al. 1996). The triggering mechanism for this formation appears to be located in the photosphere (Rao et al. 1999). The dust cloud is then accelerated by radiation pressure on the grains while the gas which has not condensed is accelerated by the collisions between the dust grains and gas. This gas can be a source of the HVA. Since there is a velocity difference of at least a few $\mathrm{km\,s^{-1}}$ (Rao & Lambert 1997) between the dust and gas clouds, they separate relatively quickly during the decline. According to this model, in the initial stages of the decline the gas has a low expansion velocity and cannot be easily detected when taking into account the blending effects with the strong sharp emission lines. In addition, during the deepest minimum, the photosphere is almost totally obscured, and the scattered photospheric light is the main contributor to the total light. Therefore the HVA cannot be seen. As the recovery progresses, the cloud dissipates and the direct photospheric light dominates the spectrum. The HVA associated with the current decline may then be seen.

However, during the observational programme of this thesis the HVA has been seen during the initial stages as well as throughout the whole decline. In the model mentioned above this can be explained by the presence of some gas clouds from previous declines, that have not yet dispersed, or by some clouds located off the line of sight, which can drift into view. In such a scenario, the HVA can be seen during the initial phase as well. In that case the recovery to maximum light may include the high velocity absorption associated with the current decline, as well as the components from other declines. If the star exhibits frequent declines (e.g. V854 Cen), there can be a high number of gas clouds, or shells, along the line of sight, so that it becomes very difficult to recognize the HVA components from the current decline. In general, there are not any specific rules in the way the HVA appears. Its position and velocity can be different from one decline to another for the same star. A schematic diagram of the evolution of the HVA, based on the 1998 decline of V854 Cen, is shown in Figure 5.4.

One cannot assume that the gas producing the HVA moves with the same velocity as the dust cloud responsible for the decline. It can be shown that, if the two velocities were the same, then the duration of a decline would be much shorter, taking into account a
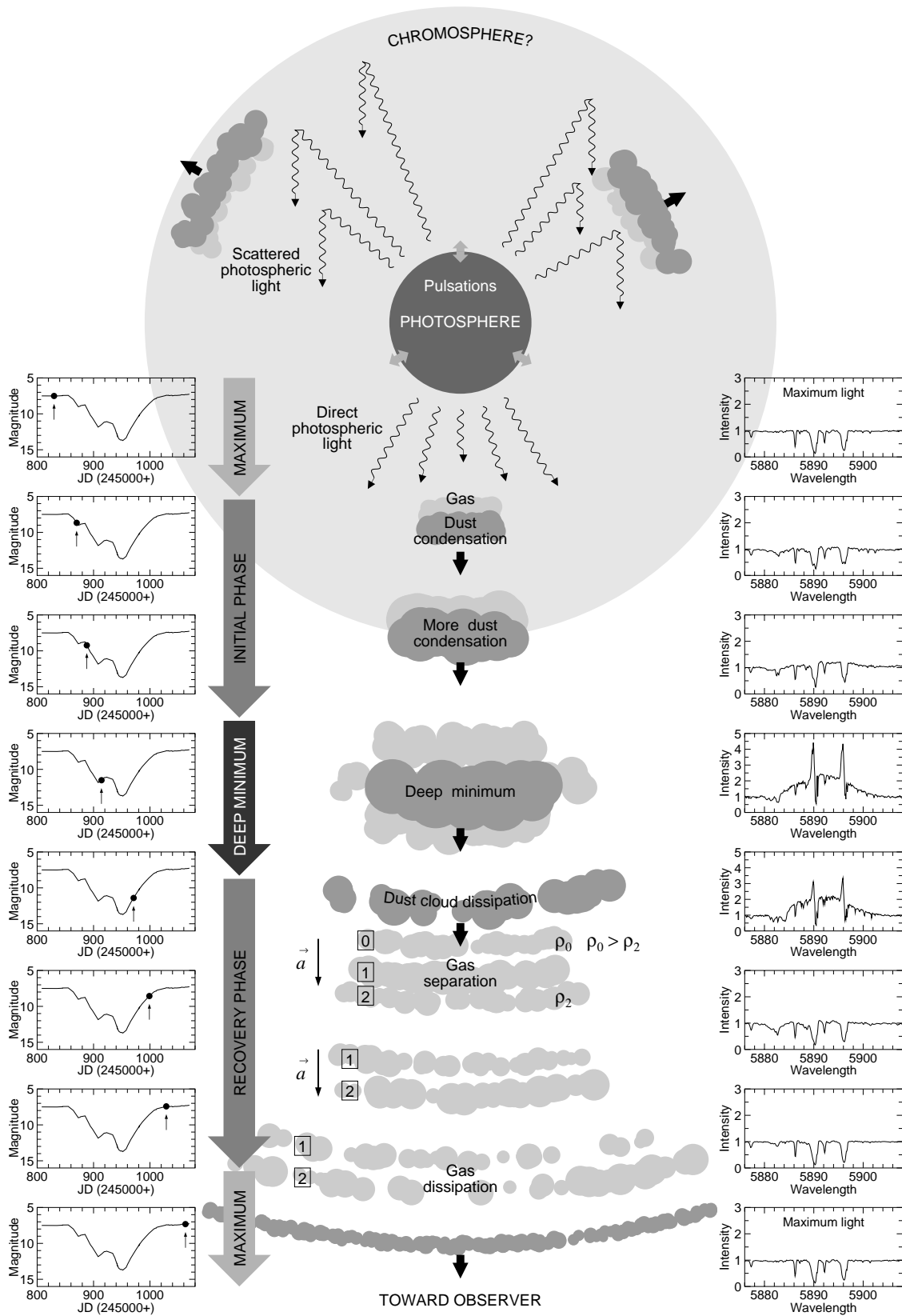
Figure 5.4: *Schematic diagram of the evolution of the high-velocity absorption during an RCB decline.*

velocity of the dust cloud of a few hundreds $km\,s^{-1}$. The dust cloud with a typical velocity of 300 $km\,s^{-1}$ in 250 days (the duration of the decline of e.g. S Aps) would move out to about $100R_*$. That would correspond to the position of the circumstellar shell. In addition, a dust cloud moving so fast would disrupt the circumstellar shell (Cottrell et al. 1990). Therefore, the dust cloud either does not move so fast, or it is not associated with the gas producing the HVA. Since the high-velocity absorption appears only during a decline, it is more possible that some mechanism reduces the initial acceleration of the dust. Rao et al. (1999) analysed the acceleration of the cloud as a function of the gas-to-dust ratio. They concluded that the high number of collisions between the dust grains and atoms (ions) of the gas during the initial stage of the decline (while the dust-to-gas ratio is still low) can slow down the cloud. In addition, the gas density in the cloud is higher close to the star. During the recovery phase, when the dust cloud starts dispersing, the number of collisions is much less and the dust-to-gas ratio may change. In this scenario the broad high-velocity absorption component (see Chapter 3) with the smallest blue shift, appearing for the short time during the decline, originates from the densest and slowest region of the gas cloud (cloud marked with ρ_0 in Figure 5.4). That component disappears soon after the separation of the gas cloud and the components from the other parts of the cloud remain. Although this is presented in Figure 5.4 as the disappearance of the cloud ρ_0, such a behaviour is difficult to explain, since one does not expect that the densest region dissipates first.

The HVA can also be explained using the model of RCB stars based on a bipolar nebula (Rao & Lambert 1993; Clayton et al. 1997). The gas and dust may be ejected radially by the radiation pressure and this can produce the blue-shifted NaI D absorption.

This discussion on the origin and evolution of various decline features and comparison with existing RCB models concludes the analysis of the decline spectra. Some other characteristics of RCB declines that can be obtained from the photometry will be examined in the next chapter.

Chapter 6

Extinction properties of the dust causing the RCB declines

6.1   Studying the properties of the RCB dust

The previous three chapters discussed the photometric and spectroscopic characteristics of the declines of RCB stars. In this chapter the extinction properties of the material causing the declines will be considered, using the recovery phase photometry of a number of RCB stars obtained from the last twelve years.

The R Coronae Borealis stars are hydrogen-deficient carbon-rich supergiants, with a characteristic pattern of variability. A significant amount of carbon dust is created in their atmospheres at random intervals, causing the photospheric brightness to drop by up to six magnitudes in a few weeks. Therefore, these stars provide a unique opportunity to study the nature and evolution of the dust material obscuring the photosphere during the decline phase. It should be emphasized that the RCB stars offer a special environment for studying the carbon grains, quite different from 'normal' carbon stars, which are both carbon and hydrogen rich.

Studying the properties of the RCB dust can also contribute to a better understanding of the characteristics of the interstellar medium (ISM), since the material ejected from the RCB (and other post-AGB) stars is, in fact, returned to the ISM. It is known (Mathis 1990) that the interstellar (IS) grains have been exposed to many complex chemical reactions during their lifetimes, being included within molecular clouds and cycled back into the diffuse ISM many times. Therefore, it is important to study the properties of the dust grains as soon as they are ejected from stars, i.e. before they are modified by their interaction with the interstellar medium. A typical IS extinction curve (see Figure 6.5) is characterized by a distinct peak in the UV region, at a wavelength of 2175 Å ($1/\lambda \approx 4.6$ μm^{-1}). This corresponds to relatively small *graphite* particles of ~ 0.02 μm (Scheffler & Elsässer 1987). However, assuming only particles of this size turns out to be insufficient to fit the extinction

curve in the visual region, where considerably larger graphite grains ($\sim 0.05\,\mu$m) are required. The position of the UV peak varies very little between the diffuse ISM and more dense IS clouds, which places some constraints on theoretical models of the IS grains.

A limited number of studies of the extinction properties of the RCB dust can be found in the literature. The UV extinction curves have been obtained for only a few RCB stars (RY Sgr: Clayton et al. 1992b; R CrB: Holm et al. 1987, Hecht et al. 1984; V348 Sgr: Jeffery 1995, Drilling et al. 1997, Hecht et al. 1998). In addition, the extinction curves of a few hydrogen-deficient (HdC) stars and other similar objects (such as the Abell 30 nebula) have been compared with the extinction curves of the dust causing the RCB declines (Jeffery 1995). They all show a peak near 2400 Å, which differs from the typical position obtained from the ISM (2175 Å). Also, the overall extinction at shorter wavelengths in the RCB dust appears less than in the ISM. The best agreement between the observed extinction curves for the RCB stars and theoretical models for different grains can be obtained for *amorphous* carbon. However, the amorphous grain model fails to match the far UV extinction and cannot explain the observed variations from one star to another. There have been some attempts to solve this problem by introducing other materials, such as fullerenes and fulleranes (Jeffery 1995) and graphite grains (Zubko 1997), but neither of these models provides satisfactory agreement with the observations in all wavelength regions.

In this chapter the extinction curves in the *UBVRI* region obtained from the recovery phase photometry of a number of declines of nine RCB stars will be analysed. The results will then be compared with the extinction curves obtained from the UV spectra of RY Sgr and R CrB, the interstellar medium and the laboratory data for different particles.

The extinction curve of the RCB dust

Both the photometric magnitudes and colours show significant changes during an RCB decline. The light curve asymmetry, with a rapid decline and a slow recovery, is accompanied by unusual colour behaviour. A noticeable colour excess in $B-V$, $U-B$, $V-R$ and $V-I$ is always observed during the recovery phase (see e.g. Figure 3.1, Chapter 3). However, significantly smaller colour changes are usually found during the initial decline stage, when the brightness is dropping rapidly by several magnitudes.

Attempts have been made to explain such colour behaviour by introducing some special optical properties of the dust causing the decline (Wing et al. 1972). However, Pugach (1991) demonstrated that the seeming differences in the optical properties of the dust during the initial and recovery phases can be due to the appearance and expansion of a dust cloud above the surface of the star. In such a case there is no need to introduce any exotic properties of the dust, and the asymmetric colour behaviour during an RCB decline can be explained using similar optical properties for the RCB dust as for the ISM.

In determining the optical properties of the dust around the RCB stars one has to make

sure that the dust distribution is uniform over the entire stellar disc. Otherwise, any partial coverage of the photosphere by a localized dust cloud (which is the case during the initial stages of the decline) will result in an overestimation of the slope in the $(V, B - V)$ plane (see Section 6.2). One can assume that the conditions of a uniform distribution are fulfilled during the recovery phase (a few magnitudes below the maximum), when the dust cloud covers the entire photosphere.

Another problem in determining the extinction curve of the newly formed dust (i.e. generated during the current decline) is that the total extinction is also affected by other factors, such as the permanent circumstellar component made of the 'old' remnant dust at $T_{\mathrm{eff}} \approx (500 - 900)$ K, as well as the constant interstellar component. In addition, the appearance and evolution of the circumstellar emission can introduce further difficulties in interpreting the RCB extinction curves.

The normal (I_λ^{N}) and obscured (I_λ^{O}) stellar intensities can be expressed by the following two equations (Zubko 1997):

$$I_\lambda^{\mathrm{N}} = \left[(I_\lambda + I_\lambda^{\mathrm{em,n}}) e^{-\tau_\lambda^{\mathrm{od}}} + I_\lambda^{\mathrm{so}} \right] e^{-\tau_\lambda^{\mathrm{is}}}, \tag{6.1}$$

$$I_\lambda^{\mathrm{O}} = \left[(I_\lambda e^{-\tau_\lambda} + I_\lambda^{\mathrm{sn}} + I_\lambda^{\mathrm{em,o}}) e^{-\tau_\lambda^{\mathrm{od}}} + I_\lambda^{\mathrm{so}} \right] e^{-\tau_\lambda^{\mathrm{is}}}, \tag{6.2}$$

where I_λ is the intrinsic stellar radiation, I_λ^{so} and I_λ^{sn} are the intensities of the stellar light scattered in the direction towards the observer by the old and newly formed dust, $I_\lambda^{\mathrm{em,n}}$ and $I_\lambda^{\mathrm{em,o}}$ are the intensities of the circumstellar emission in the non-obscured and obscured cases, while τ_λ, $\tau_\lambda^{\mathrm{od}}$ and $\tau_\lambda^{\mathrm{is}}$ represent the optical depths of the newly formed dust cloud, the remnant dust shell and the interstellar dust, respectively. Equation (6.2) applies only when the entire stellar disc is covered by the dust cloud responsible for the current decline. One can also assume that the remnant dust shell is approximately in a steady state, which is consistent with infrared observations (Feast 1979).

It can be demonstrated that the contributions of both the circumstellar emission and the radiation scattered by the old circumstellar dust during a typical decline may be neglected relative to the intrinsic stellar radiation in the visible and ultraviolet regions (Zubko 1997). In this case, the terms $(I_\lambda^{\mathrm{em,n}} e^{-\tau_\lambda^{\mathrm{od}}} + I_\lambda^{\mathrm{so}})$ and $(I_\lambda^{\mathrm{em,o}} e^{-\tau_\lambda^{\mathrm{od}}} + I_\lambda^{\mathrm{so}})$ become negligible in Equations (6.1) and (6.2), respectively. Then the extinction due to the new dust cloud can be expressed as the ratio of the obscured and unobscured intensities:

$$\frac{I_\lambda^{\mathrm{O}}}{I_\lambda^{\mathrm{N}}} = e^{-\tau_\lambda} + \frac{I_\lambda^{\mathrm{sn}}}{I_\lambda}. \tag{6.3}$$

This method is generally used for deriving the ultraviolet extinction curves from spectra obtained at maximum light and during the recovery phases of RCB declines. A similar approach can also be applied to photometry, using the magnitude-colour and colour-colour diagrams. When these diagrams are constructed relative to the light maximum, any permanent contribution to the extinction cancels out, as will be explained in the following section.

6.2   Recovery phase photometry

The photometric observations of nine RCB stars (see Table 6.1) in the last twelve years (1986–1998) have been obtained in either the *UBV* or *UBVRI* regions using the two 0.6-m telescopes equipped with automated single channel photometers at MJUO (see Chapter 2). The photometry was used to analyse the colour changes during the whole declines, and especially during the recovery phases. The characteristic behaviour of the photometric colours from the 1998 decline of V854 is presented in the magnitude-colour diagrams in Figure 6.1. A similar colour behaviour was observed by Alexander et al. (1972) and Cottrell et al. (1990). All diagrams show a characteristic 'loop' covering the entire decline phase. As the star approaches its maximum brightness (during the late recovery stage) the data points tend to follow an *asymptote*, as indicated by a straight line in each of the diagrams in Figure 6.1. The asymptotic approach to the normal brightness has been observed in all RCB declines.
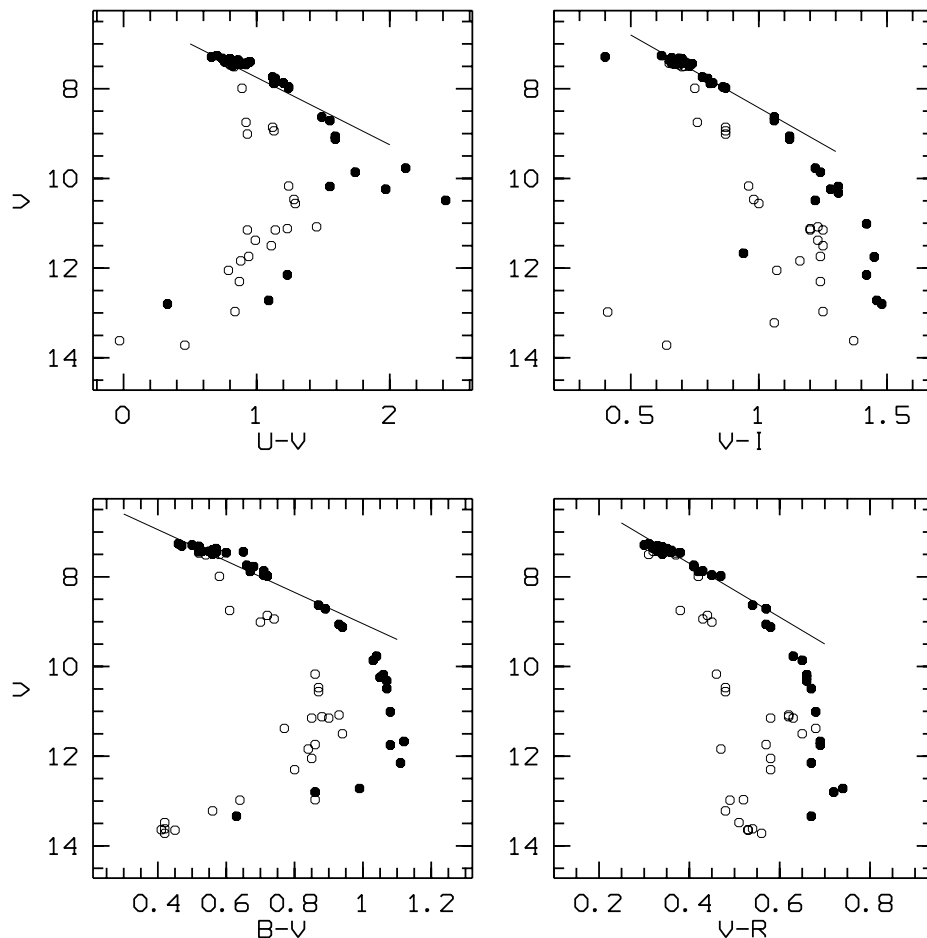
Figure 6.1: *The magnitude-colour diagrams for the 1998 decline of V854 Cen. Open circles represent the initial decline phase, while filled dots are used for the recovery phase. The asymptotes corresponding to the late recovery phase are also plotted.*
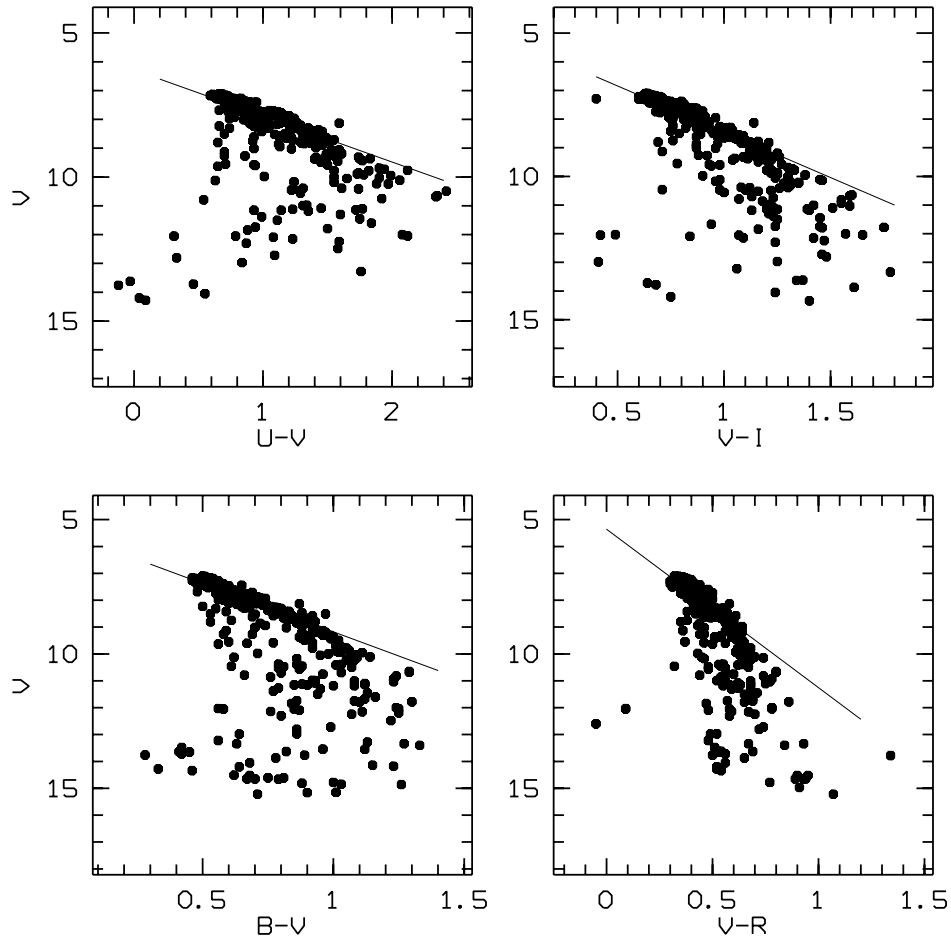
Figure 6.2: *The magnitude-colour diagrams for nine different declines of V854 Cen. The asymptotic lines corresponding to the late recovery phase are also plotted.*

Moreover, the inclination of the asymptotic line is independent of the depth of the decline and is constant for all RCB stars (see Figures 6.2 and 6.4). The asymptote represents a common line along which the colour indices would vary if the star brightness faded due to a total obscuration by a uniform dust cloud.

In order to determine the asymptotic slope of the data points in the magnitude-colour diagrams, as explained above, one has to make sure that only the points from the late recovery phase are used, by rejecting all data points that fall below a certain magnitude threshold. The threshold used in this analysis has been chosen depending on the actual depth of the decline. It is mainly between one and two magnitudes below the maximum, when the data points roughly follow a straight line in the magnitude-colour diagram. The magnitude-colour and colour-colour diagrams have been examined for all declines of each star separately. As an example, the declines of V854 Cen are presented in Figure 6.3. In addition, all declines of all RCB stars together are shown in Figure 6.4. In this case the average magnitude at maximum light has been subtracted from the photometric data for

Table 6.1: *The line slopes from the magnitude-colour and colour-colour diagrams of the nine RCB stars analysed in this chapter. N_d represents the total number of declines used in the analysis of each star.*

Star (N_d)	T_{eff} (K)	R_V	$\frac{\Delta V}{\Delta(U-V)}$	$\frac{\Delta V}{\Delta(V-R)}$	$\frac{\Delta V}{\Delta(V-I)}$	$\frac{\Delta(U-V)}{\Delta(B-V)}$	$\frac{\Delta(V-R)}{\Delta(B-V)}$	$\frac{\Delta(V-I)}{\Delta(B-V)}$
S Aps (3)	5000	4.0 ± 0.2	1.4 ± 0.2	7.4 ± 0.3	3.7 ± 0.2	2.3 ± 0.1	0.5 ± 0.1	1.0 ± 0.1
U Aqr (1)	5500	3.3 ± 0.4	1.3 ± 0.3			2.1 ± 0.1		
UW Cen (2)	6800	3.0 ± 0.3	1.3 ± 0.2	5.7 ± 0.2		2.2 ± 0.1	0.3 ± 0.1	
V854 Cen (9)	7000	3.6 ± 0.2	1.6 ± 0.2	5.9 ± 0.3	3.2 ± 0.2	1.9 ± 0.1	0.57 ± 0.10	1.1 ± 0.10
RZ Nor (2)	7000	3.4 ± 0.3	1.5 ± 0.2			2.0 ± 0.1		
RT Nor (1)	7000	3.4 ± 0.4	1.3 ± 0.3			2.4 ± 0.3		
RS Tel (4)	7000	4.6 ± 0.2	1.8 ± 0.2			2.4 ± 0.1		
V CrA (2)	7000	3.7 ± 0.3	1.5 ± 0.2			2.4 ± 0.1		
RY Sgr (2)	7000	2.6 ± 0.3	1.0 ± 0.2	5.4 ± 0.5	2.8 ± 0.2	2.4 ± 0.1	0.5 ± 0.10	0.9 ± 0.1
All stars together (26)		3.2 ± 0.1	1.2 ± 0.1	6.2 ± 0.2	3.1 ± 0.1	2.17 ± 0.04	0.48 ± 0.05	1.0 ± 0.05

each star, so that all measurements have the same zero point. The line slopes from these diagrams are presented in Table 6.1. The uncertainties in the slopes are affected by the measurement errors in the photometry, but also by the amplitude variations (pulsations) both in stellar magnitudes and colours, especially in RY Sgr ($\Delta V \sim 0^m\!.6$).

The normalized extinction[1] of the RCB dust, A_λ/A_V, has been calculated from the equation:

$$\frac{A_\lambda}{A_V} = 1 + \frac{E(m_\lambda - V)}{A_V} \tag{6.4}$$

where A_V (the total extinction in V) can be expressed in terms of the reddening factor (R_V):

$$R_V = \frac{A_V}{E(B-V)}. \tag{6.5}$$

One can use this relation to obtain the visual absorption A_V from the colour excess $E(B-V) = (B-V) - (B-V)_o$ alone. Substituting A_V from Equation (6.5) into the right-hand side of Equation (6.4) one obtains:

$$\frac{A_\lambda}{A_V} = 1 + \frac{1}{R_V}\frac{E(m_\lambda - V)}{E(B-V)} = 1 + \frac{X_\lambda}{R_V}, \tag{6.6}$$

where the colour excess $E(m_\lambda - V)$ now appears normalized with respect to $E(B-V)$. The ratio $X_\lambda = E(m_\lambda - V)/E(B-V)$ can be obtained as the slope in the colour-colour diagrams, $\Delta(m_\lambda - V)/\Delta(B-V)$, during the recovery phase. On the other hand, the reddening factor, R_V, can be obtained from the $(B-V, V)$ diagram, as the slope $\Delta V/\Delta(B-V)$. A value of

---

[1] For a more detailed explanation of some basic extinction law quantities see Appendix D.
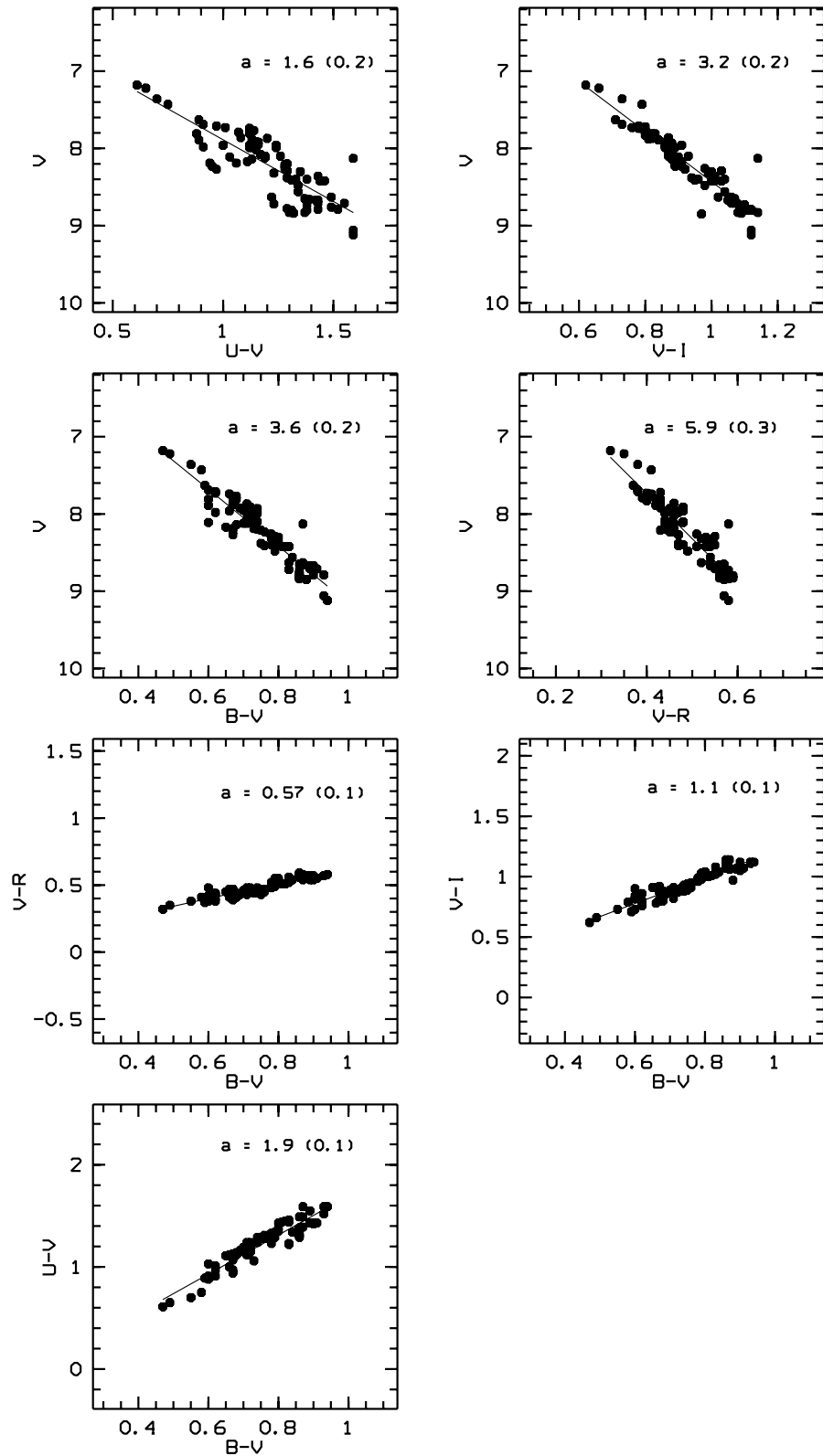
Figure 6.3: *The magnitude-colour and colour-colour diagrams from the recovery phases of nine declines of V854 Cen. The slopes, a, of the lines fitted to the data points are indicated (with their r.m.s. errors) in each diagram.*
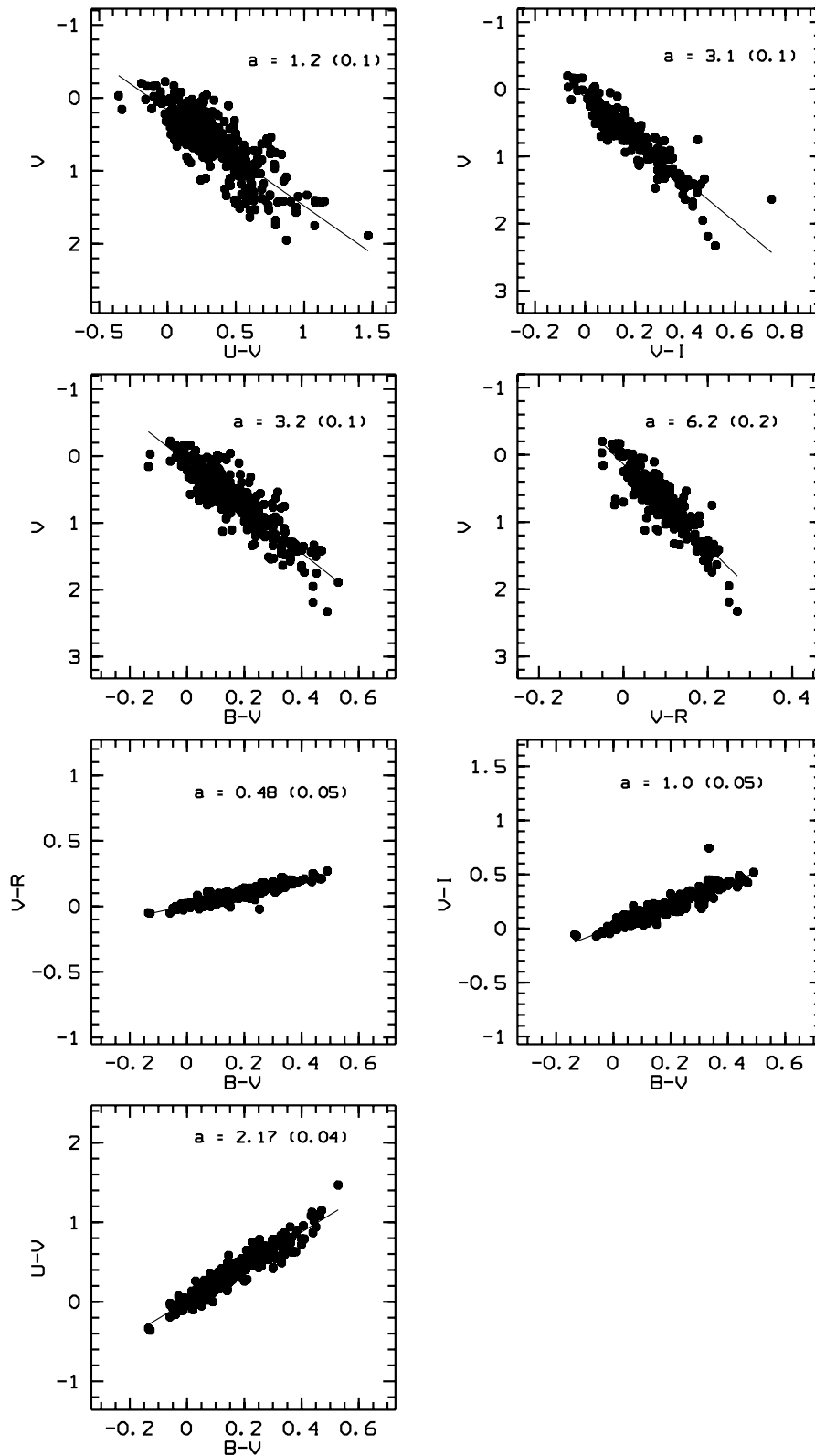
Figure 6.4: *The magnitude-colour and colour-colour diagrams for all observed RCB stars. The average magnitude (or colour) at light maximum has been subtracted from all measurements in order to bring them to the same zero point.*

Table 6.2: *The normalized extinction A_λ/A_V for the nine RCB stars analysed in this chapter.*

Star	A_U/A_V	A_B/A_V	A_R/A_V	A_I/A_V
S Aps	1.59 ± 0.1	1.25 ± 0.1	0.87 ± 0.10	0.74 ± 0.10
U Aqr	1.64 ± 0.2	1.31 ± 0.2		
UW Cen	1.75 ± 0.2	1.34 ± 0.2	0.89 ± 0.1	
V854 Cen	1.52 ± 0.1	1.28 ± 0.1	0.84 ± 0.10	0.7 ± 0.1
RZ Nor	1.59 ± 0.2	1.29 ± 0.2		
RT Nor	1.73 ± 0.2	1.30 ± 0.2		
RS Tel	1.52 ± 0.1	1.21 ± 0.1		
V CrA	1.63 ± 0.2	1.27 ± 0.2		
RY Sgr	1.94 ± 0.3	1.39 ± 0.3	0.82 ± 0.2	0.64 ± 0.2
All stars together	1.67 ± 0.1	1.31 ± 0.1	0.85 ± 0.05	0.69 ± 0.05

$R_V = 3.2 \pm 0.1$ has been derived from all RCB stars together, as shown in Figure 6.4. For individual RCB stars, values in the range $2.6 \leq R_V \leq 4.6$ have been found (see Table 6.1). One can conclude that the reddening factor during the recovery phase of an RCB decline has a value quite close to the interstellar medium, which is about 3.1 (see Appendix D). It should be noted that during the initial decline stages the reddening factor takes much higher values of about 10 to 20 (Pugach 1984). The values of the extinction, A_λ/A_V, and their uncertainties obtained using Equation (6.6) are listed in Table 6.2.

The uncertainty in A_λ/A_V cannot be derived directly from Equation (6.6), since the quantities X_λ and R_V are correlated. However, taking into account that $X_\lambda = \Delta(m_\lambda - V)/\Delta(B - V)$ and $R_V = \Delta V/\Delta(B - V)$, the whole ratio X_λ/R_V can be expressed as:

$$\frac{X_\lambda}{R_V} = \frac{\Delta(m_\lambda - V)}{\Delta V}, \tag{6.7}$$

which represents the slope of the linear fit to the data points in the $(m_\lambda - V, V)$ plane. The standard error of this slope is therefore the uncertainty in A_λ/A_V.

Discussion

A comparison can now be made between the extinction properties of the RCB dust in the optical and ultraviolet wavelength regions. The values of A_λ/A_V versus λ^{-1}, as obtained from the sample of nine RCB stars, are plotted in Figures 6.5 and 6.6, together with the interstellar extinction (IS) and various observational and laboratory data. The IS extinction was obtained from the analytical relation: $A_\lambda/A_V = a(x) + b(x)/R_V$ (Cardelli et al. 1989).
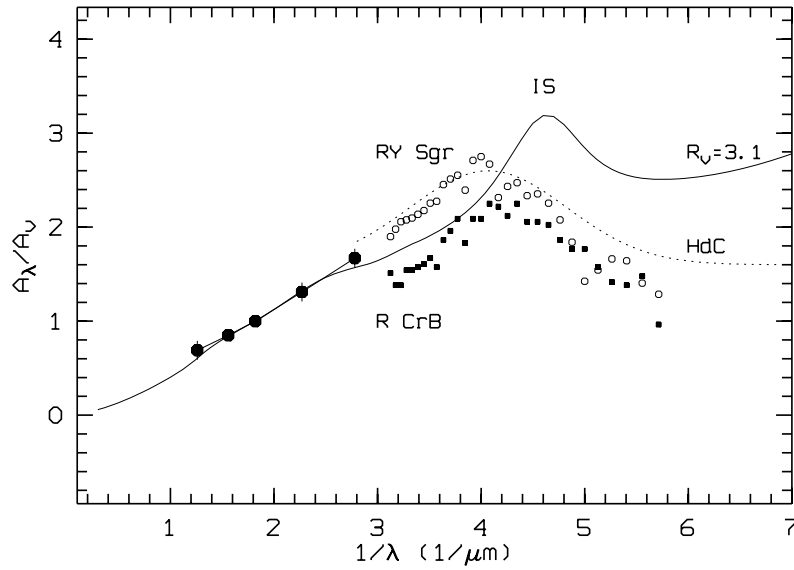
Figure 6.5: *The observed extinction for the nine RCB stars from this work (filled dots), compared with the IS extinction curve (bold line), HdC extinction (dashed line) and UV data for RY Sgr (open circles) and R CrB (filled squares).*
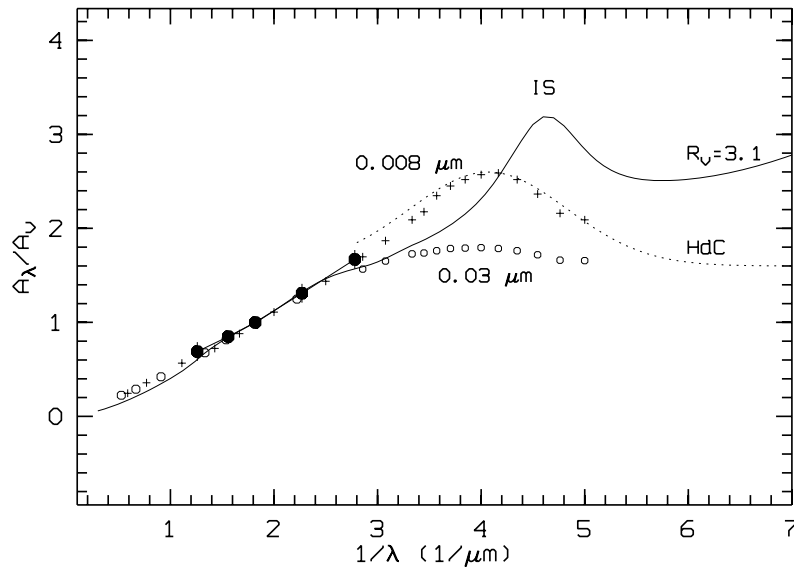
Figure 6.6: *The observed extinction for the nine RCB stars from this work (filled dots), compared with the IS extinction curve (bold line), HdC extinction (dashed line) and laboratory data for amorphous carbon particles of 0.008 μm (crosses) and 0.03 μm (open circles).*

The curve represents the mean IS extinction law (for $R_V = 3.1$), which stays close to the observational data obtained by Seaton (1979) for $1/\lambda < 7~\mu\mathrm{m}^{-1}$. The IS extinction at longer wavelengths ($1/\lambda \lesssim 2~\mu\mathrm{m}^{-1}$) is almost independent of the direction of the line of sight and is roughly linear ($A_\lambda/A_V \sim 1/\lambda$).

The UV extinction data for two cool RCB stars, RY Sgr and R CrB shown in Figure 6.5, were taken from Hecht et al. (1984). They both exhibit a strong extinction peak near $\lambda = 2400$ Å ($1/\lambda = 4.1~\mu\mathrm{m}^{-1}$), which differs from $\lambda = 2175$ Å ($1/\lambda \approx 4.6~\mu\mathrm{m}^{-1}$) in the ISM. A similar extinction peak in the UV region has been obtained from the mean extinction curve of five HdC stars (Jeffery 1995), also shown in Figures 6.5 and 6.6. The HdC extinction curve represents a gaussian fit (FWHM = $1.79~\mu\mathrm{m}^{-1}$, $1/\lambda_\mathrm{cen} = 4.07~\mu\mathrm{m}^{-1}$) through observations of two cool RCB stars (RY Sgr and R CrB, $T_\mathrm{eff} \sim 7000$ K) and two hot ones (V348 Sgr and MV Sgr, $T_\mathrm{eff} \sim 20000$ K). The data also include a high-excitation planetary nebula (Abell 30), in which the hot central star seems to have recently ejected a number of hydrogen-poor dust clouds.

The best agreement between the observed extinction curves for the RCB stars and the theoretical models of different dust grains can be obtained for amorphous carbon. The laboratory data for amorphous carbon grains of two different sizes, 0.03 μm and 0.008 μm (Borghesi et al. 1985), are shown in Figures 6.6. The UV extinction peak of the amorphous carbon coincides with the RCB data in the same region. The curves also agree with the UBVRI extinction obtained from the recovery phases of the sample of nine RCB stars analysed in this chapter. The normalized absorption for the observed RCB stars in the U region differs slightly from the mean IS curve (see Figure 6.6). The value appears to be closer to the mean UV extinction curve for the HdC stars, as well as the laboratory data for amorphous carbon grains of 0.008 μm.

The difference in the positions of the UV peaks in the RCB dust and IS extinction curves can be explained by the different nature of the dust particles responsible for the extinction in these two cases. As already mentioned above, the UV peak in the IS extinction curve is mainly caused by graphite particles, which can form only in the presence of hydrogen, normally found in the ISM. On the other hand, the amorphous carbon can form in the hydrogen-poor atmospheres of RCB stars (Hecht et al. 1984, Hecht 1991). Comparing the extinction curves of the RCB dust with the ISM, one can also notice that the overall extinction in the far UV is considerably lower in the RCB dust than in the ISM. This lower extinction is closer to the behaviour of the dense ISM with higher values ($R_V > 3.1$) of the reddening factor.

It can be concluded that the extinction properties of the dust causing the RCB declines can be reliably determined from the spectroscopy and/or photometry during the recovery phase close to light maximum. One can assume that the dust is distributed uniformly during this phase. The initial decline stage does not show any real characteristics of the dust, since the photosphere is not uniformly obscured by the dust cloud and the emission lines may

influence the photometric colours.

Although the extinction curve in the UBVRI region is not a good indicator of the type and size of particles, the present data show that the material causing the RCB declines has extinction properties similar to that of the interstellar medium. The reddening parameter (R_V) for the sample of nine cool RCB stars is in the range between 2.5 and 4.6, close to ~ 3.1 found in the ISM. In order to obtain more precise characteristics of the RCB dust, one has to examine the extinction data in the UV region, where the extinction curves are more sensitive to the nature of the material.

Chapter 7

Conclusions

This thesis presents the results of a research project undertaken at the University of Canterbury and Mt John University Observatory (MJUO) in order to examine the decline characteristics of a number of southern R Coronae Borealis (RCB) stars. These stars exhibit a unique variability, with characteristic decline phases occurring at irregular intervals, which are believed to be caused by dust cloud obscuration. However, both the unique nature of the RCB variability and the evolutionary status of these stars remain unsolved. Only a relatively small number of extensive spectroscopic studies of RCB declines can be found, mainly due to the irregularity and unpredictability of these events. A world wide campaign (Cottrell 1996) was suggested in order to provide simultaneous photometric, spectroscopic and polarimetric coverage throughout the declines of a number of RCB stars, which would enable a more detailed examination of the nature of the decline phase. As part of this campaign, nine southern RCB stars and three HdC stars were chosen for simultaneous photometric and spectroscopic observations at MJUO. The majority of stars from the programme list are typical RCB examples, with $T_{\mathrm{eff}} \sim 7000$ K. Two cool RCB stars (S Aps and U Aqr), with $T_{\mathrm{eff}} \sim 5000$ K, were also included. A total of six declines of different RCB stars were observed during the observational programme (1996 April till 1998 October).

Regular photometric observations, as part of the long-term monitoring of variable stars at MJUO, have provided the $UBVRI$ photometry and have served as alerts for the decline events. Intensive spectroscopic observations during the decline phase were obtained using the 1-m cassegrain reflector and either the medium-resolution (MRS) or the échelle spectrograph. The stars were observed less intensively at light maximum. Only two stars from the list (RY Sgr and V854 Cen) are bright enough to be observed using the échelle spectrograph both at light maximum and throughout the decline phase (down to $\sim 10^{\mathrm{m}}$). However, of these two only V854 Cen went into decline during the observational programme. All other decline events were mainly observed using the MRS.

The medium-resolution spectrograph was used intensively for the first time during this observing programme. Numerous tests were performed in order to examine the character-

istics of the spectrograph. Optimal combinations of different diffraction gratings and filters were determined, so that extensive spectroscopic coverage in the range between 3800 Å and 9000 Å was possible. In addition, some other characteristics of the spectrograph, such as the variations of the focus across the CCD chip and its dependence on the ambient temperature, were also studied. A long slit was used in order to record the sky emission lines simultaneously with the stellar spectrum, so that the contribution of the sky could be eliminated during the reduction procedure. This was especially important during the long exposures of faint RCB stars.

Although the declines of different RCB stars observed for this thesis had different durations and depths, a number of common photometric and spectroscopic characteristics were noticed. The majority of the declines (V854 Cen, S Aps, UW Cen and V CrA) exhibited complex light curves with a number of successive fadings and partial recoveries. The shallowest of them (RS Tel) was only one magnitude deep, while the deepest ones (V854 Cen and UW Cen) were about seven magnitudes deep. The shortest declines (RS Tel and RZ Nor) were about three months long. On the other hand, the decline of V CrA was four years long (only partially overlapping with the observational programme of this thesis). The declines of RS Tel and RZ Nor, being both shallow and relatively short, were characterized by mainly symmetric light curves, with the duration of the initial stage approximately equal to the duration of the recovery phase. On the other hand, more extended declines of V CrA, S Aps and V854 Cen exhibited typical asymmetric RCB light curves with shorter, rather complex initial stages and longer, relatively smooth and steady recoveries to light maximum. In addition, the multiple fadings of V854 Cen were found to be correlated with the pulsation cycle of the star.

A significant reddening of the colours, especially during the recovery phase, was observed in all declines. Some reddening was noticed during the initial declines as well. On the other hand, a strong blueing in the $U - B$ and $B - V$ colours was observed during the deepest decline phase of V854 Cen. This was further supported by spectroscopy showing the appearance of the strong broad CaII H&K components in emission during this phase, making a significant contribution to the total flux in the blue.

The declines of S Aps, UW Cen and V CrA were only partially covered by spectroscopic observations, while a more detailed coverage was obtained for V854 Cen, RZ Nor and RS Tel. The observations confirm a similar behaviour of the spectral lines during all declines. However, the spectroscopic changes are not uniquely determined by the variations in the stellar magnitude. For example, in relatively shallow declines of RS Tel and RZ Nor, the changes were seen only around the NaI D lines, while various additional features (around H$_\alpha$, CaII IR triplet and CI lines) were detected in the initial decline of V854 Cen (of a similar depth). In a similar way, the photospheric spectrum appears fully recovered at the 4$^{\rm m}$-deep partial recovery phase of UW Cen, while it is still filled in during the similar 2$^{\rm m}$-deep phase of V CrA.

The photospheric spectrum exhibits various changes during the decline, characterized by weakening (filling in) of the absorption lines as the star gets fainter. In the observed declines this is mainly caused by the sharp or broad emission superimposed on the photospheric absorption lines.

The appearance of the strong NaI D spectral lines, with a complex profile including various sharp and broad components, is the common feature of all RCB declines. The only exception is the shallow decline of RS Tel, where the NaI D emission was not detected. The sharp NaI D components, visible throughout the entire decline phase, behave as other sharp lines from the E_2 group, with a characteristic blue shift and flux distribution and a time scale of 50–100 days. The line flux starts decaying during the initial decline phase indicating a possible obscuration of the emitting region by the dust cloud. The position of the NaI D emitting region, as calculated using the acceleration of the dust cloud estimated from the high-velocity NaI D components, is in the interval between $3R_*$ and $5R_*$. This was calculated assuming the initial position of the dust cloud of $2R_*$.

The existence of the broad emission lines indicates the presence of a hot, high-velocity gas in the region around an RCB star. The broad NaI D components vary in strength from one star to another. They appear about twice as strong in V854 Cen compared with the other stars. This indicates a possible correlation between the frequency of the declines and the strength of the broad NaI D emission. The strongest broad emission is detected in V854 Cen, which exhibits very frequent declines. In each of the declines a significant amount of gas responsible for the broad emission can be formed. However, if the declines are not frequent enough, the gas would after some time become very extended and diluted[1], which would produce a much weaker broad emission. The broad lines are visible throughout the whole decline phase with a mainly constant flux indicating that they are permanent features, not affected by the dust cloud formation. This is in contrast with the behaviour of the sharp emission lines, whose flux decreases during the decline. Other broad spectral lines (H_α, CaII IR triplet, and MgI triplet), observed during the decline of V854 Cen, show a much smaller base width ($\sim 70-300$ km s^{-1}) compared to the NaI D and CaII H&K lines (~ 1000 km s^{-1}).

The observations of the high-velocity NaI D absorption (HVA) indicate that these lines are associated with the appearance of the dust cloud. The HVA absorption was observed in all declines except for the shallow one of RS Tel. The lines can be seen during various decline phases, from the early initial phase of V854 Cen, throughout the entire decline of most of the other RCB stars. A similar line profile and evolution, typical for the shell absorption, were observed during the recovery phase of all declines. A relatively high radial velocity of the HVA components (ranging from ~ -230 km s^{-1} for V CrA to ~ -400 km s^{-1} for V854 Cen), means that the gas producing these lines must have a circumstellar origin. The lines can be associated with the gas being accelerated during the process of the dust cloud formation.

---

[1]Assuming a velocity of about 300 km s^{-1}, the gas would extend to about $2500\,R_*$ in about 10 years.

In such a case, the lines should be seen mainly during the recovery phase of a deep decline. The existence of the HVA during the initial decline of V854 Cen can be explained by the presence of some gas clouds from previous declines, that have not yet dispersed, or by some clouds located off the line of sight which can drift into view.

When the HVA is analysed as a single complex profile, a constantly increasing blue shift is detected throughout the recovery phase. This can be interpreted as an acceleration of the gas. A range of accelerations was obtained, between 0.5 cm s^{-2} for S Aps and 2 cm s^{-2} for UW Cen. The parameters of the HVA (i.e. the velocity and acceleration) were used to calculate the location of the line emitting regions with respect to the position of the dust cloud formation.

This thesis includes the first almost complete photometric and spectroscopic coverage of a decline of V854 Cen. Various emission features were observed during this decline. The lines were classified into three groups, as the sharp and broad emission and high-velocity absorption. In general, the lines could be included into one of the E_1, E_2 and BL groups, introduced with the first emission line classification by Alexander et al. (1972). The lines from each of these groups were suggested to originate from three distinct regions. However, some additional characteristics of the emission lines that were observed indicate a different origin than suggested by the E_1/E_2/BL model.

The low-excitation sharp emission lines of elements such as BaII, TiII and ScII exhibit typical characteristics of the E_2 region. Their analysis suggests that the lines originate from a region slowly moving away from the star (according to the blue shift of about 3 km s^{-1} relative to the stellar velocity). However, a complex profile of these lines, with one central and two slightly broader side components, seems to indicate the existence of a shell with its outer region expanding faster than the inner parts. While the central component is produced by the inner region, the two side components originate from the two portions of the outer shell, one moving away and the other moving towards the observer. The whole region becomes obscured by the dust cloud during the initial decline phase, according to the decay in the absolute line fluxes, but no interaction with the dust cloud can be noticed. Therefore, the calculated position of the E_2 region is at about $3.5R_*$. The excitation temperature of these lines was found to be about ~ 5600 K for all three components, which is somewhat lower than the photospheric value (~ 7000 K).

The high-excitation lines of CI, OI and MgI, with a characteristic decay time scale typical for the E_1 lines (few weeks), were observed only during the initial decline phase. The lines are red shifted by a few km s^{-1} with respect to the stellar velocity, indicating that they may originate from the photosphere and can be related to the shock triggering the decline.

The forbidden spectral lines of [OI], [CI] and [CaII], that were observed during the 1998 decline of V854 Cen, are an indicator of the existence of a nebula surrounding the star. The lines exhibit a similar blue shift of about ~ 5 km s^{-1} as the lines from the E_2 group. However, their slightly broader profile compared with the other sharp emission lines, as well

as a constant flux distribution, suggest a possibly different origin.

The lines from the C_2 molecular Swan system, which are a clear indicator of a cool emitting region, were detected in emission during the decline of V854 Cen. The lines show characteristics of the E_2 group, with a profile slightly wider than the instrumental one, a blue shift of $\sim 1.5\,\mathrm{km\,s^{-1}}$ with respect to the stellar velocity, and a decay time scale similar to the other E_2 lines. The Swan system can also be seen in absorption, as observed in the deep declines of V854 Cen and S Aps.

The detailed study of the 1998 decline of V854 Cen shows that the emission lines, according to their evolution, can be classified into the E_1, E_2 and BL groups, but they do not necessarily have to originate from the three corresponding regions surrounding the star. The properties of the sharp NaI D lines obtained from a number of declines, and also the characteristics of the low-excitation lines from the 1998 decline of V854 Cen, suggest that the position of the E_2 region is more likely to be closer to the star (between $3R_*$ and $5R_*$), assuming the dust cloud formation at about $2R_*$. On the other hand, the high-excitation lines of CI and OI, classified as E_1 (with a shock-induced red shift) can in fact originate from the photosphere. Finally, the broad lines (BL group) show a constant absolute flux throughout the decline phase and, therefore, the region of their origin is not affected or obscured by the dust cloud causing the decline. More detailed observations, including a larger number of RCB declines, would confirm whether these characteristics are a common feature of all RCB stars.

The extinction properties of the material causing the RCB declines were also analysed by studying the recovery phase photometry of a number of declines of nine programme stars over a longer period of time. The analysis of the magnitude-colour and colour-colour diagrams demonstrates that all declines exhibit a similar asymptotic approach to the normal brightness, with roughly the same line slope that does not depend on the decline depth. Assuming a uniform obscuration of the photosphere by the dust cloud during the recovery phase, the extinction properties of the material were determined. The reddening factor of $R_V \approx 2.5 - 4.6$ was derived, close to the value found in the interstellar medium ($R_V \sim 3.1$).

A number of characteristics of the RCB declines observed and studied in this thesis can be further investigated, by combining the existing data with additional high-resolution spectroscopic observations. For instance, it is still not clear whether the multicomponent structure of the low-excitation sharp emission lines, as observed during the 1998 decline of V854 Cen (Chapter 3) and during the 1995/96 decline of R CrB (Rao et al. 1999), is typical for all RCB stars. Another question is whether the fluxes of various emission lines observed during the RCB declines (low-excitation sharp lines, broad and forbidden lines) stay constant from one decline to another, which would be evidence of their permanent nature. An extensive coverage of a number of declines of V854 Cen would also reveal any expected changes in the NaI D shell components, which have remained unchanged in the last few years. The behaviour of the high-velocity NaI D absorption needs further investigation. The

question still remains how often these lines can appear during the initial decline phase and whether there is any connection between their appearance and the frequency of the declines.

Due to the obvious difficulties in obtaining a sufficient number of high-resolution spectra during the unpredictable and rapidly changing decline phase of an RCB star, it seems that our understanding of these unusual events have advanced rather slowly so far, one small step at a time.

Appendix A

The medium-resolution spectrograph

Table A.1: *Settings for 150 lmm^{-1}.*

Grating tilt (wavelength region)	Order	Filter	Lamps (Exposure time)	
			Comparison	White
35 (5000–7200) Å	2nd	GG475	HeAr (15s)	Tungsten (0.1s)
100 (7000–9200) Å	2nd	RG695	HeNe (2s)	Tungsten (0.1s)
35 (3320–4750) Å	3rd	BG12	HeAr (30s)	Tungsten (15s)

Table A.2: *Settings for 300 l mm^{-1}*.

Grating tilt (wavelength region)	Order	Filter	Lamps (Exposure time)	
			Comparison	White
210 (5100–6200) Å 255 (5700–6800) Å 300 (6400–7500) Å	2nd	GG475	HeAr (30s)	Tungsten (0.2s)
420 (8000–9100) Å 490 (9000–10100) Å	2nd	RG695	HeNe (10s)	Tungsten (1s)
135 (8000–10000) Å	1st	RG695	HeNe (5s)	Tungsten (1s)
255 (3800–4500) Å	3rd	BG12	HeAr (60s)	Tungsten (5s)
330 (4500–5250) Å	3rd	GG420 + BG28	HeAr (120s)	Tungsten (10s)

Table A.3: *Settings for 600* lmm^{-1}.

Grating tilt (wavelength region)	Order	Filter	Lamps (Exposure time)	
			Comparison	White
580 (5200–5800) Å 660 (5750–6300) Å 740 (6300–6850) Å 870 (7000–7550) Å	2nd	GG475	HeAr (60s)	Tungsten (1s)
1020 (8000–8550) Å	2nd	RG695	HeAr (60s)	Tungsten (1s)
420 (8000–9000) Å 490 (9000–10000) Å	1st	RG695	HeNe (5s)	Tungsten (1s)
660 (3800–4200) Å	3rd	BG12	HeAr (120s)	Tungsten (60s)
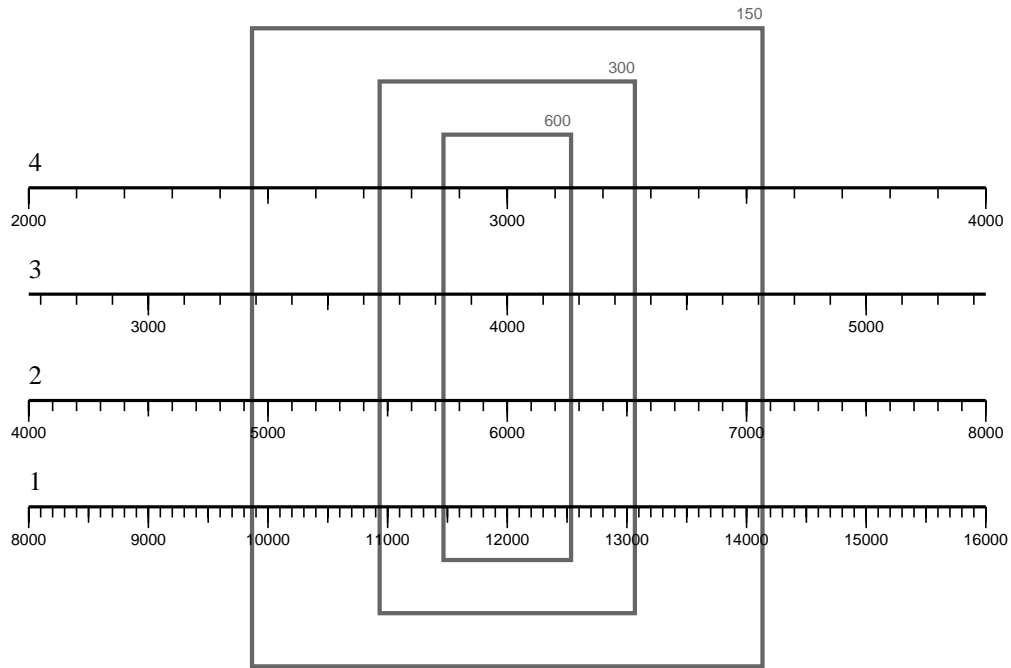
Figure A.1: Four diffraction orders (1–4) of the MRS with the corresponding wavelength scales in angstroms. The three rectangles represent the wavelength ranges covered by different gratings (600, 300 and 150 l mm^{-1}) on the Thomson $576{\times}384$ CCD chip.
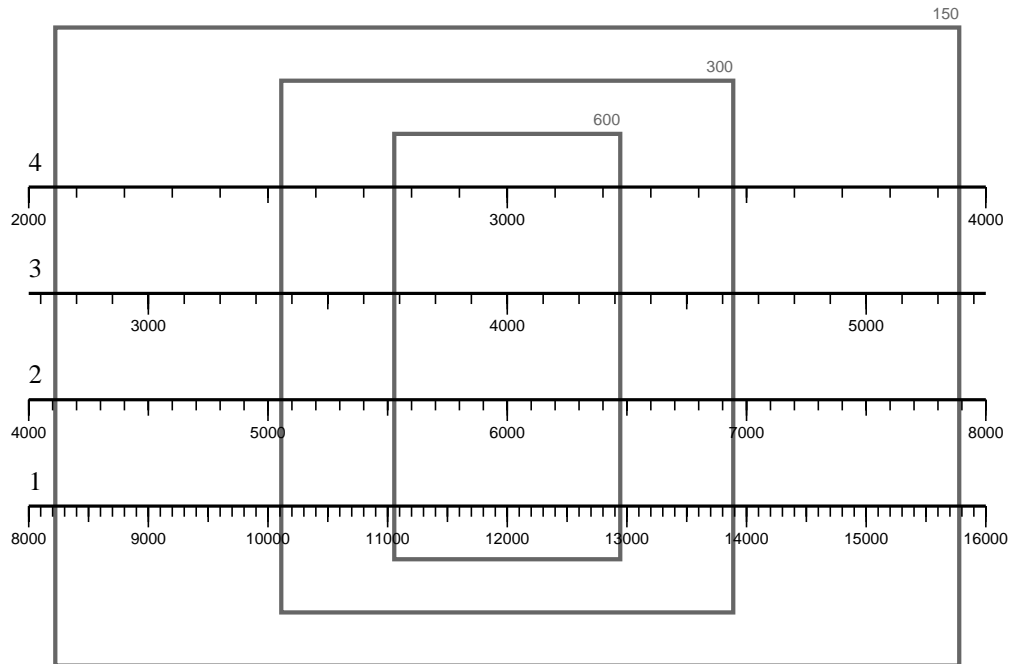
Figure A.2: The same as Figure A.1, but for the SITe $1024{\times}1024$ CCD chip.

Appendix B

Apparent magnitude correction due to interstellar reddening

The measured apparent magnitude (m_λ) can be corrected for the interstellar extinction by using the following formula:

$$m_{\lambda 0} = m_\lambda - A_\lambda, \tag{B.1}$$

where $m_{\lambda 0}$ is the apparent magnitude in absence of extinction, and A_λ is the total extinction in the direction towards the star. The extinction A_λ is proportional to the colour excess $E(B-V)$ and can be calculated from the interstellar extinction curve (Cardelli et al. 1989) as:

$$A_\lambda = [a(x)R_V + b(x)] \times E(B-V), \tag{B.2}$$

where R_V is the reddening factor and $a(x)$ and $b(x)$ are the coefficients defined at $x = 1/\lambda$.

Most of the RCB stars included in this thesis are found relatively close to the galactic plane (with galactic latitudes not exceeding $\pm 10°$ to $20°$), so that they can be significantly reddened. In general, the reddening in the direction towards these stars can be estimated by comparing their flux distribution with the spectra of intrinsically similar objects at higher galactic latitudes, where the reddening can be neglected. The estimated intrinsic V_0 and $(B-V)_0$ for the programme RCB stars have been taken from Lawson et al. (1990). The colour excess $E(B-V)$ can be easily calculated from these values and the existing photometry. It ranges between 0 (for V854 Cen) and 0.56 (for RZ Nor). Only the decline spectra of V854 Cen have been flux-calibrated in this thesis, in which case the interstellar reddening can be neglected.

Appendix C

The uncertainties in spectral line parameters

Isolated spectral lines analysed in this thesis have been modelled as Gaussian functions, using the standard non-linear fitting procedure (Newton-Raphson method) in MIDAS. As a result of the fitting process, three parameters are obtained: the relative intensity (I), position of the line centre (λ_{cen}) and full width at the half maximum ($a = \text{FWHM}$), together with their uncertainties. A typical uncertainty in all parameters is less than 2%. The equivalent width of a Gaussian spectral line is calculated as: $W = D \times I \times a$, where $D = \sqrt{\pi/4 \ln 2}$. One should bear in mind that the parameters I and a are *correlated*, so that the uncertainty in the equivalent width cannot be obtained simply by using a formula for a function of two independent variables. The proper error-propagation method must be used instead (see e.g. Brandt 1999, p. 37). This method requires not only the standard uncertainties for the parameters, but also their correlation matrix, which is obtained as a result of the fitting process. In the case of a single Gaussian fit, the standard error of the equivalent width can be calculated using the following formula:

$$\sigma_W^2 = \left(a^2 \, \sigma_I^2 + I^2 \, \sigma_a^2 + 2 \, a \, I \, \rho_{Ia} \, \sigma_I \, \sigma_a \right) D^2, \tag{C.1}$$

where: σ_I and σ_a are standard errors of the Gaussian parameters and ρ_{Ia} is the correlation coefficient (for a single Gaussian $\rho_{Ia} = -0.5774$).

The error propagation method has also been applied in the case of the three-component Gaussian fits of the low-excitation sharp emission lines in Chapter 2. The full matrix equation has been used:

$$S = J \, \Sigma \, J^{\text{T}}, \tag{C.2}$$

where Σ and S are the covariance matrices of the input and output parameters, respectively, and J is the Jacobian of the transformation.

The uncertainties in the line flux measurements (σ_{F_l}) depend on the uncertainties in the

equivalent width (σ_W) and continuum flux (σ_{F_c}) and has been calculated from:

$$\left(\frac{\sigma_{F_l}}{F_l}\right)^2 = \left(\frac{\sigma_W}{W}\right)^2 + \left(\frac{\sigma_{F_c}}{F_c}\right)^2, \tag{C.3}$$

where a typical uncertainty of the continuum flux at the line position is between 3% and 8%.

The radial velocity error depends only on the uncertainty in the central position of the line ($\sigma_{\lambda_{\rm cen}}$) and has been calculated from:

$$\sigma_{v_r} = \sigma_{\lambda_{\rm cen}} \frac{c}{\lambda_{\rm lab}}. \tag{C.4}$$

Appendix D

The extinction law quantities

The total extinction A_λ in a given bandpass centred at the wavelength λ is defined as the difference between the measured and intrinsic magnitudes in the same wavelength range:

$$A_\lambda = m_\lambda - m_{\lambda,0}. \tag{D.1}$$

The dependence of the extinction on the wavelength is called the *extinction law*.

In practice, it is more convenient to use the *normalized* extinction (X), defined by:

$$X = \frac{E(m_\lambda - V)}{E(B - V)}, \tag{D.2}$$

where $E(m_\lambda - V)$ and $E(B - V)$ are colour excesses:

$$\left. \begin{array}{rclcl} E(m_\lambda - V) & = & (m_\lambda - V) - (m_\lambda - V)_0 & = & A_\lambda - A_V, \\ E(B - V) & = & (B - V) - (B - V)_0 & = & A_B - A_V. \end{array} \right\} \tag{D.3}$$

Instead of using photometric colours, the extinction law can also be expressed directly as the ratio A_λ/A_V. Some relations become more obvious when this form is used. For example, a linear relationship between A_λ/A_V and the reciprocal reddening factor R_V^{-1} has been demonstrated in a wide wavelength range (Cardelli et al. 1989).

The reddening factor, usually used for the interstellar medium, is defined by:

$$R_V = \frac{A_V}{E(B - V)}. \tag{D.4}$$

The best available mean value for R_V is 3.1 ± 0.1 (Seaton 1979, Cardelli et al. 1989). This enables the visual absorption A_V to be obtained from the colour excess $E(B - V)$. However, the reddening factor depends very much on the environment along the line of sight. There are significant deviations from the mean value when the interstellar dust is concentrated in clouds ($4 < R_V < 6$).

Appendix E

Tables and diagrams

Table E.1: *Measured parameters of sharp emission lines throughout the 1998 decline of V854 Cen (see Chapter 3) from the medium-resolution spectra: W_λ – equivalent width, f_{cont} – continuum flux at the line position, F_{line} – line flux and V_{r} – radial velocity.*

Element	λ [Å]	Multiplet	Day number	W_λ [Å]	f_{cont} $[10^{-16}\mathrm{W\,m^{-2}\,Å^{-1}}]$	F_{line} $[10^{-16}\mathrm{W\,m^{-2}}]$	V_{r} $[\mathrm{km\,s^{-1}}]$
TiII	5211.544	103	50	0.372	0.71	0.26	-30.3
			76	0.121	0.76	0.09	
	5226.534	70	50	1.761	0.71	1.25	-27.1
			66	0.502	1.25	0.63	
			67	0.368	1.23	0.45	
			76	0.845	0.77	0.65	
			77	1.159	0.65	0.76	
	5262.104	70	50	0.705	0.71	0.50	-28.6
	5336.809	69	35	0.512	2.82	1.44	
			38	0.686	2.11	1.45	
			50	1.490	0.72	1.07	-29.9
			66	0.575	1.27	0.73	
			67	0.492	1.24	0.61	
			74	0.755	1.06	0.80	
			76	0.795	0.77	0.61	
			77	1.022	0.66	0.67	

Table E.2: *V854 Cen – sharp emission lines from MRS spectra (continued).*

Element	λ [Å]	Multiplet	Day number	W_λ [Å]	$f_{\rm cont}$ $[10^{-16}{\rm W\,m^{-2}\,Å^{-1}}]$	$F_{\rm line}$ $[10^{-16}{\rm W\,m^{-2}}]$	$V_{\rm r}$ $[{\rm km\,s^{-1}}]$
TiII	5381.020	69	31	0.200	4.84	0.96	
			35	0.309	2.82	0.87	
			38	0.463	2.11	0.98	
			50	1.217	0.72	0.88	-27.5
			67	0.426	1.25	0.53	
			74	0.651	1.06	0.69	
			76	0.759	0.77	0.59	
			77	0.823	0.66	0.54	
			103	0.540	0.36	0.19	
			104	0.617	0.41	0.26	
	5418.802	69	31	0.199	4.84	0.96	
			35	0.299	2.83	0.84	
			38	0.314	2.11	0.66	
			50	0.790	0.72	0.57	-27.3
			67	0.244	1.25	0.31	
			74	0.279	1.06	0.30	
			76	0.357	0.78	0.28	
			77	0.416	0.66	0.28	
			104	0.316	0.42	0.13	
	6491.610	91	36	0.257	2.49	0.64	
			36	0.276	2.49	0.69	
			38	0.303	2.07	0.63	
			38	0.292	2.07	0.60	
			39	0.324	1.85	0.60	
			50	0.649	0.76	0.50	-29.4
			50	0.685	0.76	0.52	-32.1
			66	0.190	1.35	0.26	-29.3
			67	0.138	1.31	0.18	
			74	0.186	1.09	0.20	
			74	0.250	1.09	0.27	
			76	0.339	0.78	0.26	
			76	0.228	0.78	0.18	-32.8
			104	0.223	0.48	0.11	
			104	0.193	0.48	0.09	

Table E.3: *V854 Cen – sharp emission lines from MRS spectra (continued).*

Element	λ [Å]	Multiplet	Day number	W_λ [Å]	f_{cont} $[10^{-16}\,\text{W}\,\text{m}^{-2}\,\text{Å}^{-1}]$	F_{line} $[10^{-16}\,\text{W}\,\text{m}^{-2}]$	V_{r} $[\text{km}\,\text{s}^{-1}]$
TiII	6717.911	112	31	0.074	4.42	0.33	
			36	0.110	2.44	0.27	
			50	0.222	0.77	0.17	-25.4
			74	0.058	1.09	0.06	
YII	5200.42	20	50	1.200	0.70	0.85	-28.2
			74	0.531	1.04	0.55	
			76	0.652	0.76	0.50	
			77	0.526	0.65	0.34	
	5205.73	20	50	1.295	0.71	0.91	-23.8
			76	0.751	0.76	0.57	
			77	1.050	0.65	0.69	
	5289.82	20	50	0.235	0.71	0.17	-24.3
	5402.78	35	50	0.628	0.72	0.45	-25.4
			67	0.304	1.25	0.38	
			74	0.263	1.06	0.28	
			76	0.289	0.77	0.22	
			77	0.557	0.66	0.37	
	5473.40	27	50	0.384	0.72	0.28	-28.8
			67	0.257	1.26	0.32	
	5480.75	27	50	0.349	0.73	0.25	-27.1
	5497.42	27	31	0.158	4.83	0.76	
			35	0.188	2.83	0.53	
			38	0.305	2.12	0.65	
			50	0.603	0.73	0.44	-26.1
			74	0.173	1.07	0.18	
			76	0.284	0.78	0.22	
			77	0.377	0.66	0.25	
			103	0.342	0.36	0.12	
			104	0.253	0.42	0.11	
	5509.91	19	35	0.317	2.83	0.90	
			38	0.428	2.12	0.91	
			50	1.058	0.73	0.77	-28.2
			67	0.430	1.26	0.54	
			74	0.441	1.07	0.47	

Table E.4: *V854 Cen – sharp emission lines from MRS spectra (continued).*

Element	λ [Å]	Multiplet	Day number	W_λ [Å]	f_{cont} $[10^{-16}\text{W m}^{-2}\,\text{Å}^{-1}]$	F_{line} $[10^{-16}\text{W m}^{-2}]$	V_{r} $[\text{km s}^{-1}]$
	5509.91	19	76	0.509	0.78	0.40	
			77	0.524	0.66	0.35	
			104	0.340	0.42	0.14	
YII	5662.95	38	31	0.236	4.81	1.14	
			35	0.397	2.83	1.12	
			36	0.377	2.58	0.97	
			37	0.434	2.34	1.02	
			38	0.477	2.13	1.01	
			39	0.652	1.89	1.23	
			50	1.452	0.74	1.07	-26.1
			51	1.296	0.79	1.02	-22.6
			66	0.567	1.31	0.74	
			67	0.526	1.28	0.67	
			74	0.584	1.08	0.63	
			75	0.730	0.92	0.67	-25.2
			76	0.821	0.78	0.64	-27.9
			77	0.815	0.67	0.54	-31.5
			103	0.863	0.38	0.32	
			104	0.633	0.43	0.28	
	6613.74	26	31	0.112	4.47	0.50	
			50	0.388	0.77	0.30	-31.1
	6795.41	26	38	0.232	2.03	0.47	
			39	0.224	1.81	0.41	
			50	0.365	0.77	0.28	-30.1
			74	0.119	1.09	0.13	
			76	0.048	0.77	0.04	

Table E.5: *V854 Cen – sharp emission lines from MRS spectra (continued).*

Element	λ [Å]	Multiplet	Day number	W_λ [Å]	f_{cont} $[10^{-16}\mathrm{W\,m^{-2}\,Å^{-1}}]$	F_{line} $[10^{-16}\mathrm{W\,m^{-2}}]$	V_{r} $[\mathrm{km\,s^{-1}}]$
BaII	5853.675	2	31	0.188	4.77	0.90	
			36	0.299	2.57	0.77	
			37	0.338	2.34	0.79	
			38	0.321	2.12	0.68	
			39	0.376	1.89	0.71	
			50	0.682	0.75	0.51	-24.3
			51	0.669	0.80	0.53	-26.7
			74	0.214	1.09	0.23	
			75	0.297	0.92	0.27	
			76	0.210	0.79	0.17	
			77	0.260	0.67	0.17	
			103	0.220	0.39	0.09	
			105	0.164	0.52	0.09	
	6141.718	2	31	0.309	4.68	1.45	
			35	0.499	2.79	1.40	
			36	0.588	2.54	1.49	-26.6
			36	0.599	2.54	1.52	-29.4
			37	0.596	2.31	1.38	
			38	0.669	2.11	1.41	-27.0
			38	0.635	2.11	1.34	-29.9
			39	0.706	1.88	1.32	
			50	1.460	0.76	1.10	-26.3
			50	1.522	0.76	1.15	-23.5
			51	1.446	0.81	1.17	-29.0
			66	0.543	1.34	0.73	
			67	0.531	1.31	0.69	
			74	0.698	1.09	0.76	
			74	0.665	1.09	0.73	
			76	0.873	0.79	0.69	
			76	0.913	0.79	0.72	
			77	1.125	0.67	0.75	
			103	1.025	0.40	0.41	
			104	0.834	0.46	0.39	
			105	0.747	0.54	0.40	

Table E.6: *V854 Cen – sharp emission lines from MRS spectra (continued).*

Element	λ [Å]	Multiplet	Day number	W_λ [Å]	f_{cont} [10^{-16}W m^{-2} Å^{-1}]	F_{line} [10^{-16}W m^{-2}]	V_{r} [km s^{-1}]
BaII	6496.896	2	31	0.285	4.53	1.29	
			36	0.537	2.49	1.33	
			36	0.561	2.49	1.40	
			38	0.565	2.07	1.17	
			38	0.529	2.07	1.09	
			39	0.662	1.85	1.22	-25.1
			50	1.375	0.76	1.05	-29.7
			50	1.244	0.76	0.95	-27.7
			66	0.498	1.35	0.67	
			67	0.390	1.31	0.51	
			74	0.524	1.09	0.57	
			74	0.592	1.09	0.65	
			76	0.781	0.78	0.61	
			76	0.648	0.78	0.51	
			104	0.686	0.48	0.33	
			104	0.538	0.48	0.26	
FeII	5284.092	41	50	0.419	0.71	0.30	-28.2
	5362.864	48	50	0.328	0.72	0.23	-29.1
			67	0.185	1.25	0.23	
			74	0.143	1.06	0.15	
			76	0.188	0.77	0.14	
			77	0.178	0.66	0.12	
			103	0.439	0.36	0.16	
FeI	5371.493	15	31	0.174	4.84	0.84	
			35	0.318	2.82	0.90	
			50	0.564	0.72	0.41	-29.1
	5429.699	15	50	0.229	0.72	0.00	-25.3
FeII	6432.654	40	31	0.079	4.55	0.36	
			36	0.134	2.50	0.34	
			38	0.177	2.08	0.37	
			38	0.161	2.08	0.33	
			39	0.206	1.85	0.38	
			50	0.365	0.76	0.28	-29.0
			50	0.462	0.76	0.35	

Table E.7: *V854 Cen – sharp emission lines from MRS spectra (continued).*

Element	λ	Multiplet	Day	W_λ	f_{cont}	F_{line}	V_r
	[Å]		number	[Å]	$[10^{-16}\mathrm{W\,m^{-2}\,\text{Å}^{-1}}]$	$[10^{-16}\mathrm{W\,m^{-2}}]$	$[\mathrm{km\,s^{-1}}]$
FeII	6432.654	40	67	0.074	1.31	0.10	
			74	0.065	1.09	0.07	
			74	0.115	1.09	0.13	
			76	0.125	0.78	0.10	
			76	0.179	0.78	0.14	
			104	0.189	0.48	0.09	
			104	0.074	0.48	0.04	
	6456.38	74	31	0.242	4.54	1.10	
			36	0.352	2.49	0.88	
			36	0.286	2.49	0.71	
			38	0.377	2.07	0.78	
			38	0.408	2.07	0.85	
			39	0.402	1.85	0.74	
			50	0.631	0.76	0.48	
			50	0.471	0.76	0.36	-27.6
			66	0.358	1.35	0.48	
			67	0.275	1.31	0.36	
			74	0.376	1.09	0.41	
			74	0.273	1.09	0.30	
			76	0.445	0.78	0.35	
			76	0.225	0.78	0.17	
			104	0.212	0.48	0.10	
			104	0.299	0.48	0.14	
	6516.053	40	31	0.101	4.52	0.45	
			36	0.141	2.48	0.35	
			36	0.140	2.48	0.35	
			38	0.200	2.07	0.41	
			38	0.184	2.07	0.38	
			39	0.298	1.84	0.55	
			50	0.439	0.76	0.34	
			50	0.347	0.76	0.27	-25.2
			66	0.194	1.35	0.26	
			67	0.221	1.31	0.29	
			74	0.136	1.09	0.15	

Table E.8: *V854 Cen – sharp emission lines from MRS spectra (continued).*

Element	λ [Å]	Multiplet	Day number	W_λ [Å]	f_{cont} [10^{-16}W m^{-2} Å^{-1}]	F_{line} [10^{-16}W m^{-2}]	V_r [km s^{-1}]
FeII	6516.053	40	74	0.086	1.09	0.09	
			76	0.216	0.78	0.17	
			76	0.230	0.78	0.18	
			104	0.202	0.48	0.10	
			104	0.201	0.48	0.10	
ScII	5239.823	26	50	2.067	0.71	1.46	-27.8
			74	1.324	1.05	1.39	
			76	1.415	0.77	1.08	
			77	1.695	0.66	1.11	
	5357.195	30	50	0.403	0.72	0.29	-27.4
			67	0.145	1.25	0.18	
			74	0.171	1.06	0.18	
			103	0.314	0.36	0.11	
	5526.809	31	31	0.413	4.83	1.99	
			35	0.665	2.83	1.88	
			38	0.794	2.12	1.69	
			50	2.050	0.73	1.49	-31.9
			66	0.842	1.29	1.09	
			67	0.817	1.27	1.03	
			74	1.087	1.07	1.17	
			76	1.340	0.78	1.04	
			77	1.678	0.66	1.11	
			103	2.322	0.37	0.85	
			104	1.959	0.42	0.83	
	5552.25	25	31	0.123	4.83	0.59	
			35	0.232	2.83	0.66	
			38	0.275	2.12	0.58	
			50	0.433	0.73	0.32	-28.4
			74	0.260	1.07	0.28	
			77	0.340	0.66	0.23	
			103	0.511	0.37	0.19	
			104	0.275	0.43	0.12	
	5640.971	29	31	0.224	4.82	1.08	
			35	0.476	2.83	1.35	

Table E.9: *V854 Cen – sharp emission lines from MRS spectra (continued).*

Element	λ [Å]	Multiplet	Day number	W_λ [Å]	f_{cont} $[10^{-16}\mathrm{W\,m^{-2}\,\text{Å}^{-1}}]$	F_{line} $[10^{-16}\mathrm{W\,m^{-2}}]$	V_{r} $[\mathrm{km\,s^{-1}}]$
ScII	5640.971	29	38	0.465	2.12	0.99	
			50	1.213	0.73	0.89	-26.4
			66	0.672	1.31	0.88	
			67	0.595	1.28	0.76	
			74	0.773	1.08	0.83	
			76	0.996	0.78	0.78	
			77	1.164	0.67	0.78	
			103	0.910	0.37	0.34	
			104	0.702	0.43	0.30	
	5684.190	29	31	0.289	4.81	1.39	
			35	0.501	2.83	1.42	
			38	0.606	2.13	1.29	
			50	1.414	0.74	1.04	-28.4
			66	0.515	1.31	0.67	
			67	0.517	1.28	0.66	
			74	0.772	1.08	0.83	
			76	0.863	0.78	0.68	
			77	1.037	0.67	0.69	
			103	1.140	0.38	0.43	
			104	0.822	0.44	0.36	
	6245.629	28	31	0.426	4.64	1.97	
			35	0.689	2.78	1.91	
			36	0.685	2.53	1.73	
			38	0.823	2.10	1.73	
			38	0.867	2.10	1.82	
			50	1.884	0.76	1.43	-22.4
			50	1.758	0.76	1.33	-24.9
			66	0.818	1.34	1.10	
			67	0.698	1.31	0.92	
			74	0.912	1.09	1.00	
			74	0.931	1.09	1.02	
			76	1.178	0.78	0.92	
			76	1.286	0.78	1.01	
			77	1.548	0.66	1.03	

Table E.10: *V854 Cen – sharp emission lines from MRS spectra (continued).*

Element	λ [Å]	Multiplet	Day number	W_λ [Å]	f_{cont} $[10^{-16}\text{W}\,\text{m}^{-2}\,\text{Å}^{-1}]$	F_{line} $[10^{-16}\text{W}\,\text{m}^{-2}]$	V_{r} $[\text{km}\,\text{s}^{-1}]$
ScII	6245.629	28	103	0.915	0.41	0.37	
			104	0.925	0.47	0.43	
			105	0.669	0.54	0.36	
	6309.902	28	36	0.364	2.52	0.92	
			38	0.485	2.09	1.01	
			50	0.936	0.76	0.71	-30.2
			67	0.295	1.31	0.39	
			74	0.467	1.09	0.51	
			76	0.509	0.78	0.40	
			104	0.375	0.47	0.18	
	6320.854	28	36	0.323	2.52	0.81	
			38	0.368	2.09	0.77	
			50	0.841	0.76	0.64	-29.5
			67	0.239	1.31	0.31	
			74	0.309	1.09	0.34	
			76	0.327	0.78	0.26	
			104	0.376	0.47	0.18	
	6604.60	19	31	0.502	4.47	2.25	
			36	0.945	2.47	2.33	
			38	1.043	2.05	2.14	
			39	1.217	1.83	2.23	
			50	2.005	0.77	1.54	-26.4
			66	0.738	1.35	0.99	-25.9
			74	0.944	1.09	1.03	-27.4
			76	1.353	0.78	1.05	-28.5
			104	1.071	0.49	0.52	

Table E.11: *Measured parameters of sharp emission lines throughout the 1998 decline of V854 Cen from convolved high-resolution (échelle) spectra: W_λ – equivalent width, f_{cont} – continuum flux at the line position, F_{line} – line flux and V_r – radial velocity.*

Element	λ [Å]	Multiplet	Day number	W_λ [Å]	f_{cont} $[10^{-16}\text{W}\,\text{m}^{-2}\,\text{Å}^{-1}]$	F_{line} $[10^{-16}\text{W}\,\text{m}^{-2}]$	V_r $[\text{km}\,\text{s}^{-1}]$
BaII	5853.675	2	52	0.478	0.85	0.41	-25.4
			54	0.346	0.97	0.34	-27.3
			54	0.368	0.97	0.36	-24.0
	6141.718	2	52	1.052	0.86	0.91	-26.6
			54	0.813	0.98	0.80	-26.3
			111	0.142	1.11	0.16	-32.1
	6496.896	2	52	0.908	0.87	0.79	-25.2
			54	0.645	0.99	0.64	-25.4
			111	0.106	1.11	0.12	-32.2
FeII	5284.092	41	52	0.249	0.81	0.20	
	5362.864	48	52	0.220	0.82	0.18	-27.3
			54	0.172	0.93	0.16	-26.9
FeI	5371.493	15	52	0.214	0.82	0.00	-29.9
			54	0.116	0.93	0.11	-27.3
	5429.699	15	52	0.088	0.82	0.07	-30.9
			54	0.038	0.94	0.04	
FeII	6432.654	40	52	0.226	0.87	0.20	-26.9
			54	0.165	0.99	0.16	-23.9
	6456.38	74	52	0.287	0.87	0.25	
			54	0.290	0.99	0.29	
	6516.053	40	52	0.326	0.87	0.28	-31.8
			54	0.240	0.99	0.24	-32.5
			54	0.221	0.99	0.22	-27.2
ScII	5239.823	26	52	1.258	0.80	1.01	-29.9
			54	0.966	0.91	0.88	-28.9
			111	0.172	1.02	0.17	-29.6
	5357.195	30	52	0.251	0.82	0.20	-29.6
			54	0.217	0.93	0.20	-30.9
	5526.809	31	52	1.354	0.83	1.12	-26.9
			54	1.139	0.94	1.08	-29.2
			111	0.417	1.07	0.45	-29.0

Table E.12: *V854 Cen – sharp emission lines from échelle spectra (continued).*

Element	λ [Å]	Multiplet	Day number	W_λ [Å]	$f_{\rm cont}$ $[10^{-16}{\rm W\,m^{-2}\,Å^{-1}}]$	$F_{\rm line}$ $[10^{-16}{\rm W\,m^{-2}}]$	$V_{\rm r}$ $[{\rm km\,s^{-1}}]$
ScII	5552.25	25	52	0.220	0.83	0.18	-25.6
			54	0.167	0.95	0.16	
	5640.971	29	52	1.017	0.84	0.85	-26.7
			54	0.748	0.95	0.71	-31.6
			111	0.197	1.09	0.21	-31.4
	5684.190	29	52	0.987	0.84	0.83	-24.7
			54	0.762	0.96	0.73	-22.8
			111	0.148	1.09	0.16	
	6245.629	28	52	1.338	0.86	1.16	-22.1
			54	0.980	0.98	0.96	-22.8
			111	0.172	1.11	0.19	-31.8
	6604.60	19	52	1.613	0.87	1.41	-22.4
			54	1.221	0.99	1.21	-22.7
			111	0.256	1.10	0.28	-30.7
TiII	5211.544	103	52	0.285	0.80	0.23	-28.5
			54	0.213	0.91	0.19	-23.4
	5226.534	70	52	1.142	0.80	0.92	-24.9
			54	0.867	0.91	0.79	-26.2
			111	0.224	1.02	0.23	-31.4
	5262.104	70	52	0.327	0.81	0.26	-24.6
			54	0.282	0.92	0.26	-27.1
	5336.809	69	52	1.115	0.81	0.91	
			54	0.903	0.93	0.84	
			111	0.141	1.04	0.15	-32.4
	5381.020	69	52	0.652	0.82	0.53	-25.2
			54	0.451	0.93	0.42	-22.0
	5418.802	69	52	0.595	0.82	0.49	-23.4
			54	0.401	0.93	0.37	-28.5
	6491.610	91	52	0.488	0.87	0.42	-25.9
			54	0.346	0.99	0.34	-27.9
	6717.911	112	52	0.111	0.87	0.10	
			54	0.083	0.99	0.08	

Table E.13: *V854 Cen – sharp emission lines from échelle spectra (continued).*

Element	λ [Å]	Multiplet	Day number	W_λ [Å]	f_{cont} [10^{-16}W m^{-2}Å^{-1}]	F_{line} [10^{-16}W m^{-2}]	V_r [km s^{-1}]
YII	5200.42	20	52	0.974	0.80	0.78	-30.7
			54	0.722	0.91	0.66	-33.7
			111	0.163	1.01	0.17	-30.7
	5205.73	20	52	1.057	0.80	0.85	-32.3
			54	0.813	0.91	0.74	-32.5
			111	0.169	1.01	0.17	-31.2
	5289.82	20	52	0.140	0.81	0.11	-24.2
			54	0.125	0.92	0.12	-22.1
	5402.78	35	52	0.337	0.82	0.28	-24.5
			54	0.229	0.93	0.21	-26.3
	5473.40	27	52	0.169	0.82	0.14	
			54	0.120	0.94	0.11	
			54	0.134	0.94	0.13	
	5480.75	27	52	0.189	0.83	0.16	
			54	0.100	0.94	0.09	
	5497.42	27	52	0.205	0.83	0.17	
			54	0.227	0.94	0.21	
			54	0.152	0.94	0.14	
	5509.91	19	52	0.785	0.83	0.65	-27.6
			54	0.576	0.94	0.54	-28.8
			111	0.105	1.07	0.11	-30.2
	5662.95	38	52	0.877	0.84	0.74	-28.6
			54	0.692	0.95	0.66	-29.8
			111	0.127	1.09	0.14	-31.8
	6613.74	26	52	0.255	0.87	0.22	-29.7
			54	0.208	0.99	0.21	-23.6

Table E.14: *Measured parameters of the NaI D components from the high-resolution spectra of V854 Cen during the 1998 decline: equivalent widths (W_λ), radial velocities (V_r) and FWHM values for broad component (b), sharp emission (s1, s2), high velocity absorption (h1, h2) and shell absorption (a1, a2).*

Day No.	$W_\lambda^{(b)}$ [Å]	$V_r^{(s1)}$ [km s^{-1}]	$V_r^{(s2)}$ [km s^{-1}]	FWHM$^{(s1)}$ [km s^{-1}]	FWHM$^{(s2)}$ [km s^{-1}]	$W_\lambda^{(s1)}$ [Å]	$W_\lambda^{(s2)}$ [Å]	$W_\lambda^{(h1)}$ [Å]	$W_\lambda^{(h2)}$ [Å]	$V_r^{(a1)}$ [km s^{-1}]	$V_r^{(a2)}$ [km s^{-1}]	$W_\lambda^{(a1)}$ [Å]	$W_\lambda^{(a2)}$ [Å]
-142										-212.6	-213.0	0.23	0.20
10	2.2							0.44	0.23	-212.0	-213.1	0.19	0.15
13	2.1							0.66	0.19	-210.0	-211.6	0.19	0.16
13	3.0							0.64	0.28	-213.2	-214.1	0.21	0.15
14	2.5							0.58	0.23	-213.2	-214.6	0.20	0.14
28	3.6							0.75	0.20	-212.8	-214.3	0.21	0.15
52	21.5	-28.3	-29.9	28	26	1.76	1.80	0.99	0.38	-209.6	-206.9	0.14	0.08
54	16.2	-32.7	-31.7	25	27	1.20	1.32	1.12	0.36	-211.4	-209.5	0.18	0.09
54	16.3	-30.3	-30.0	25	29	1.44	1.67	1.07	0.36	-210.6	-209.4	0.12	0.07
111	14.3	-28.9	-30.8	29	33	0.75	1.25	1.81	0.37	-212.5	-220.7		
123	5.6							1.75	0.96	-213.0	-212.5	0.18	0.13
125	4.4							1.60	1.02	-213.3	-214.4	0.22	0.17
139	2.5							1.09	0.45	-214.4	-215.8	0.20	0.15
139	1.3							1.07	0.46	-214.4	-216.0	0.23	0.18
150								0.54	0.18	-213.0	-214.2	0.21	0.17
153								0.40	0.15	-214.0	-215.0	0.20	0.16
169								0.27	0.13	-212.8	-214.2	0.21	0.15
169								0.23	0.11	-212.6	-214.0	0.20	0.17
201										-214.8	-215.3	0.22	0.17
203										-214.7	-215.6	0.22	0.17
475										-214.1	-214.8	0.19	0.15
479	3.4									-216.2	-216.8	0.19	0.18

Table E.15: *Parameters of the NaI D components from the medium-resolution spectra of V854 Cen during the 1998 decline using a model of the NaI D region, as described in Chapter 2: equivalent widths (W_λ) of broad (b), sharp (s1, s2) and high-velocity (h1, h2) components, continuum flux density (f_{cont}) and line fluxes (F_{line}) of sharp emission lines.*

Day No.	f_{cont} $[10^{-16}\,\mathrm{W\,m^{-2}\,\mathring{A}^{-1}}]$	$W_\lambda^{(\mathrm{b})}$ [Å]	$W_\lambda^{(\mathrm{s1})}$ [Å]	$W_\lambda^{(\mathrm{s2})}$ [Å]	$F_{\mathrm{line}}^{(\mathrm{s1})}$ $[10^{-16}\,\mathrm{W\,m^{-2}}]$	$F_{\mathrm{line}}^{(\mathrm{s2})}$ $[10^{-16}\,\mathrm{W\,m^{-2}}]$	$W_\lambda^{(\mathrm{h1})}$ [Å]	$W_\lambda^{(\mathrm{h2})}$ [Å]
10	13.8	1.4	0.10	0.12	1.38	1.66	0.43	0.21
13	8.3	2.4	0.19	0.22	1.58	1.83	0.55	0.28
13	8.9	2.2	0.17	0.19	1.49	1.66	0.64	0.32
14	9.1	2.2	0.15	0.17	1.38	1.53	0.70	0.35
16	11.0	1.8	0.13	0.15	1.44	1.60	0.64	0.32
17	11.0	1.8	0.15	0.16	1.61	1.79	0.48	0.24
25	12.0	1.6	0.14	0.15	1.67	1.85	0.48	0.24
28	7.2	2.7	0.26	0.29	1.90	2.11	0.53	0.27
31	4.7	4.2	0.46	0.52	2.18	2.43	0.80	0.40
35	2.6	7.5	0.75	0.84	1.95	2.17	1.12	0.56
36	2.4	8.2	0.86	0.96	2.07	2.30	1.12	0.56
37	2.4	8.2	0.81	0.90	1.95	2.17	1.21	0.61
38	2.3	8.5	0.92	1.03	2.13	2.36	1.12	0.56
39	2.1	9.3	1.04	1.16	2.18	2.43	1.28	0.64
50	0.6	30.6	3.14	3.49	2.01	2.24	1.28	0.64
52	0.9	21.8	2.62	2.91	2.36	2.62	1.36	0.68
54	1.1	18.5	2.06	2.29	2.18	2.43	1.36	0.68
54	1.1	17.2	2.02	2.24	2.30	2.55	1.36	0.68
66	1.6	12.2	1.19	1.32	1.90	2.11	1.33	0.67
74	1.1	18.5	1.90	2.11	2.01	2.24	1.46	0.73
75	0.9	21.8	2.04	2.27	1.84	2.04	1.46	0.73
76	0.8	24.5	2.30	2.55	1.84	2.04	1.46	0.73
77	0.7	28.0	2.71	3.01	1.90	2.11	1.46	0.73
103	0.3	65.3	3.80	4.33	1.14	1.30	1.46	0.73
105	0.5	39.2	2.74	3.10	1.37	1.55	0.80	0.40
111	1.2	16.3	1.18	1.35	1.42	1.62	1.60	0.80
123	3.5	5.6	0.34	0.39	1.19	1.36	1.76	0.88
125	4.3	4.6	0.29	0.33	1.25	1.42	1.60	0.80
137	11.7	1.7	0.11	0.13	1.31	1.49	0.88	0.44
139	13.8	1.4	0.09	0.09	1.19	1.36	0.90	0.45
150	28.0	0.7	0.04	0.05	1.14	1.30	0.43	0.21
153	31.0	0.6	0.04	0.05	1.32	1.47	0.37	0.19
169	38.0	0.5	0.03	0.03	1.19	1.36	0.22	0.11
169	40.0	0.5	0.03	0.03	1.28	1.23	0.24	0.12
201	41.0	0.5	0.04	0.04	1.44	1.60	0.00	0.00
203	38.6	0.5	0.04	0.04	1.49	1.66	0.00	0.00
219	37.0	0.5	0.04	0.04	1.38	1.53	0.00	0.00

Table E.16: *The strongest identified lines (P and R branches) of the C_2 Swan (0–0) system. The wavelengths of the P and R lines have been taken from Amiot (1983). The radial velocities of blended lines have been calculated for an average wavelength.*

λ_{air} (Å)	Line	V_r (km s^{-1})	λ_{air} (Å)	Line	V_r (km s^{-1})
5159.440	$P_1(28)$		5149.065	$P_1(37)$	
5159.466	$P_2(27)$	-27.5	5149.098	$P_2(36)$	-27.7
5159.592	$P_3(26)$		5149.201	$P_3(35)$	
			5149.323	$R_1(8)$	
5158.496	$P_1(29)$				
5158.548	$P_2(28)$	-27.9	5148.603	$R_3(7)$	-27.8
5158.658	$P_3(27)$				
			5148.316	$R_2(8)$	-25.1
5157.607	$P_1(30)$		5146.802	$R_2(9)$	-27.2
5157.622	$P_2(29)$	-26.3			
5157.745	$P_3(28)$		5146.460	$R_1(10)$	
			5146.065	$P_1(39)$	
5156.523	$P_1(31)$		5146.097	$P_2(38)$	-26.5
5156.572	$P_2(30)$	-25.9	5146.199	$P_3(37)$	
5156.677	$P_3(29)$				
			5144.564	$P_1(40)$	
5155.510	$P_1(32)$		5144.564	$P_2(39)$	-26.6
5155.515	$P_2(31)$	-26.6	5144.681	$P_3(38)$	
5155.644	$P_3(30)$				
5155.583	$R_3(2)$		5143.854	$R_3(10)$	-26.2
5156.080	$R_2(2)$	-27.8	5141.637	$R_1(13)$	-27.5
5156.128	$R_1(2)$		5141.195	$P_1(42)$	
			5141.194	$P_2(41)$	-26.1
5152.504	$R_2(5)$	-26.1	5141.310	$P_3(40)$	
5151.805	$P_1(35)$		5137.575	$P_1(44)$	
5151.845	$P_2(34)$	-26.0	5137.573	$P_2(43)$	-26.5
5151.949	$P_3(33)$		5137.683	$P_3(42)$	
5151.894	$R_1(6)$				
			5135.561	$P_1(45)$	
5150.545	$P_1(36)$		5135.575	$P_2(44)$	-26.4
5150.545	$P_2(35)$	-25.6	5135.685	$P_3(43)$	
5150.667	$P_3(34)$				
			5133.706	$P_1(46)$	
5149.775	$R_2(7)$	-26.2	5133.704	$P_2(45)$	-26.0
			5133.812	$P_3(44)$	
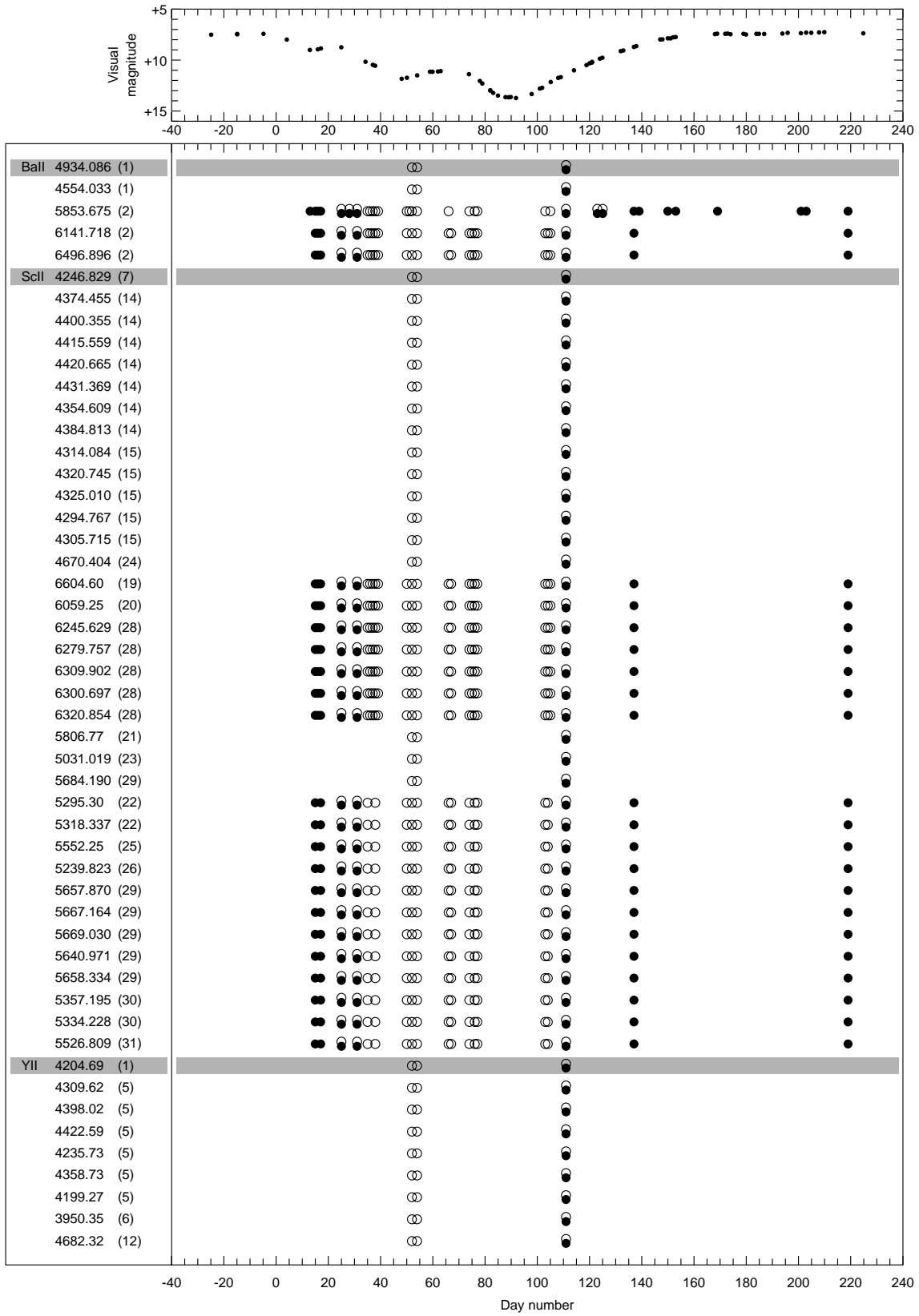
Figure E.1: *List of spectral lines identified in the 1998 decline of V854 Cen:* ● *– absorption,* ○ *– emission and* ●○ *– emission and absorption.*
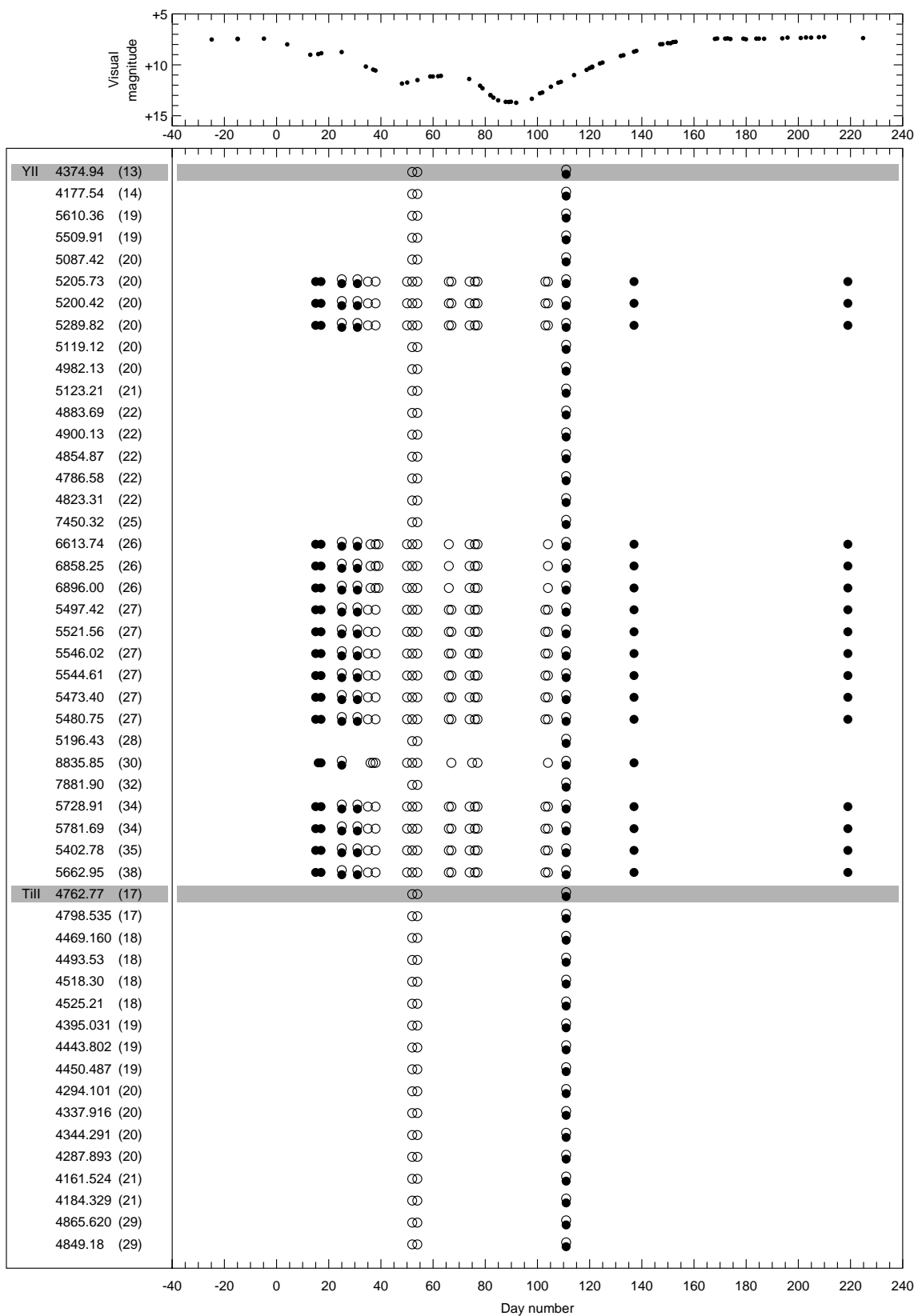
Figure E.2: *List of spectral lines identified in the 1998 decline of V854 Cen (continued).*
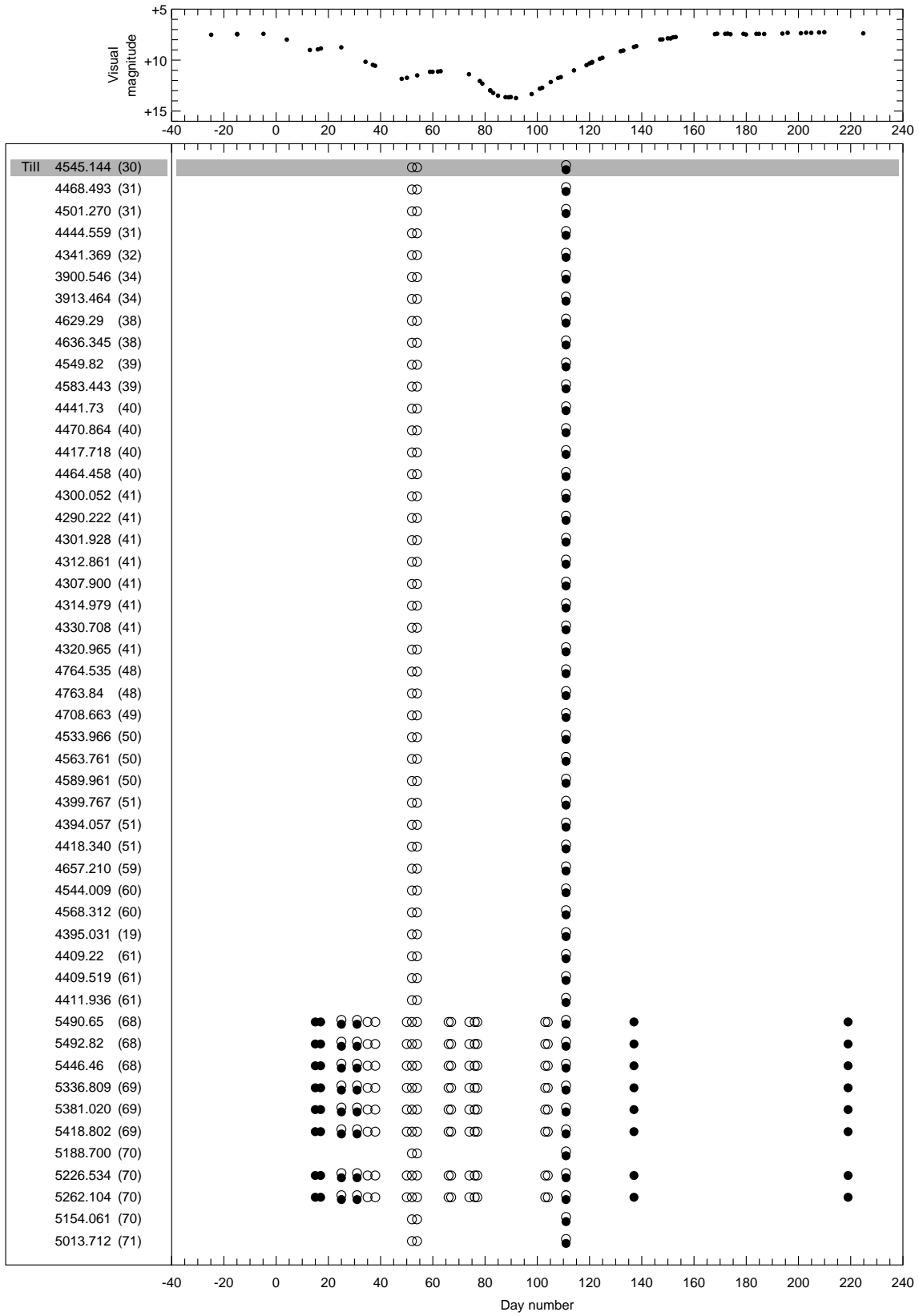
Figure E.3: *List of spectral lines identified in the 1998 decline of V854 Cen (continued).*
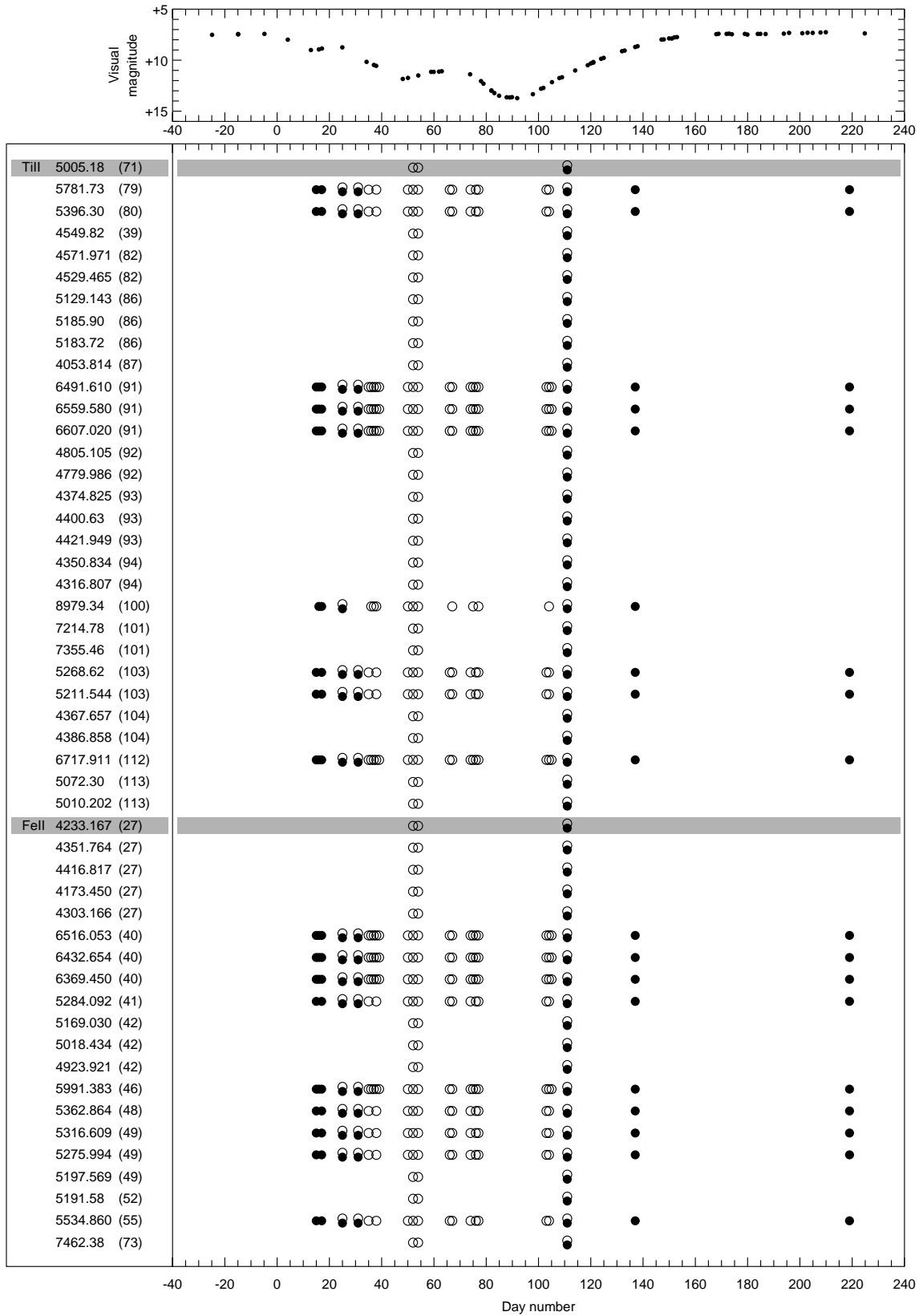
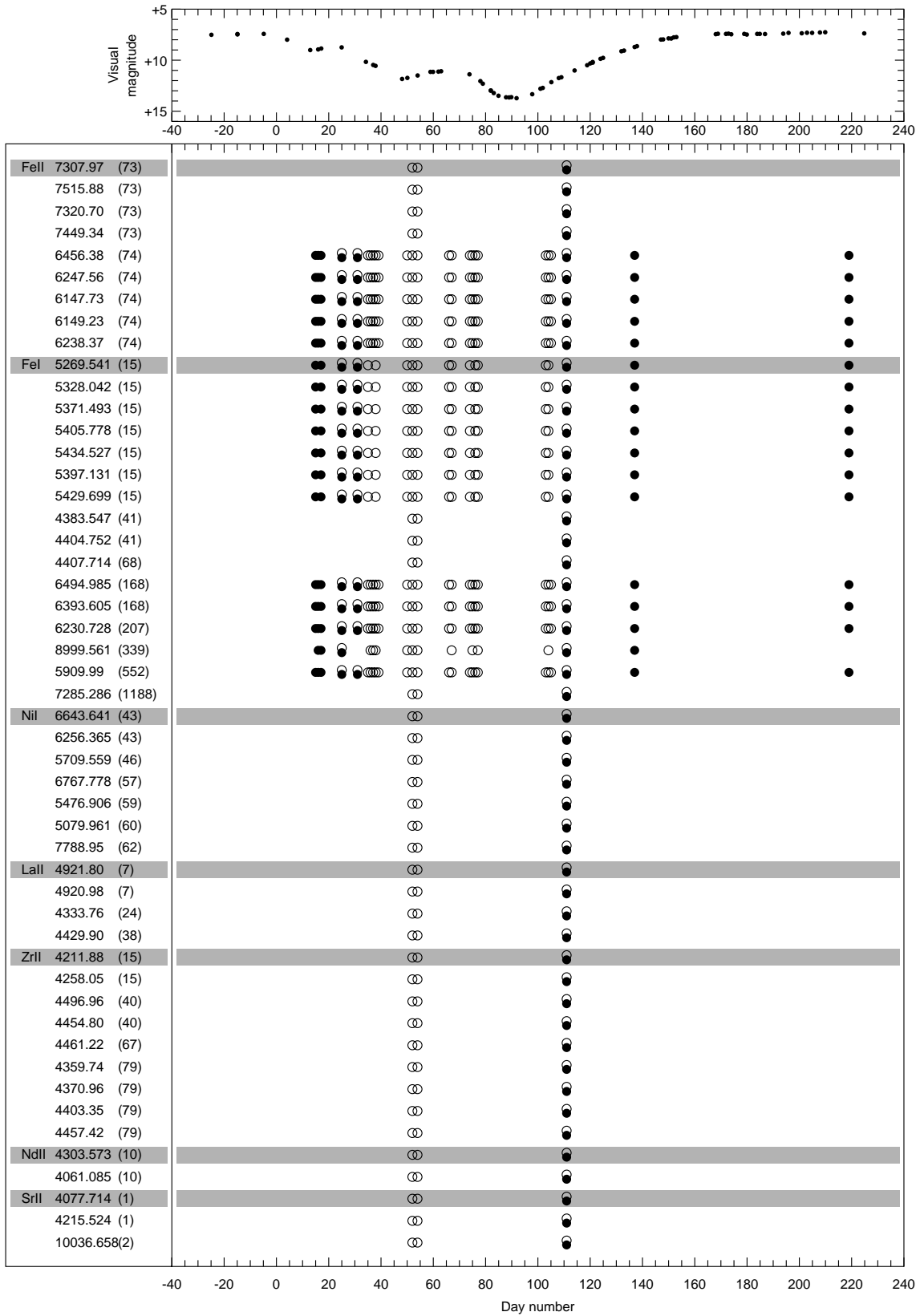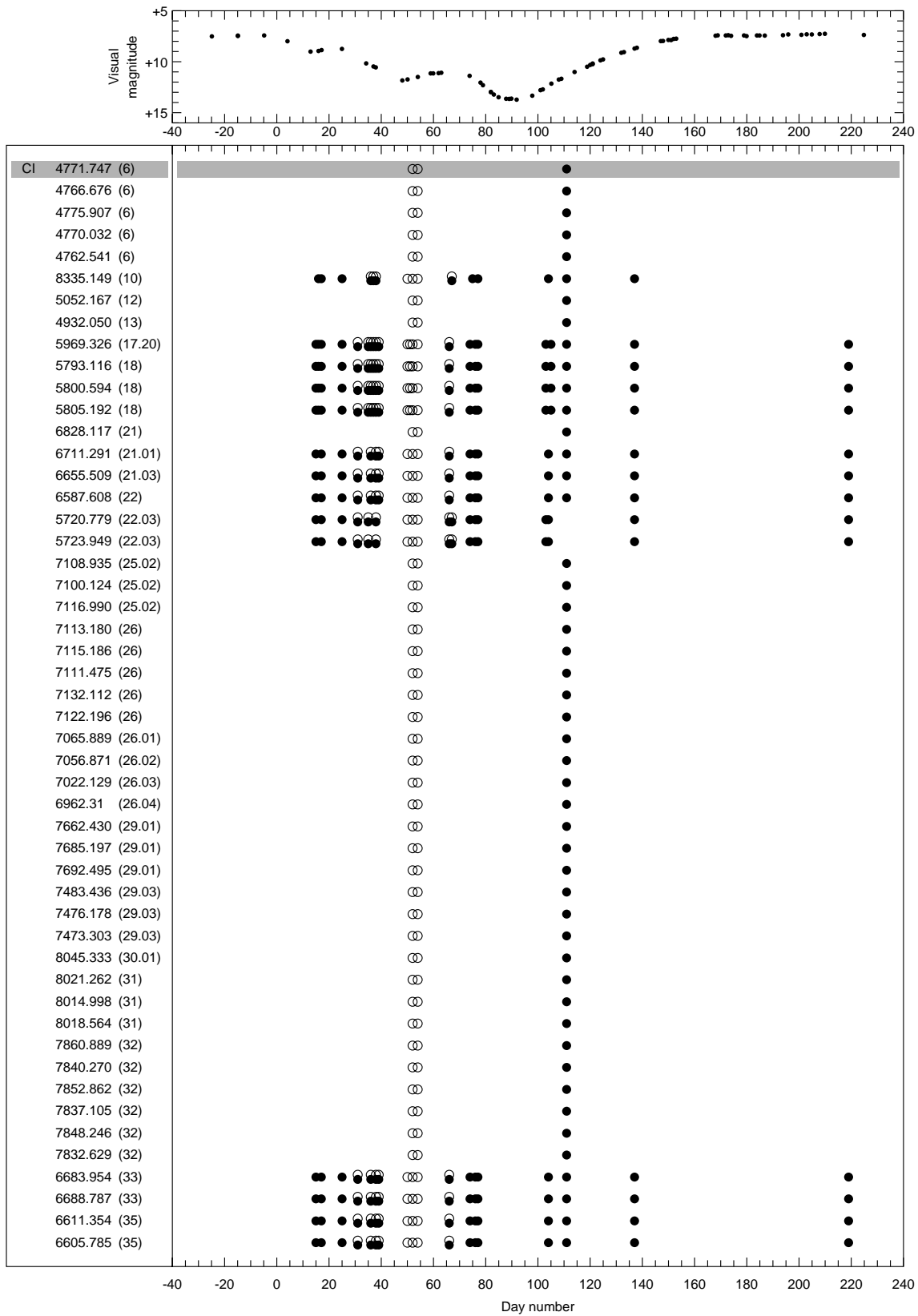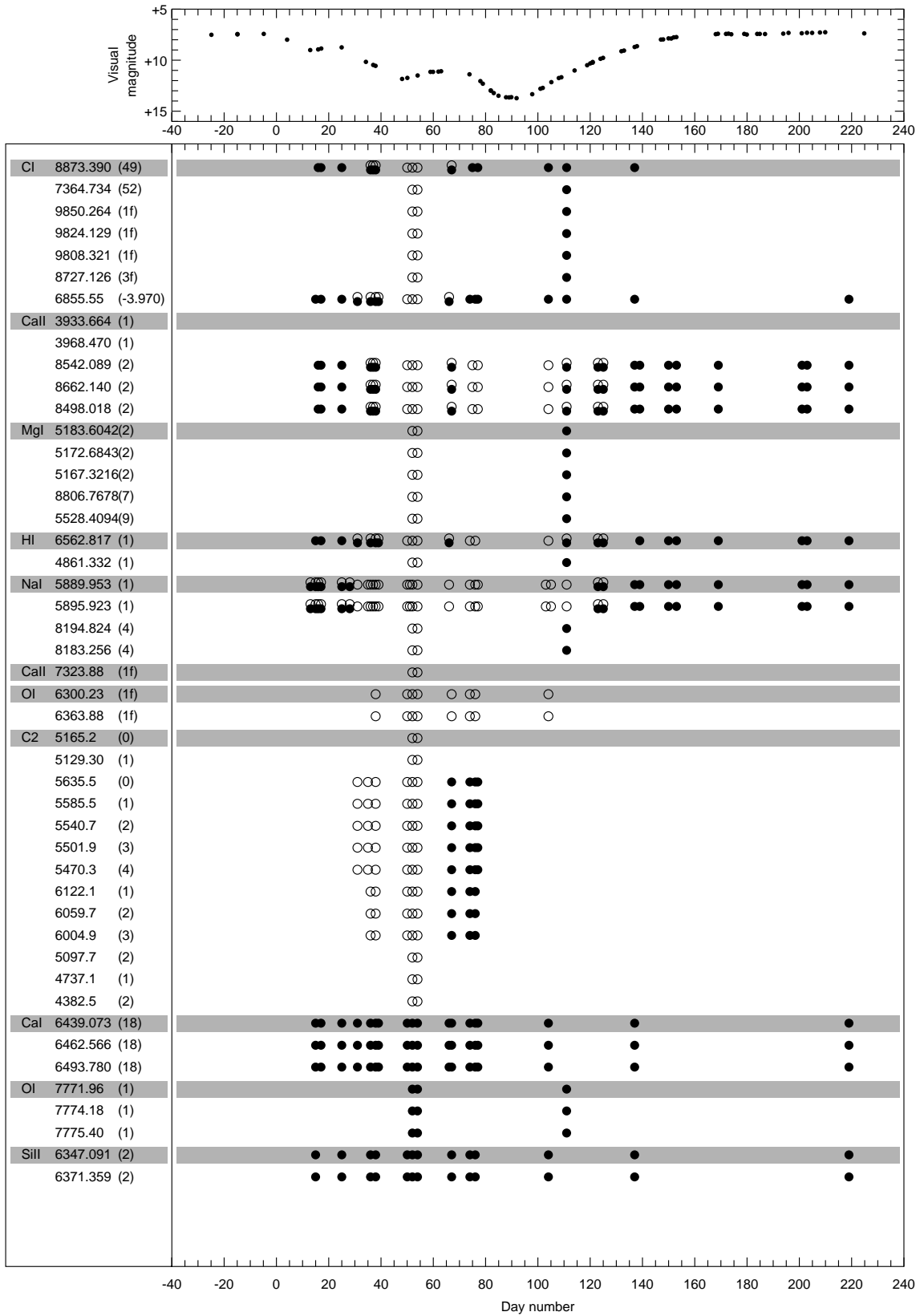Figure E.4: *List of spectral lines identified in the 1998 decline of V854 Cen (continued).*

Figure E.5: *List of spectral lines identified in the 1998 decline of V854 Cen (continued).*

Figure E.6: *List of spectral lines identified in the 1998 decline of V854 Cen (continued).*

Figure E.7: *List of spectral lines identified in the 1998 decline of V854 Cen (continued).*

Appendix F

Other RCB stars at maximum light and HdC stars

RCB stars

Three of the RCB stars from the programme list (RY Sgr, RT Nor and U Aqr) did not exhibit any declines during the observing period (from 1996 April till 1998 October). They were monitored at light maximum regularly, together with the three hydrogen-deficient stars that were used for comparison. The photometric measurements and some typical low-resolution spectra of these stars are presented in Figures F.1–F.8.
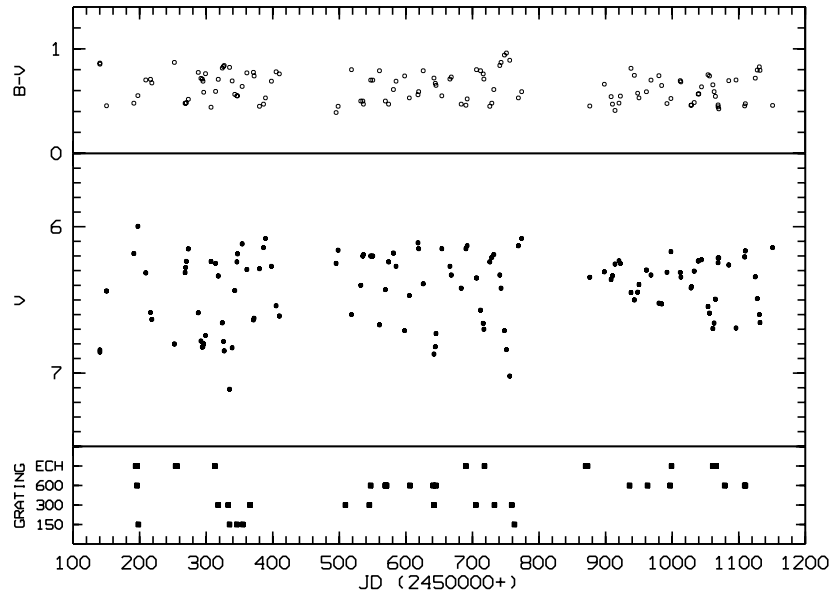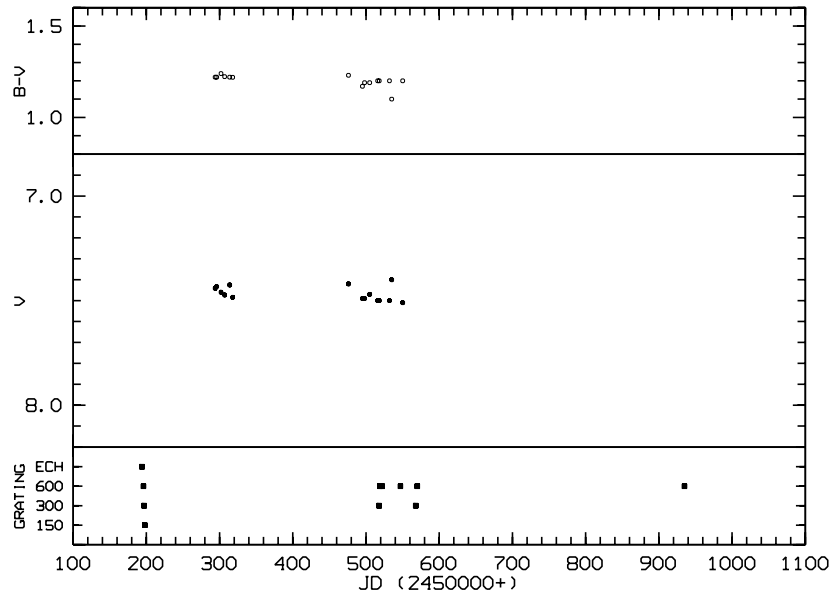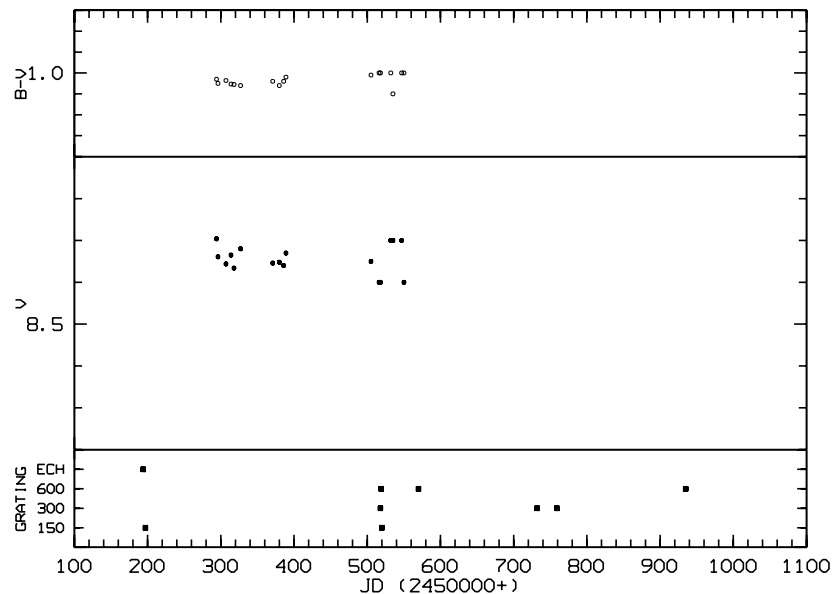

Figure F.1: *V magnitude and colour changes of RY Sgr and the times at which spectroscopic observations were obtained.*
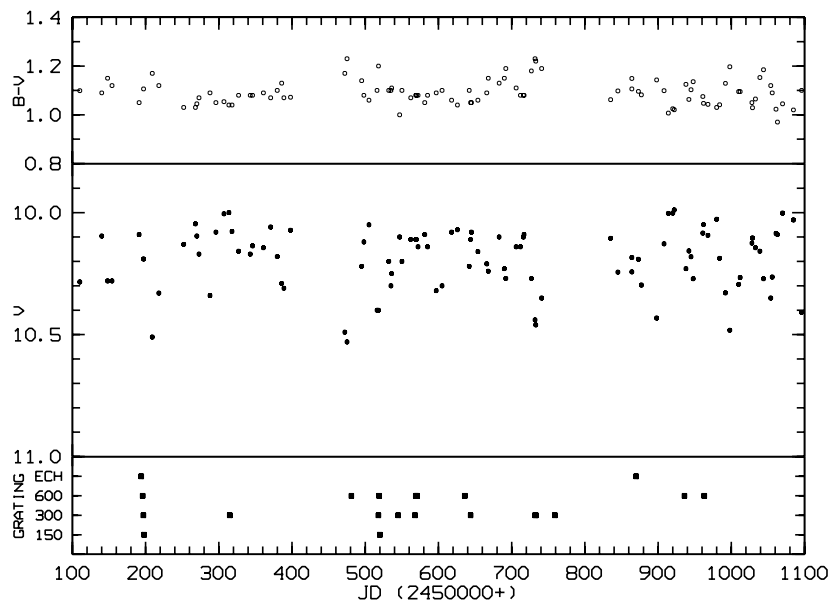
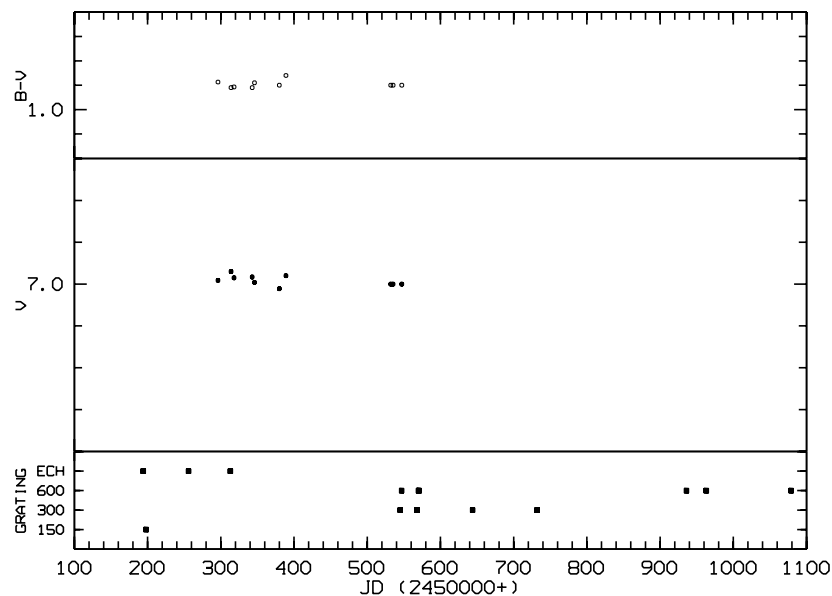Figure F.2: *V magnitude and colour changes of RT Nor and the times at which spectroscopic observations were obtained.*
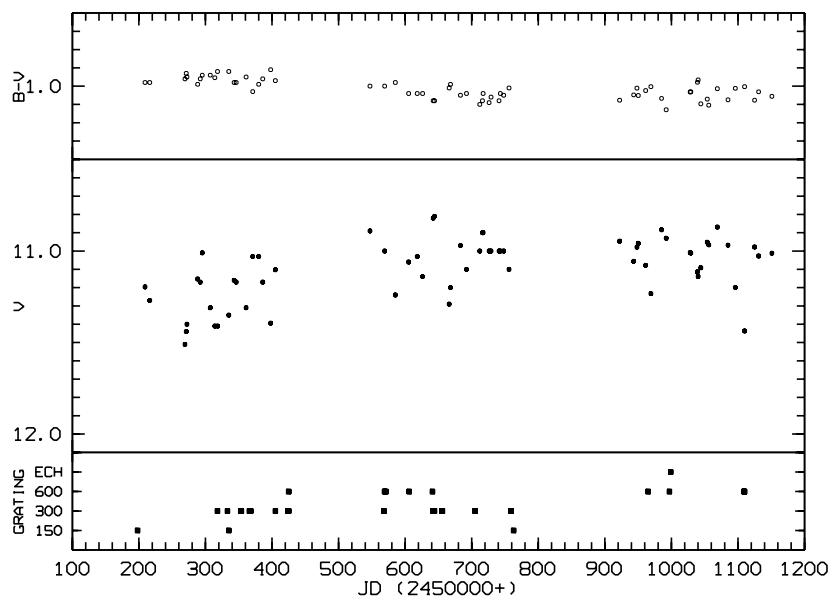
Figure F.3: *V magnitude and colour changes of U Aqr and the times at which spectroscopic observations were obtained.*
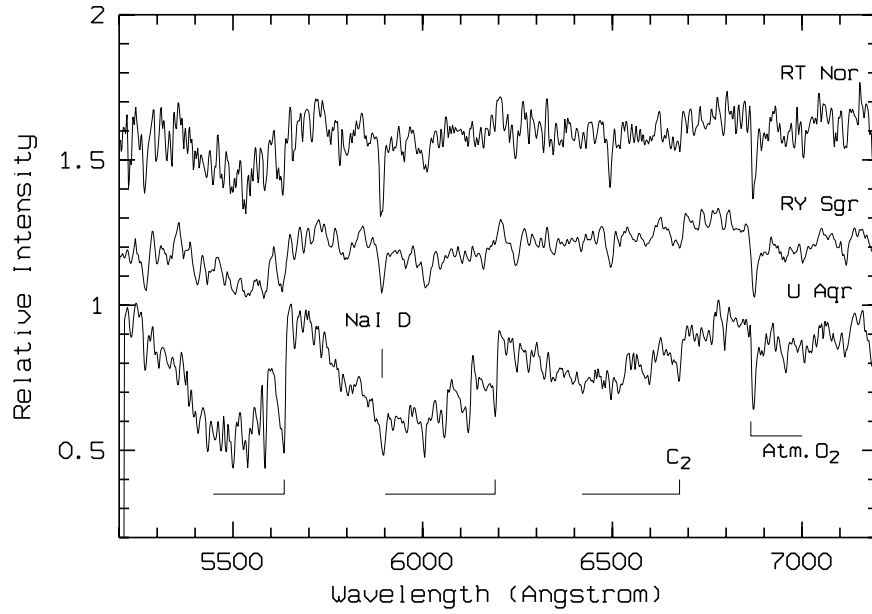
Figure F.4: *Low-resolution maximum-light spectra of two typical RCB stars, RT Nor and RY Sgr ($T_{eff} \sim 7000$ K), and a cool RCB stars, U Aqr ($T_{eff} \sim 5000$ K). The position of the NaI D lines and the bandheads of the C_2 Swan system are indicated.*

Hydrogen-deficient stars

Figure F.5: *V magnitude and colour changes of HD 137613 and the times at which spectroscopic observations were obtained.*

Figure F.6: *V magnitude and colour changes of HD 148839 and the times at which spectro-scopic observations were obtained.*

Figure F.7: *V magnitude and colour changes of HD 182040 and the times at which spectro-scopic observations were obtained.*
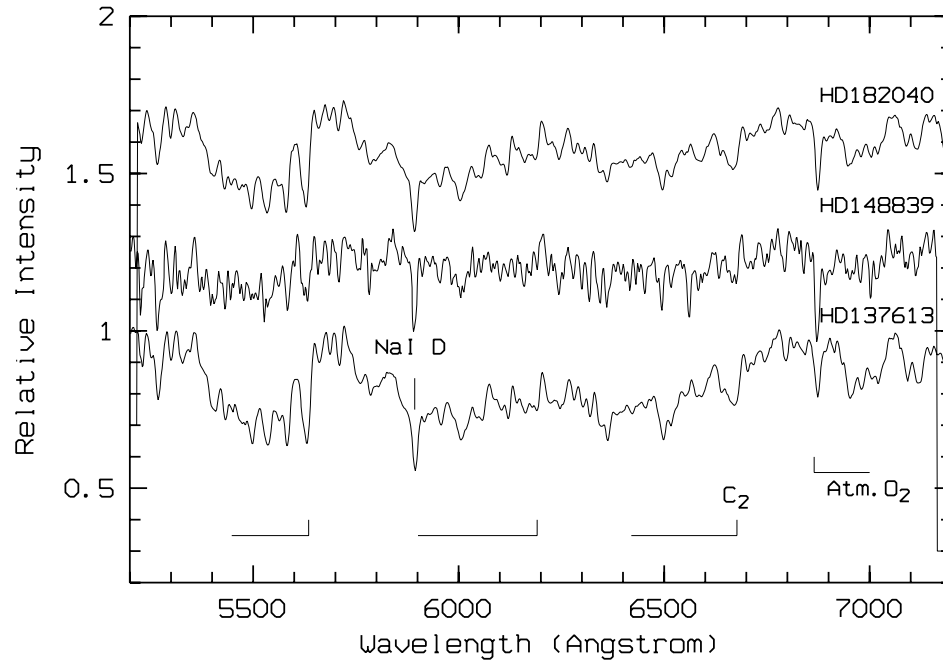
Figure F.8: *Low-resolution spectra of HD 137613, HD 148839 and HD 182040. The position of the NaI D lines and the bandheads of the C_2 Swan system are indicated.*

Acknowledgements

First I would like to thank my supervisor, Peter Cottrell, for suggesting this project to me and for offering his guidance and help throughout the work on this thesis. Peter was always there with his enthusiasm and with useful ideas that helped me to overcome all those problems that every student faces during a work like this.

Since the declines of RCB stars are irregular and unpredictable events, the observations could not be planned in all details and a number of people had to be involved. I would like to thank Pam Kilmartin and Alan Gilmore for obtaining regular photometry of the RCB stars and for informing me about any sudden changes in the stellar magnitudes indicating a possible decline. Pam and Alan were always there to offer their help with the instruments, or simply to keep me company and invite me for a nice meal or an enjoyable chat. John Baker, Stephen Barlow and Nigel Frost were always ready to change the instrument at short notice and to ensure that everything was functioning well. I also want to thank Karen, Michael, Dan, Orlon and Stuart for collecting some important spectra of V854 Cen during their own observing time. Albert Jones provided me with his photometric observations throughout this work and he was informing me regularly about any new declines.

A number of overseas astronomers who visited this department during my work should also be mentioned. Peter Woitke contributed with useful suggestions regarding the material presented in Chapter 6. Numerous discussions with David Lambert and Kameswara Rao helped me to have a better insight into the nature of RCB declines. David also provided three very important high-resolution spectra of V854 Cen.

My time spent in the Department was always enjoyable thanks to the astronomy students: Irene, Lyndon, John, Orlon, Stuart, Dan and others.

Throughout the work on this thesis I was supported by a University of Canterbury Doctoral Scholarship and a Marsden Fund studentship. I would also like to thank Zonta International for an Amelia Earhart Award in 1999. My trip to Europe to attend the IAU Colloquium No. 176 in Budapest and the PhD Conference '99 in Kecskémet, Hungary was supported by: the Frank Bradshaw and Elizabeth Pepper Wood Fund, the Marsden Fund, the Royal Society of New Zealand – Canterbury Branch, the IAU and the Department of Physics and Astronomy.

I have to mention here all my colleagues and friends from Belgrade Observatory, especially

Ištvan, Luka, Gojko, Beba and Jelisaveta, with whom I have had many useful discussions over all these years. Thanks also to my parents and my family in Yugoslavia who have always understood my wish to study astronomy, even if that meant going far away.

Finally, I want to thank Jovan, who made all this worth doing. And our precious little daughter Natasha, who kept waking me up early enough every morning, just to make sure that her mummy was working on her thesis.

References

Alcock C., Allsman R. A., Alves D. R., Axelrod T. S., Becker A., Bennett D. P., Clayton G. C., Cook K. H., Freeman K. C., Griest K., Guern J. A., Kilkenny D., Lehner M. J., Marshall S. L., Minniti D., Peterson B. A., Pratt M. R., Quinn P. J., Rodgers A. W., Stubbs C. W., Sutherland W., Welch D. L., 1996, 'The MACHO project Large Magellanic Cloud variable star inventory IV. New R Coronae Borealis stars', ApJ 470, 583–590

Alcock C., Allsman R. A., Alves D. R., Axelrod T. S., Becker A., Bennett D. P., Clayton G. C., Cook K. H., Dalal N., Drake A. J., Freeman K. C., Geha M., Gordon K. D., Griest K., Kilkenny D., Lehner M. J., Marshall S. L., Minniti D., Missett K. A., Nelson C. A., Peterson B. A., Popowski P., Pratt M. R., Quinn P. J., Stubbs C. W., Sutherland W., Tomaney A., Vandehei T., Welch D. L., 2001, 'The MACHO project LMC variable star inventory X. The R Coronae Borealis stars', ApJ, in press, astro-ph/0102262

Alexander J. B., Andrews P. J., Catchpole R. M., Feast M. W., Lloyd Evans T., Menzies J. W., Wisse P. N. J., Wisse M., 1972, 'A spectroscopic and photometric study of the pulsating R Coronae Borealis type variable, RY Sagittarii', MNRAS 158, 305–360

Amiot C., 1983, 'Fourier spectroscopy of the $^{12}C_2$, $^{13}C_2$ and $^{12}C^{13}C$ (0–0) Swan bands', ApJ Suppl. Ser. 52, 329–340

Asplund M., 1995, 'Spectroscopy of RY Sagittarii during the 1993 minimum', A&A 294, 763–772

Asplund M., 1997, 'Evolution and variability of the R Coronae Borealis stars', PhD thesis, Uppsala University

Asplund M., Gustafsson B., Lambert D. L., Rao N. K., 1997, 'A stellar endgame – the born-again Sakurai's object', A&A 321, L17–L20

Asplund M., Gustafsson B., Rao N. K., Lambert D. L., 1998, 'Abundance similarities between the R CrB star V854 Cen and the born-again Sakurai's object', A&A 332, 651–660

Barnes S. I., Clark M., Cottrell P. L., Hearnshaw J. B., Petterson O. K. L., Pollard K. R., Pritchard J. D., Richards A., Tobin W., 2000, 'Characteristics of the Mt John Series 200 CCD system', Southern Stars 39, 1–8

Beck H., Sedlmayr E., 1998, 'Dust formation in the environments of hot stars', in The molecular astrophysics of stars and galaxies, Hartquist T. W., Williams D. A. (eds.), Clarendon Press, Oxford, p. 371

Bessell M. S., 1979, 'UBVRI photometry II: The Cousins VRI system, its temperature and absolute flux calibration, and relevance for two-dimensional photometry', PASP 91, 589–607

Bessell M. S., 1993, 'Photometric systems', Proceedings of the IAU Colloquium No. 136: 'Stellar photometry – current techniques and future developments', Butler C. J., Elliott I. (eds.), Cambridge University Press, Cambridge, pp. 22–39

Bond H. E., Luck R. E., Newman M. J., 1979, 'The extraordinary composition of U Aquarii', ApJ 233, 205–210

Borghesi A., Bussoletti E., Colangeli L., 1985, 'Amorphous carbon grains: laboratory measurements in the 2000 Å– 40 μm range', A&A 142, 225–231

Brandt S., 1999, 'Data Analysis', Springer-Verlag, New York

Bransden B. H., Joachain C. J., 1983, 'Physics of atoms and molecules', Longman Group Limited, London

Cardelli J. A., Clayton G. C., Mathis J. S., 1988, 'The determination of ultraviolet extinction from the optical and near-infrared', ApJ 329, L33–L37

Cardelli J. A., Clayton G. C., Mathis J. S., 1989, 'The relationship between infrared, optical, and ultraviolet extinction', ApJ 345, 245–256

Clayton G. C., 1996, 'The R Coronae Borealis stars', PASP 108, 225–241

Clayton G. C., Whitney B. A., Stanford S. A., Drilling J. S., Judge P. G., 1992a, 'The unusual ultraviolet chromospheric spectrum of the R Coronae Borealis star, V854 Centauri (NSV 6708), at minimum light', ApJ 384, L19–L23

Clayton G. C., Whitney B. A., Stanford S. A., Drilling J. S., 1992b, 'Observations of R Coronae Borealis stars in decline: Empirical arguments for dust formation near the stellar surface', ApJ 397, 652–663

Clayton G. C., Whitney B. A., Mattei J. A., 1993a, 'Long-term variations in dust production in R Coronae Borealis', PASP 105, 832–835

Clayton G. C., Lawson W. A., Whitney B. A., Pollacco D. L., 1993b, 'High-velocity spectral features in V854 Centauri: evidence for dust formation?', MNRAS 264, L13–L16

Clayton G. C., Lawson W. A., Cottrell P. L., Whitney B. A., Stanford S. A., de Ruyter F., 1994, 'An ultraviolet and visible spectroscopic study of a pulsational cycle of RY Sagittarii', ApJ 432, 785–792

Clayton G. C., Whitney B. A., Meade M. R., Babler B., Bjorkman K. S., Nordsieck K. H., 1995, 'Long-term spectroscopic and photometric monitoring of R Coronae Borealis near maximum light', PASP 107, 416–426

Clayton G. C., Bjorkman K. S., Nordsieck K. H., Zellner N. E. B., Schulte-Ladbeck R. E., 1997, 'Evidence for a bipolar geometry in R Coronae Borealis?', ApJ 476, 870–874

Clayton G. C., Kilkenny D., Welch D. L., 1999a, 'New R Coronae Borealis stars in the LMC, discovered in the MACHO photometry database', Proceedings of the IAU Symposium No. 190: 'New views of the Magellanic Clouds', Chu Y.-H., Suntzeff N., Hesser J., Bohlender D. (eds.), p. 361

Clayton G. C., Ayres T. R., Lawson W. A., Drilling J. S., Woitke P., Asplund M., 1999b, 'First Observations of an R Coronae Borealis Star with the Space Telescope Imaging Spectrograph: RY Sagittarii near Maximum Light', ApJ 515, 351–355

Clayton G. C., Kilkenny D., Welch D. L., 2000, 'New R Coronae Borealis stars in the LMC, discovered in the MACHO photometry database', Proceedings of the IAU Colloquium No. 176: 'The impact of large-scale surveys on pulsating star research', ASP Conference Series, Szabados L., Kurtz D. W. (eds.), pp. 114–115

Collins G. W., 1989, 'The fundamentals of stellar astrophysics', W. H. Freeman and Company, New York

Cottrell P. L., 1996, 'R Coronae Borealis stars: current status of the observational data', Proceedings of the colloquium: 'Hydrogen deficient stars', ASP conference series Vol. 96, Jeffery C. S., Heber U. (eds.), p. 13

Cottrell P. L., Lambert D. L., 1982, 'The chemical composition of R Coronae Borealis and XX Camelopardalis', ApJ 261, 595–611

Cottrell P. L., Lawson W. A., 1998, 'Hipparcos observations of hydrogen-deficient carbon stars', PASA 15, 179–182

Cottrell P. L., Lawson W. A., Buchhorn M., 1990, 'The 1988 decline of R Coronae Borealis', MNRAS 244, 149–167

Cousins A. W. J., 1983, 'UBV photometry of E-region standard stars of intermediate brightness', Circ. South African Astron. Obs. 7, 36–46

Drilling J. S., Hecht J. H., Clayton G. C., Mattei J. A., Landolt A. U., Whitney B. A., 1997, 'The ultraviolet extinction curve for circumstellar dust formed in the hydrogen-poor environment of V348 Sagittarii', ApJ 476, 865–869

Evans A., Whittet D. C. B., Davies J. K., Kilkenny D., Bode M. F., 1985, 'IUE observations of RCB stars during extinction minima', MNRAS 217, 767–778

Fadeyev Yu. A., 1988, 'Carbon dust formation in R Coronae Borealis stars', MNRAS 233, 65–78

Feast M. W., 1975, 'The R Coronae Borealis type variables', Proceedings of the IAU Symposium No. 67: 'Variable stars and stellar evolution', Sherwood V. E., Plaut L. (eds.), D. Reidel Publishing Company, Dordrecht, pp. 129–141

Feast M. W., 1979, 'Recent work on the R-Coronae stars', Proceedings of the IAU Colloquium No. 46: 'Changing trends in variable star research', Bateson F. M., Smak J., Urch I. M. (eds.), University of Waikato, Hamilton, p. 246

Feast M. W., 1997, 'The R Coronae Borealis stars – II. Further inferences from the infrared data', MNRAS 285, 339–357

Fuhr J. R., Martin G. A., Wiese W. L., 1988, 'Atomic transition probabilities: iron through nickel', J. Phys. Chem. Ref. Data 17, Suppl. 4

Glass I. S., 1978, 'The long-term infrared behavior of RCB stars', MNRAS 185, 23

Goncharova R. I., Koval'chuk G. U., Pugach A. F., 1983, 'Cyclic variations of the light of R CrB and their connection with the nonperiodic fadings of the brightness', Astrophysics 19, 161–168

Goswami A., Rao N. K., Lambert D. L., Smith V. V., 1997, 'The spectrum of the cool R Coronae Borealis variable S Apodis in a deep decline', PASP 109, 270–273

Gray D. F., 1992, 'The observation and analysis of stellar photospheres', 2nd edition, Cambridge University Press, Cambridge

Hearnshaw J. B., 1977, 'The Cassegrain échelle spectrograph at Mt John Observatory', Proc. Astron. Soc. Australia 3 (2), 102–103

Hecht J. H., 1991, 'The nature of the dust around R Coronae Borealis stars: Isolated amorphous carbon or graphite fractals?', ApJ 367, 635–640

Hecht J. H., Holm A. V., Donn B., Wu C.-C., 1984, 'The dust around R Coronae Borealis type stars', ApJ 280, 228–234

Hecht J. H., Clayton G. C., Drilling J. S., Jeffery C. S., 1998, 'Ultraviolet observations of the hot R Coronae Borealis-type star V348 Sagittarii during a deep minimum', ApJ 501, 813

Herbig G. H., 1949, 'The spectrum of R Coronae Borealis at the 1948–1949 minimum', ApJ 110, 143–155

Holm A. V., Doherty L. R., 1988, 'Ultraviolet spectroscopy of R Coronae Borealis', ApJ 328, 726–733

Holm A. V., Wu C.-C., Doherty L. R., 1982, 'The circumstellar extinction of RY Sagittarii', PASP 94, 548–552

Holm A. V., Hecht J., Wu C.-C., Donn B., 1987, 'The fading of R Coronae Borealis', PASP 99, 497–508

Humphreys R. M., Ney E. P., 1974, 'Infrared stars in binary systems', ApJ 190, 339–347

Iben I. Jr., Tutukov A. V., Yungelson L. R., 1996, 'On the origin of R CrB and other hydrogen-deficient stars', Proceedings of the colloquium: 'Hydrogen deficient stars', ASP conference series Vol. 96, Jeffery C. S., Heber U. (eds.), p. 409

Jeffery C. S., 1995, 'The ultraviolet properties of cool material ejected by hydrogen-deficient stars', A&A 299, 135–143

Jeffery C. S., 1996, 'Surface properties of extreme helium stars', Proceedings of the colloquium: 'Hydrogen deficient stars', ASP conference series Vol. 96, Jeffery C. S., Heber U. (eds.), p. 152

Joy A. H., Humason M. L., 1923, 'The spectrum of R Coronae at minimu', PASP 35, 325

Kilkenny D., 1995, 'Hydrogen-deficient stars: recent work at the SAAO', Ap&SS 230, 53–61

Kilkenny D., Marang F., 1989, 'NSV 6708: hydrogen in an R Coronae Borealis star', MN-RAS 238, 1P–6P

Kilkenny D., Whittet D. C. B., 1984, 'Infrared photometry and broadband flux distributions of southern R Coronae Borealis stars', MNRAS 208, 25

Kilkenny D., Lloyd Evans T., Bateson F. M., Jones A. F., Lawson W. A., 1992, 'V517 Oph – a probable new RCB star', Obs. 112, 158–161

Krishna Swami K. S., 1997, 'Physics of comets', 2nd edition, World Scientific, Singapore

Kurucz R. L., Bell B., 1993, 'Atomic line data', CD-ROM No. 23, Harvard-Smithsonian Center for Astrophysics, Cambridge, USA

Lambert D. L., 1986, 'The chemical composition of cool stars. II - The hydrogen deficient stars', Proceedings of the IAU Colloquium No. 87: 'Hydrogen deficient stars and related objects', Hunger K., Schönberner D., Rao N. K. (eds.), D. Reidel Publishing Company, Dordrecht, pp. 127–147

Lambert D. L., Rao N. K., 1994, 'The R Coronae Borealis stars – a few mere facts', JApA 15, 47–67

Lambert D. L., Sheffer Y., Danks A. C., Arpigny C., Magain P., 1990a, 'High-resolution spectroscopy of the C_2 Swan 0–0 band from comet P/Halley', ApJ 353, 640–653

Lambert D. L., Rao N. K., Giridhar S., 1990b, 'High resolution spectroscopy of R Coronae Borealis during the 1988–1989 minimum', JApA 11, 475–490

Lamers H. J. G. L. M., Cassinelli J. P., 1999, 'Introduction to stellar winds', Cambridge University Press, Cambridge

Lawson W. A., 1992, 'Spectroscopy of the R Coronae Borealis star V854 Cen through a decline onset', MNRAS 258, 33P–36P

Lawson W. A., Cottrell P. L., 1989, 'The R Coronae Borealis star NSV 6708', MNRAS 240, 689–700

Lawson W. A., Cottrell P. L., Kilmartin P. M., Gilmore A. C., 1990, 'The photometric characteristics of cool hydrogen-deficient carbon stars', MNRAS 247, 91–117

Lawson W. A., Cottrell P. L., Clark M., 1991, 'Radial velocity variations of the R Coronae Borealis star RY Sgr', MNRAS 251, 687–692

Lawson W. A., Cottrell P. L., Gilmore A. C., Kilmartin P. M., 1992, 'Predicting mass-loss events in R Coronae Borealis stars: declines of V854 Cen', MNRAS 256, 339–348

Lawson W. A., Maldoni M. M., Clayton G. C., Valencic L., Jones A. F., Kilkenny D., van Wyk F., Roberts G., Marang F., 1999, 'The fall and rise of V854 Centauri: long-term ultraviolet spectroscopy of a highly active R Coronae Borealis star', AJ 117, 3007–3020

Loreta E., 1934, Astr. Nach. 254, 151

Martin G. A., Fuhr J. R., Wiese W. L., 1988, 'Atomic transition probabilities: scandium through manganese', J. Phys. Chem. Ref. Data 17, Suppl. 3

Mathis J. S., 1990, 'Interstellar dust and extinction', Annu. Rev. Astron. Astrophys. 28, 37–70

McNaught R. H., Dawes G., 1986, 'NSV 6708', IAU Circ. 4233 (ed. Marsden B. G.)

Mihalas D., 1978, 'Stellar atmospheres', 2nd edition, W. H. Freeman and Company, San Francisco

Milone L. A., 1990, 'Identification charts for southern R Coronae Borealis stars', Ap&SS 172, 263–271

Moore C. E., 1972, 'A multiplet table of astrophysical interest', NSRDS-NBS 40, US Department of Commerce, National Bureau of Standards, Washington, D.C.

Moore C. E., 1993, 'Tables of spectra of hydrogen, carbon, nitrogen and oxygen atoms and ions', CRC Press, Boca Raton, Florida, USA

Moore C. E., Minnaert M. G. J., Houtgast J., 1966, 'The solar spectrum 2935 Å to 8770 Å', National Bureau of Standards Monograph, Washington

Nandy K., Thompson G. I., Jamar C., Monfils A., Wilson R., 1975, 'Studies of ultraviolet interstellar extinction with the sky-survey telescope of the TD-1 satellite I. Results for three galactic regions', A&A 44, 195–203

Nankivell G. R., Rumsey N., Hearnshaw J. B., Cottrell P. L., 1986, 'The optical system of the Mt John 1-metre telescope', Proceedings of the IAU Symposium No. 118: 'Instrumentation and research programmes for small telescopes', Hearnshaw J. B., Cottrell P. L. (eds.), D. Reidel Publishing Company, Dordrecht, p. 101

Noyes R. W., Avrett E. H., 1987, 'The solar chromosphere', in Spectroscopy of astrophysical plasmas, Dalgarno A., Layzer D. (eds.), Cambridge University Press, Cambridge, pp. 125–164

O'Keefe J. A., 1939, 'Remarks on Loreta's hypothesis concerning R Coronae Borealis', ApJ 90, 294

Osterbrock D. E., 1974, 'Astrophysics of gaseous nebulae', W. H. Freeman and Company, San Francisco

Palmer B. A., Engleman R. Jr., 1983, 'Atlas of the thorium spectrum', Los Alamos National Laboratory, LA-9615

Pandey G., Rao N. K., Lambert D. L., 1996, 'The emission-line spectrum of the hot R Coronae Borealis star MV Sgr', MNRAS 282, 889–899

Payne-Gaposchkin C., 1963, 'The 1960 minimum of R Coronae Borealis', ApJ 138, 320–341

Pearse R. W. B., Gaydon A. G., 1976, 'The identification of molecular spectra', 4$^{\text{th}}$ edition, Chapman and Hall, London

Pigott E., 1797, Phil. Trans. Roy. Soc. Part I, 133

Pollacco D. L., Tadhunter C. N., Hill P. W., 1990, 'The evolutionary status of the peculiar variable star V348 Sagittarii', MNRAS 245, 204–216

Pollacco D. L., Hill P. W., Houziaux L., Manfroid J., 1991, 'Nebulae around R Coronae Borealis stars – clues to their evolutionary status?', MNRAS 248, 1P–4P

Pollard K. R., 1994, 'The nature of the low mass supergiants: RV Tauri and R Coronae Borealis variables', PhD thesis, University of Canterbury

Pollard K. R., Cottrell P. L., Lawson W. A., 1994, 'An abundance analysis of R Coronae Borealis stars in the Galaxy and the LMC', MNRAS 268, 544–560

Pritchard J. D., 1997, 'CCD photometry of eclipsing binary star systems in the Large and Small Magellanic Clouds', PhD thesis, University of Canterbury

Pugach A. F., 1984, 'A model of the R Coronae Borealis phenomenon', Sov. Astron. 28, 288–293 (also: Astron. Zh. 61, 491, in Russian)

Pugach A. F., 1990, 'Interpretation of photometric observations of R Coronae Borealis. Light curves', Sov. Astron. 34, 646–649 (also: Astron. Zh. 67, 1280, in Russian)

Pugach A. F., 1991, 'Interpretation of photometric observations of R Coronae Borealis. Color features', Sov. Astron. 35, 61–65 (also: Astron. Zh. 68, 122, in Russian)

Pugach A. F., 1992, 'Interpretation of photometric observations of R Coronae Borealis. A noncentral eclipse by an inhomogeneous cloud', Sov. Astron. 36, 612–618 (also: Astron. Zh. 69, 1195, in Russian)

Pugach A. F., Koval'chuk G. U., 1994, 'Interpretation of R Coronae Borealis photometric observations: The synthetic light curve', Astron. Rep. 38, 219–224 (also: Astron. Zh. 71, 250, in Russian)

Pugach A. F., Skarzhevskii V. O., 1993, 'Interpretation of photometric observations of R Coronae Borealis. Approximation tables', Sov. Astron. 37, 169–175 (also: Astron. Zh. 70, 327, in Russian)

Rao N. K., Lambert D. L., 1993, 'High resolution spectroscopy of the R Coronae Borealis star, V854 Centauri, during a deep minimum', AJ 105, 1915–1926

Rao N. K., Lambert D. L., 1997, 'High-resolution spectroscopy of R CrB – pulsations, shells and mass loss', MNRAS 284, 489–498

Rao N. K., Lambert D. L., 2000, 'High-resolution spectroscopy of V854 Cen in decline – absorption and emission lines of C_2 molecules', MNRAS 313, L33–L37

Rao N. K., Lambert D. L., Adams M. T., Doss D. R., Gonzalez G., Hatzes A. P., James C. R., Johns-Krull C. M., Luck R. E., Pandey G., Reinsch K., Tomkin J., Woolf V. M., 1999, 'The 1995–96 decline of R Coronae Borealis: high-resolution optical spectroscopy', MNRAS 310, 717–744

Reader J., Corliss C. H., 1980, 'Wavelengths and transition probabilities for atoms and atomic ions, Part I. Wavelengths', NSRDS – National Standard Reference Data System

Renzini A., 1990, 'Evolutionary scenarios for R CrB stars', Proceedings of the colloquium: 'Confrontation between stellar pulsation and evolution', ASP conference series Vol. 11, p. 549

Rieke G. H., Lebofsky M. J., 1985, 'The interstellar extinction law from 1 to 13 microns', ApJ 288, 618–621

Schatzman E. L., Praderie F., 1993, 'The stars', Springer-Verlag, Berlin

Scheffler H., Elsässer H., 1987, 'Physics of the Galaxy and interstellar matter', Springer-Verlag, Berlin

Schönberner D., 1986, 'Evolutionary status and origin of extremely hydrogen-deficient stars', Proceedings of the IAU Colloquium No. 87: 'Hydrogen deficient stars and related objects', Hunger K., Schönberner D., Rao N. K. (eds.), D. Reidel Publishing Company, Dordrecht, pp. 471–480

Schönberner D., 1996, 'How are hydrogen-deficient stars formed?', Proceedings of the colloquium: 'Hydrogen deficient stars', ASP conference series Vol. 96, Jeffery C. S., Heber U. (eds.), pp. 433–442

Schott G., 1989, 'Optical Glass Filters', Schott Glaswerke, Mainz, Germany

Seaton M. J., 1979, 'Interstellar extinction in the UV', MNRAS 187, 73P–76P

Skuljan J., 1999, 'A study of moving groups of stars in our Galaxy', PhD thesis, University of Canterbury

Skuljan Lj., Cottrell P. L., 1999, 'Spectroscopic and photometric observations of the R Coronae Borealis stars S Apodis and RZ Normae throughout their recent declines', MNRAS 302, 341–348

Skuljan Lj., Cottrell P. L., 2000a, 'Photometry of R Coronae Borealis stars during the recovery phases of their declines', Proceedings of the IAU Colloquium No. 176: 'The impact of large-scale surveys on pulsating star research', ASP Conference Series, Szabados L., Kurtz D. W. (eds.), pp. 113–113

Skuljan Lj., Cottrell P. L., 2000b, 'Spectroscopy of R Coronae Borealis stars during their declines', Proceedings of the PhD Conference'99: 'The variable stars' Kecskémet, Hungary (in press)

Sobolev V. V., 1958, 'The formation of emission lines', Pergammon Press, New York

Soker N., Clayton G. C., 1999, 'Dust formation above cool magnetic spots in evolved stars', MNRAS 307, 993–1000

Spite F., Spite M., 1979, 'Spectra of RY Sgr near minimum light', A&A 80, 61

Strömgren B., 1948, 'On the density distribution and chemical composition of the interstellar gas', ApJ 108, 242–275

Surenndiranath R., Rangarajan K. E., Rao N. K., 1986, 'Preliminary analysis of the broad HeI emission lines in R CrB', Proceedings of the IAU Colloquium No. 87: 'Hydrogen deficient stars and related objects', Hunger K., Schönberner D., Rao N. K. (eds.), D. Reidel Publishing Company, Dordrecht, p. 199

Tobin W., 1992, 'Gain, noise and related characteristics of the Mt John Photometrics CCD system', Southern Stars 34 (8), 421–429

Tobin W., Hearnshaw J. B., Kershaw G. M., Nankivell G. R., Persson S., Rumsey N., Thirkettle R., 1998, 'A focal reducer for the Mt John échelle spectrograph', Southern Stars 37 (7), 197–205

Trimble V., Kundu A., 1997, 'Parallaxes and proper motions of prototypes of astrophysically interesting classes of stars. I. R Coronae Borealis variables', PASP 109, 1089–1092

Tull R. G., MacQueen P. J., Sneden C., Lambert D. L., 1995, 'The high-resolution cross-dispersed échelle white-pupil spectrometer of the McDonald Observatory 2.7-m telescope', PASP 107, 251–264

Vanture A. D., Wallerstein G., 1995, 'A spectrum of RY Sgr during recovery from its 1993 minimum', PASP 107, 244–249

Walker H. J., 1985, 'IRAS photometry of dust shells around hydrogen-deficient stars', A&A 152, 58

Wamsteker W., 1981, 'Standard stars and calibration for JHKLM photometry', A&A 97, 329–333

Warner B., 1967, 'The hydrogen-deficient carbon stars', MNRAS 137, 119

Webbink R. F., 1984, 'Double white dwarfs as progenitors of R Coronae Borealis stars and Type I supernovae', ApJ 277, 355

Weiss A., 1987, 'Linear nonadiabatic pulsations of R CrB models', A&A 185, 178

Whitney B. A., Clayton G. C., Schulte-Ladbeck R. E., Meade M. R., 1992, 'Spectropolarimetry of V854 Centauri at minimum light: clues to the geometry of the dust and emission-line region', AJ 103, 1652–1657

Wiese W. L., Martin G. A., 1980, 'Wavelengths and transition probabilities for atoms and atomic ions, Part II. Transition probabilities', NSRDS – National Standard Reference Data System

Wiese W. L., Smith M. W., Miles B. M., 1969, 'Atomic transition probabilities Vol. 2: sodium through calcium. A critical data compilation', NSRDS-NBS 22, US Department of Commerce, National Bureau of Standards, Washington, D.C.

Wilson O. C., Merrill P. W., 1937, 'Analysis of the intensities of the interstellar D lines', ApJ 86, 44–69

Wing R. F., Baumert J. H., Strom S. E., Strom K. M., 1972, 'Infrared photometry of R CrB during its recent decline', PASP 84, 646–647

Woitke P., 1997, 'Radiative heating and cooling in circumstellar envelopes', PhD thesis, Technische Universität Berlin

Woitke P., 1998, 'Time-dependent behavior of cool-star winds', Proceedings of the ESO Workshop: 'Cyclical variability in stellar winds', Kaper L., Fullerton A. W. (eds.), Springer-Verlag, Berlin, p. 278

Woitke P., Goeres A., Sedlmayr E., 1996, 'On the gas temperature in the shocked circumstellar envelopes of pulsating stars II. Shock induced condensation around R Coronae Borealis stars', A&A 313, 217–228

Zubko V. G., 1997, 'On the interpretation of the extinction curves of R Coronae Borealis stars', MNRAS 289, 305–317